THE USE OF BOREHOLE TEMPERATURE MEASUREMENTS TO INFER CLIMATIC CHANGES IN ARCTIC ALASKA

by

Gary D. Clow

A dissertation submitted to the faculty of
The University of Utah
in partial fulfillment of the requirements for the degree of

Doctor of Philosophy

in

Geophysics

Department of Geology and Geophysics

The University of Utah

May 2017

The University of Utah Graduate School

STATEMENT OF DISSERTATION APPROVAL

The dissertation of **Gary D. Clow**
has been approved by the following supervisory committee members:

Thure E. Cerling and David S. Chapman ,	Chairs	**9 Jan 2017** Date Approved
Douglas Kip Solomon ,	Member	**9 Jan 2017** Date Approved
Edwin D. Waddington ,	Member	**9 Jan 2017** Date Approved
Michael S. Zhdanov ,	Member	**9 Jan 2017** Date Approved

by **Thure E. Cerling** , Chair/Dean of
the Department/College/School of **Geology and Geophysics**
and by **David B. Kieda** , Dean of The Graduate School.

ABSTRACT

Periodic temperature measurements in the DOI/GTN-P Deep Borehole Array on the western Arctic Slope of Alaska have shown a strong near-surface permafrost warming over the last 40 years, particularly since $\sim$ 1990. Due to the manner in which these deep wells were drilled, the portion of the observed permafrost warming caused by climate change has remained unclear. Other factors that have strongly influenced temperatures near the wellbores include the heat deposited into permafrost during drilling and local-landscape changes associated with drilling operations (creation of reserve pits and drill pads). Multidimensional heat-transfer models capable of assessing the magnitude of the drilling and local-landscape disturbances near the wellbores have not been available. For the western Arctic Slope, such models must be capable of simulating heat-transfer processes in layered fine-grained mudrocks whose thermal properties are highly nonlinear due to the occurrence of unfrozen water at temperatures well below 0°C. An assessment of the drilling and landscape-change effects also requires knowledge of the specific thermophysical properties occurring at the well sites. Little information has been available about these properties on the western Arctic Slope.

To establish the portion of the observed permafrost warming related to drilling and landscape-change effects, multidimensional (2-D cylindrical, 3-D cartesian) numerical heat-transfer models were created that simulate heat flow in layered heterogenous materials surrounding a wellbore, phase changes, and the unfrozen water properties of a wide range of fine-grained sediments. Using these models in conjunction with the borehole temperature measurements, the mean thermophysical properties of permafrost rock units on the western Arctic Slope were determined using an optimization process. Incorporation of local meteorological information into the optimization allows a more refined estimate of the thermal properties to be determined at a well site. Applying this methodology to the East Simpson #1 well on the Beaufort Sea coast (70°55.046′N, 154°37.286′W), the freezing point of permafrost is found to be -1.05°C at this site and thermal diffusivities

range 0.22–0.40 $\times 10^{-6}\,\mathrm{m^2\,s^{-1}}$. Accounting for the drilling and landscape-change effects, tundra adjacent to East Simpson is found to have warmed 5.1 K since the mid-1880s. Of this, 3.1 K (60%) of the warming has occurred since 1970.

CONTENTS

LIST OF TABLES

CHAPTER 1

INTRODUCTION

From 1975 to 1981, 28 test wells were drilled in the National Petroleum Reserve–Alaska (NPR-A) as part of a petroleum exploration program overseen by the U.S. Department of the Interior [*Gryc*, 1988]. These 1–6 km deep wells penetrated marine and nonmarine sedimentary sequences between the Brooks Range and the Arctic Ocean. Most of the well sites are located on the low-lying Arctic Coastal Plain while a few are in the rolling foothills to the south. Permafrost in this area is 'continuous', being 200–400 m thick. Wells drilled by the petroleum industry on the Arctic Slope were almost always either put into production or plugged and abandoned long before the wells could return to thermal equilibrium. Realizing the NPR-A test wells provided a rare opportunity to obtain 'undisturbed' temperatures in permafrost, the U.S. Geological Survey (USGS) requested that 21 of the wells (**Figure 1.1**) be completed in a manner that would allow high-precision temperature measurements to be made over many years. This involved filling the borehole casing with a nonfreezing fluid (diesel oil) above a cement plug installed 200–900 m below the surface, depending on the well. Information obtained from the borehole temperature measurements was expected to provide better estimates for the depth of permafrost and of the physical conditions controlling the occurrence of ice, unfrozen water, and gas hydrates in permafrost than were currently available.

After monitoring temperatures in these wells for several years, it became clear that the temperature profiles also contained evidence of recent climate change in arctic Alaska. Without the disruptive effects of groundwater flow, thick continuous permafrost provides an excellent medium in which to capture the subsurface thermal response to temperature changes on the earth's surface. Using this idea and temperatures from the NPR-A monitoring wells and from the nearby Prudhoe Bay oil field, Art Lachenbruch published a series of papers in the 1980s [*Lachenbruch et al.*, 1982; *Lachenbruch and Marshall*, 1986; *Lachenbruch et*

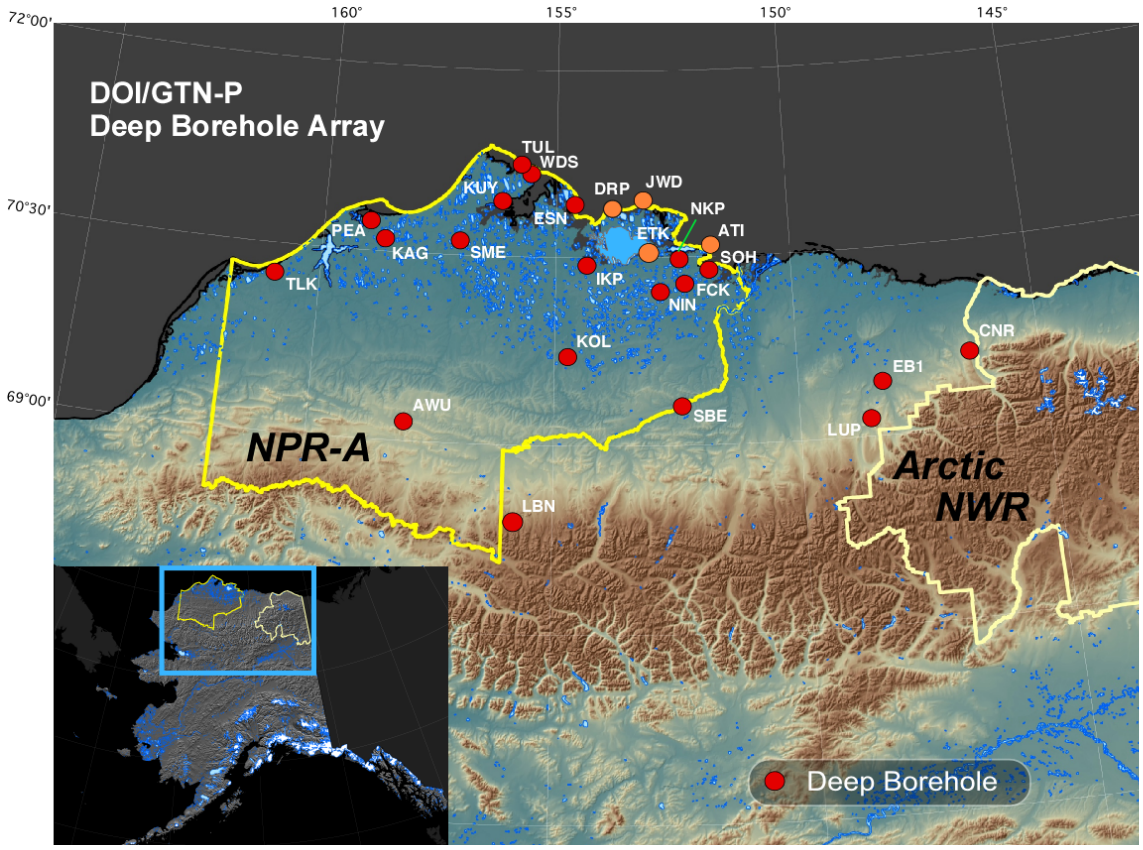

Figure 1.1: Location of the DOI/GTN-P boreholes used to monitor the thermal state of permafrost on the Arctic Slope of Alaska. Those located in the National Petroleum Reserve–Alaska (NPR-A) are the focus of the current study.

al., 1988] in which he inferred that surface temperatures in the Alaskan Arctic had warmed 2–4 K during the previous few decades. Given the paucity of long-term instrumental records in the Arctic documenting recent climate change, Lachenbruch's work was particularly important.

By the late 1990s and early 2000s, atmosphere-ocean general circulation models (AOGCMs) were consistently projecting that the largest climate changes during this century will occur in the Arctic, especially in arctic Alaska and the adjacent Bering, Beaufort, and Chukchi Seas [*IPCC*, 2001; *Chapman and Walsh*, 2007; *Walsh*, 2008]. If the climate projections are correct, every aspect of the arctic environment is expected to be significantly affected over the next few decades [*ACIA*, 2004; *Clow et al.*, 2011]. This region is particularly vulnerable to climate change and its impacts due to the prevalence of ice-rich permafrost which is projected to degrade significantly during this century [*USARC*, 2003; *Lawrence et*

al., 2008]; in the Arctic, permafrost forms the foundation upon which terrestrial ecosystems and human infrastructure are built. Improved understanding of the climate system also showed that the Arctic, although relatively small, can have a significant impact on the global climate system through ice-albedo feedbacks and the potential loss to the atmosphere of vast amounts of methane (a potent greenhouse gas) stored in permafrost.

Given the potential severity of climate impacts in arctic Alaska, plans were made to resume temperature measurements in the NPR-A wells after a decade-long hiatus. In 1999, the 21 NPR-A wells were incorporated into the Global Terrestrial Network for Permafrost (GTN-P), a new component of the Global Climate Observing System (GCOS) and one of its primary subnetworks, the Global Terrestrial Observing System (GTOS). This formalized the use of the borehole array for monitoring the thermal state of permafrost (TSP), one of the Essential Climate Variables (ECVs) tracked by the global climate observing systems [*Sessa and Dolman*, 2008; *Smith and Brown*, 2009]. Upon inclusion into GTN-P, the NPR-A wells became the largest array of deep ($>$ 125 m) boreholes in the world used for monitoring temperatures in permafrost [*IPA*, 2010]. The array is unique in that it also provides one of the longest records of permafrost thermal state. As management of the array was shared by two U.S. Department of the Interior (DOI) agencies (USGS and the Bureau of Land Management), the array became known as the DOI/GTN-P Deep Borehole Array. About the same time, USGS also began deploying automated climate-monitoring stations in the NPR-A to better understand the nature of the recent permafrost warming observed there. Periodic temperature measurements in the borehole array resumed in 2002. With the advent of GTN-P, the purpose of the borehole array had shifted from trying to reconstruct past climate changes through 'borehole paleothermometry', to one of monitoring changes in the thermal state of permafrost in this globally important data-sparse region.

Although the continuous permafrost of arctic Alaska is in some ways an ideal medium in which to monitor for climate change, there remain several challenges to correctly interpret the temperature data from the NPR-A wells. These challenges include: (a) Little information is available about the thermophysical properties of permafrost found in the NPR-A. In contrast to nearby Prudhoe Bay, permafrost in the NPR-A consists of fine-grained sediments. Phase-change effects in fine-grained permafrost are complicated by the existence of unfrozen water which can exist at temperatures as low as -15°C, depending

on the porosity and sediment texture [*Davis*, 2001; *Watanabe and Mizoguchi*, 2002]. This behavior produces strong nonlinear volumetric heat capacities and thermal diffusivities that must be accounted for in any thermal model used to interpret the NPR-A temperature data. Some 1-D numerical heat-transfer models do exist for fine-grained permafrost. However, application of these models to the interpretation of NPR-A borehole temperature data is limited by our lack of knowledge about the thermophysical properties of materials present at the well sites. (b) Since it is the climate signal we're interested in, the large thermal disturbance caused by drilling these deep exploration wells must be determined and corrected for. However, none of the existing drilling-disturbance models can simulate the intermittent drilling schedule that was necessary for some of the deeper wells, the effect of the earth's surface on the drilling disturbance in the upper 100 m where the climate signal occurs, or the phase-change effects that occur around the wellbores while drilling through permafrost. (c) Drilling operations in the NPR-A during the 1970s and 1980s required the construction of a reserve pit to handle the circulating drilling muds and a drill pad to support the drilling rig and camp. These landscape-change features largely remain to this day. The magnitude of thermal disturbance at the wellbore caused by the reserve pits and drilling pads is sensitive to the thermophysical properties of the permafrost surrounding the well. Even if the thermal properties were known, a multidimensional heat-transfer model would be required to account for the strong lateral heat flow effects expected around the reserve pits and drill pads. No such heat-transfer model exists for fine-grained permafrost.

The purpose of the current study is to resolve these issues so that we can ultimately extract the climate signal from the borehole temperature measurements made in arctic Alaska over the past 40 years. The temperature logging system used to make the measurements since 2002 was actually developed for another purpose, reconstructing past temperature changes over the polar ice sheets using geophysical inverse methods [*Cuffey et al.*, 1995; *Cuffey and Clow*, 1997; *Dahl-Jensen et al.*, 1998]. When applied to climate reconstruction, these methods are now referred to as 'borehole paleothermometry'. **Chapter 2** of this dissertation utilizes Backus-Gilbert inverse methods to assess our ability to detect (or resolve) past climate changes using borehole temperature measurements. This analysis provided the design requirements for a new temperature-logging system developed specifically

for borehole paleothermometry. **Chapter 3** provides a description of the new logging system and a detailed analysis of the measurement uncertainties. Several different logging systems and methods were used to acquire the pre-2002 temperature measurements in the NPR-A boreholes. **Chapter 4** discusses the creation of a homogeneous data set from the measurements obtained by these disparate logging systems. This includes a discussion of the data processing methods used with the different measurement systems. **Chapter 5** presents a new 2-D analytical method for assessing the magnitude of the thermal drilling disturbance caused by drilling deep boreholes and the rate at which the disturbance dissipates. The method accounts for a variety of conditions at the borehole wall, intermittent drilling schedules, phase changes in the surrounding medium, and vertical heat-transfer effects in addition to the radial. **Chapter 6** provides a new 3-D analytical method for determining the subsurface thermal disturbance due to landscape changes. This method is used to estimate the thermal effects of the reserve pits and drill pads associated with the NPR-A boreholes, of the moving shoreline near the coastal wells, and of the eroding reserve pit wall at the Awuna well in the Arctic Foothills. The physics underpinning a new heat-transfer model for fine-grained permafrost is described in **Chapter 7**. Numerical implementation of the model in the following coordinate systems is described: 1-D and 3-D cartesian, 1-D radial, and 2-D cylindrical. **Chapter 8** provides an overview of the geologic setting of the western Arctic Slope (NPR-A). In addition, it provides constraints on the sediment texture, porosity, and grain thermal conductivity of permafrost deeper than $\sim$ 50 m at each of the NPR-A well sites using a transient heat-flow analysis of the drilling-corrected temperature logs. The 2-D cylindrical permafrost model (Chapter 7) is used in conjunction with the drilling-corrected temperature logs to locate the base of ice-rich permafrost (B-IRP) and associated permafrost freezing point at each of the well sites. **Chapter 9** presents the 'site calibration' method used to determine the thermal properties of the upper 50 m of permafrost and the temperature offset between the drill pad and surrounding tundra at a well site. With this calibration, the climate signal can be extracted from the borehole temperature measurements. This includes an estimate of the local mean surface temperature during the 1800s (end of the Little Ice Age), the temperature increase between the LIA and the drilling of the hole ($\sim$ 1980), the temperature change between $\sim$ 1980 and the present, and the local long-term difference between 3-m air temperatures

and 120-cm ground temperatures which is related to characteristics of the seasonal snowpack. The method is subsequently applied to the East Simpson No. 1 well on the Beaufort Sea coast and the implications of the results discussed. Finally, **Chapter 10** summarizes the findings of this study.

1.1 References

ACIA (2004), *Impacts of a Warming Arctic, Arctic Climate Impact Assessment*, Cambridge University Press, Cambridge, United Kingdom, 1046 pp.

Chapman, W.L., and Walsh, J.E. (2007), Simulations of arctic temperature and pressure by global coupled models, *J. Climate*, 20, 609–632.

Clow, G.D., DeGange, A.R., Derksen, D.V., and Zimmerman, C.E. (2011), Climate Change Considerations, in *An Evaluation of the Science Needs to Inform Decisions on Outer Continental Shelf Energy Development in the Chukchi and Beaufort Seas, Alaska*, edited by Holland-Bartels, L., and Pierce, B., U.S. Geological Survey Circular 1370, p. 81–108.

Cuffey, K.M., Clow, G.D., Alley, R.B., Stuiver, M., Waddington, E.D., and Saltus, R.W. (1995), Large arctic temperature change at the Wisconsin-Holocene glacial transition, *Science*, 270, 455–458, doi:10.1126/science.270.5235.455.

Cuffey, K.M., and Clow, G.D. (1997), Temperature, accumulation, and ice sheet elevation in central Greenland through the last deglacial transition, *J. Geophys. Res. Oceans*, 102, 26,383–26,396, doi:10.1029/96JC03981.

Dahl-Jensen, D., Mosegaard, K., Gundestrup, N., Clow, G.D., Johnsen, S.J., Hansen, A.W., and Balling, N. (1998), Past temperatures directly from the Greenland ice sheet, *Science*, 282, 268–271, doi:10.1126/science.282.5387.268.

Davis, N. (2001), *Permafrost - A Guide to Frozen Ground in Transition*, Univ. of Alaska Press, Fairbanks, 351 pp.

Gryc, G. (1988), Geology and exploration of the National Petroleum Reserve in Alaska, 1974 to 1982, *USGS Professional Paper 1399*, U.S. Geological Survey, 940 pp.

International Permafrost Association (2010), IPA-IPY thermal state of permafrost (TSP) snapshot borehole inventory, National Snow and Ice Data Center, Boulder, Colorado USA, doi:10.7265/N57D2S25.

IPCC (2001), *Climate Change 2001: The Scientific Basis. Contribution of Working Group I to the Third Assessment Report of the Intergovernmental Panel on Climate Change*, edited by Houghton et al., Cambridge University Press, Cambridge, United Kingdom and New York, NY, USA, 881 pp.

Lachenbruch, A.H., and Marshall, B.V. (1986), Changing climate: geothermal evidence from permafrost in the alaskan Arctic, *Science*, 234, 689–696.

Lachenbruch, A.H., Sass, J.H., Marshall, B.V., and Moses, T.H., Jr. (1982), Permafrost, heat flow, and the geothermal regime at Prudhoe Bay, Alaska, *J. Geophys. Res.*, 87, 9301–9316.

Lachenbruch, A.H., Cladouhos, T.T, and Saltus, R.W. (1988), Permafrost temperature and the changing climate, in *Proceedings of the Fifth International Conference on Permafrost*, Trondheim, Norway, 2–5 August 1988, vol. 3, 9–17.

Lawrence, D.M., Slater, A.G., Tomas, R.A., Holland, M.M., and Deser, C. (2008), Accelerated arctic land warming and permafrost degradation during rapid sea ice loss, *Geophys. Res. Lett.*, 35, L11506, doi:10.1029/2008GL033985.

Sessa, R., and Dolman, H. (eds.), (2008), Terrestrial essential climate variables for climate change assessment, mitigation and adaption, *GTOS 52*, Global Terrestrial Observing System, Food and Agricultural Organization of the United Nations, Rome.

Smith, S., and Brown, J. (2009), Assessment of the status of the development of the standards for the Terrestrial Essential Climate Variables - T7 - Permafrost and seasonally frozen ground, *GTOS 62*, Global Terrestrial Observing System, Food and Agricultural Organization of the United Nations, Rome.

U.S. Arctic Research Commission (2003), Climate Change, Permafrost, and Impacts on Civil Infrastructure, *USARC Special Report 01-03*, U.S. Arctic Research Commission, 63 pp.

Walsh, J.E. (2008), Climate of the arctic marine environment, *Ecological Applications*, 18(2) Supplement, S3–S22.

Watanabe, K., and Mizoguchi, M. (2002), Amount of unfrozen water in frozen porous media saturated with solution, *Cold Reg. Sci. Technol.*, 34, 103–110.

CHAPTER 2

RESOLVING POWER OF BOREHOLE TEMPERATURE MEASUREMENTS FOR CLIMATE-CHANGE DETECTION

2.1 Abstract

The ability of borehole temperature data to resolve past climatic events is investigated using Backus-Gilbert inversion methods. Two experimental approaches are considered: 1) the data consist of a single borehole temperature profile, and 2) the data consist of climatically-induced temperature transients measured within a borehole during a monitoring experiment. The sensitivity of the data's resolving power to the vertical distribution of the measurements, temperature measurement errors, the inclusion of a local meteorological record, and the duration of a monitoring experiment, are investigated. The results can be used to help interpret existing surface temperature histories derived from borehole temperature data and to optimize future experiments for the detection of climatic signals.*

2.2 Introduction

Do we have the resolving power to detect past climatic events of duration dt utilizing present-day borehole-temperature measurements? Just how clearly can we see back in time? Compared with other climatic-reconstruction methods (e.g., tree-ring and isotopic methods), the resolving power of borehole-temperature (BT) measurements is relatively poor. This is primarily a consequence of the heat diffusion process. Uncertainties in the temperature measurements further degrade the resolving power of the data. Thus, *any* ground surface temperature (GST) history derived from a set of BT measurements will be

---

*This chapter was originally published as: Clow, G.D. (1992), The extent of temporal smearing in surface-temperature histories derived from borehole temperature measurements, *Palaeogeography, Palaeoclimatology, Palaeoecology*, 98, 81–86.

a temporally "smeared" rendition of the actual GST history that occurred in the vicinity of the borehole. It is of fundamental importance to quantify the degree of temporal smearing when attempting to define the character of past climatic changes from a set of borehole temperatures.

This research note presents results from a study to assess the amount of temporal detail that is potentially available in a GST history derived from a set of borehole-temperature measurements. Two experimental approaches are considered. In the first, the data consist of the climatic component of a single BT profile (i.e., assume the steady-state effects due to thermal conductivity variations, topography, etc. have been accounted for). In the second approach, the data consist of the temperature transients ($\partial T/\partial t$) presently occurring at depth in response to past climatic changes, where T is the temperature and t is time. These transients are assumed to be measured either by monitoring a fixed thermistor string in a borehole or through precision relogging where great care has been taken to accurately relocate the measurement depths. For the single profile approach, we investigate the sensitivity of the resolving power to the vertical distribution of the measurements, the temperature-measurement uncertainty σ, and the possible availability of a local meteorological record. For the second approach, the sensitivity of the resolving power to the length of the monitoring period Δt is investigated. This assessment has two objectives: 1) To provide an interpreter with the means for determining if a climatic event in a proposed GST history may be real or if its duration is simply too short to be resolved by the available data. Several cases exist in the literature from various scientific fields where models have been proposed with far too much detail, considering the data from which they were derived. 2) To establish criteria for optimizing BT experiments specifically for the detection of past climatic events.

2.3 Methods

The physical model employed in this analysis is simply a 1-dimensional homogeneous half-space in which heat transfer is solely by conduction. The data consist of temperature measurements distributed over N depths ($z_i;\ i = 1, N$) for the single-profile experiments. For the monitoring experiments, the data consist of temperature transients $(\Delta T/\Delta t)_i$ recorded over a period Δt at each of the N depths. In either case, the uncertainty

σ in the temperature measurements is assumed to be independent of depth. In order to reduce computer time, the measurement depths were distributed such that the ratio (z_{i+1}/z_i) remained fixed for all i, rather than spacing them evenly. With this distribution, each data point contributes an identical amount of information to a reconstructed GST history.†

Given the physical model and the locations of the temperature measurements, Backus-Gilbert inversion methods [*Backus and Gilbert*, 1968, 1970] were used to assess the resolving power of the BT data. Because the inverse problem is linear (as cast), an *estimate* of the surface temperature at some time τ_o in the past can be expressed as a weighted average of the *true* GST history $T_s(\tau)$ in the vicinity of τ_o

$$< T_s(\tau_o) > \; = \int \tilde{\delta}(\tau, \tau_o) T_s(\tau) d\tau, \tag{2.1}$$

where $\tilde{\delta}(\tau, \tau_o)$ is the resolving function associated with time τ_o. A quantity known as the *spread* is defined,

$$S(\tau_o) = 12 \int [(\tau - \tau_o)\, \tilde{\delta}(\tau, \tau_o)]^2 d\tau, \tag{2.2}$$

which provides a measure of the finest detail that can be resolved at τ_o; $S(\tau_o)$ has units of time in the present context. Climatic events occurring in the vicinity of τ_o with duration less than $S(\tau_o)$ cannot be resolved by the available data. The Backus-Gilbert methods provide the means for determining the most delta-like resolving functions consistent with the physics of the problem, the spatial distribution of the data, and the measurement uncertainties, and hence establishes the optimal resolution (minimum spread) that can be achieved using as given dataset.

This analysis assumes that the information about the local GST history is extracted entirely from the borehole temperature data. In some cases, additional information about the GST history can be incorporated into the Backus-Gilbert analysis (e.g., the inclusion of meteorological data, discussed below), allowing us to assess how this a priori informa-

---

†When $(z_{i+1}/z_i) =$ constant $\forall_i$, the angle

$$\psi = cos^{-1}[\frac{< G_i, G_{i+1} >}{\| G_i \| \| G_{i+1} \|}]$$

between adjacent data kernels G_i, G_{i+1} is constant $\forall_i$, at least when the data consist of a single borehole temperature profile. The data kernels are thus as independent of one another as possible. See for example *Dorman and Lewis* [1972].

tion improves our resolving power. However, many forms of a priori information that constrain either the timing or magnitude of past GST changes cannot be incorporated into the Backus-Gilbert analysis. An example of such information is the timing and general magnitude of the last ice age, provided by ice and deep-sea sediment cores. GST inversions incorporating such a priori information may be capable of resolving features with more detail than is suggested by the Backus-Gilbert analysis. Formal inversions of BT data currently do not incorporate past climatic events as a priori information. Thus, the GST histories published to date, resulting from any of the presently used inversion techniques, e.g., Functional Space Inversion [*Shen and Beck*, 1991], Spectral Inversion [*Wang*, 1992], and Control Theory [*MacAyeal et al.*, 1991], are bound by the resolution constraints determined by the Backus and Gilbert methods.

2.4 Results

2.4.1 Single BT-profile experiments

Figure 2.1 shows how the spread $S(\tau_o)$, calculated for climatic events at time τ_o in the past, depends on the location of the deepest measurement point to be utilized in a GST inversion, η_N, and on the error-amplification factor (σ_T/σ), where σ_T is the uncertainty in a calculated GST history. Depth is expressed in the dimensionless form

$$\eta = \frac{z}{\sqrt{4\kappa\tau_o}}, \tag{2.3}$$

where κ is the thermal diffusivity. If the lower section of a BT profile is used to define the long-term equilibrium profile $T_e(z) = T_o + \Gamma z$ [see *Lachenbruch and Marshall*, 1986], η_N may be regarded as the deepest point just above the section used to define $T_e(z)$. The error-amplification factor expresses the extent to which uncertainties in the temperature data (σ) propagate into a GST history derived from the data. Given the magnitude of the climate signals we are trying to detect and the level of uncertainty typically present in current temperature measurements, the nominal range of interest for (σ_T/σ) is roughly 10–500.

As shown in **Figure 2.1**, our ability to resolve events in the vicinity of time τ_o is optimal if η_N is greater than ~ 3.0. The resolving power progressively degrades for smaller values of η_N and becomes essentially nonexistent $[S(\tau_o) > \tau_o]$ when $\eta_N < 1.7$. As expected, the resolving power can be improved by accepting a larger uncertainty σ_T in a derived GST

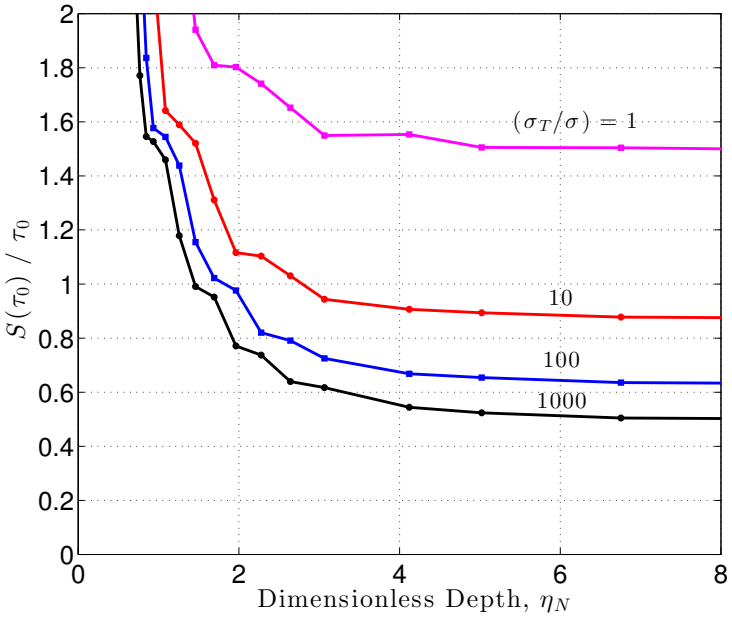

Figure 2.1: Sensitivity of the fractional spread $S(\tau_o)/\tau_o$ to the location of the deepest measurement point η_N for various values of the error-amplification factor. The resolving kernels $\tilde{\delta}(\tau, \tau_o)$, from which the spread is determined (Eq. 2), typically have one or more secondary peaks preceding the primary peak near $\tau = \tau_o$. The structure in the curves seen in this figure are associated with changes in the optimal number of resolving-function secondary peaks as η_N varies.

history, assuming a fixed value for σ. This is a consequence of the familiar tradeoff between model resolution and model uncertainty. For any particular study, the useful upper limit for σ_T is established by the magnitude of the climatic signals we are trying to detect. If σ_T is fixed at this upper limit, **Figure 2.1** reveals that the resolving power can be improved by simply reducing the measurement uncertainty σ. However, σ must be reduced by at least an order of magnitude to gain much improvement. This is particularly true at high (σ_T/σ) values.

Suppose, as an example, that the deepest observation available for a GST inversion is located at $z_N = 600$ m and that the uncertainty in the temperature measurements is ~ 5 mK. Further, suppose that the climate signals we are trying to detect have a magnitude of 2–3 K so that we wish to limit the uncertainty in our derived GST histories to ~ 0.5 K. In this case, our ability to resolve climatic events is optimal from the present time back to about 320 yr B.P., assuming $\kappa = 10^{-6}$ m^2 s^{-1}. The resolving power degrades considerably for older events and is essentially nonexistent for events beyond 1000 yr B.P.

The upper portion of a BT profile is normally truncated to avoid seasonal effects. Additional truncation of the record may be required if the liquid level in the borehole lies more than 20 m below the surface. **Figure 2.2** shows that the resolving power is nearly independent of the location of the shallowest measurement point η_1 until some critical value is reached, at which point the resolving power of the data degrades catastrophically. The critical η_1-value has a strong dependence on the error-amplification factor. Suppose the upper 20 m of a BT profile is truncated. In this case, we lose our ability to resolve events for only the past 1–2 years, even if the error-amplification factor is as low as 10. Thus, in the context of climate change, the practice of truncating the upper portion of a BT record to avoid seasonal effects causes little loss of information.

For the results presented in **Figure 2.1** and **Figure 2.2**, the vertical spacing ratio was set to $(z_{i+1}/z_i) \approx 1.05$, resulting in a data spacing Δz of about 1.0 m at a depth of 20 m. How much can the resolving power be improved by decreasing the data spacing? To investigate this, η_1 and η_N were fixed at 0.45 and 6.32, respectively, while the density of points between these limits was varied. **Figure 2.3** shows that the resolving power is only weakly dependent on the data spacing, at least for the range of data spacings considered here [$(z_{i+1}/z_i) > 1.015$; $\Delta z > 30$ cm at depth 20 m]. Reducing the data spacing by an order of magnitude [e.g., by reducing (z_{i+1}/z_i) from 1.15 to 1.015], produces only a minor improvement in the temporal resolution, particularly when (σ_T/σ) exceeds ≈ 50. From these results, it is apparent that more is to be gained by reducing the uncertainty in the temperature measurements σ by an order of magnitude than by decreasing the data spacing by a factor of 10.

Geothermal-research groups currently utilize a wide variety of data spacings, ranging from 0.5 cm to 10 m. At the U.S. Geological Survey, a common practice is to obtain a temperature measurement every 30.5 cm (every foot) when logging a borehole. Given this spacing and a good depth range ($\eta_1 < 1.3$ and $\eta_N > 3.0$) for events at time τ_o, the resolving width $S(\tau_o)$ can be expected to range from $0.79\,\tau_o$ to $0.52\,\tau_o$ for error-amplification factors ranging between 10 and 500. Thus, under the best conditions, climatic events of duration $0.52\,\tau_o$ occurring in the vicinity of time τ_o, should just be resolvable when the data spacing is ≈ 30 cm.

Occasionally, a long-term meteorological record is available from a weather station

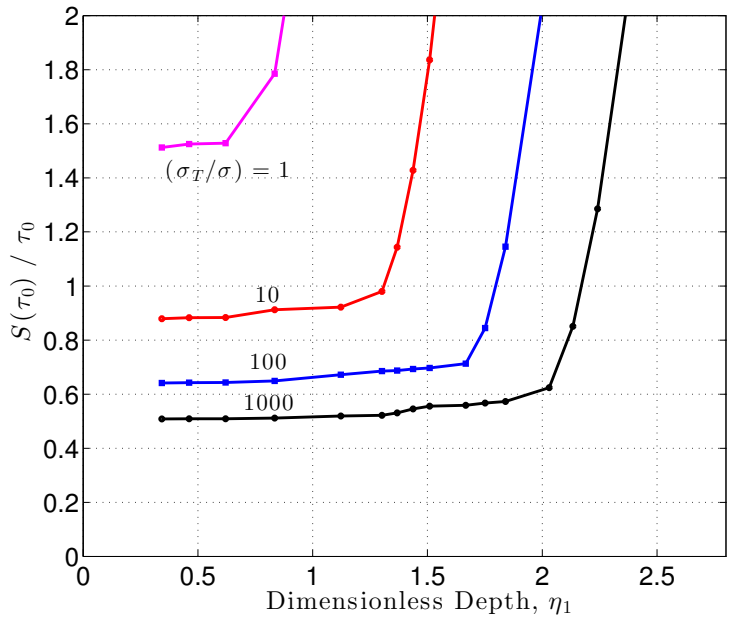

Figure 2.2: Sensitivity of the fractional spread to the depth of the shallowest measurement point η_1.

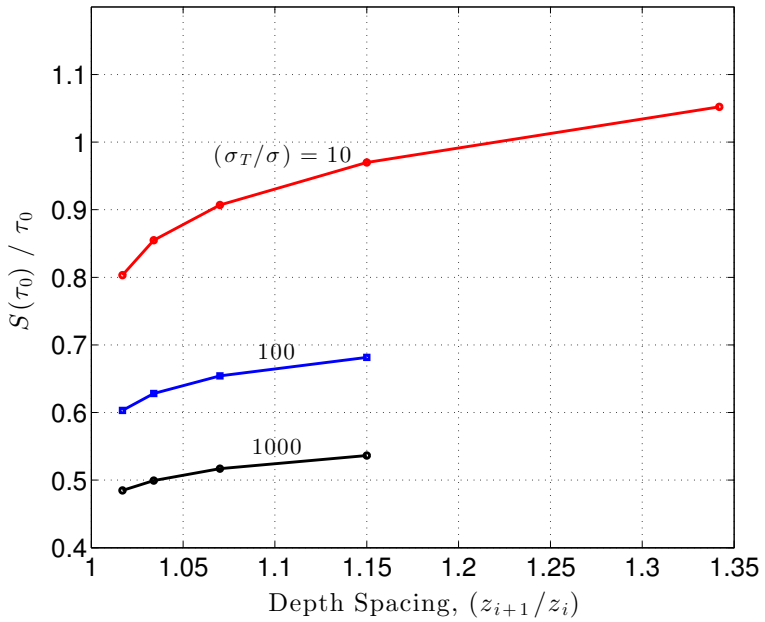

Figure 2.3: Sensitivity of the fractional spread to the vertical spacing of the data points.

sufficiently close to a borehole that the local GST history can be regarded as known from the present ($\tau = 0$) back to the beginning of the weather record at $\tau = \tau_{\text{met}}$. This is true only if the connection between ground surface temperature and air temperature is well understood at the site. Supposing the connection is known, to what extent does this additional information help us resolve events older than τ_{met}? To answer this question, Backus-Gilbert inversions were performed incorporating the GST history over the period $\tau \in (0, \tau_{\text{met}})$ as a priori information. As shown in **Figure 2.4**, inclusion of the meteorological data in the inversion process does enhance our ability to resolve climatic events up to 2–3 times older than τ_{met}. The improvement is modest but it does occur for a wide range of (σ_T/σ) values.

2.4.2 Monitoring experiments

The use of temperature-transient measurements $(\Delta T/\Delta t)_i$ at depth to reconstruct past GSTs is very attractive because it removes many of the ambiguities inherent in the climatic interpretation of a single BT profile. How long must these temperature changes be monitored before we can adequately resolve past climatic events? The trade-off curves (fractional spread versus the error-amplification factor) for several monitoring experiments are shown in **Figure 2.5**. For these experiments, the sampling depths ranged from $\eta_1 = 0.45$ to $\eta_N = 6.32$. As expected, the resolving power of the transient data is strongly dependent on the error-amplification factor with larger factors being advantageous. For an error-amplification factor of 500 ($\sigma = 1.0$ mK, $\sigma_T = 0.5$ K), we can just begin to resolve past climate events when the subsurface transients have been monitored for a period of $0.09\,\tau_o$; optimal resolution occurs when the monitoring period Δt exceeds $0.15\,\tau_o$. Thus, successful monitoring experiments will need to be fairly long term. Even if the measurement precision can be maintained at 1.0 mK, subsurface transients would need to be monitored for 9–15 years before we can resolve climatic events that occurred 100 years ago.

2.5 Conclusions

For climate-detection experiments utilizing a single borehole temperature profile, our ability to resolve events that occurred in the vicinity of time τ_o in the past is optimized if

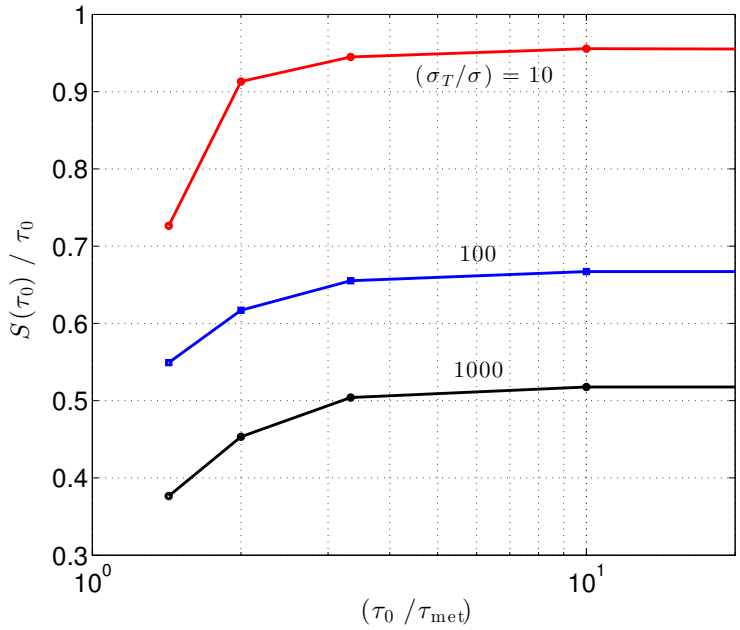

Figure 2.4: Sensitivity of the fractional spread to the inclusion of meteorological data from time $\tau = 0$ to $\tau_{\rm met}$ in the inversion process.

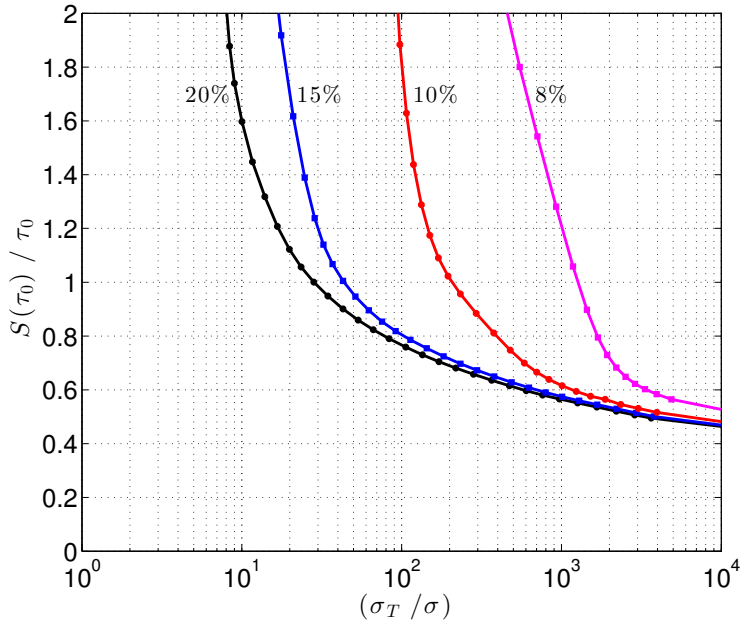

Figure 2.5: Trade-off curves for experiments where subsurface temperature transients are monitored for a period Δt. Curves are parameterized by their $(\Delta t/\tau_o)$ value.

the deepest measurement point is located at $z_N > 3\sqrt{4\kappa\tau_o}$. The practice of truncating the upper ≈ 20 m of a profile to avoid seasonal effects causes little loss of climate information. The resolving power of the BT data is found to be only weakly dependent on the vertical data spacing, particularly for large error-amplification factors (σ_T/σ). As a consequence, more resolving power can be gained by reducing the temperature-measurement uncertainty σ by an order of magnitude than by decreasing the data spacing by a factor of 10. If a local meteorological record is available back to time τ_{met} before present, inclusion of this information in the inversion process can enhance our ability to resolve climatic events back to 2–3 times τ_{met}. Finally, although the use of subsurface temperature-transient measurements to infer past climatic changes is in some ways very attractive, these measurements would have to be maintained over a fairly long period. In order to adequately resolve climatic events occurring 100 years ago, the subsurface transients would need to be monitored for at least 9–15 years.

2.6 References

Backus, G., and Gilbert, F. (1968), The resolving power of gross earth data, *Geophys. J. R. Astr. Soc.*, 16, 169–205.

Backus, G., and Gilbert, F. (1970), Uniqueness in the inversion of inaccurate gross Earth data, *Phil. Trans. R. Soc. Lond.*, A266, 123–192.

Dorman, L.M., and Lewis, B.T.R. (1972), Experimental isostasy, 3. Inversion of the isostatic Green function and lateral density changes, *J. Geophys. Res.*, 77, 3068–3077.

Lachenbruch, A.H., and Marshall, B.V. (1986), Changing climate: geothermal evidence from permafrost in the alaskan Arctic, *Science*, 234, 689–696.

MacAyeal, D.R., Firestone, J., and Waddington, E. (1991), Paleothermometry by control methods, *J. Glaciol.*, 37, 326–338.

Shen, P.Y., and Beck, A.E. (1991), Least squares inversion of borehole temperature measurements in functional space, *J. Geophys. Res.*, 96, 19,965–19,979.

Wang, K. (1992), Estimation of ground surface temperatures from borehole temperature data, *J. Geophys. Res.*, 97, 2095–2106.

CHAPTER 3

DEVELOPMENT OF A NEW BOREHOLE TEMPERATURE LOGGING SYSTEM FOR CLIMATE-CHANGE DETECTION

3.1 Abstract

This paper provides an updated technical description of the USGS Polar Temperature Logging System (PTLS) and a complete assessment of the measurement uncertainties. This measurement system is used to acquire subsurface temperature data for climate-change detection in the polar regions and for reconstructing past climate changes using the "borehole paleothermometry" inverse method. Specifically designed for polar conditions, the PTLS can measure temperatures as low as -60° Celsius with a sensitivity ranging from 0.02 to 0.19 millikelvin (mK). A modular design allows the PTLS to reach depths as great as 4.5 kilometers with a skid-mounted winch unit or 650 meters with a small helicopter-transportable unit. The standard uncertainty (u_T) of the ITS-90 temperature measurements obtained with the current PTLS range from 3.0 mK at -60° Celsius to 3.3 mK at 0° Celsius. Relative temperature measurements used for borehole paleothermometry have a standard uncertainty (u_T^r) whose upper limit ranges from 1.6 mK at -60° Celsius to 2.0 mK at 0° Celsius. The uncertainty of a temperature sensor's depth during a log depends on specific borehole conditions and the temperature near the winch and thus must be treated on a case-by-case basis. However, recent experience indicates that when logging conditions are favorable, the 4.5-kilometer system is capable of producing depths with a standard uncertainty (u_Z) on the order of 200–250 parts per million.*

---

*This chapter was originally published as: Clow, G.D. (2008), USGS Polar Temperature Logging System, Description and Measurement Uncertainties, *U.S. Geological Survey Techniques and Methods 2–E3*, available at: http://pubs.usgs.gov/tm/02e03.

3.2 Introduction

In 1993, the U.S. Geological Survey (USGS) began developing a new borehole temperature logging system specifically to address emerging climate issues in the polar regions. This system, referred to as the USGS Polar Temperature Logging System (PTLS), has two primary functions. (1) Periodically obtain subsurface temperature data from arrays of polar boreholes for climate-change detection. Monitoring data acquired by the PTLS in northern Alaska contributes to the Global Climate Observing System (GCOS) through the Global Terrestrial Network for Permafrost (GTN–P). (2) Acquire data for the reconstruction of past climate changes in the polar regions using '' borehole paleothermometry''. Climate reconstructions derived from borehole temperature measurements are hindered by considerable temporal smearing due to heat diffusion processes. While it cannot be eliminated, the extent of the temporal averaging can be minimized through optimal experimental design. Application of Backus-Gilbert inverse methods to the paleoclimate reconstruction problem shows that our ability to resolve past climatic events can be optimized by reducing the uncertainty in the temperature measurements to no more than 0.1 percent of the paleoclimate signal we are attempting to detect [*Clow*, 1992]. In most places on Earth, surface-temperature changes during the Holocene were on the order of ± 1 K. Thus to enhance our ability to resolve past climate events of this magnitude, it is desirable to reduce the uncertainty of the borehole temperature measurements to about 1 mK. Paleoclimate reconstruction has been the primary driver for the design requirements of the PTLS since its requirements are much more stringent than those needed for detecting contemporary climate change.

The objectives of this chapter are to provide an updated technical description of the PTLS logging system and an analysis of the measurement uncertainties. This system and its uncertainties were originally described by *Clow et al.* [1996]. However, the PTLS is a continually evolving system, warranting an updated description. In addition, calibration facilities and procedures have changed significantly since 1996. The current chapter provides a much more complete analysis of the measurement uncertainties than was possible in *Clow et al.* [1996]. The need for such an analysis is twofold: (1) The usefulness of scientific data produced by monitoring systems critically depends on the availability of thorough uncertainty analyses. This is particularly true of climate-monitoring systems.

(2) To reconstruct past climate changes using borehole paleothermometry, one needs to know the uncertainties of the data. This requirement, shared by all geophysical inverse techniques [*Parker*, 1994], determines the very structure of the derived climate histories. In conformance with ISO standards [*ISO*, 1993a, b], we use the CIPM[†] approach for expressing and evaluating the measurement uncertainties of the PTLS.

3.3 System description

3.3.1 PTLS design overview

A variety of system designs presently are used to measure temperatures in geophysical boreholes. Most systems use either a temperature-dependent resistive element (thermistor or RTD) or a piezoelectric crystal whose resonant frequency is temperature-sensitive for the sensing element. In the former case, the resistance of the sensing element is measured by a custom-built electronic bridge or by a commercial resistance readout. An advantage of a custom bridge is that it can be made small enough to be included in an instrument package located at the downhole end of the logging cable, keeping the electronic lead lengths to the sensor relatively short. Such a package can be designed to measure several other parameters as well, such as fluid pressure and borehole inclination, and the resulting data either stored within the instrument package or digitally transmitted to the surface. A significant disadvantage of this approach for precision thermometry is the difficulty of maintaining the calibration of the electronic bridge while the instrument package experiences temperature changes of 10–30 K during the course of a logging experiment. The associated calibration drift of the bridge can produce temperature measurement errors of 10 mK, or more. Application of new technologies may substantially reduce these errors, making high-precision downhole digital thermometers possible in the near future. The current alternative is to locate the resistance-measuring circuitry on the surface. The advantages of this strategy are: (1) a high-quality commercial resistance readout can be utilized for the measuring circuitry instead of having to develop custom miniaturized circuits, (2) the readout can be maintained at a constant temperature, eliminating temperature-related drift in the measurement circuit, and (3) the calibration of the readout can be periodically rechecked while measurements are in progress. However, the long

[†]International Committee for Weights and Measures.

lead lengths between the resistance readout and the sensor, potentially up to 10 km, make the measurements vulnerable to several sources of instrumental error. Great care must be exercised to minimize these errors. Logging systems with a downhole electronic bridge generally acquire temperature measurements while lowering the sensor downhole at a constant speed (''continuous'' logging). Another common technique is to acquire data with the probe stopped at a fixed depth; repeating this process at multiple depths yields an incremental or ''stop-and-go'' temperature log. Systems with the resistance-measuring circuitry on the surface are sometimes limited to this mode. Although incremental logging yields measurements at a limited number of depths, these measurements are free of the ''slip-ring'' noise (see Section 3.3.2) inherent in continuous temperature logs obtained with surface measurement circuitry.

Considering the advantages and disadvantages of various system designs along with our scientific objectives, the following requirements were established for the Polar Temperature Logging System: the system must be modular and flexible so it can use a variety of sensors, can make measurements using either downhole or surface measurement circuitry, can be operated in either the continuous or incremental logging modes, and can utilize different length logging cables depending on borehole depth and available logistics. In addition, the system must be able to measure temperatures as low as $-60°C$ with an uncertainty of about 1 mK, reach depths comparable to the maximum thickness of the polar ice sheets (4–5 km), work in the presence of strong environmental noise (e.g., changing electrostatic fields), and be rugged enough to survive offloading from military cargo aircraft. The PTLS evolved from a number of refinements to a conventional temperature logging system design, thereby avoiding the need to build a radically new system. This approach took advantage of the USGS' considerable experience in borehole thermometry. Negative-temperature-coefficient (NTC) hermetically sealed thermistors were selected for the primary temperature sensors because of their ruggedness, stability, and high temperature coefficient, which helps produce a high system sensitivity. A commercial resistance readout located on the surface is normally used for the resistance-measuring circuitry. This circuitry is suspended inside a Faraday cage maintained at $23 \pm 0.5°C$ for the duration of an experiment; thermal stability is provided by microprocessor-controlled etched-foil heaters. As an alternative to surface measurement circuitry, a prototype downhole digital

thermometer utilizing NTC thermistors has been used with the PTLS. However, this device is still in the testing phase and will not be discussed further here. Other major system components include a 4-conductor logging cable mounted on a motorized winch (**Figure 3.1**). Two different size winches are currently available: a small helicopter-transportable unit with 650 m of cable, and a much larger skid-mounted unit capable of reaching 4.5 km. A "slip-ring" assembly provides electrical continuity between the logging cable and the surface electronics. Depth information is provided by an optical encoder mounted on a calibrated measuring wheel. A laptop computer controls the system, both displaying and storing the measured resistance, depth, time, and logging speed. Cable tension provided by a strain-gage force transducer is displayed on a separate monitor. To minimize electrical noise, all components are powered by DC batteries except for the winch motors. The Faraday cage surrounding the resistance readout, used in conjunction with cable shielding, helps isolate the measurement circuitry from the remaining sources of electrical noise.

The three fundamental measurements made by the PTLS are the sensor resistance, sensor depth, and time of data acquisition. For the time measurements, we simply rely on the computer's onboard clock. The resistance and depth measurements are more involved and are described in detail in the following sections. Resistance measurements are

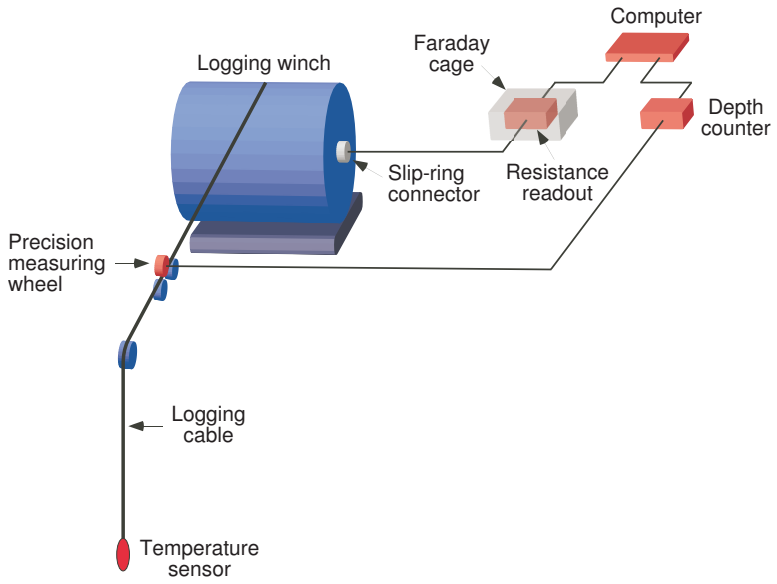

Figure 3.1: Layout of the USGS Polar Temperature Logging System when using surface measurement circuitry.

subsequently converted to temperature using a 4-term conversion function.

3.3.2 Resistance (temperature) measurement system

3.3.2.1 Kelvin circuit

To measure the resistance, a Kelvin (4-wire) circuit is used in both the downhole and the surface measurement-circuitry configurations (**Figure 3.2**). During this measurement, the resistance readout produces a highly regulated current (I_s) that passes through the sensor. The resulting voltage drop (ΔV) across the probe is detected by the readout's high-impedance inputs, and the probe's resistance calculated from $\tilde{R}_s = \Delta V / I_s$. This 4-wire measurement eliminates the effect of the lead resistance (R_L) along each conductor between the resistance readout and the temperature sensor. There are, however, several sources of systematic error that potentially require correction.

3.3.2.2 Resistance corrections

Leakage paths between the conductors of the Kelvin circuit can produce significant systematic error, particularly when the probe resistance R_s is large. Such unintended paths arise due to leakage currents passing directly through the conductor insulation, moisture absorption by the insulation, or leakage due to contaminants on the surface of the insulation or connectors. Leakage currents between the circuit's sense lines or between the current-carrying lines will reduce the measured resistance by

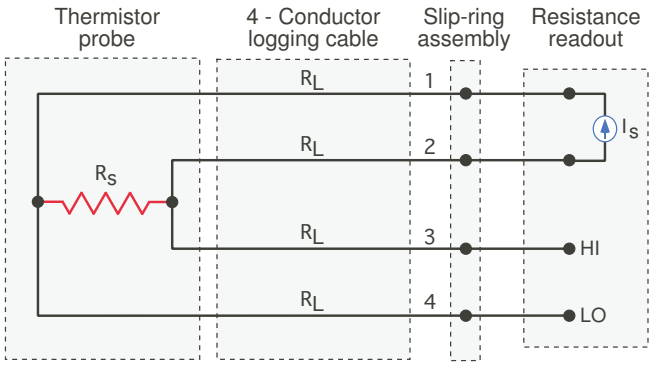

Figure 3.2: Kelvin (4-wire) resistance circuit used by the PTLS when the measurement circuitry is located on the surface. The test current I_s passes through lines 1 and 2 while the voltage drop across R_s is measured using the sense lines (3, 4). With downhole circuitry, an electronic bridge is connected directly to the probe.

$$\delta R_l \;=\; \frac{R_s^2}{R_s + R_l} \tag{3.1}$$

where R_l is the leakage resistance. Teflon is used for the Kelvin circuit insulation because of its high volume resistivity (greater than $10^{16}\,\Omega{\cdot}\mathrm{m}$), low water absorption, and a surface that tends to repel many films. This problem is further controlled by rigorously cleaning the connectors and by using a sensor with a low resistance R_s. Part of our logging protocol is to measure the resistance R_l between each pair of conductors immediately before each logging experiment. If R_l is less than 10 GΩ for any pair of conductors, the log is aborted until the problem is rectified. R_l is greater than 20 GΩ for nearly all logging experiments conducted with the PTLS.

A capacitor is occasionally introduced between the readout's sense lines to perform high-frequency noise filtering. This also delays the response of the circuit so that the measured resistance is too low by

$$\delta R_c \;=\; \tau\,\frac{\partial R_s}{\partial t}. \tag{3.2}$$

$\tau = R_s C$ is the circuit's natural response time where C is the capacitance. If a filtering capacitor is used, the resistance offset δR_c is controlled by keeping τ small relative to the measurement integration time of the resistance readout and by using a slow logging speed v so that the rate of resistance change $\partial R_s/\partial t \;=\; v\,\alpha_T\,R_s\,(\partial T/\partial z)$ is also small; α_T is the sensor's temperature coefficient of resistance ($\alpha_T \;\equiv\; R_s^{-1}\,\partial R_s/\partial T$). With typical logging speeds (2.5–5.5 $\mathrm{cm{\cdot}s^{-1}}$) and temperature gradients ($\partial T/\partial z \leq 50\ \mathrm{mK{\cdot}m^{-1}}$), the most rapid resistance changes are on the order of $10^{-4} R_s$ per second. Without the filtering capacitor, C is determined by the capacitance of the logging cable (76 nF for the 650-m "short" cables and 0.68 μF for the 4,600-m "long" cable).

As the current I_s passes through the temperature sensor, power dissipates within the probe at a rate $P = I_s^2\,R_s$. This warms the probe, effectively reducing its resistance by

$$\delta R_h \;=\; \frac{\alpha_T\,(I_s R_s)^2}{P_d} \tag{3.3}$$

where P_d is the probe's power dissipation constant. The best strategy for minimizing self-heating is to use a resistance readout with a small source current I_s and a probe with a relatively low resistance. The source current for the resistance readout used with the PTLS is $\leq 10\,\mu$A.

To provide modularity, the Kelvin circuit consists of a number of components attached to one another using high-quality electrical connectors (**Figure 3.2**). Different portions of the circuit operate at vastly different temperatures with the sensor-end of the circuit often being 30–70 K colder than the resistance readout. This situation has the potential to generate significant thermoelectric voltages (thermal EMFs) between electrical junctions separating dissimilar metals through the Seebeck effect [*McGee*, 1988]. The sum of the thermal EMFs can be found by integrating the Seebeck coefficient Q around the entire circuit, starting and ending at the resistance readout's HI and LO sense connections (junctions a_1 and a_2),

$$V_{\text{emf}} \;=\; -\int_{a_1}^{a_2} Q(T)\,dT. \tag{3.4}$$

Q depends primarily on metal composition and secondarily on temperature. If the metal compositions on the HI side of the circuit exactly match those on the LO side, the total thermal EMF can be expressed by

$$V_{\text{emf}} \;=\; -\int_{a_1}^{b_1} Q_A(T)\,dT \;-\; \int_{b_1}^{c_1} Q_B(T)\,dT \;-\; \int_{c_2}^{b_2} Q_B(T)\,dT \;-\; \int_{b_2}^{a_2} Q_A(T)\,dT \tag{3.5}$$

where subscripts 1 and 2 refer to the HI and LO sides of the circuit, respectively; Q_A is the Seebeck coefficient for the metal conductor between junctions a_1 and b_1 (and between a_2 and b_2), Q_B is the coefficient for the metal between junctions b_1 and c_1, and so forth. Equation (3.5) can be rewritten in terms of the adjacent junction pairs on the HI and LO sides of the circuit (e.g., a_1 and a_2),

$$V_{\text{emf}} \;=\; \left[\int_{a_2}^{a_1} Q_A(T)\,dT + \int_{b_1}^{b_2} Q_A(T)\,dT\right] \;+\; \left[\int_{b_2}^{b_1} Q_B(T)\,dT + \int_{c_1}^{c_2} Q_B(T)\,dT\right] \;+\; \cdots\,. \tag{3.6}$$

If the temperature difference between adjacent junction pairs is small enough that the temperature dependence of the Seebeck coefficient can be ignored, Eq. (3.6) reduces to

$$V_{\text{emf}} \;=\; -Q_A\,(T_{a_2} - T_{a_1}) \;+\; (Q_A - Q_B)\,(T_{b_2} - T_{b_1}) \;+\; (Q_B - Q_C)\,(T_{c_2} - T_{c_1}) \;+\; \cdots\,. \tag{3.7}$$

Thus, thermal EMFs can be controlled by minimizing the temperature difference between adjacent junction pairs. Based on this analysis, we use a number of strategies to minimize thermal EMFs in the PTLS' Kelvin circuit: (1) The use of dissimilar metals is kept to a minimum. Except for the junctions themselves, the circuit paths consist almost entirely of copper or silver-plated copper. (2) Where a dissimilar metal occurs on the HI side of the

circuit, the metal is matched with an identical metal at the corresponding location on the LO side. (3) The temperature difference between adjacent junction pairs is minimized. This is accomplished by locating the junctions of an adjacent pair as close together as possible, locating junction pairs within the thermally controlled Faraday cage where thermal gradients are very small, and (or) by locating junction pairs within high-conductivity metal shells where temperature gradients are also small. Before every experiment, the resistance readout is warmed up for at least an hour to minimize thermal EMFs within the readout itself. Considering the estimated temperature differences at the adjacent junction pairs and the values of the Seebeck coefficients, the total thermal EMF for the Kelvin circuit is estimated to be on the order of 0.5 μV with the dominant sources occurring at the slip-ring assembly. Current-reversal experiments with both the 650-m logging cables and the 4,600-m cable confirm that V_{emf} is typically $\leq 0.5\,\mu$V. This voltage offset increases the measured resistance by

$$\delta R_e = \frac{V_{\text{emf}}}{I_s}. \tag{3.8}$$

In 2008, the simple constant-current source that the PTLS had used was changed to a reversing source. This allowed us to switch to a current-reversal technique where a "resistance measurement" is found by averaging two measurements made with currents of opposite polarity. With this approach, the thermal EMFs produced during each polarity completely cancel out so that $\delta R_e = 0$.

The first three systematic errors ($\delta R_l, \delta R_c, \delta R_h$) can be controlled by using a sensor with a relatively small resistance. However, an additional constraint imposed by the resistance readout is that R_s must be much greater than the lead resistance R_L for each leg of the Kelvin circuit in order to make an accurate resistance measurement. At a minimum, R_s should be at least 20 times R_L. Other factors that help control the systematic errors are a small capacitance C, a slow logging speed v, a small source current I_s, carefully matching the composition of the wires, and keeping the temperature difference between adjacent junction pairs as small as possible. Despite efforts to control leakage paths, the capacitance effect, self-heating, and thermal EMFs, small systematic errors will remain. We attempt to eliminate these errors by applying Eqs. (3.1)–(3.3) and (3.8) as corrections to the resistance $\tilde{R}_s$ recorded by the resistance readout to obtain our estimate of the temperature sensor's true resistance,

$$R_s = \tilde{R}_s + (\delta R_l + \delta R_c + \delta R_h - \delta R_e). \tag{3.9}$$

Figure 3.3 shows the magnitude of the resistance corrections for the PTLS under typical operating conditions. Expressed in terms of temperature, the corrections are generally limited to 0.1–0.2 mK. The uncertainty of these systematic error corrections is discussed in Section 3.4.1.2.

3.3.2.3 Noise

Several sources of noise also perturb the resistance measurements when the measurement circuitry is located on the surface. These sources include electrostatic coupling, electromagnetic EMFs, triboelectric effects, and switching effects. Depending on the source, the noise generated within the circuit consists either of extraneous voltages V' or extraneous currents I'. The resistance readout internally converts the extraneous voltages into an apparent resistance noise, $R' = (V'/I_s)$, while the extraneous currents are converted

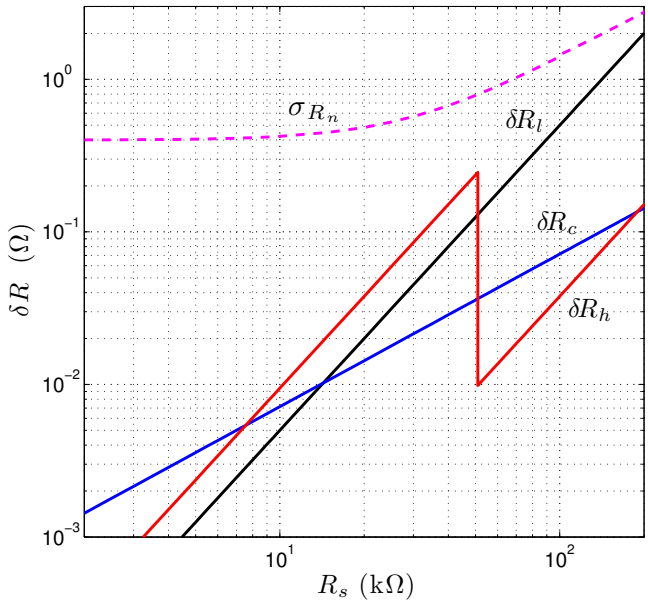

Figure 3.3: Magnitude of the resistance corrections $\delta R_l, \delta R_c, \delta R_h$ under typical operating conditions; δR_e is essentially zero with the current PTLS design. In this example, the capacitance correction δR_c assumes a logging speed of 5.5 centimeters per second, a temperature gradient of 25 mK m^{-1}, and a capacitance C such that $\tau = 10$ ms. Equivalent temperature corrections are given by $\Delta T_\mathrm{x} = \delta R_\mathrm{x}/(\alpha_T R_s)$. Also shown is the approximate standard deviation σ_{R_n} of the raw noise (Eq. 3.10) generated in the Kelvin circuit under typical conditions.

to $R' = R_s(I'/I_s)$. In the latter case, the apparent resistance noise increases in direct proportion to the temperature sensor's resistance.

3.3.2.3.1 Individual noise components

Electrostatic coupling occurs when an electrically charged object such as the system operator moves near the Kelvin circuit, generating currents in the conductors. In polar environments, significant electrostatic interference can also be caused by electric charges transferred to the sheath of the logging cable by dry blowing snow. Electromagnetic voltages (EMFs) are generated when a changing magnetic field passes through the conductive loop represented by the Kelvin circuit, or when some portion of the conductive loop (e.g., the logging cable) moves relative to a magnetic field. For the PTLS, nearby AC fields, winch motors, and the Earth's magnetic field are potential sources of electromagnetic voltages. We use several strategies to mitigate the noise generated by electrostatic coupling and electromagnetic EMFs:

(1) Once a temperature log is initiated, the system runs in an automated mode, allowing the system operator to remain an adequate distance from the Kelvin circuit.

(2) The entire system is shielded from the wind and blowing snow as much as possible by operating it inside an insulated shelter. The Faraday cage and associated electronics are always operated within a protective shelter. If the wellhead cannot also be located inside the shelter, the shelter is placed as close as possible to the wellhead to minimize the amount of exposed logging cable.

(3) To minimize AC power fields, all system components are powered by DC batteries except for the winch motors.

(4) The most sensitive portions of the Kelvin circuit, especially the resistance readout, are kept as far as possible from the winch motors.

(5) All movement around the Kelvin circuit is kept to a minimum during a temperature log.

(6) The loop area of the circuit is minimized by using twisted-wire cables.

(7) The resistance readout is electrically shielded inside a Faraday cage. All the cables are also electrically shielded.

Given these noise-reduction strategies, the dominant sources of noise for the PTLS are believed to be due to switching effects within the electromechanical "slip-ring" assembly and to the triboelectric effect. Triboelectric currents arise from charges generated between the insulation and conductors of the logging cable as it flexes over the sheave wheels that guide it into a borehole. Triboelectric currents can also occur when the logging cable vibrates in the wind. We manage the triboelectric currents by providing a smooth path into the borehole, logging downhole at a slow steady pace with negligible accelerations, and by keeping the logging cable shielded from strong winds as much as possible. The slip-ring noise is controlled by using high-quality slip-rings.

The internal noise of the resistance readout also contributes a small amount of noise to the recorded resistances, as does the truncation error associated with the instrument's finite resistance resolution ΔR_r. Combining the readout noise with that due to the extraneous voltages and currents generated within the Kelvin circuit, the standard deviation of the noise in the resistance measurements is given by

$$\sigma_{R_n} = \left[(a\Delta R_r)^2 + \left(\frac{V'}{I_s} \right)^2 + \left(\frac{R_s I'}{I_s} \right)^2 \right]^{1/2}. \tag{3.10}$$

Although the noise varies between temperature logs, depending on circumstances, the constants in Eq. (3.10) are generally on the order of $a \approx 0.33$, $V' \approx 4\,\mu$V, and $I' \approx 0.14$ nA for the PTLS under most conditions. Extraneous voltages dominate the noise for probe resistances less than 20 kΩ while extraneous currents dominate when $R_s > 40$ kΩ (**Figures 3.3–3.4**); the readout's contribution is relatively small at all resistances. The raw noise described by Eq. (3.10) can be substantially reduced by judiciously applying the resistance readout's internal filters or by installing a filtering capacitor between the circuit's sense lines. When these hardware noise filters are used, the noise $\sigma_{\tilde{R}_n}$ actually present in the recorded resistances is less than σ_{R_n}. The remaining noise is largely removed during data processing by using wavelet denoising techniques.

3.3.2.4 Temperature sensors

Equations (3.1)–(3.3) show that the temperature sensor is an important factor in determining the characteristics of the overall measurement system. The primary sensors used with the PTLS consist of a parallel-series network of 15 negative-temperature-coefficient

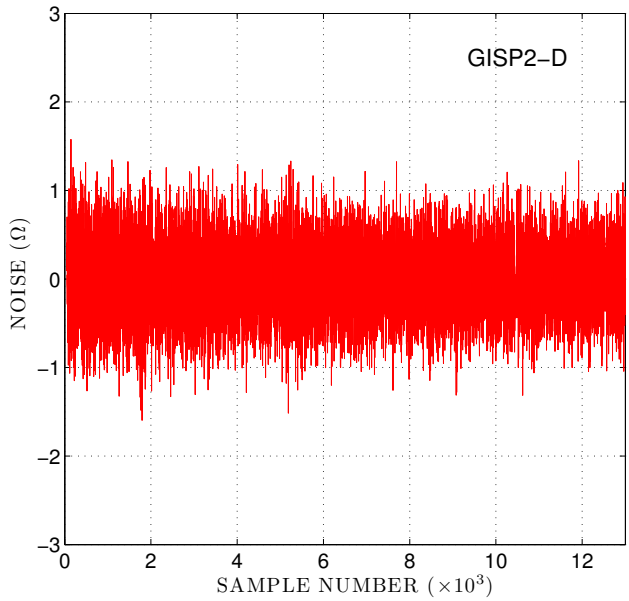

Figure 3.4: Raw noise for a typical logging experiment. This record was acquired from the nonconvecting portion of the GISP2-D borehole (central Greenland) without the use of hardware noise filters. In this example, the standard deviation of the noise was $\sigma_{R_n} = 0.40\,\Omega$ with sensor resistances R_s ranging from 11.9 to 12.7 kΩ.

(NTC) thermistors divided into three packets.[‡] Each packet is hermetically sealed in glass (**Figure 3.5**) to prevent changes in the oxidation state of the metal oxide thermistors and to relieve strain where the leads are attached to the ceramic body of the thermistors. As a result, the probes have good long-term stability with typical drift rates of $\leq$ 0.025 percent per year. The packets are wired in parallel so that only one third of the resistance readout's excitation current I_s passes through any given thermistor bead, minimizing the self-heating effect. To improve the ruggedness of the design, the thermistor packets are completely enclosed in a 4.0-mm-diameter stainless-steel shell, allowing the probes to withstand the pressures encountered at 7–8 km in liquid-filled boreholes and the effects of corrosive chemicals such as n-butyl acetate (many of the deep boreholes drilled by the United States polar programs are filled with n-butyl acetate). The use of many small thermistor beads, glass encapsulation, and a high-conductivity steel shell all help to produce a

[‡]A similar design appropriate for temperatures at midlatitudes is described by *Sass et al.* [1971]. The midlatitude version has a much higher resistance than the polar model and contains 20 thermistors divided into two packets.

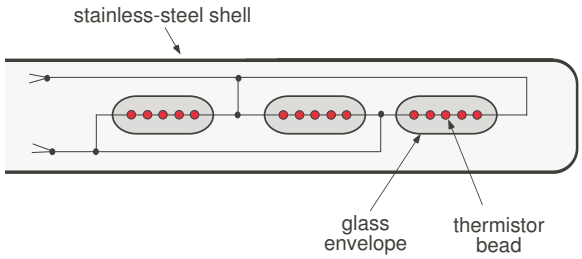

Figure 3.5: PTLS temperature sensor. The sensor consists of a parallel-series network of 15 small bead thermistors divided into three sealed packets. Beads extend over a 10-centimeter length within the 4-millimeter-diameter stainless-steel shell. The resistance readout measures the combined resistance of the parallel-series network.

high power-dissipation constant P_d. The P_d-value for these custom probes is 55 mW·K^{-1} in circulating xylene and is believed to be similar when logging through n-butyl acetate while the α_T values range from about -0.045 K^{-1} at 0°C to -0.065 K^{-1} at -60°C (**Figure 3.6**). An inevitable disadvantage of this probe design is the relatively slow response time. In n-butyl acetate, the measured time constant is about 7 seconds. Five series of custom probes, each with a different 0°C resistance, are currently available to optimize the characteristics of the PTLS for any given experiment.

To convert sensor resistance to temperature, we use the 4-term calibration function

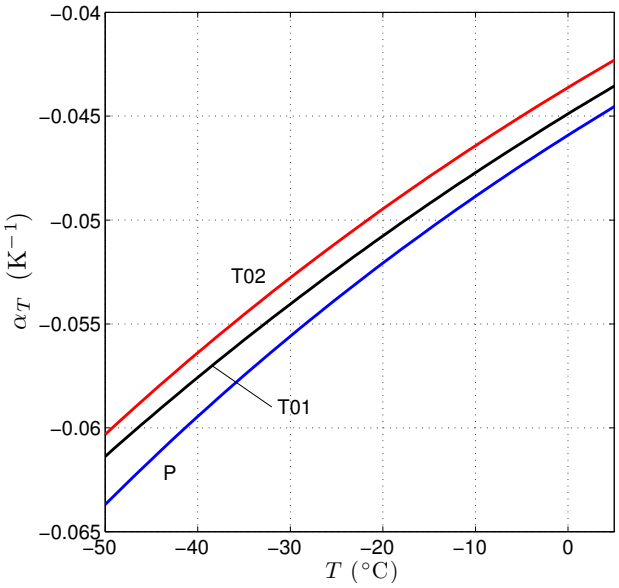

Figure 3.6: Temperature coefficient of resistance (α_T) for the P, T01, and T02 probe series used with the Polar Temperature Logging System. These probe series have a nominal resistance of 27 kΩ, 3.7 kΩ, and 2.5 kΩ at 0°C, respectively.

$$T^{-1} = a_0 + a_1(\ln R_s) + a_2(\ln R_s)^2 + a_3(\ln R_s)^3 \tag{3.11}$$

where the constants a_i are determined for each sensor just before every field season in our thermal calibration facility, and T is expressed in Kelvin. Equation (3.11) is an extension of the often-used 3-term Steinhart-Hart equation [*Steinhart and Hart*, 1968], which proves inadequate for our purposes. An F-test [e.g., *Bevington*, 1969] demonstrates that a much better fit to our calibration data can be obtained with the 4-term function than with the standard Steinhart-Hart equation, particularly at temperatures below 0°C. Sample temperature-calibration data and the resulting 4-term calibration fit (Eq. 3.11) are shown in **Figure 3.7**.

The temperature resolution of the Kelvin circuit,

$$\Delta T_r \approx \frac{\Delta R_r}{\alpha_T R_s} \tag{3.12}$$

depends on the ratio of the smallest resistance resolvable by the resistance readout ΔR_r to the probe resistance R_s. Thus, to achieve sub-mK sensitivity, $\Delta R_r / R_s$ must be less than 5 x 10^{-5}. For the resistance readout currently used with the PTLS, the $\Delta R_r / R_s$ ratio ranges from 1.0 x 10^{-5} (worst case) to 1.0 x 10^{-6} (best case). The resulting temperature resolution

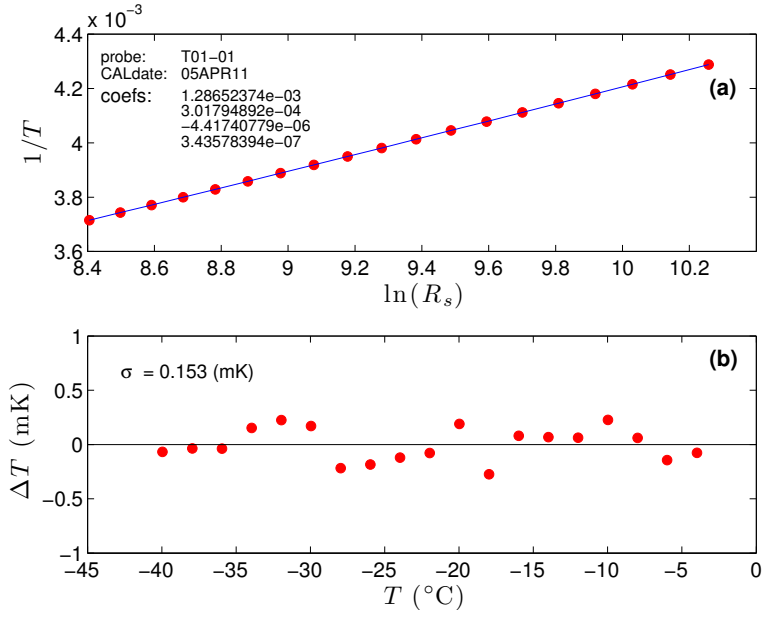

Figure 3.7: Sample calibration data for one of the temperature sensors (T01-01) along with the best 4-term Steinhart-Hart fit to the data **(a)**. In this case, residuals from the fit to the calibration data have a standard deviation of 0.153 mK **(b)**.

is less than 0.2 mK under all conditions (**Figure 3.8**). With the resistance readout used prior to 2008, ΔT_r ranged from 0.1 to 1.1 mK; by judicious selection of the temperature probe for pre-2008 logging experiments, the resolution could almost always be reduced to less than 0.6 mK.

3.3.3 Depth-measurement system

3.3.3.1 System description

Depth information is obtained by measuring the angular rotation $d\theta$ of a precision measuring wheel located within the winch assembly (**Figure 3.1**) that is pressed tightly against the logging cable. Wheel rotation is detected by an optical shaft encoder that transmits quadrature waveforms to a bidirectional counter. The counter then converts angular rotation to distance (or depth) using $d\tilde{z} = (R_w + r)\, d\theta$, where r and R_w are the radii of the logging cable and measuring wheel, respectively. The fundamental limit of the depth resolution is determined by the effective radius of the measuring system $(R_w + r)$ and the number of quadrature pulses output per revolution by the optical encoder. For the 4.5-km system, this limit is 0.254 cm. An additional limitation is imposed by the depth counter. For the 6-digit counter currently used with the PTLS, the depth resolution Δz_r is

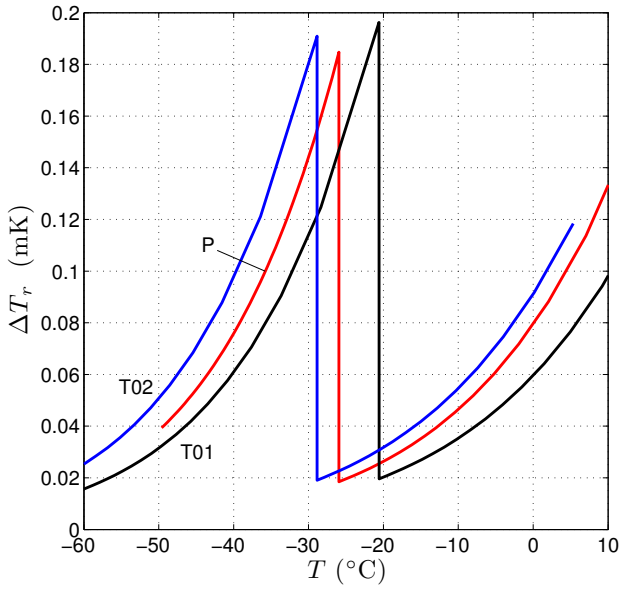

Figure 3.8: Temperature resolution of the current PTLS when using the P, T01, and T02 probe series.

1.0 cm over the system's full depth range, although it can be set to $\Delta z_r = 0.30$ cm when collecting depth-calibration data. Before 2007, Δz_r was 0.3 cm for boreholes less than 545 m deep and 3.0 cm for deeper holes due to the limited buffer size of the bidirectional counter used at that time.

3.3.3.2 Depth corrections

To account for the force-dependent strains affecting the depth-measuring system, a depth-calibration function C_d is established for each unique logging environment. This is done by moving the logging cable downhole approximately 40 m and comparing the distance $\tilde{\mathcal{L}}$ reported by the depth counter with the distance $\mathcal{L}$ measured by a fiberglass surveying tape that has a low temperature coefficient of thermal expansion (9.3 x 10^{-6} K^{-1}); $\mathcal{L}$ is taken to be a measure of the "true" distance. C_d is then defined by

$$C_d(\tilde{Z}) \equiv \frac{\mathcal{L}(\tilde{Z})}{\tilde{\mathcal{L}}(\tilde{Z})} - 1 \tag{3.13}$$

where $\tilde{Z}$ is the depth of the sensor-end of the cable (according to the counter) when the $(\mathcal{L}, \tilde{\mathcal{L}})$-data are collected. Depth-calibration data are acquired with the sensor-end of the cable at multiple depths $\tilde{Z}_i$ spanning as much of a borehole's depth range as possible. Temperature changes in the measuring wheel and in the test section of logging cable also affect the calibration data. Although we attempt to maintain a consistent temperature during the calibration period, temperature changes do sometimes occur. To remove the temperature effects, we define thermally corrected C_d values by

$$C_d(T_w^\star, \tilde{Z}_i) = C_d(T_{w_i}, \tilde{Z}_i) - \left(\frac{R_w}{R_n}\right) e_{wrT_w} - \left(\frac{r}{R_n}\right) e_{crT_w} - \alpha f_T (T_w^\star - T_{w_i}) \tag{3.14}$$

where $T_w^\star$ is a reference calibration temperature and T_{w_i} is the temperature at the measuring wheel when the sensor-end of the cable is at $\tilde{Z}_i$. The second and third terms on the right-handside of Eq. (3.14) account for changes in the effective radius of the measuring system due to thermal strains while the fourth term accounts for the thermally induced longitudinal strain in the cable as it enters the relatively cold, air-filled portion of the borehole. Assuming the temperature of the cable is approximately T_{w_i} when passing over the measuring wheel, the radial strains in the wheel and cable (e_{wrT_w}, e_{crT_w}) are both given by

$$e_{xrT_w} = \sqrt{\frac{1 + \beta(T_{w_i} - T_w^\star)}{1 + \alpha(T_{w_i} - T_w^\star)}} - 1 \tag{3.15}$$

where α and β are the linear and volumetric coefficients of thermal expansion. Our measuring wheels are isotropic disks so that $\beta = 3\alpha$. Factor $R_n = m/\Delta\theta_r$ is the nominal radius used by the depth counter where m is the counter's internal multiplier and $\Delta\theta_r$ is the encoder's angular resolution. Parameter f_T is the fraction of the temperature difference $T_{w_i} - T(h)$ experienced by the cable during a calibration test where $T(h)$ is the temperature at the bottom of the air-filled portion of the borehole; f_T is typically about 0.3.

Once the thermally corrected C_d values have been determined, a least-squares fit is made to

$$\mathcal{F}(\tilde{Z}_i) \;=\; C_d(T_w^\star, \tilde{Z}_i) \;-\; C_d(T_w^\star, \tilde{Z}^\star) \tag{3.16}$$

where $\tilde{Z}^\star$ is a reference calibration depth selected from one of the $\tilde{Z}_i$ values near the middle of the depth range; reference temperature $T_w^\star$ is generally taken to be the T_{w_i} value for the calibration data acquired at $\tilde{Z}_i = \tilde{Z}^\star$. The depth-calibration function is then given by the sum of the reference C_d-value and the experimentally determined function $\mathcal{F}(\tilde{Z})$, which isolates the force-dependent effects of the depth-measuring system relative to $C_d(T_w^\star, \tilde{Z}^\star)$,

$$C_d(T_w^\star, \tilde{Z}) \;=\; C_d(T_w^\star, \tilde{Z}^\star) \;+\; \mathcal{F}(\tilde{Z}). \tag{3.17}$$

Figure 3.9 shows an example $\mathcal{F}(\tilde{Z})$ determined from depth-calibration data acquired in the 1-km-deep Siple Dome A borehole in West Antarctica.

With the availability of the $\mathcal{F}(\tilde{Z})$ and $C_d(T_w^\star, \tilde{Z})$ functions, the total length of cable spooled into a borehole during a logging experiment can be found by integrating the distances $d\tilde{z}$ reported by the depth counter weighted by the depth-calibration function,

$$Z \;\approx\; \int_o^{\tilde{Z}} \left[1 + C_d(T_w^\star, \tilde{Z} - \tilde{z})\,\right] d\tilde{z}. \tag{3.18}$$

Substituting from Eq. (3.17) and letting

$$\delta Z_F \;=\; \int_o^{\tilde{Z}} \mathcal{F}(\tilde{Z} - \tilde{z})\, d\tilde{z} \tag{3.19}$$

be the correction for the force-dependent effects, the length Z becomes

$$Z \;\approx\; \left[1 + C_d(T_w^\star, \tilde{Z}^\star)\right] \tilde{Z} \;+\; \delta Z_F. \tag{3.20}$$

This estimate accounts for most of the tension-induced radial and longitudinal strains within the logging cable and mechanical strains in the logging winch. However, a number

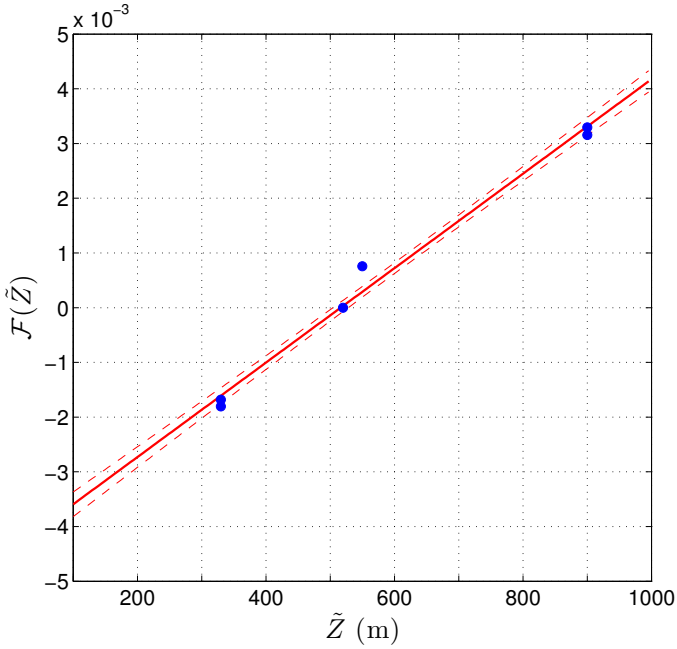

Figure 3.9: Least-squares fit to $\mathcal{F}(\tilde{Z}_i)$ values determined from depth-calibration data acquired in the Siple Dome A borehole, West Antarctica. Dashed lines indicate the uncertainty ($\pm 1\sigma$) of the least-squares fit.

of additional corrections must be made to obtain an estimate of the true sensor depth during a logging experiment. These include a correction for the buoyancy of the logging tool when immersed in the borehole fluid, for temperature changes near the measuring wheel affecting the radius of the depth-measuring system, and for thermal strain in the cable as it moves downhole.

The correction for tool buoyancy consists of a simple offset that occurs when the logging tool enters the borehole fluid:

$$\delta Z_{clF}^{bt} = \begin{cases} 0 & Z < h \\ Kg\,(m_t^f - m_t^a)(h + \Delta x), & Z > h \end{cases} \tag{3.21}$$

K is the elastic stretch coefficient of the cable, g is the gravitational acceleration, m_t^f and m_t^a are the weights of the logging tool in the borehole fluid and in air, h is the depth to the air/fluid interface in the borehole, and Δx is the horizontal distance between the measuring wheel and the hole. When logging with any of our temperature sensors, δZ_{clF}^{bt} is less than the resolution of the depth system and can be ignored. However, other tools for which δZ_{clF}^{bt} may be larger (e.g., sonic and optical loggers) are occasionally used with

our logging winch, so we include the buoyancy correction for completeness.

The temperature of the measuring wheel during a logging experiment can be significantly different from the reference calibration temperature $T_w^\star$. If the temperature of the wheel is T_w, the radial strain e_{wrT_w} in the wheel relative to its calibration state can be found from Eq. (3.15). Since T_w may vary considerably during a long logging run, the correction for the thermally induced radial change of the wheel is found through an integration:

$$\delta Z_{wrT} \;=\; \left(\frac{R_w}{R_n}\right) \int_o^{\tilde{Z}} e_{wrT_w}(\tilde{z})\, d\tilde{z}. \tag{3.22}$$

The corresponding thermally induced radial strain in the cable near the measuring wheel has a negligible effect (< 10 ppm) on the estimated depths and can be ignored.

In polar environments, the fluid and overlying air column in a borehole are typically much colder than conditions on the surface near the logging winch. Thus, the logging cable will contract as it moves beyond the measuring wheel and enters the borehole. By the time a section of cable reaches depth z, it will experience a thermally induced longitudinal strain,

$$e_{clT}(z) \;=\; \alpha\,[T(z) - T_w]\,, \tag{3.23}$$

relative to its length when it passed over the measuring wheel. Some of this strain is built into the depth-calibration function C_d. Subtracting this portion, the correction for the thermally induced longitudinal strain in the cable is

$$\delta Z_{clT} \;=\; \int_h^Z e_{clT}(z)\, dz \;-\; \alpha f_T\,[\,T(h) - T_w^\star]\, Z. \tag{3.24}$$

Applying these corrections to Eq. (3.20), our estimate of the true sensor depth during a logging experiment is

$$Z \;=\; \left[1 + C_d(T_w^\star, \tilde{Z}^\star)\,\right] \tilde{Z} \;+\; \delta Z_F \;+\; \delta Z_{clF}^{bt} \;+\; \delta Z_{wrT} \;+\; \delta Z_{clT}. \tag{3.25}$$

For most situations, δZ_F is the largest correction and δZ_{clT} is the second largest.

3.4 Measurement uncertainties

A variety of factors influence the uncertainty of the quantities being measured by the PTLS. For the temperature-measurement process, the primary uncertainties include those related to the PTLS resistance readout, uncertainties in the corrections made for systematic

errors in the Kelvin circuit measurements (Eqs. 3.1, 3.2, 3.3, 3.8), and uncertainties in the temperature sensor calibration used to convert measured resistance to temperature. The primary uncertainties for the depth-measurement process are related to the depth corrections (Eqs. 3.19, 3.21, 3.22, 3.24).

This section provides an analysis of the measurement uncertainties following CIPM guidelines [*ISO*, 1993b]. It is assumed the resistance-measuring circuitry is located on the surface since the PTLS is normally operated in this mode; several of the uncertainties to be described are not present when using downhole measurement circuitry, although the temperature-related drift of the circuit potentially can be quite large. With the CIPM approach, the components of a measurand's uncertainty are classified according to the method used to evaluate them. Type A uncertainty evaluations are based on statistical analysis of a series of observations while Type B evaluations are performed "by other means" using sound scientific judgment. The information used in a Type B analysis may, for example, include a general knowledge or experience with an instrument or the behavior of a material, manufacturer's specifications, or calibration reports. The degree of uncertainty for each component is given in terms of the standard uncertainty u_i that describes the interval within which a quantity should occur with 67 percent probability. The combined standard uncertainty of a measurement is obtained by combining the individual Type A and Type B standard uncertainties using the propagation of uncertainty law [*Taylor and Kuyatt*, 1994, Appendix A]. We implement the propagation law using the "root-sum-of-squares" (RSS) method. Although some of the uncertainties to be discussed are quite small with the current version of the PTLS, they were in some cases substantially larger with previous PTLS versions and therefore are discussed for completeness.

3.4.1 ITS-90 temperature uncertainties

3.4.1.1 Resistance readout uncertainties

The PTLS generally utilizes a commercial readout to measure the resistance of a temperature sensor during a logging experiment. Sources of uncertainty related to the resistance readout include the uncertainty of the resistance standards used to calibrate the readout, nonlinearity across the resistance scales, and internal noise. Current field procedures require temperature logs be completed within 24 hours of the readout's latest calibration.

3.4.1.1.1 Resistance standards

Immediately before each logging experiment, the resistance readout is calibrated using 10 kΩ and 100 kΩ DC resistance standards (Fluke 742A), and a 0 Ω short. In preparation for making measurements at the fixed calibration points, the readout and resistance standards are warmed up and then maintained at 23 ± 0.5°C for at least one hour. Once acquired, the calibration data are used to determine the coefficients in a quadratic function $f_c(R)$ which is used to correct the readout's measurements at other resistances. The uncertainties at the calibration points are found by combining the calibration uncertainty of the standards themselves (0.5 ppm for the 10-kΩ standard, 1.25 ppm for the 100-kΩ standard) with the uncertainty associated with their long-term drift (2.0 ppm·yr^{-1} for the 10-kΩ standard and 3.0 ppm·yr^{-1} for the 100-kΩ standard). With annual recalibration, the combined standard uncertainty of the resistance standards (in normalized form) is $u_{s,n} \equiv (u_s/R_s) = 2.1$ ppm at 10 kΩ and 3.2 ppm at 100 kΩ. These uncertainties are propagated to other resistances using a function of the same form as $f_c(R)$.

A different set of resistance standards was used prior to 2008. These standards were periodically calibrated using an instrument with a standard uncertainty of 58 ppm. Long-term drift between calibrations introduced an additional 58 ppm of uncertainty, yielding a combined standard uncertainty for these older standards of $u_{s,n} = 82$ ppm at both 10 kΩ and 100 kΩ.

3.4.1.1.2 Resistance readout's short-term uncertainty

The quoted short-term accuracy of the resistance readout currently used with the PTLS is $\pm 0.25\,\Omega$ for $R_s < 5$ kΩ and ± 50 ppm for 5 kΩ $\leq R_s \leq$ 200 kΩ. This specification includes the nonlinearity of the readout across the measurement range and internal noise. According to the manufacturer, the accuracy $(\pm a)$ specifies the width of a rectangular (uniform) probability distribution function; this PDF is taken to have a corresponding standard uncertainty of $a/\sqrt{3}$ [*Taylor and Kuyatt*, 1994]. Thus the short-term standard uncertainty of the readout is $u_r = 0.14\ \Omega$ for $R_s < 5$ kΩ and $u_{r,n} \equiv (u_r/R_s) = 29$ ppm for 5 kΩ $\leq R_s \leq$ 200 kΩ. Before 2008, a different readout was used whose accuracy included a component for the full-scale resistance value R_f. For this instrument the short-term standard uncertainty was $u_{r,n} = 11.6 + 5.8\,(R_f/R_s)$ ppm.

3.4.1.1.3 Combined resistance-readout uncertainty $\mathbf{u_{\tilde{R}_s}}$

Combining the uncertainties of the resistance standards with the short-term accuracy of the readout, we obtain the combined standard uncertainty $u_{\tilde{R}_s}$ of the resistance readout measurements. With the currently used resistance standards, $u_{\tilde{R}_s}$ is dominated by the short-term uncertainty of the readout itself. Thus $u_{\tilde{R}_s} = 0.14\,\Omega$ for $R_s < 5$ kΩ. For the more common sensor resistances ($R_s \geq 5$ kΩ), the combined standard uncertainty is $u_{\tilde{R}_s,n} \equiv (u_{\tilde{R}_s}/R_s) = 29$ ppm. Prior to 2008 the uncertainty of the standards was the major contributor to $u_{\tilde{R}_s}$ at most resistances, leading to combined readout uncertainties $u_{\tilde{R}_s,n}$ ranging from 83 to 107 ppm. Since both of the uncertainty components (u_s, u_r) are classified as Type B, the combined uncertainty of the resistance readout is also Type B.

3.4.1.2 Kelvin circuit uncertainties

As discussed in Section 3.3.2, the Kelvin circuit monitored by the resistance readout introduces multiple sources of systematic error in the resistance measurements. These sources include leakage paths between the circuit's electrical conductors, capacitance effects, self-heating effects, and thermal EMFs. Although we correct for the systematic errors, there are uncertainties associated with the corrections. In addition, electrostatic coupling, electromagnetic EMFs, triboelectric currents, and switching effects within the slip-ring assembly all generate noise in the Kelvin circuit. This noise is largely removed during data processing by using 1D wavelet denoising techniques [*Misiti et al.*, 2005]. However, because the noise removal process is imperfect, there remains an uncertainty in the resistance measurements associated with the noise.

3.4.1.2.1 Leakage paths

Applying the propagation of uncertainty law to the leakage path correction δR_l (Eq. 3.1), the standard uncertainty u_l of the leakage correction is given by

$$u_l = \frac{R_s}{(R_s + R_l)^2} \sqrt{(R_s + 2R_l)^2\, u_{R_s}^2 + R_s^2\, u_{R_l}^2} \tag{3.26}$$

where u_{R_l} is the standard uncertainty of leakage resistance R_l. Since $R_l \gg R_s$ for all operational conditions, we can re-express the leakage-path uncertainty in the normalized form

$$u_{l,n} \equiv \left(\frac{u_l}{R_s}\right) = \sqrt{4\left(\frac{u_{R_s}}{R_l}\right)^2 + \left(\frac{R_s}{R_l}\right)^2 \left(\frac{u_{R_l}}{R_l}\right)^2}. \tag{3.27}$$

The leakage resistance R_l is always ≥ 10 GΩ for the PTLS while the standard uncertainty of its determination is $u_{R_l} \approx 11.5$ GΩ based on the specifications of the measuring instrument. With such high R_l values, the second term within the square root of Eq. (3.27) exceeds the first term by about 10^8. Thus the standard uncertainty of the leakage correction reduces to

$$u_{l,n} = \left(\frac{R_s}{R_l}\right)\left(\frac{u_{R_l}}{R_l}\right). \tag{3.28}$$

3.4.1.2.2 Capacitance effects

The standard uncertainty u_c of the capacitance correction δR_c (Eq. 3.2) is given by

$$u_c = \tau R' \sqrt{\left(\frac{u_{R_s}}{R_s}\right)^2 + \left(\frac{u_C}{C}\right)^2 + \left(\frac{u_{R'}}{R'}\right)^2} \tag{3.29}$$

where $R' = \partial R_s / \partial t$ is the rate of resistance change while logging downhole. The accuracy of the instrument used to measure the capacitance of the logging cable, or of any filtering capacitors, establishes the relative capacitance uncertainty (u_C/C). Based on the manufacturer's specifications and a rectangular PDF, $(u_C/C) \simeq 0.0074$. This term completely dominates (u_{R_s}/R_s), which is of the order 10^{-4} or smaller. Using a Taylor Series expansion, the relative uncertainty of R' is found to be

$$\left(\frac{u_{R'}}{R'}\right) \approx \frac{1}{\sqrt{3}}\left(\frac{1}{m} + \frac{\Delta t_r}{\Delta t}\right) \tag{3.30}$$

where Δt is the sampling rate, Δt_r is the resolution of the time measurements (determined by the computer's clock), and m is a measure of the resistance change between samples relative to the resolution ΔR_r of the resistance readout,

$$m = \frac{R_{i+1} - R_{i-1}}{2\Delta R_r}. \tag{3.31}$$

Our sampling rates are slow enough that $\Delta t_r / \Delta t \ll 1/m$ under all circumstances. Dropping negligible terms, the standard uncertainty of the capacitance correction becomes

$$u_{c,n} \equiv \left(\frac{u_c}{R_s}\right) = \frac{C\Delta R_r}{\Delta t}\sqrt{\frac{1}{3} + m^2\left(\frac{u_C}{C}\right)^2}. \tag{3.32}$$

3.4.1.2.3 Self-heating effects

For the self-heating correction δR_h (Eq. 3.3), the associated standard uncertainty u_h is given by

$$u_h = \frac{\alpha_T I_s^2 R_s^2}{P_d} \sqrt{4\left(\frac{u_{I_s}}{I_s}\right)^2 + \left(\frac{u_{R_s}}{R_s}\right)^2 + \left(\frac{u_{P_d}}{P_d}\right)^2}. \tag{3.33}$$

The relative uncertainty of the power dissipation constant (u_{P_d}/P_d) is estimated to be roughly 0.1, which is several orders of magnitude larger than either (u_{I_s}/I_s) or (u_{R_s}/R_s). Dropping negligible terms, the uncertainty of the self-heating correction is

$$u_{h,n} \equiv \left(\frac{u_h}{R_s}\right) = \frac{\alpha_T I_s^2 R_s}{P_d}\left(\frac{u_{P_d}}{P_d}\right). \tag{3.34}$$

3.4.1.2.4 Thermal EMFs

The standard uncertainty u_e of the thermal EMF correction δR_e (Eq. 3.8) is

$$u_e = \frac{1}{I_s}\sqrt{u_{V_{\text{emf}}}^2 + V_{\text{emf}}^2\left(\frac{u_{I_s}}{I_s}\right)^2}. \tag{3.35}$$

Since the relative uncertainty of the regulated test current I_s is several orders smaller than that of the thermoelectric voltages, the standard uncertainty of the thermal EMF correction is simply

$$u_{e,n} \equiv \left(\frac{u_e}{R_s}\right) = \frac{u_{V_{\text{emf}}}}{I_s R_s}. \tag{3.36}$$

Prior to 2008, $u_{V_{\text{emf}}}$ was estimated to be about the same magnitude as V_{emf} ($\sim 0.5\,\mu$V). However, with the current PTLS design, V_{emf} is essentially zero and thus, so is $u_{V_{\text{emf}}}$ and u_e.

3.4.1.2.5 Noise

Extensive tests with noisy synthetic data show that the wavelet denoising methods used during data processing reduce the noise in the recorded resistances by a factor of 8. Thus the standard uncertainty of the resistance measurements due to instrumental noise is $u_n \approx \sigma_{\tilde{R}_n}/8$ where $\sigma_{\tilde{R}_n} \leq \sigma_{R_n}$ (see discussion, Section 3.3.2.3).

3.4.1.2.6 Summary of Kelvin circuit uncertainties

Equations (3.28), (3.32), (3.34), and (3.36) indicate the uncertainties (u_l, u_c, u_h, u_e) of the Kelvin-circuit resistance corrections depend on the specific conditions during a temperature log and thus must be treated on a case-by-case basis. Despite the need to specifically

consider the conditions for each experiment when evaluating the uncertainties, some general statements can be made. (1) Of the resistance-correction uncertainties, the uncertainty of the leakage-path correction (u_l) is the largest with the current PTLS operating under normal conditions (**Figure 3.10**). (2) Without the use of the resistance readout's internal filters or a filtering capacitor, the uncertainty u_n due to noise is the dominant Kelvin-circuit uncertainty for sensor resistances less than 20–30 kΩ. Even with the use of hardware filters to reduce the noise uncertainty, u_n is generally still the dominant uncertainty at low resistances ($R_s < 20$ kΩ). (3) At high resistances ($R_s > 70$ kΩ), the uncertainty of the leakage-path correction (u_l) is the dominant uncertainty. (4) All the uncertainties associated with the resistance corrections and noise are less than 0.1 mK for sensor resistances in the range 10–170 kΩ. (5) The uncertainties (u_l, u_c, u_h, u_e) associated with the Kelvin-circuit resistance corrections are all classified as Type B uncertainties while the noise uncertainty u_n is Type A.

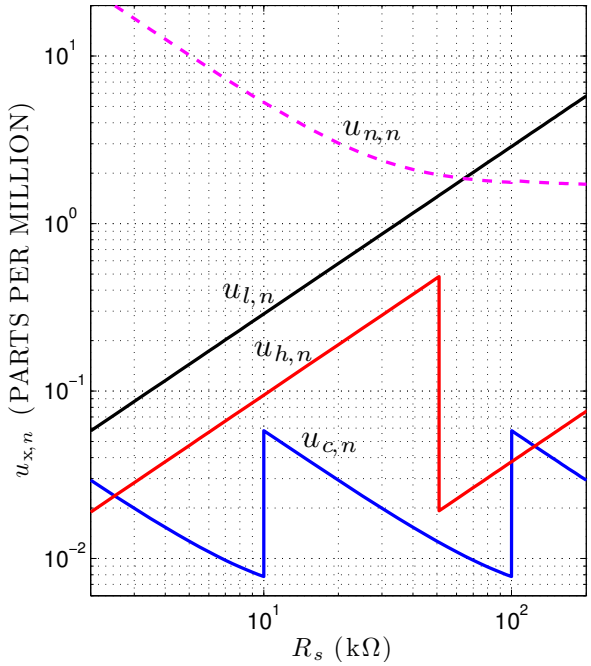

Figure 3.10: Standard uncertainties (u_l, u_c, u_h) associated with the resistance corrections, displayed in normalized form $u_{x,n} \equiv (u_x/R_s)$, for typical operating conditions. In this example, the uncertainty of the capacitance correction (u_c) corresponds to the case shown in **Figure 3.3** ($v = 5.5$ centimeters per second, $\partial T/\partial z = 25$ mK m^{-1}, $\tau = 10$ ms, $C = \tau/R_s$). The uncertainty of the thermal EMF correction (u_e) is essentially zero with the current PTLS design. The noise uncertainty (u_n) shown by the dashed line represents an upper bound for most operating conditions; it assumes hardware noise filters are not used. Equivalent temperature uncertainties are given by $u_{x,n}/\alpha_T$.

3.4.1.3 Temperature-sensor calibration uncertainties

Before every set of field experiments, the PTLS temperature sensors are calibrated on the ITS-90 temperature scale [*Mangum and Furukawa*, 1990] at the USGS thermal calibration facility in Lakewood, Colorado. Temperatures on the ITS-90 scale are defined in terms of a set of fixed points (melting, boiling, and triple points of pure substances), interpolating instruments, and equations relating the property measured by each interpolating instrument to temperature. Between 13.8 K and 1,235 K, the official interpolating instrument is the standard platinum resistance thermometer (SPRT). Thus, equations describing how the resistance of a standard SPRT varies with temperature are embodied in the definition of the ITS-90 temperature scale. To calibrate the PTLS temperature sensors, we use a 25.5-Ω quartz-sheath SPRT as our local standard. The probes to be calibrated are inserted into a copper equilibration block that is immersed in a temperature-controlled fluid bath; the SPRT is positioned in the equilibration block at the same distance from the center as the probes. The copper block effectively damps short-term temperature fluctuations in the calibration bath and improves the uniformity of the thermal field surrounding the probes and the SPRT. Once the bath stabilizes at a predetermined calibration point, the data-acquisition system simultaneously acquires the SPRT reference temperature $T^\star$ and the resistance $R^\star$ of each temperature sensor being tested. This process is repeated across the entire calibration range in 2-K increments with upcoming field experiments determining the calibration limits. Total least squares is then used to find the constants (a_i) in the 4-term calibration function (Eq. 3.11) from the $(T^\star, R^\star)$ calibration data. Residuals from this fit typically have standard deviations ranging from 0.20 to 0.45 mK.

The uncertainty of the resulting PTLS temperature-sensor calibrations is determined by a number of factors, including: the uncertainty of the SPRT calibration at ITS-90 fixed points, the propagation of error between those points, the accuracy of the SPRT readout, the accuracy of the thermistor scanner, and the magnitude of the temporal and spatial temperature variations within the calibration bath. The residuals from the least-squares fit to the calibration data do not reflect many aspects of the total uncertainty of the temperature-sensor calibration.

3.4.1.3.1 SPRT reference temperatures $\boldsymbol{T^{\star}}$

The uncertainty of the SPRT reference temperature $T^{\star}$ is determined by the uncertainty of the SPRT calibration and the accuracy of the instrument (readout) used to monitor the SPRT temperatures. Our quartz SPRT was most recently calibrated by Hart Scientific (American Fork, Utah) who provided expanded uncertainties (coverage factor $k = 2$) at fixed calibration points between -200°C and 0°C. The equivalent standard uncertainties are 0.5 mK at -197°C, 0.2 mK at -38.8344°C (triple point of mercury), and 0.1 mK at 0.010°C (triple point of water). Because the definition of the ITS-90 temperature scale over this range is based on equations describing the behavior of a standard SPRT, the calibration uncertainties between the fixed points are of the same order as those at the adjacent fixed points. We use error propagation curves provided by the National Institute of Standards and Technology to determine how the uncertainties at the triple point of mercury (TPHg) and triple point of water (TPW) propagate to other temperatures. Combining the propagated TPHg and TPW uncertainties, the standard uncertainty of the SPRT calibration ranges from 0.27 mK at -60°C to 0.10 mK at 0.01°C.

The accuracy of the SPRT readout is $\pm 0.0005\,\Omega$ for SPRT resistances less than $25\,\Omega$ and ± 20 ppm of the reading at higher resistances. Based on the thermal response of SPRTs [*McGee*, 1988], these specifications translate to a standard uncertainty ranging from 2.77 mK at -60°C to 2.90 mK at 0°C. Combining the uncertainty of the SPRT calibration with that of the SPRT readout, we obtain the standard uncertainty $u_{T^{\star}}$ of the SPRT reference temperatures. The combined uncertainty $u_{T^{\star}}$ is clearly dominated by the uncertainty of the SPRT readout with values ranging from 2.79 mK at -60°C to 2.90 mK at 0°C (**Figure 3.11**). Since the uncertainty of the SPRT calibration and the SPRT readout are both evaluated using Type B methods, the uncertainty of the SPRT temperature measurements is also classified as Type B.

3.4.1.3.2 Temperature-sensor resistance measurements $\boldsymbol{R^{\star}}$

The resistance of the PTLS temperature sensors being calibrated is monitored using an 8-channel thermistor scanner whose accuracy is ± 100 ppm of the reading. Based on a uniform PDF, the corresponding standard uncertainty $u_{R^{\star}}$ of the scanner's resistance measurements is 58 ppm. Expressed in terms of temperature, $u_{R^{\star}}$ ranges from 0.88 mK at

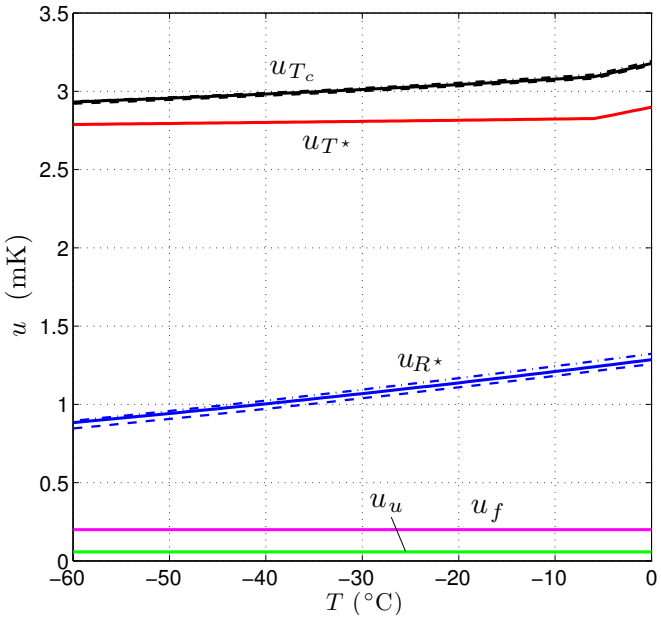

Figure 3.11: Combined standard uncertainty u_{T_c} of the PTLS temperature-sensor calibration. Also shown are the standard uncertainties of the individual components: $u_{T^\star}$ is the uncertainty of the SPRT reference temperature, $u_{R^\star}$ is the uncertainty of the temperature-sensor resistance measurements, u_f is the uncertainty associated with temperature fluctuations in the calibration bath, and u_u is the uncertainty due to bath nonuniformity. The three $u_{R^\star}$ curves (dashed, solid, dash-dot) show the uncertainty of the resistance measurements for the P, T01, and T02 probe series, respectively.

−60°C to 1.28 mK at 0°C for the T01 probe series; $u_{R^\star}$ is approximately 3 percent less for the P probe series and 2 percent more for the T02 probes (**Figure 3.11**). This is a Type B uncertainty. As with the SPRT readout, the thermistor scanner is operated within the 18–28°C range in order to achieve full accuracy.

3.4.1.3.3 Calibration bath and high-conductivity equilibration block

Other sources that affect the uncertainty of the temperature-sensor calibrations include temporal and spatial variations of the thermal field within the calibration bath. Both of these sources can cause temperature offsets between the probes being calibrated and the reference SPRT. The stability of the calibration bath (Hart model 7060) is reported to be ±2.5 mK at −60°C. This figure represents an expanded uncertainty with coverage factor $k = 2$. Experiments at −20°C confirm this value. Thus we take the stability of the bath to be ±2.5 mK across the full calibration range; the corresponding standard uncertainty u_{b_f} of the bath fluctuations is 1.25 mK. Several experiments were done to determine the

nonuniformity of the thermal field in the central portion of the bath where the calibrations are performed. We find that the standard uncertainty u_{b_u} of the spatial variations in this region is 2.5 mK.

To further control the stability and uniformity of the thermal field experienced by the probes and SPRT during calibration, we use a 7.62-cm-diameter, high-conductivity (copper) equilibration block within the calibration bath. The SPRT and PTLS probes are inserted in tight-fitting holes located 2.90 cm from the center. Heat-transfer simulations show that thermal fluctuations in the bath with periods less than 0.1 minute are completely damped at the position of the probes, while those with periods of 3 minutes (where the largest bath fluctuations occur) are damped by a factor of about 0.4 (function f, **Figure 3.12**). These fluctuations would not be an issue if the PTLS probes and the SPRT had identical time constants so that they would synchronously warm and cool in response to the temperature fluctuations. However, the time constant of the SPRT (18.5 seconds) is much longer than that of the PTLS temperature sensors (4.0 seconds) in this situation. Convolving the response functions of the SPRT and the PTLS temperature sensors [*Saltus and Clow*, 1994] with synthetic temperature fluctuations shows that the maximum temperature discrepancy between the SPRT and the probes caused by dissimilar time constants occurs at a period of about 0.8 minute (function g, **Figure 3.12**). However, little power occurs at such short periods due to the damping of the block. Considering the joint effects of equilibration block damping and the dissimilar time constants, the largest discrepancies between the recorded SPRT temperatures and the probe temperatures occur at periods of 2–3.5 minutes (function $f \cdot g$, **Figure 3.12**). This coincidentally matches the period where the bath fluctuations have their greatest power. The resulting standard uncertainty in temperature-sensor calibration related to bath fluctuations is $u_f = (0.16)\, u_{b_f} = 0.20$ mK.

Persistent temperature gradients always exist to some extent in calibration baths due to imperfect mixing of the bath fluid. Experiments with the Hart 7060 bath show that the standard uncertainty of the thermal field in the vicinity of the equilibration block is $u_{b_u} = 2.5$ mK. However, the field inside the block is expected to be much more uniform. To quantify the uniformity, the resistance change of an array of thermistors located within the block was monitored while the block was rotated about its central axis; the bath was held at a fixed temperature (to within u_{b_f}) during these tests. After removing temporal

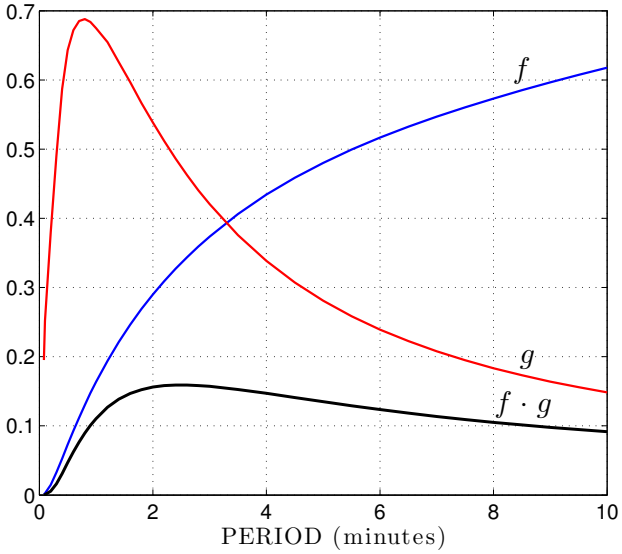

Figure 3.12: Damping of temperature fluctuations in the calibration bath by the high-conductivity equilibration block. Function $f = (u_p/u_{b_f})$ describes the relative damping provided by the block; u_{b_f} is the magnitude of the bath fluctuations while u_p is the magnitude of the fluctuations inside the block near the probes and SPRT. The block is essentially opaque to short-period fluctuations (< 0.1 minute) but is transparent to periods longer than 30 minutes. Function $g = (u_f/u_p)$ shows the relative temperature discrepancy between the SPRT and the probes caused by their dissimilar time constants. Combining the block damping with the dissimilar time-constant effect, the standard uncertainty of the temperature-sensor calibration due to bath fluctuations is $u_f = (f \cdot g)\, u_{b_f}$. The product $(f \cdot g)$ reaches a maximum value of 0.16 at periods of 2–3.5 minutes.

fluctuations due to bath instability, the thermal field was found to be uniform to within ± 0.10 mK inside the block at the location of the probes. The primary uncertainty of this determination is associated with the noise of the thermistor scanner (roughly ± 0.04 mK) as the experiment effectively removed uncertainties associated with the calibration of the individual thermistors: calibration, long-term drift, and nonlinearity of the thermistor scanner; and bath stability. The standard uncertainty of the temperature-sensor calibration related to bath nonuniformity is then estimated to be $u_u = 0.10/\sqrt{3} = 0.06$ mK. Both bath uncertainties (u_f, u_u) are classified Type A.

3.4.1.3.4 Combined temperature-sensor calibration uncertainty $\boldsymbol{u_{T_c}}$

Combining the uncertainty of the SPRT temperature measurements, of the thermistor scanner, and of the bath variations, the combined standard uncertainty u_{T_c} of the

temperature-sensor calibrations ranges from 2.93 mK at $-60°C$ to 3.18 mK at $0°C$ (**Figure 3.11**). Although the thermistor scanner and the bath variations contribute to u_{T_c}, the uncertainty of the SPRT temperature is the dominant factor in the combined calibration uncertainty. A small dependence of $u_{R^\star}$ on the α_T-characteristics of each probe series produces about a 1 percent difference in the combined uncertainty at any given temperature; this effect is small enough that it can be ignored. Because both Type A and Type B methods were used to evaluate the component uncertainties, the combined calibration uncertainty u_{T_c} is classified as Type A,B.

3.4.1.4 Combined ITS-90 temperature uncertainties

Combining the resistance-readout uncertainty ($u_{\tilde{R}_s}$), the resistance-correction uncertainties (u_l, u_c, u_h, u_e), the uncertainty due to instrumental noise (u_n), and the temperature-sensor calibration uncertainty (u_{T_c}), we finally obtain the total standard uncertainty u_T of the PTLS temperature-measurement process. In order to express u_T in terms of temperature, most of the component uncertainties ($u_R, u_l, u_c, u_h, u_e, u_n$) must be converted from resistances, where they are more naturally defined, to temperatures. This conversion involves the α_T-characteristics of the temperature sensors. Thus, the total uncertainty of the temperature-measurement process depends to some extent on which probe is used during a logging experiment. This is particularly true at warm temperatures due to the degradation of the resistance readout's accuracy at resistances less than 5 kΩ (**Figure 3.13**). To avoid this degradation, we strive always to select a probe whose resistance will remain above 5 kΩ for the duration of an experiment; thus the T02 probes, for example, are used only at temperatures below $-15°C$ while the P-series probes can be used up to at least $0°C$. With this constraint, the standard uncertainty of the temperature-measurement process ranges from 3.0 mK at $-60°C$ to 3.3 mK at $0°C$ with the current PTLS. As shown in **Figure 3.13**, the total temperature uncertainty u_T is strongly dominated by the temperature-sensor calibration uncertainty u_{T_c} with the current PTLS design. The resistance readout contributes 0.5–0.6 mK to the total while the upper limit of the noise contribution is generally $\leq$ 0.25 mK. Individual resistance-correction uncertainties (u_l, u_c, u_h, u_e) are less than 0.1 mK under all normal conditions. The combined uncertainty u_T of the ITS-90 temperature measurements is a Type A,B uncertainty.

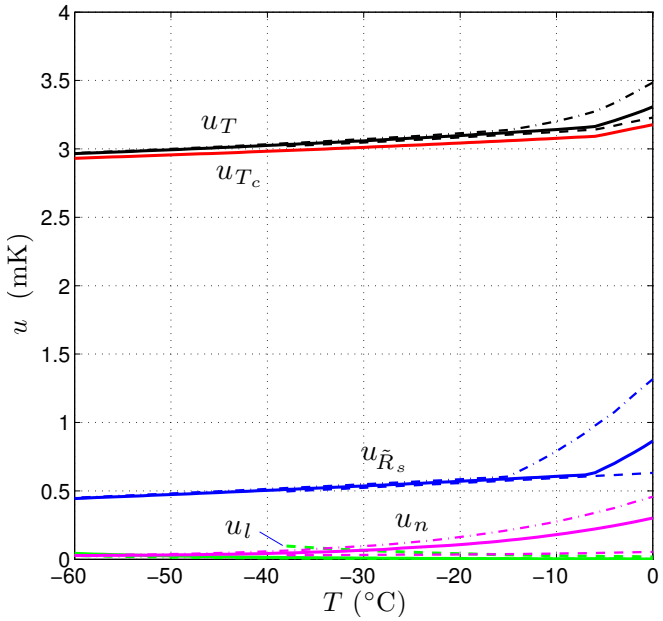

Figure 3.13: Combined standard uncertainty u_T of the ITS-90 temperature measurements obtained with the current PTLS when using the P, T01, and T02 probe series (dashed, solid, dash-dot lines, respectively). Also shown are the primary contributors to u_T, specifically, u_{T_c}, the standard uncertainty of the temperature-sensor calibrations, and $u_{\tilde{R}_s}$, the standard uncertainty of the resistance measurements. The u_n curves represent the upper bound for the noise uncertainty under most operating conditions; they assume the hardware noise filters are not used. The standard uncertainty of the resistance corrections is less than 0.1 mK in all situations.

Several of the temperature uncertainty components were larger before 2008, especially the resistance readout uncertainty $u_{\tilde{R}_s}$, the uncertainty of the thermal EMF correction (u_e), and the uncertainty of the capacitance correction (u_c). During 1993–2007, $u_{\tilde{R}_s}$ was about 3 times larger (1.4–2.1 mK) than with the current system. In addition, the thermal EMF uncertainty was comparable to the noise uncertainty u_n rather than being zero. Although larger, u_c was still less than 0.03 mK and thus of little consequence. Combining all the components, the total standard uncertainty u_T of the temperature-measurement process during 1993–2007 ranged from 3.2 mK at -60°C to 3.8 mK at 0°C.

3.4.2 Relative temperature uncertainties

Section 3.4.1 focused on the standard uncertainty u_T of the PTLS temperature measurements relative to the ITS-90 absolute temperature scale. For climate-change detection, this is the appropriate measure of uncertainty. However when reconstructing past climatic changes using borehole paleothermometry, we are not as concerned about uncertainties

relative to international absolute measurement scales as we are about the potential distortion of a temperature profile by measurement errors that could be misinterpreted as being due to climate change; to date, borehole paleothermometry generally has been used to analyze the shape of individual temperature profiles. Thus the offset of an entire temperature log due to miscalibration or system drift will not affect a reconstructed climate history and is of little importance in this context. For borehole paleothermometry, the appropriate uncertainties are those that describe the uncertainty of a temperature profile's shape, or expressed another way, the standard uncertainty (u_T^r) of the temperature measurements from a single temperature log relative to one another.

An assessment of the temperature uncertainties discussed in Section 3.4.1 shows that nearly all are associated with errors that potentially can distort a profile's shape and thus should be included in the combined standard uncertainty u_T^r of relative temperature measurements. However, because the long-term drift of a high-quality instrument will not in general produce an error that distorts a profile, the drift component of a readout's accuracy specification can be dropped while the nonlinearity and internal noise components should be retained. With this change, the standard uncertainty u_T^r of the relative temperature measurements produced by the PTLS ranges from 1.6 mK at $-60°$C to 2.0 mK at 0°C (**Figure 3.14**). The standard uncertainty $u_{T_c}^r$ of the temperature-sensor calibration (based on instrument specifications) is still the largest contributor, ranging from 1.6 mK at $-60°$C to 1.8 mK at 0°C. These uncertainty values are likely to be overestimates because the dominant source of uncertainty affecting $u_{T_c}^r$ and u_T^r is the SPRT readout, and it is used only over 1 percent of its range, whereas the nonlinearity specification pertains to the instrument's entire range. Still, without tests to quantify the uncertainty over such a restricted range, we must use the manufacturer's stated full-range uncertainty. At this time we simply note that the residuals from fitting the sensor calibration data to Eq. (3.11) typically have standard deviations ranging from 0.20 to 0.45 mK, suggesting $u_{T_c}^r$ (and thus u_T^r) may be substantially smaller than the values based on the SPRT readout's full-range nonlinearity specification. To accommodate this possibility, we state that the "upper limit" of u_T^r ranges from 1.6 mK at $-60°$C to 2.0 mK at 0°C. As with u_T, the uncertainty u_T^r of relative temperature measurements is classified Type A,B. The u_T^r upper limit before 2008 was very similar to the current value, ranging from 1.6 mK at $-60°$C to 2.1 mK at 0°C.

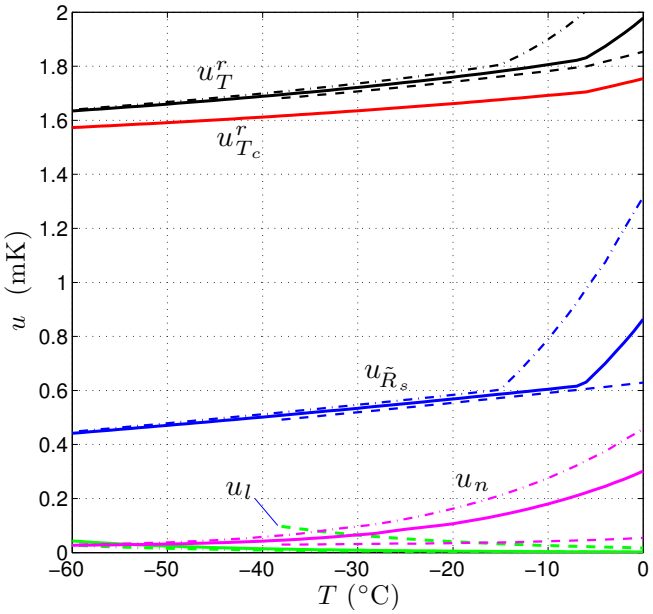

Figure 3.14: Combined standard uncertainty u_T^r of relative temperature measurements and the individual uncertainty components. The u_T^r and $u_{T_c}^r$ curves represent upper limits. Symbols are identical to those used in **Figure 3.13**.

3.4.3 Depth uncertainties

It is difficult to accurately determine the depth below surface with any borehole logging system. With the PTLS, systematic depth errors arise from force-induced strains in the logging cable and winch, tool buoyancy, temperature changes that alter the radius of the measuring wheel, and thermally induced longitudinal strains in the logging cable once it enters the relatively cold borehole. We attempt to correct for these errors (Section 3.3.3), although there are uncertainties in the corrections. Errors also potentially arise from slippage of the cable on the measuring wheel, debris in the wheel's cable groove, and downhole cable hangups. Cable slippage is minimized by logging at a slow, steady pace (5.5 cm·s^{-1}, or less). If slippage occurs with the PTLS, some of it presumably is incorporated in the depth-calibration factor C_d; depth calibration data are collected at the same downward speed and tensions as utilized during a log. The boreholes we log in polar environments are invariably filled with a clean, nonfreezing fluid (for example, n-butyl acetate, arctic diesel fuel, or a nonaromatic equivalent). As a result, debris in the groove of the measuring wheel that would alter the effective radius of the measuring system has generally not been an issue. Cable and (or) logging-tool hangups within a borehole

do sometimes occur. These are detected by monitoring cable tension. When hangups occur, the log is either stopped and restarted once the tool is past the impediment or the logging run is terminated, depending on the severity of the hangup and the objective of the experiment. In the former case, a depth offset with an unknown uncertainty may occur at the obstruction; in the latter case, no depth error arises. When cable hangups do not occur, we are able to quantify the uncertainty u_Z of the logging sensor's true depth Z using the root-sum-square method. Individual uncertainties contributing to u_Z are as follows:

3.4.3.1 Recorded depth measurements

The leading term in our estimated true sensor depth (Eq. 3.25) involves the depth recorded by the counter weighted by a calibration factor, $[1 + C_d(T_w^\star, \tilde{Z}^\star)]\,\tilde{Z}$. Since $C_d(T_w^\star, \tilde{Z}^\star)$ is simply a reference value that is always $\ll 1$, the standard uncertainty of this term is equivalent to the uncertainty $u_{\tilde{Z}}$ of the measurements reported by the depth counter. We establish $u_{\tilde{Z}}$ through statistical analysis of multiple determinations of a borehole's total depth according to the counter. Given the PTLS' operating environment, $u_{\tilde{Z}}$ is believed to primarily reflect variations in cable slippage on the measuring wheel.

3.4.3.2 Force-induced strains

Starting with Eq. (3.19), the standard uncertainty u_F of the depth correction for force-induced strains (δZ_F) is found to be

$$u_F \;=\; \int_o^{\tilde{Z}} u_{\mathcal{F}}(\tilde{Z} - \tilde{z})\, d\tilde{z} \tag{3.37}$$

where $u_{\mathcal{F}}(\tilde{Z})$ is the standard uncertainty of the experimentally determined function $\mathcal{F}(\tilde{Z})$. When $\mathcal{F}(\tilde{Z})$ is adequately represented by a linear function, its depth-dependent uncertainty is

$$u_{\mathcal{F}}(\tilde{Z}) \;=\; \sigma \sqrt{\frac{1}{n} + \frac{\left(\tilde{Z} - <\tilde{Z}_i>\right)^2}{\sum\limits_{i=1}^{n} \left(\tilde{Z}_i - <\tilde{Z}_i>\right)^2}}\,. \tag{3.38}$$

Here, σ is the standard deviation of the $\mathcal{F}_i$ data, $<\tilde{Z}_i>$ is the mean value of the calibration depths $\tilde{Z}_i$, and n is the number of depth-calibration points [*Bowker and Lieberman*, 1972]. More complicated expressions are required when $\mathcal{F}(\tilde{Z})$ is nonlinear.

3.4.3.3 Tool buoyancy

Applying the propagation of uncertainty law to the tool buoyancy correction δZ_{clF}^{bt} (Eq. 3.21), the standard uncertainty u_{bt} of this correction is

$$u_{bt} = \delta Z_{clF}^{bt} \left[\left(\frac{u_K}{K}\right)^2 + \left(\frac{u_{\Delta m}}{\Delta m}\right)^2 + \left(\frac{u_h}{h+\Delta x}\right)^2 + \left(\frac{u_{\Delta x}}{h+\Delta x}\right)^2 \right]^{1/2} \tag{3.39}$$

where $\Delta m = m_t^f - m_t^a$. The fractional uncertainty (u_K/K) of the logging cable's elastic stretch coefficient is estimated to be about 0.1. This greatly exceeds the fractional uncertainties associated with the mass difference Δm and the lengths h and Δx. Thus, uncertainty u_{bt} is well approximated by

$$u_{bt} \;=\; Kg(m_t^f - m_t^a)\,(h+\Delta x)\left(\frac{u_K}{K}\right). \tag{3.40}$$

3.4.3.4 Radial strain of measuring wheel, thermal

Letting $\phi(t) = T_w(t) - T_w^\star$, the standard uncertainty u_{wT} of the correction for the thermally induced radial strain of the measuring wheel (δZ_{wrT}, Eq. 3.22) during a log is

$$u_{wT} = \left(\frac{R_w}{R_n}\right) \left[u_\alpha^2 \left(\int_o^{\tilde{Z}} \frac{\partial e_{wrT_w}}{\partial \alpha}\, d\tilde{z} \right)^2 + u_\phi^2 \left(\int_o^{\tilde{Z}} \frac{\partial e_{wrT_w}}{\partial \phi}\, d\tilde{z} \right)^2 \right]^{1/2} \tag{3.41}$$

where

$$\begin{aligned} \frac{\partial e_{wrT_w}}{\partial \alpha} &= \phi\,(1+3\alpha\phi)^{-1/2}\,(1+\alpha\phi)^{-3/2} \\ \frac{\partial e_{wrT_w}}{\partial \phi} &= \alpha\,(1+3\alpha\phi)^{-1/2}\,(1+\alpha\phi)^{-3/2}. \end{aligned}$$

The uncertainty u_α of the measuring wheel's thermal expansion coefficient is estimated to be of order 0.1α while uncertainty u_ϕ is typically 0.1–1.0 K. With these values, u_α and u_ϕ are both significant contributors to u_{wT}.

3.4.3.5 Longitudinal strain of logging cable, thermal

Uncertainties in the logging cable's thermal expansion coefficient α, the temperature difference $\psi = T(z) - T_w$, and parameter f_T are all significant contributors to the uncertainty u_{cT} of the correction for the thermally induced length change of the cable as it

descends a borehole (δZ_{clT}, Eq. 3.24). Applying the propagation of uncertainty law to δZ_{clT} and dropping negligible terms, u_{cT} is given by

$$u_{cT} = \left[\left(\frac{u_\alpha}{\alpha} \right)^2 \left(\int_h^Z e_{clT}\, dz \right)^2 + u_\psi^2 \left[\alpha \left(Z - h \right) \right]^2 + u_{f_T}^2 \left\{ \alpha \left[T(h) - T_w^\star \right] Z \right\}^2 \right]^{1/2} . \quad (3.42)$$

For the logging cable, the fractional uncertainty (u_α / α) is estimated to be 0.1; u_ψ ranges 0.1–1.0 K while u_{f_T} is about 0.1.

3.4.3.6 Combined depth uncertainty u_Z

Combining the individual uncertainties, the standard uncertainty of a sensor's true depth is

$$u_Z = \sqrt{u_{\tilde{Z}}^2 + u_F^2 + u_{bt}^2 + u_{wT}^2 + u_{cT}^2} \, . \quad (3.43)$$

Ordinarily, $u_{\tilde{Z}}$ and u_F are the dominant contributors to u_Z. Uncertainty components ($u_{\tilde{Z}}$, u_F) are classified as Type A uncertainties, while (u_{bt}, u_{wT}, u_{cT}) are Type B. The combined depth uncertainty u_Z is thus Type A,B. The magnitude of the individual components and of the combined uncertainty depend to a large degree on specific borehole conditions and the temperature near the winch.

3.4.4 Example: proposed WAIS Divide borehole, Antarctica

To illustrate the magnitude of the uncertainties and the degree to which they can vary with depth, we consider the conditions at the proposed WAIS Divide Ice Core site in West Antarctica (79°28′ S., 112°05′ W.). **Figure 3.15a** shows the "best-guess" temperature profile within the ice sheet at this location based on ice-flow modeling (Tom Neumann, written commun., 2006). We anticipate the fluid in the proposed borehole will be stably stratified (nonconvecting) within 2,000 m of the surface once the hole is completed. **Figure 3.15b** shows the uncertainty of the resistance corrections assuming the hole is logged with the current PTLS using a T01-series probe, the logging speed is 5.5 cm·s^{-1}, a 0.47-μF filtering capacitor is used, and the hardware noise filters are off. With a T01-series probe, the sensor resistance should range from 20.2 kΩ at the coldest temperatures encountered (−33.9°C) to 4.6 kΩ at the bottom of the hole. The standard uncertainty (u_l, u_h, u_c, u_e) of the resistance corrections are expected to be less than 0.011 mK at all depths while the uncertainty u_n associated with electrical noise is predicted to increase from about 0.06 mK in the upper 2,000 m of the borehole to 0.24 mK at the bottom.

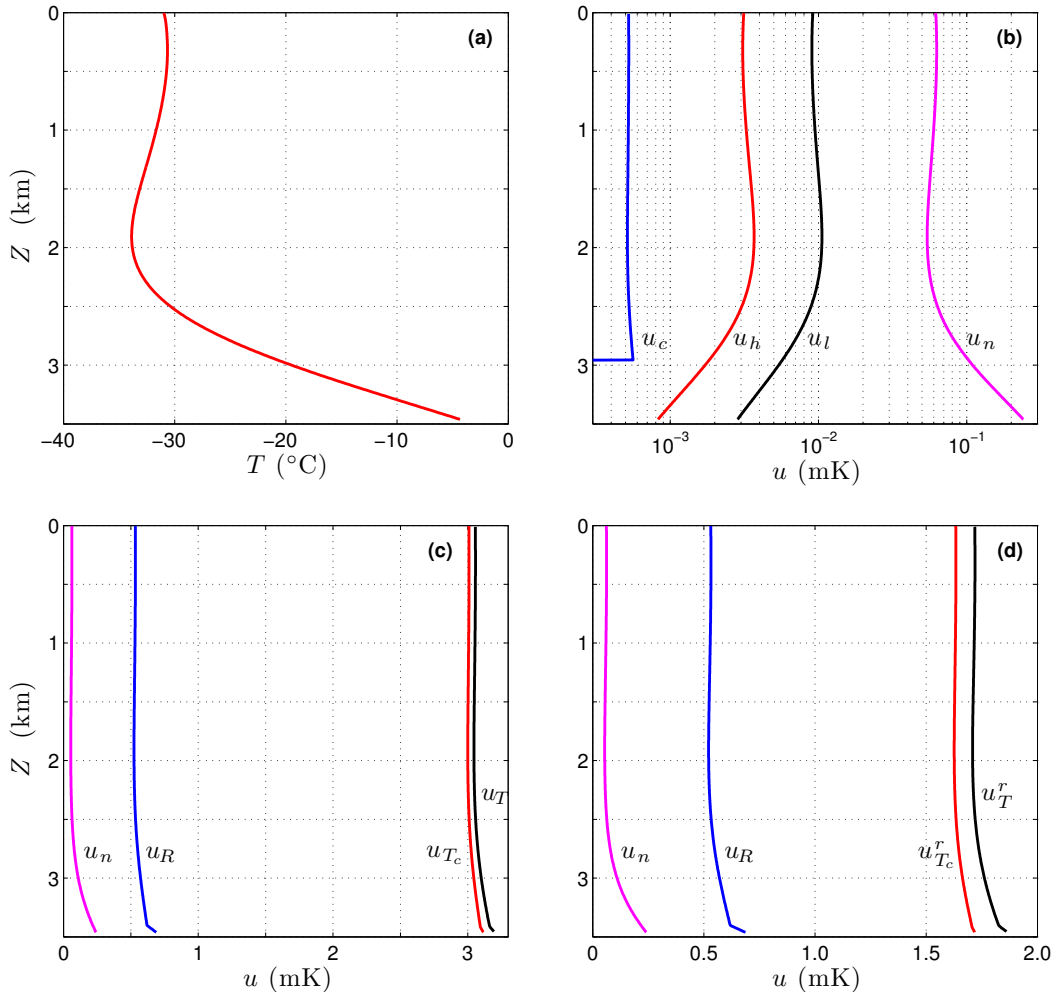

Figure 3.15: Temperature-measurement uncertainties for the proposed 3.5-kilometer deep WAIS Divide borehole in West Antarctica. **(a)** Best-guess temperature profile at this site based on ice-flow modeling. **(b)** Expected resistance-correction uncertainties (u_l, u_h, u_c) and the noise uncertainty (u_n) assuming the hole is logged with the current PTLS using a T01-series probe at 5.5 centimeters per second. **(c)** Combined standard uncertainty (u_T) of the ITS-90 temperature measurements along with the largest contributing uncertainties. **(d)** Combined standard uncertainty (u_T^r) of the relative temperature measurements along with the largest contributing uncertainties. The u_T^r and $u_{T_c}^r$ curves are upper limits.

Despite the 30-K temperature change along the profile, the combined standard uncertainty u_T of the ITS-90 temperature measurements has only a small depth dependence, varying from 3.05 mK in the upper 2,000 m to 3.19 mK at the bottom (**Figure 3.15c**). This stems from the weak temperature dependence of the dominant term, u_{T_c}. Similarly, the combined standard uncertainty u_T^r of the relative temperature measurements that would be used for borehole paleothermometry is only mildly depth-dependent (**Figure 3.15d**),

ranging from 1.71 mK in the upper 2,000 m to 1.86 mK at the base of the ice sheet (about 3,465 m).

Figure 3.16 shows the uncertainty of the temperature sensor's location (depth) when logging the WAIS Divide borehole using plausible values for various parameters. However, it must be emphasized the true depth uncertainties for WAIS Divide temperature logs will depend on the actual borehole conditions and parameter values that occur during those logs. These factors will not be known until the borehole is completed and the hole

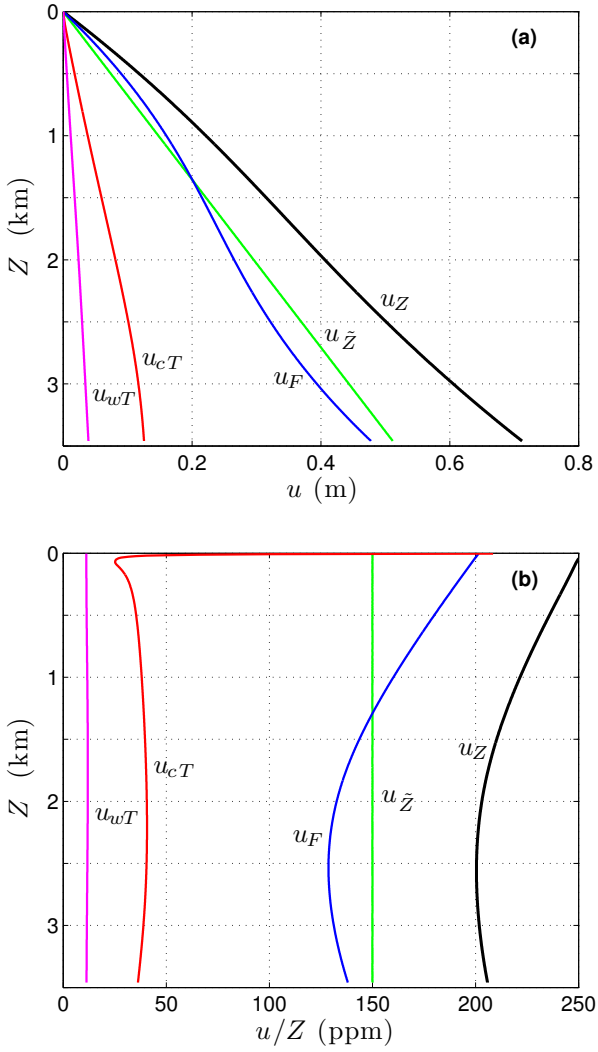

Figure 3.16: Depth uncertainties for the proposed WAIS Divide borehole as a function of sensor depth Z based on plausible values for various parameters. (u_F, u_{cT}, u_{wT}) are the standard uncertainties of the primary depth corrections while $u_{\tilde{Z}}$ is the standard uncertainty of the measurements reported by the depth counter. The combined standard uncertainty u_Z of the sensor's true depth ranges from 200 to 250 ppm.

has been logged several times. For the example shown in **Figure 3.16**, we assume the temperature $T_w(t)$ of the measuring wheel follows a diurnal cosine-function, fluctuating $\pm 5^{\circ}$C about a mean value of -10°C, i.e., typical summertime temperatures inside the drilling structure where the logging winch will be located. The reference calibration temperature of the wheel ($T_w^{\star}$) is taken to be -10°C, the fluid level in the borehole is set at the firn/ice transition ($h = 73$ m), parameter f_T is 0.3, and uncertainties u_ϕ and u_ψ are both 1 K. With these values, the standard uncertainty u_{wT} of the depth correction for the thermally induced radial strain in the measuring wheel during a log is limited to 11–12 ppm. The correction for the shortening of the cable in the cold borehole has a standard uncertainty u_{cT} ranging from 25 ppm near the surface to a peak value of about 40 ppm when the sensor reaches $Z \approx 1{,}800$ m. For a PTLS temperature sensor, the uncertainty u_{bt} of the tool buoyancy correction is less than 2 ppm and can be ignored.

To account for force-dependent effects on the depth measuring system, we assume in this example that nine pairs of depth-calibration data ($\mathcal{L}$, $\tilde{\mathcal{L}}$) are collected across the range of borehole depths and that the standard deviation of the fit to the resulting $\mathcal{F}_i$ data is $\sigma = 3.0\text{x}10^{-4}$. This value for σ is intermediate between that obtained in the recently logged 1-km Siple Dome A borehole ($2.4\text{x}10^{-4}$) and the 3-km GISP2-D borehole ($4.1\text{x}10^{-4}$); GISP2-D was logged before the PTLS winch had a level-wind system, so a much higher value for σ is expected from those logs than would occur today. With the proposed set of calibration data, the standard uncertainty u_F of the depth correction for force-induced strains ranges from 200 ppm near the surface to a minimum value of 130 ppm at $Z \approx$ 2,500 m. The greatest unknown in the projected depth uncertainties for the WAIS Divide borehole involves the standard uncertainty $u_{\tilde{Z}}$ of the measurements reported by the depth counter. For the final set of logs obtained in the Siple Dome A borehole, the uncertainty $u_{\tilde{Z}}$ was about 140 ppm. Thus, when logging conditions are favorable, the repeatability of the measurements reported by the depth counter is fairly high. In the WAIS Divide example, we use a nominal value for $u_{\tilde{Z}}$ of 150 ppm. Combining the individual uncertainty terms, the standard uncertainty of the temperature sensor's true depth ranges from 200 to 250 ppm (**Figure 3.16b**).

3.5 Summary

From its origins in the early 1990s, the USGS Polar Temperature Logging System has evolved into a reliable high-precision data-acquisition system for cold polar environments. This field-proven system has been extensively used in Greenland, Antarctica, and arctic Alaska. With a temperature resolution better than 0.2 mK, the PTLS is capable of detecting small subsurface temperature changes due to fluid convection and other phenomena. Our initial goal of reducing the uncertainty of the temperature measurements to about 1 mK has proven difficult to achieve. The standard uncertainty u_T of the system's ITS-90 temperature measurements is 3.0–3.3 mK. This is more than adequate for climate-change detection and monitoring, especially in the Arctic where contemporary surface-temperature changes exceeding 1 K/decade have recently been observed. Relative temperature measurements used to reconstruct past climate changes with borehole paleothermometry have a standard uncertainty u_T^r whose upper limit ranges from 1.6 to 2.0 mK. This is tantalizingly close to 1 mK.

The uncertainty of the temperature sensor's location (depth) during a log depends on specific borehole conditions and the temperature near the measuring wheel. Thus the depth uncertainty must be treated on a case-by-case basis. However, recent experience with our large winch indicates that when conditions are favorable (that is the winch is operated within a shelter, steady power is available for the winch motor, fluid in the borehole is free of debris, and so forth), the 4.5-km system can produce depths with a standard uncertainty u_Z on the order of 200–250 ppm. The small helicopter-transportable winches have undergone a number of design changes recently. Although the depth-measurement system for the small winches is very similar to the 4.5-km system, we do not yet have enough information about various parameters to quantitatively assess u_Z for logs acquired with these portable winches. The current specifications for the USGS Polar Temperature Logging System are summarized in **Table 3.1**.

Table 3.1: Specifications of the USGS Polar Temperature Logging System, mid-2008.

Temperature range	−60°C to +23°C	
Temperature resolution	0.02–0.19 mK	
Depth range	0–4,500 m	
Depth resolution	1.0 cm	
Standard uncertainty, ITS-90 temperature measurements	3.0–3.3 mK	(Type A,B)
Standard uncertainty, relative temperature measurements	1.6–2.0 mK†	(Type A,B)
Standard uncertainty, depth measurements	200–250 ppm‡	(Type A,B)

† Upper limit, ‡ 4.5-km winch with favorable logging conditions.

3.6 Notation and symbols

C	capacitance
$C_d(T_w, \tilde{Z})$	depth calibration function
e_{clT}	strain, cable, longitudinal, thermal
e_{crT}	strain, cable, radial, thermal
e_{wrT}	strain, measuring wheel, radial, thermal
$\mathcal{F}(\tilde{Z})$	force-dependent function
g	gravitational acceleration
h	depth to air/fluid interface in a borehole
K	elastic stretch coefficient
I_s	source current
I'	extraneous current (noise)
P_d	power-dissipation constant, thermistor
Q	Seebeck coefficient
r	radius, logging cable
R_l	interconductor leakage resistance
R_L	lead resistance (Kelvin circuit)
R_s	temperature-sensor resistance (true)
$\tilde{R}_s$	temperature-sensor resistance (measured)
R_n	nominal radius used by depth counter
R_w	radius, depth-measuring wheel
$R^\star$	sensor resistance during calibration
t	time
T	temperature
T_w	measuring wheel temperature
$T_w^\star$	reference depth-calibration temperature
$T^\star$	SPRT reference temperature
u_{bt}	standard uncertainty, tool buoyancy correction
u_c	standard uncertainty, capacitance correction
u_{cT}	standard uncertainty, correction for thermal strain (longitudinal) of logging cable
u_e	standard uncertainty, thermal EMFs
u_f	standard uncertainty of temperature-sensor calibration due to bath fluctuations
u_F	standard uncertainty, force-induced corrections

$u_{\mathcal{F}}$ standard uncertainty of function $\mathcal{F}$
u_h standard uncertainty, self-heating correction
u_l standard uncertainty, leakage correction
u_n standard uncertainty, instrumental noise
u_r standard uncertainty, resistance readout
$u_{\tilde{R}_s}$ combined standard uncertainty, resistance readout measurements
$u_{R^\star}$ standard uncertainty, temperature-sensor resistance measurements during calibration
u_s standard uncertainty, resistance standards
u_T combined standard uncertainty, ITS-90 temperature measurements
u_T^r combined standard uncertainty, relative temperature measurements
u_{T_c} combined standard uncertainty, temperature-sensor calibration
$u_{T^\star}$ combined standard uncertainty, SPRT reference temperature
u_u standard uncertainty of temperature-sensor calibration due to bath nonuniformity
u_{wT} standard uncertainty, correction for thermal strain of depth measuring wheel
u_Z combined standard uncertainty, sensor depth
$u_{\tilde{Z}}$ standard uncertainty of sensor depth (as reported by counter)
v logging speed
V voltage
V' extraneous voltage (noise)
V_{emf} thermoelectric voltage (thermal EMF)
z true depth coordinate
$\tilde{z}$ counter depth coordinate
Z sensor depth (true)
$\tilde{Z}$ sensor depth (reported by counter)
$\tilde{Z}^\star$ reference calibration depth
α coefficient of thermal expansion, linear
α_T coefficient of resistance, thermistor
β coefficient of thermal expansion, volumetric
δR_c resistance correction, capacitance
δR_e resistance correction, thermal EMFs
δR_h resistance correction, self-heating
δR_l resistance correction, leakage
ΔR_r resistance resolution
ΔT_r temperature resolution
Δt data sampling rate
Δx horizontal distance between measuring wheel and borehole
Δz_r depth resolution
δZ_{clF}^{bt} depth correction, tool buoyancy, cable, longitudinal
δZ_{clT} depth correction, cable, longitudinal, thermal
δZ_F depth correction, force-induced strains
δZ_{wrT} depth correction, measuring wheel, radial, thermal
σ_{R_n} standard deviation of resistance noise
$\sigma_{\tilde{R}_n}$ standard deviation of recorded noise
τ circuit response time

3.7 References

Bevington, P.R. (1969), *Data Reduction and Error Analysis for the Physical Sciences*, New York, McGraw-Hill, 336 p.

Bowker, A.H., and Lieberman, G.J. (1972), *Engineering Statistics* (2d ed.), Englewood Cliffs, N.J., Prentice-Hall, 641 p.

Clow, G.D. (1992), The extent of temporal smearing in surface-temperature histories derived from borehole temperature measurements, *Palaeogeography, Palaeoclimatology, Palaeoecology*, 98, 81–86.

Clow, G.D., Saltus, R.W., and Waddington, E.D. (1996), A new high-precision borehole temperature logging system used at GISP2, Greenland and Taylor Dome, Antarctica, *J. Glaciol.*, 42, 576–584.

ISO (1993a), *International Vocabulary of Basic and General Terms in Metrology* (2d ed.): International Organization for Standardization, Geneva, Switzerland, 59 p. (ISBN 92-67-01075-1)

ISO (1993b), *Guide to the Expression of Uncertainty in Measurement: International Organization for Standardization*, Geneva, Switzerland, 110 p. (ISBN 92-67-10188-9)

Mangum, B.W., and Furukawa, G.T. (1990), Guidelines for realizing the International Temperature Scale of 1990 (ITS-90), *NIST Technical Note 1265*, National Institute of Standards and Technology, 176 p.

McGee, T.D. (1988), *Principles and Methods of Temperature Measurement*, New York, Wiley, 581 p.

Misiti, M., Misiti, Y., Oppenheim, G., and Poggi, J. (2005), *Wavelet Toolbox User's Guide*, Fourth printing, Natick, Massachusetts, The MathWorks Inc., 1034 p.

Parker, R.L. (1994), *Geophysical Inverse Theory*, Princeton, N.J., Princeton University Press, 386 p.

Saltus, R.W., and Clow, G.D. (1994), Deconvolution of continuous borehole temperature logs: algorithms and accuracies, *USGS Open-File Report 94–254*, U.S. Geological Survey, 42 pp.

Sass, J.H., Lachenbruch, A.H., Munroe, R.J., Greene, G.W., and Moses, T.H., Jr. (1971), Heat flow in the western United States, *J. Geophys. Res.*, 76, 6376–6413.

Steinhart, J.S., and Hart, S.R. (1968), Calibration curves for thermistors, *Deep-Sea Res.*, 15, 497–503.

Taylor, B.N., and Kuyatt, C.E. (1994), Guidelines for evaluating and expressing the uncertainty of NIST measurement results, *NIST Technical Note 1297*, National Institute of Standards and Technology, 20 p.

CHAPTER 4

CREATION OF A 40-YEAR HOMOGENEOUS BOREHOLE TEMPERATURE DATASET FROM THE ARCTIC SLOPE OF ALASKA

4.1 Abstract

A homogeneous set of temperature measurements obtained from the DOI/GTN-P Deep Borehole Array between 1973 and 2013 is presented. The 23-element array is located on the Arctic Slope of Alaska, a region of cold continuous permafrost. Most of the monitoring wells are situated on the arctic coastal plain between the Brooks Range and the Arctic Ocean, while others are in the foothills to the south. The data represent the true temperatures in the wellbores and surrounding rocks at the time of the measurements; they have not been corrected to remove the thermal disturbance caused by drilling the wells. With a few exceptions, the drilling disturbance is estimated to have been of order 0.1 K or less by 1989. Thus, most of the temperature measurements acquired during the last 25 years are little affected by the drilling disturbance. The data contribute to ongoing efforts to monitor changes in the thermal state of permafrost in both hemispheres by the Global Terrestrial Network for Permafrost (GTN-P), one of the primary subnetworks of the Global Terrestrial Observing System (GTOS). The data will also be useful for refining our basic understanding of the physical conditions in permafrost in arctic Alaska, as well as providing important information for validating predictive models used for climate impact assessments. The processed data are available from the ACADIS repository at http://dx.doi.org/10.5065/D6N014HK.*

---

*This chapter was originally published as: Clow, G.D. (2014), Temperature data acquired from the DOI/GTN-P Deep Borehole Array on the Arctic Slope of Alaska, 1973–2013, *Earth Syst. Sci. Data*, **6**, 201–218, doi:10.5194/essd-6-201-2014.

4.2 Introduction

The Arctic is highly sensitive to increases in global mean air temperature as exemplified by the large and persistent physical and biological changes currently being observed there [*Jeffries et al.*, 2012, 2013]. In turn, the Arctic can have a significant impact on the global climate system through ice-albedo feedbacks and the potential loss of vast amounts of methane (a potent greenhouse gas) stored in permafrost to the atmosphere. Despite this, the Arctic remains a data-sparse region, limiting our understanding of critical processes and our ability to project future environmental conditions. To address this issue, several initiatives have been undertaken to develop comprehensive observing systems for the atmosphere, ocean, and terrestrial components of the arctic climate system (e.g., the Sustaining Arctic Observing Networks initiative). These observing systems are generally built from an aggregation of many national or regional observing networks. The success of these comprehensive observing systems critically depends on the contributions from the individual networks.

Here we focus on one such network designed to monitor the thermal state of permafrost on the Arctic Slope of Alaska. The origin of the network began 40 yr ago. From 1975 to 1981, 28 test wells were drilled in the National Petroleum Reserve–Alaska (NPR-A) as part of a petroleum exploration program overseen by the US Department of the Interior [*Gryc*, 1988]. These 1–6 km deep wells (**Figure 4.1**) penetrated marine and nonmarine sedimentary sequences between the Brooks Range and the Arctic Ocean. Most of the well sites are on the low-lying arctic coastal plain while a few are in the rolling foothills to the south. Permafrost in this area is "continuous", being 200–400 m thick. As with all deep wells, temperatures in the wellbores and surrounding rocks were significantly disturbed by the addition of drilling muds, circulating fluids, and other processes during drilling. This thermal drilling disturbance eventually dissipates over many years [*Lachenbruch and Brewer*, 1959]. Wells drilled by the petroleum industry on the Arctic Slope of Alaska were almost always either put into production or plugged and abandoned long before the wells could return to thermal equilibrium. Realizing the NPR-A test wells provided a rare opportunity to obtain "undisturbed" temperatures in permafrost, the US Geological Survey (USGS) requested that 21 of the wells (**Table 4.1**) be completed in a manner that would allow high-precision temperature measurements to be made over many years. This

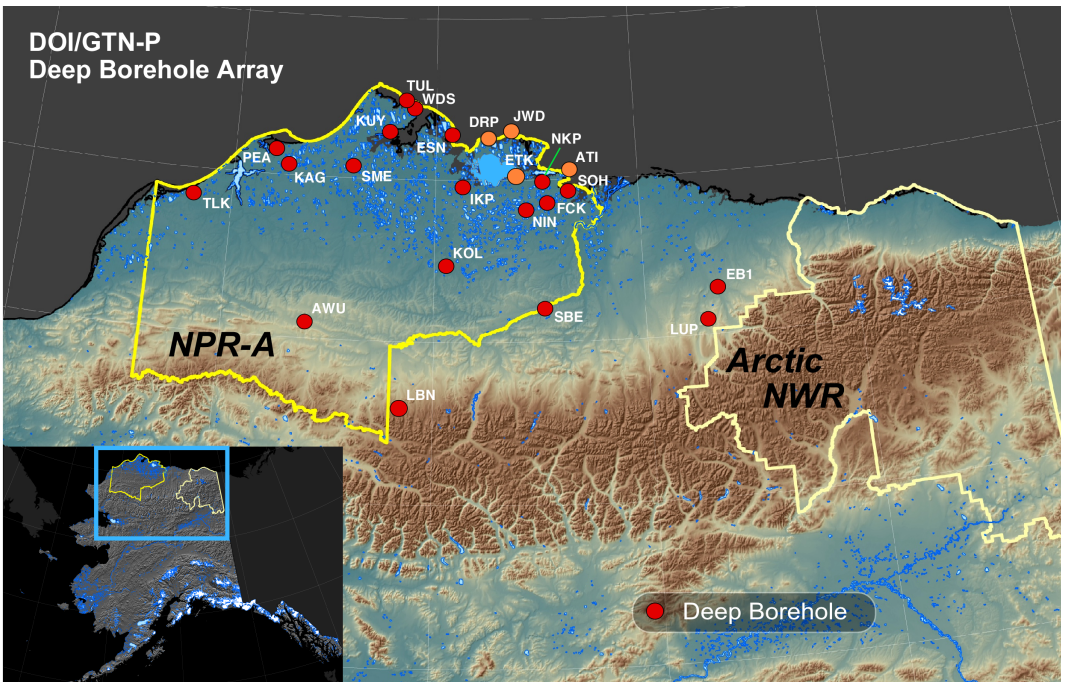

Figure 4.1: Location of the 23 DOI/GTN-P boreholes used to monitor the thermal state of permafrost (TSP) in the National Petroleum Reserve–Alaska (NPR-A) and near the Arctic National Wildlife Refuge. Wells indicated by orange symbols have been plugged and are no longer accessible.

involved filling the borehole casing with a nonfreezing fluid (diesel oil) above a cement plug installed 200–900 m below the surface, depending on the well. Four other wells to the east were preserved in a similar manner through the courtesy of Mobil, Exxon, BP, Sinclair, and Forest Oil Companies. Information obtained from the borehole temperature measurements was expected to provide better estimates of the regional permafrost thickness and of the physical conditions controlling the occurrence of ice, unfrozen water, and gas hydrates in permafrost than was currently available.

After monitoring temperatures in these wells for several years, it became clear that the temperature profiles also contained evidence of recent climate change in arctic Alaska. The theory behind this climate-change effect is that any change in the surface energy balance would generate a downward propagating thermal wave. Without the disruptive effects of groundwater flow, this thermal wave is effectively preserved in cold continuous permafrost, although the magnitude of the signal dissipates over time. With sufficiently sensitive instruments, a climate-induced thermal wave could be detected and the associated change in surface temperature inferred. Using this idea and temperatures from the NPR-

Table 4.1: USGS and GTN-P well codes, location, maximum accessible depth, and date of first temperature log for the DOI/GTN-P monitoring wells. Boreholes coupled with a nearby DOI/GTN-P climate station are indicated.

Borehole	USGS Code	GTN-P Code	Latitude (north)	Longitude (west)	Depth (m)	First Log (yr-mon-day)	Climate Station
Atigaru Test Well #1	ATI	US 01	70°33.348′	151°43.229′	648	1977 Dec 14	
Awuna Test Well #1	AWU	US 02	69°09.193′	158°01.355′	884	1981 Aug 22	•
Drew Point Test Well #1	DRP	US 03	70°52.762′	153°54.202′	640	1978 Sep 17	•
East Simpson Test Well #1	ESN	US 04	70°55.046′	154°37.286′	600	1979 Sep 13	
East Teshekpuk Test Well #1	ETK	US 05	70°34.171′	152°56.815′	727	1977 Dec 17	•
Echooka Unit #1	EB1	US 93	69°23.994′	148°16.313′	595	1973 Sep 26	
Ikpikpuk Test Well #1	IKP	US 07	70°27.305′	154°20.082′	615	1980 Sep 10	•
J. W. Dalton Test Well #1	JWD	US 08	70°55.207′	153°08.454′	483	1979 Sep 13	
Koluktak Test Well #1	KOL	US 10	69°45.144′	154°36.669′	227	1981 Aug 23	•
Kugrua Test Well #1	KAG	US 09	70°35.191′	158°39.923′	582	1978 Sep 15	
Kuyanak Test Well #1	KUY	US 11	70°55.869′	156°04.092′	856	1981 Aug 25	
Lisburne Test Well #1	LBN	US 12	68°29.061′	155°41.773′	532	1980 Sep 09	
Lupine Unit #1	LUP	US 92	69°06.051′	148°37.290′	469	1975 Aug 15	
North Inigok Test Well #1	NIN	US 13	70°15.435′	152°46.139′	625	1982 Aug 31	
North Kalikpik Test Well #1	NKP	US 14	70°30.550′	152°22.070′	660	1978 Sep 16	
Peard Bay Test Well #1	PEA	US 15	70°42.939′	159°00.042′	591	1979 Sep 15	
Seabee Test Well #1	SBE	US 16	69°22.809′	152°10.522′	393	1980 Sep 09	•
South Harrison Test Well #1	SOH	US 18	70°25.468′	151°44.071′	399	1977 Dec 16	
South Meade Test Well #1	SME	US 17	70°36.872′	156°53.601′	549	1979 Sep 14	•
Tulageak Test Well #1	TUL	US 20	71°11.338′	155°44.228′	756	1981 Aug 24	
Tunalik Test Well #1	TLK	US 19	70°12.358′	161°04.153′	556	1980 Sep 15	•
West Dease Test Well #1	WDS	US 21	71°09.524′	155°37.983′	823	1980 Sep 14	
West Fish Creek Test Well #1	FCK	US 06	70°19.600′	152°03.634′	735	1977 Dec 11	•

A monitoring wells and from the nearby Prudhoe Bay oil field, Lachenbruch published a series of papers in the 1980s [*Lachenbruch et al.*, 1982, 1988b; *Lachenbruch and Marshall*, 1986] in which he inferred surface temperatures in the Alaskan Arctic had warmed 2–4 K since 1900. Given the paucity of long-term instrumental records in the Arctic documenting recent climate change, Lachenbruch's work was particularly important. Soon thereafter, other researchers began to use subsurface permafrost temperatures to document recent climate changes in the North American Arctic, for example: *Nielsen and Beck* [1989]; *Mareschal and Beltrami* [1992]; *Beltrami and Mareschal* [1992]; *Osterkamp and Romanovsky* [1999]; *Smith et al.* [2005]; *Osterkamp and Jorgenson* [2006]; *Taylor et al.* [2006]; *Smith et al.* [2010]; *Romanovsky et al.* [2010].

In 1999, the 21 NPR-A temperature-monitoring wells were incorporated into the Global Terrestrial Network for Permafrost (GTN-P), a new component of the Global Climate Observing System (GCOS) and one of its primary subnetworks, the Global Terrestrial Observing System (GTOS). This formalized the use of the borehole array for monitoring

the *thermal state of permafrost* (TSP), one of the Essential Climate Variables (ECVs) tracked by the global climate observing systems [*Sessa and Dolman*, 2008; *Smith and Brown*, 2009]. Upon inclusion into GTN-P, the NPR-A wells became the largest array of deep ($>$ 125 m) boreholes in the world used for monitoring temperatures in permafrost [*IPA*, 2010]. The array is unique in that it also provides one the longest records of permafrost thermal state. As management of the array was shared by two US Department of the Interior (DOI) agencies (USGS and the Bureau of Land Management), the array became known as the DOI/GTN-P Deep Borehole Array. Two of the four wells that had been preserved for USGS temperature monitoring to the east of the NPR-A (Lupine and Echooka, **Figure 4.1**, **Table 4.1**) were later incorporated into GTN-P, bringing the total number of wells in the DOI/GTN-P Borehole Array to 23. Beginning in 1998, USGS also began deploying automated climate-monitoring stations in the NPR-A to better understand the nature of the recent permafrost warming observed there. Nine of the climate stations were co-located with DOI/GTN-P boreholes to form "permafrost observatories" (**Table 4.1**), although two of the boreholes were subsequently plugged and abandoned due to the threat of coastal erosion. Data from the DOI/GTN-P climate stations are available from *Urban and Clow* [2014].

Here we present the temperature data acquired from the DOI/GTN-P Borehole Array in arctic Alaska over the 40 yr period, 1973–2013. The data represent the true temperatures in the wellbores and surrounding rocks at the time of the measurements; they have not been "corrected" to remove the thermal disturbance caused by drilling the wells. For the great majority of wells, the drilling disturbance is estimated to have been of order 0.1 K or less by 1989. Thus, most of the temperature measurements acquired over the last 25 yr are little affected by the drilling disturbance. The dataset presented here is intended to serve as the reference point from which datasets corrected for the drilling disturbance will be derived, enhancing the usefulness of the earlier temperature logs. In addition, analysis of the uncorrected temperature logs can provide important information about the ice and unfrozen water content in the permafrost zone. As shown in **Figure 4.2**, temperature measurements in the DOI/GTN-P monitoring wells were concentrated during distinct field campaigns that occurred during 1977–1984, 1989, 2002–2003, 2007–2008, and 2012–2013. Measurements were curtailed during the 1990s due to funding limitations, except for a few

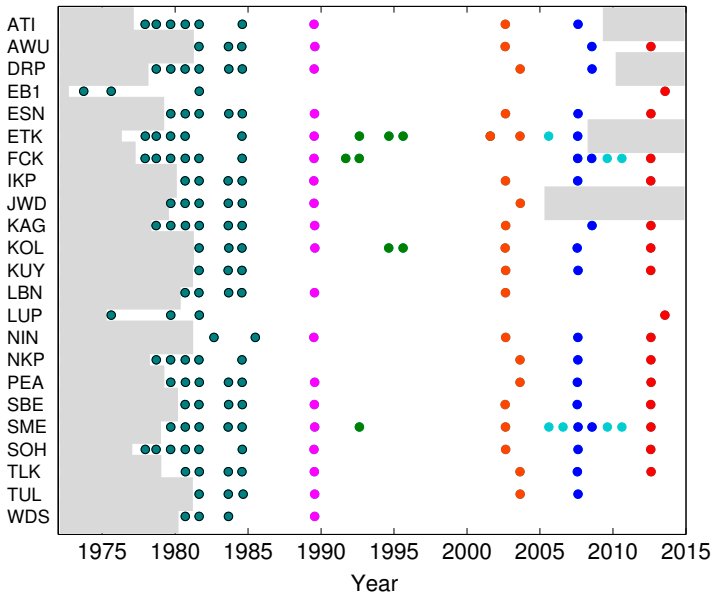

Figure 4.2: Temperature logging history for the DOI/GTN-P Deep Borehole Array. Major field campaigns occurred during 1977–1984 (teal), 1989 (magenta), 2002–2003 (orange-red), 2007–2008 (blue), and 2012–2013 (red). Gray areas indicate times before well completion, and in some instances when the wells have been plugged and abandoned due to coastal erosion issues.

experimental logs designed to test design changes in the temperature logging system. Measurements were resumed in 2002 under a GTN-P protocol specifying that contributing deep borehole arrays be resampled every 5 yr (**Figure 4.3**). By 2010, four of the monitoring wells (ATI, DRP, ETK, JWD) had been plugged and abandoned due to coastal erosion and were no longer accessible. Data from the DOI/GTN-P Borehole Array will be useful for documenting how the thermal state of permafrost is changing on the Arctic Slope of Alaska in response to climate change. Given the important role that permafrost has in shaping the regional landscape, this information is critical for understanding how lakeshore, river, and coastal environments may change in the near future; anticipating impacts on terrestrial ecosystem habitats; and for making well-informed land management decisions in the face of rapid climate change. The data will also be useful for refining our basic understanding of the physical conditions occurring within permafrost in this region.

Figure 4.3: Measuring temperatures in the Koluktak (KOL) Test Well No. 1, National Petroleum Reserve–Alaska. This well is typical of the other wells in the DOI/GTN-P Borehole Array.

4.3 Instruments and methods

4.3.1 Borehole temperature measurements

The "portable" logging system used by the US Geological Survey to measure temperatures in the DOI/GTN-P boreholes consists of a custom temperature sensor whose resistance is determined by a resistance readout (digital multimeter) using a 4-wire Kelvin circuit. This circuit effectively compensates for the resistance of the logging cable and various connectors that provide the electrical path between the downhole temperature sensor and the resistance readout located on the surface (**Figure 4.4**). The temperature sensor consists of a parallel-series network of negative-temperature-coefficient (NTC) thermistors hermitically sealed in glass. These in turn are enclosed in a thin (4 mm diameter) stainless steel shell to isolate the thermistors from pressure effects and corrosive chemicals. The resulting probe design has proved to be rugged and stable, and provides a high temperature sensitivity [*Sass et al.*, 1971; *Clow*, 2008].

Several refinements have been made to the portable system since the 1970s when measurements began in the DOI/GTN-P boreholes. To minimize weight, the early version of the system did not have a slip-ring assembly. Temperatures were measured at fixed depths, typically every 1.5 or 3.0 m, and the logging cable disconnected from the resistance readout when moving from one measurement depth to the next. At each depth, measure-

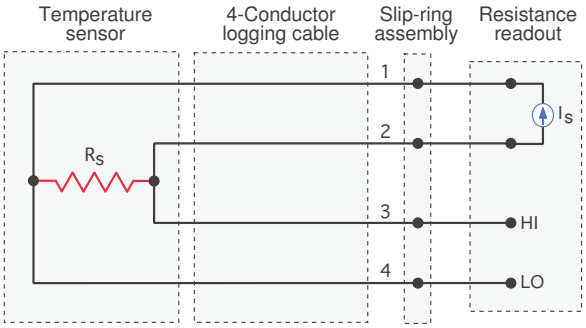

Figure 4.4: Kelvin (4-wire) resistance circuit used by the USGS portable logging system. The test current I_s passes through lines 1 and 2 while the voltage drop across the probe resistance R_s is measured using the sense lines (3, 4). Logging cables used with the portable system are 450–900 m long. The resistance readout is located on the surface.

ments were made until the sensor approached thermal equilibrium with the surrounding environment. A high-quality slip-ring connector was introduced to the system in 1984, allowing measurements to be acquired while the sensor was moving continuously downhole; a circuit triggered the system to acquire a measurement every 30 cm. The depth and sensor resistance measurements were automatically recorded on magnetic tape. A logging speed of $\sim 10\ \mathrm{cm\,s^{-1}}$ was used with this system.

One disadvantage of the rugged probe design is the relatively slow response time ($\tau \in$ 7–15 s). Given the thermal memory of the probe, a time deconvolution is required to determine the actual temperature at any given depth from the temperature measurements while the sensor is moving. To assist with the deconvolution, the resistance readout was upgraded in 1991 enabling measurements to be triggered on even time increments (every 2 s) while a computer provided the time of each triggering event. The primary data stream then consisted of time, depth, and sensor resistance. The logging speed was also reduced to 2.5–5 $\mathrm{cm\,s^{-1}}$ to reduce the magnitude of the deconvolution correction. With a triggering rate of 2 s, this decreased the depth interval between measurements to 5–10 cm. An additional change aimed at improving the results of the time deconvolution was to replace the hydraulic clutch that regulated the probe descent with a motor drive to reduce variations in the probe's downhole speed. The new resistance readout also offered 10 times the resolution while simultaneously reducing the test current I_s by a factor of ten. The latter feature reduced the heating of the thermistor beads during a measurement due to the test current by 10^2. Utilizing another capability of the new readout, the measuring

circuit was recalibrated before each temperature log using a set of "standard" resistors.

Efforts were made through the 1990s to further reduce the uncertainty of the resistance measurements. Issues that were addressed included drift of the measurement circuitry due to environmental changes during a log and spurious electrical noise caused by the winch motor, the presence of the system operator, blowing snow, and other sources. By 1999, these issues were effectively resolved by locating the resistance readout in a Faraday cage maintained at 23 ± 0.5°C for the duration of a logging experiment. The system has changed little since that time. A complete description of the current system (**Figure 4.5**) and the associated measurement uncertainties is given by *Clow* [2008]. Although a complete uncertainty analysis was not done for the early version of the portable system, *Sass et al.* [1971] and *Lachenbruch et al.* [1988a] state that the precision of the measurements was better than 0.01 K while the absolute accuracy was "probably only a few hundredths of a degree." This level of uncertainty persisted through at least 1991. The standard uncertainty of the ITS-90 temperature measurements made with the current (post-1999) logging system ranges from 3.0 mK at −60°C to 3.3 mK at 0°C.

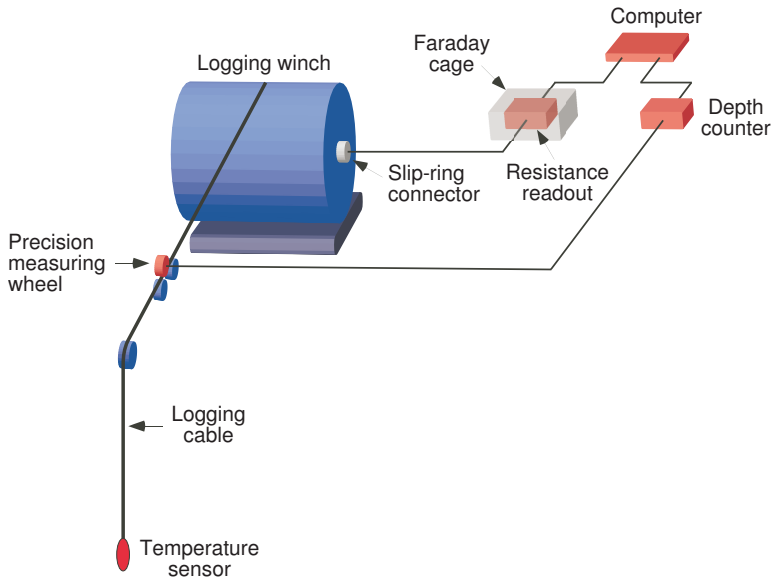

Figure 4.5: Layout of the post-1999 version of the USGS portable temperature logging system used in arctic Alaska.

4.3.2 Data processing

The processing of the temperature logs consists of several steps that depends on whether the data were acquired at fixed depth intervals (pre-1984) or while the sensor was moving continuously downhole. For the continuously obtained data, the processing steps include: (1) correcting the measured resistances for systematic biases, (2) converting the resistances to temperature, (3) removing noise from the signal, and (4) deconvolving the signal to correct for the thermal memory of the probe. The last step is unnecessary for the fixed interval data.

4.3.2.1 Resistance corrections

Several sources of systematic error exist for the temperature-sensor resistance measurements. These include: (a) leakage currents between the conductors of the Kelvin circuit due to dirt, moisture, or imperfections in the conductor insulation, (b) capacitance effects, (c) heating of the probe due to the passage of the test current, and (d) thermal EMFs (thermoelectric voltages). These sources are discussed in detail by *Clow* [2008]. The magnitude of the associated resistance offsets can be summarized as follows:

$$\delta R_{\mathrm{l}} = \frac{R_{\mathrm{s}}^2}{R_{\mathrm{s}} + R_{\mathrm{l}}} \qquad \text{(leakage currents)} \tag{4.1}$$

$$\delta R_{\mathrm{c}} = R_{\mathrm{s}} C \frac{\partial R_{\mathrm{s}}}{\partial t} \qquad \text{(capacitance effects)} \tag{4.2}$$

$$\delta R_{\mathrm{h}} = \frac{\alpha_{\mathrm{T}} \left(I_{\mathrm{s}} R_{\mathrm{s}}\right)^2}{P_{\mathrm{d}}} \qquad \text{(self heating)} \tag{4.3}$$

$$\delta R_{\mathrm{e}} = \frac{V_{\mathrm{emf}}}{I_{\mathrm{s}}} \qquad \text{(thermal EMFs)} \tag{4.4}$$

where R_{s} is the probe resistance, R_{l} is the interconductor resistance, C is the circuit capacitance, I_{s} is the test current, V_{emf} is the sum of the thermoelectric voltages, α_{T} is the sensors's temperature coefficient of resistance ($\alpha_{\mathrm{T}} \equiv R_{\mathrm{s}}^{-1}\, \partial R_{\mathrm{s}} / \partial T$), P_{d} is the sensor's power dissipation constant, T is temperature, and t is time. In an attempt to correct for the systematic biases, Eqs. (4.1)–(4.4) are applied as corrections to the resistance $\tilde{R}_{\mathrm{s}}$ measured by the logging system's resistance readout to obtain an estimate of the temperature sensor's true resistance,

$$R_{\mathrm{s}} = \tilde{R}_{\mathrm{s}} + (\delta R_{\mathrm{l}} + \delta R_{\mathrm{c}} + \delta R_{\mathrm{h}} - \delta R_{\mathrm{e}}). \tag{4.5}$$

Expressed in terms of temperature, these corrections are generally limited to 0.1–0.2 mK. No attempt was made to correct the pre-1991 resistance measurements because the magnitude of the corrections is less than the resolution of the pre-1991 resistance readout.

4.3.2.2 Resistance-to-temperature conversion

Prior to borehole logging experiments, each sensor is calibrated in a temperature calibration bath at the USGS. A standard platinum resistance thermometer (SPRT) certified by the US National Institute of Standards and Technology is used as the calibration standard. Before 1991, the calibration data for each sensor were fit to the equation proposed by *Swartz* [1954],

$$\mathcal{T} = \frac{a_0}{a_1 + \log R_s} - a_2 \tag{4.6}$$

in the manner described by *Sass et al.* [1971]. Using the best-fit values for the calibration constants (a_0, a_1, a_2), the sensor resistances R_s obtained during a logging experiment are converted to temperature $\mathcal{T}$.

In 1992, a multiyear effort to upgrade certain aspects of the USGS temperature calibration facility was initiated. These upgrades included a higher quality SPRT, a more sensitive and stable SPRT resistance readout, and a temperature calibration bath with a more stable and uniform temperature field that was also capable of reaching much colder temperatures ($-60°$C). In conjunction with these changes, the calibration function used to fit the higher quality data was changed to,

$$\mathcal{T}^{-1} = a_0 + a_1(\ln R_s) + a_2(\ln R_s)^2 + a_3(\ln R_s)^3, \tag{4.7}$$

where a_0, a_1, a_2, and a_3 are now the calibration constants and $\mathcal{T}$ is expressed in Kelvin. This 4-term function offered a more precise fit to the calibration data, particularly below 0°C. Equation (4.7) is an extension of the often used 3-term Steinhart–Hart equation [*Steinhart and Hart*, 1968] which proved inadequate for our purposes. **Figure 4.6** shows sample calibration data and the resulting 4-term calibration fit for one of the USGS temperature sensors.

4.3.2.3 Denoising

Since the deconvolution step amplifies noise by up to an order of magnitude at periods less than 3–4 probe time constants (45–60 s for the DOI/GTN-P borehole records), it is

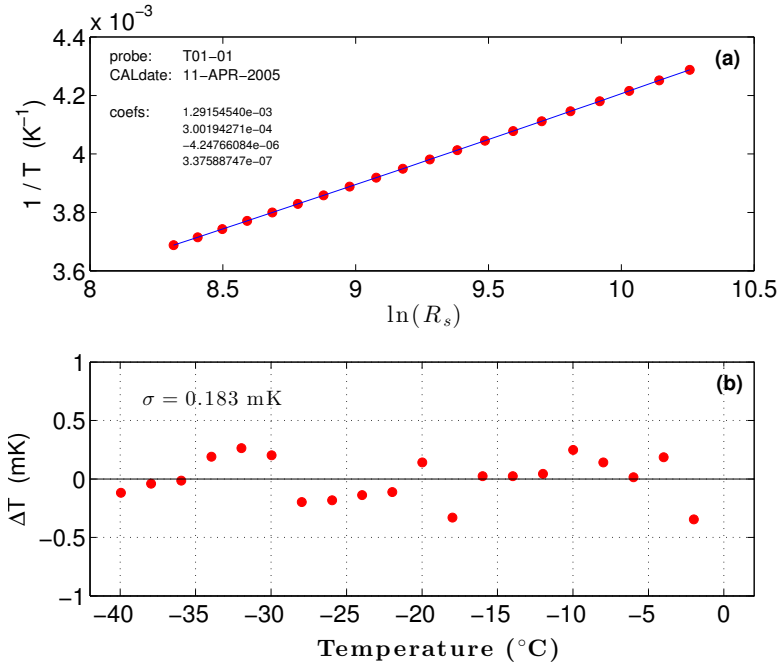

Figure 4.6: Sample calibration data over the range -40 to -2°C for one of the USGS temperature sensors (T01-01) along with the best-fit 4-term calibration function **(a)**. Panel **(b)** shows the residuals from the calibration fit. In this example, the standard deviation of the calibration residuals is 0.183 mK.

essential to remove as much of the high- and mid-frequency noise as possible before attempting to deconvolve the data. Three different types of noise need to be considered for the DOI/GTN-P temperature records: (1) outliers due to a sudden change in the electric field surrounding the measuring circuit (pre-1999 measurements), (2) instrumental noise, and (3) rapid temperature oscillations due to convection of the borehole fluid. An important consideration is that the frequency content of the climate signal present in these temperature records changes with depth. In addition, the magnitude and frequency of borehole convective noise is sensitive to the temperature gradient $\partial T/\partial z$ and thus also changes with depth. Given the nature of the signal and the noise, simple band-pass filtering cannot be used to remove the noise while still preserving the essence of the climate signal.

For the DOI/GTN-P borehole temperature measurements, denoising is accomplished using a discrete wavelet analysis [*Strang and Nguyen*, 1996]. Wavelet denoising allows thresholds to be set so that a real signal rising above the noise can be preserved while

noise is removed, even if they occur at the same frequency. Given the smooth nature of the underlying temperature signal, order-3 Coiflets were selected for the analyzing wavelets; these wavelets appear ideal for this purpose, being relatively smooth and nearly symmetric. Wavelet denoising was performed at spatial scales finer than 3.4 m (periods $\leq$ 64 s) for the post-1991 logs, and finer than 5.0 m for the earlier continuous logs. The top and bottom of the logs were extended slightly to minimize border distortion. During the first pass through the wavelet denoising, data points more than 3.5 standard deviations from the smooth denoised signal are identified as outliers and removed. As the outliers may have distorted the denoised signal on the first pass, the outlier-free data are passed through the wavelet denoising a second time. **Figure 4.7** shows the temperature measurements and resulting denoised signal from a portion of a representative DOI/GTN-P temperature log.

Incrementally obtained temperature logs (pre-1984) were not denoised as they contain insufficient information to perform the kind of denoising analysis described above. In addition, noise amplification during the deconvolution step is not a concern since these logs do not require a temporal deconvolution.

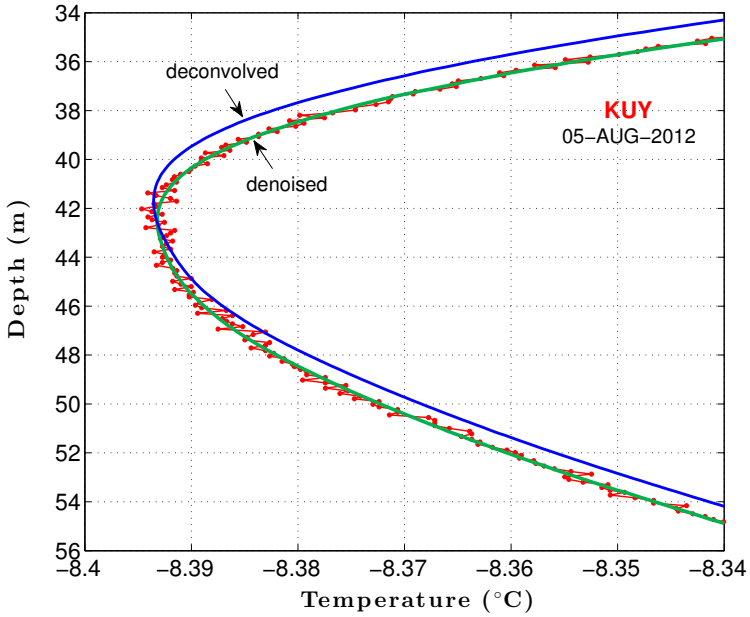

Figure 4.7: Portion of a sample DOI/GTN-P temperature log (Kuyanak Test Well #1, 5 August 2012). The temperature measurements $\mathcal{T}$ are shown in red while the denoised signal is given by the green line. Blue line shows the deconvolved signal, which represents the actual temperatures T in the borehole taking into account the response time of the moving probe.

4.3.2.4 Deconvolution

The USGS temperature probes have a time constant τ of 7–15 s, depending on the thermophysical properties of the fluid filling the borehole. Since τ is greater than the sampling rate (2 s), a measurement represents an average of what the probe has experienced during the last few time constants. More exactly, the temperature measurements $\mathcal{T}$ are given by the convolution of the actual temperatures in the borehole (T) with the logging system's impulse response function $h(t)$,

$$\mathcal{T}(t) = \int_{-\infty}^{\infty} h(t-\mu)\, T(\mu) d\mu. \tag{4.8}$$

Given the low capacitance of the system's measurement circuit, the system response is dominated by the characteristics of the temperature probe. Following *Nielsen and Balling* [1984], the impulse response function is taken to be,

$$h(t) = \begin{cases} 0\,, & t < t_o \\ \dfrac{1}{\tau} \exp\left(-\dfrac{t-t_o}{\tau}\right), & t \geq t_o \end{cases} \tag{4.9}$$

where t_o is the time delay before the system begins to sense a temperature change. Time constant experiments with the USGS temperature sensors indicate t_o is much less than the sampling rate [*Saltus and Clow*, 1994].

Recognizing that a temperature log is a finite-length discrete sampling of the actual temperatures in a borehole, Eq. (4.8) can be approximated by the summation,

$$\mathcal{T}_i = \sum_{j=1}^{n} h_j\, T_{i-j+1} \tag{4.10}$$

where n is the number of terms in the response function h. Using serial division, Eq. (4.10) can be inverted to find the actual borehole temperatures in terms of the measurements [*Saltus and Clow*, 1994],

$$T_i = \frac{\mathcal{T}_i - \sum_{j=1}^{n-1} h_{j+1}\, T_{i-j}}{h_1}, \quad i \geq 2. \tag{4.11}$$

Beginning in 1991, the temperature sensor was always allowed to reach thermal equilibrium at a fixed depth in the borehole fluid before beginning to move the sensor downhole. In this case, the first value T_1 is equal to the measured value $\mathcal{T}_1$ and we can take $T_{i-j} = \mathcal{T}_1$ when $(i-j) \leq 0$ in Eq. (4.11). This procedure was generally not used for the pre-1991

temperature logs. Rather, the temperature sensor was lowered from the surface into the borehole fluid without pausing. The deconvolution errors for the first 60 s (3–4 τ) of these logs are quite large. Hence, the upper few meters of the 1984–1991 logs are discarded. Returning to **Figure 4.7**, we can see the relationship between the actual temperatures in a borehole (deconvolved signal) and the measurements obtained by the logging system for a sample DOI/GTN-P temperature log.

4.4 DOI/GTN-P borehole temperatures

4.4.1 Temperature-depth profiles

The processed temperature-depth profiles $T(z)$ derived from the 1973–2013 DOI/GTN-P borehole logs are shown in **Figures 4.8–4.30**. Digital versions of the temperature profiles are available from the ACADIS repository [*Clow*, 2013]. Gaps apparent in some of the profiles are almost entirely due to logging tool hangups. These occur when the temperature sensor temporarily "hangs" on a borehole casing weld or other minor obstruction and then subsequently slips by. Due to the sensor's relatively long time constant and uncertainties regarding the sensor's actual location during these hangups, it is difficult to recover the true well temperatures at these locations. The data are masked in these sections to avoid reporting erroneous values. Since the focus of current well-monitoring efforts is to capture climate change effects, the more recent temperature logs are generally made only to $\sim$ 200 m as little temperature change is expected beyond this depth. Efforts to occasionally log beyond 200 m will still be made in the future in an attempt to track small changes in the base of permafrost over time.

4.4.2 Drilling disturbance

The DOI/GTN-P monitoring wells were drilled using conventional rotary drilling techniques. In the process, a drilling fluid is pumped downhole through the drill pipe to the bottom of the well to pick up the drill cuttings for return to the surface via the annulus between the drill pipe and the borehole wall. As a result, heat is exchanged between the circulating drill fluid and the borehole wall at a rate that depends on their relative temperature difference and the physical properties of the two media. As the fluid tends to take on the average temperature of the rock column penetrated by the borehole, the net effect is to cool the lower portion of a deep borehole while the upper portion warms. After

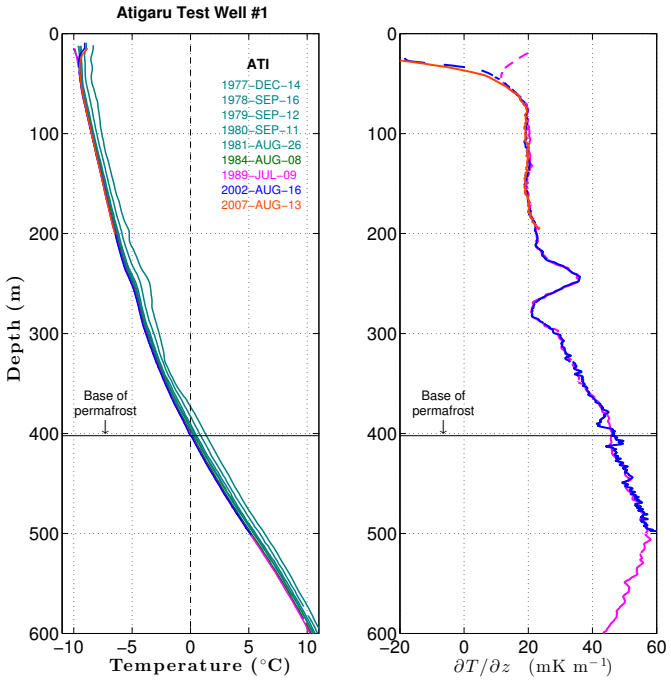

Figure 4.8: Temperature profiles in the Atigaru Test Well No. 1, color-coded by acquisition date (left). Due to the dissipation of the drilling disturbance, the temperature profiles cool progressively over time. Thus, the first log (1977-DEC-14) is the warmest of the series. Temperature gradients calculated from the 1989, 2002, and 2007 logs are shown in the right panel using the same color coding. Black horizontal line shows the base of permafrost.

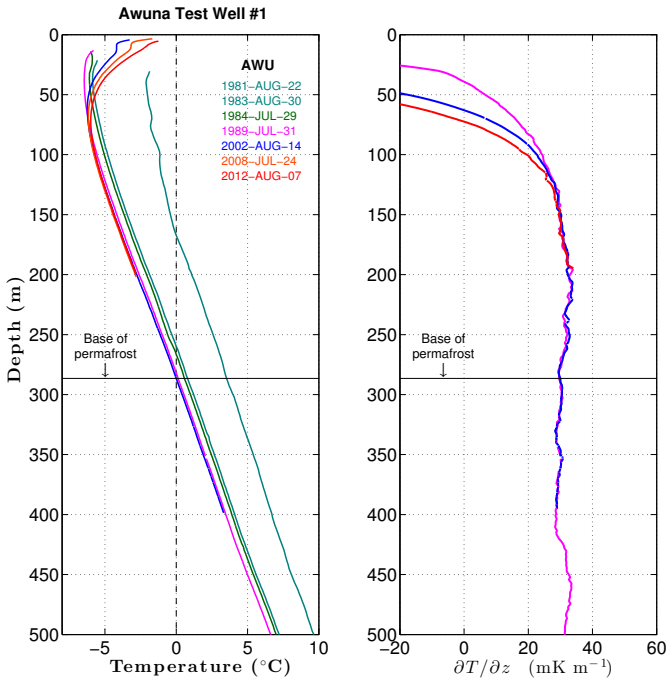

Figure 4.9: Temperature profiles in the Awuna Test Well No. 1, color-coded by acquisition date (left). Temperature gradients calculated from the 1989, 2002, and 2012 logs are shown in the right panel.

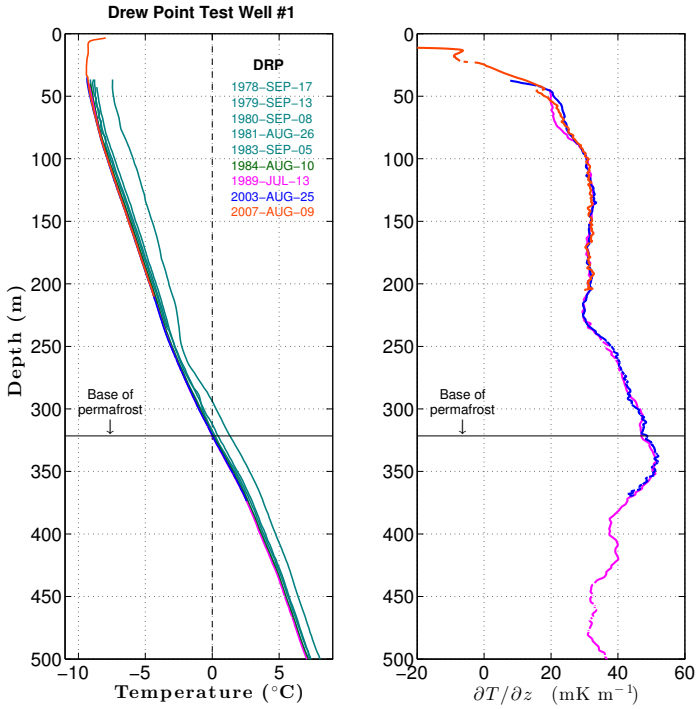

Figure 4.10: Temperature profiles in the Drew Point Test Well No. 1, color-coded by acquisition date (left). Temperature gradients calculated from the 1989, 2003, and 2007 logs are shown in the right panel.

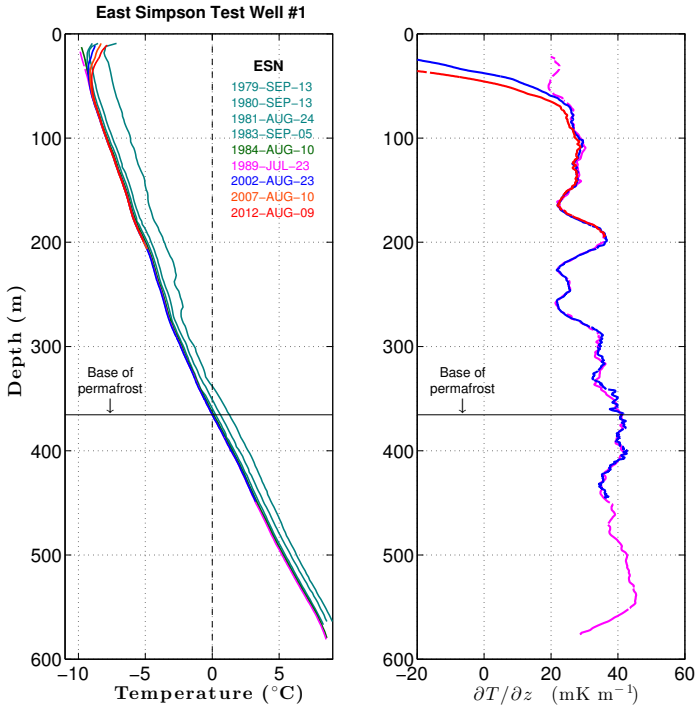

Figure 4.11: Temperature profiles in the East Simpson Test Well No. 1, color-coded by acquisition date (left). Temperature gradients calculated from the 1989, 2002, and 2012 logs are shown in the right panel.

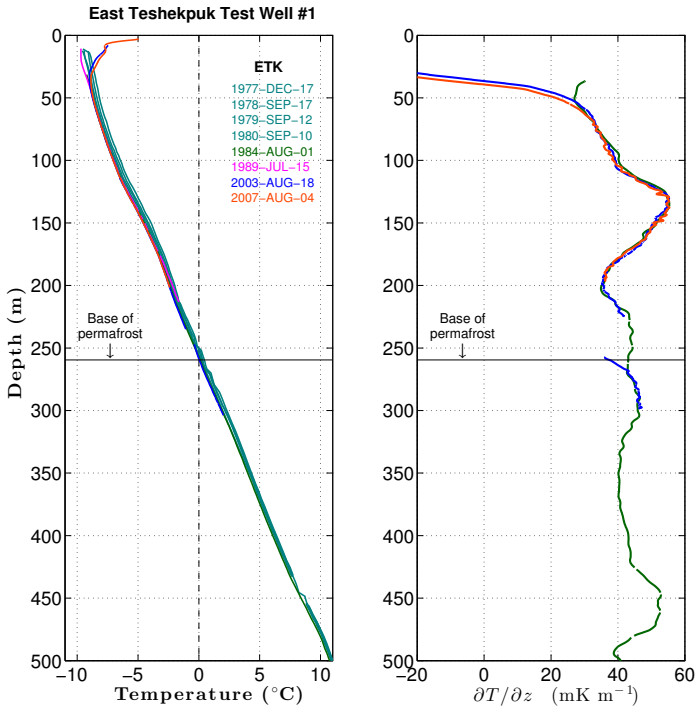

Figure 4.12: Temperature profiles in the East Teshekpuk Test Well No. 1, color-coded by acquisition date (left). Temperature gradients calculated from the 1984, 2003, and 2007 logs are shown in the right panel.

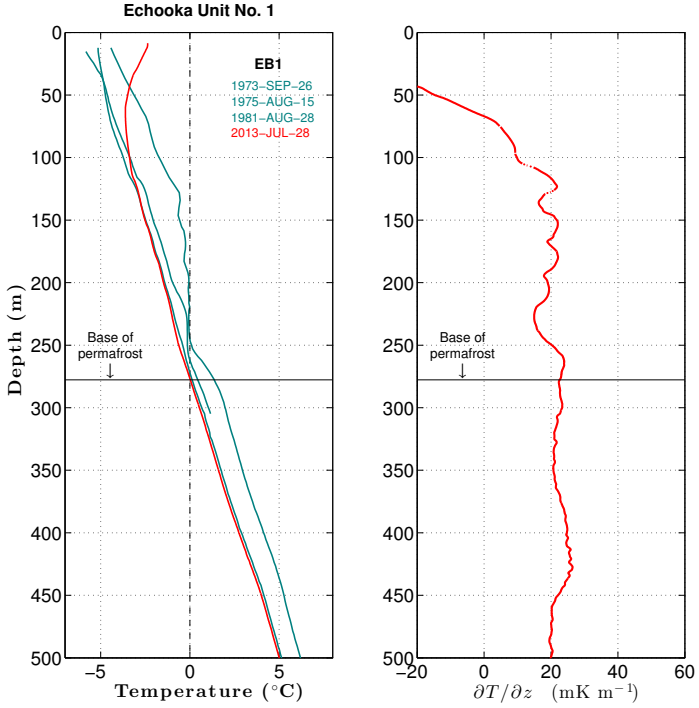

Figure 4.13: Temperature profiles in the Echooka Unit No. 1 well, color-coded by acquisition date (left). The temperature gradient calculated from the 2013 log is shown in the right panel.

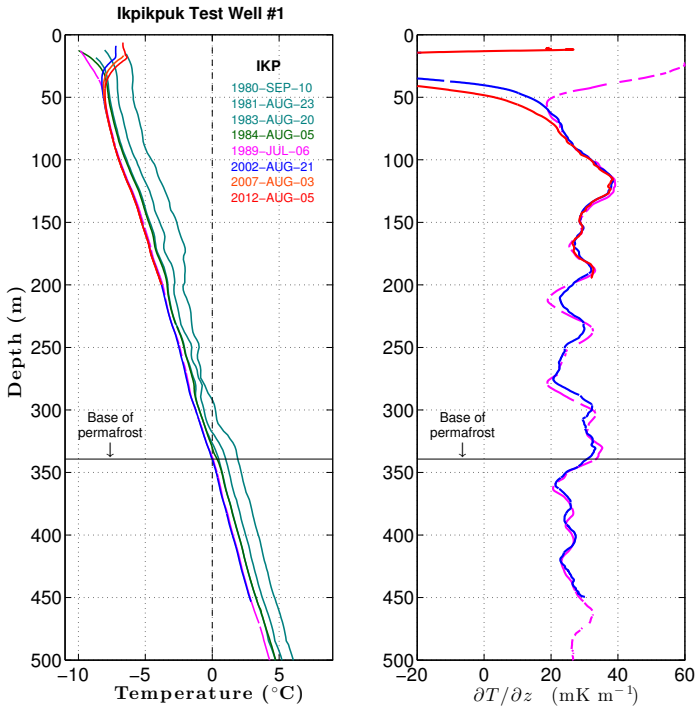

Figure 4.14: Temperature profiles in the Ikpikpuk Test Well No. 1, color-coded by acquisition date (left). Temperature gradients calculated from the 1989, 2002, and 2012 logs are shown in the right panel.

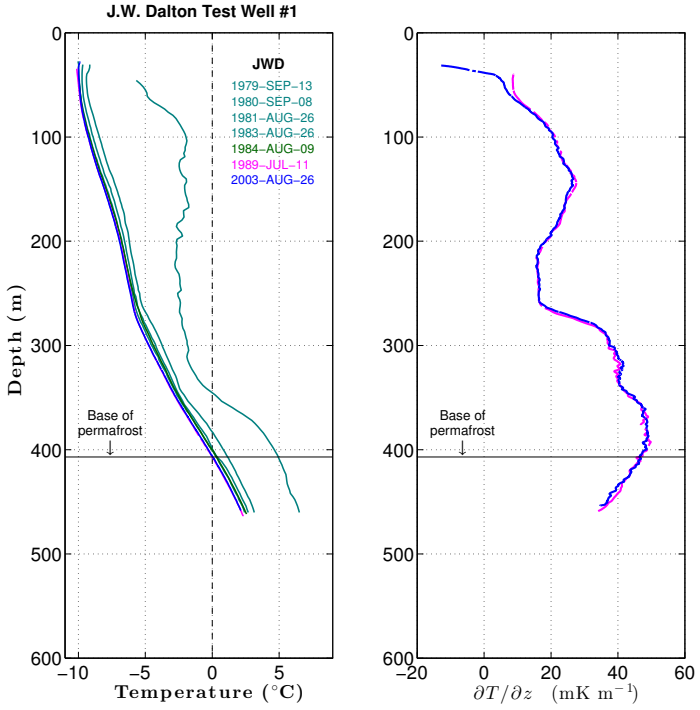

Figure 4.15: Temperature profiles in the J. W. Dalton Test Well No. 1, color-coded by acquisition date (left). Temperature gradients calculated from the 1989 and 2003 logs are shown in the right panel.

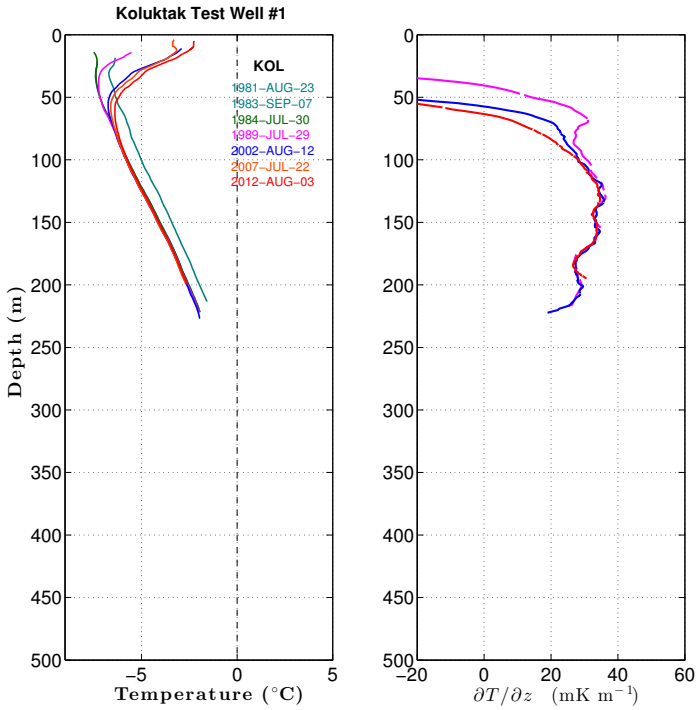

Figure 4.16: Temperature profiles in the Koluktak Test Well No. 1, color-coded by acquisition date (left). Temperature gradients calculated from the 1989, 2002, and 2012 logs are shown in the right panel.

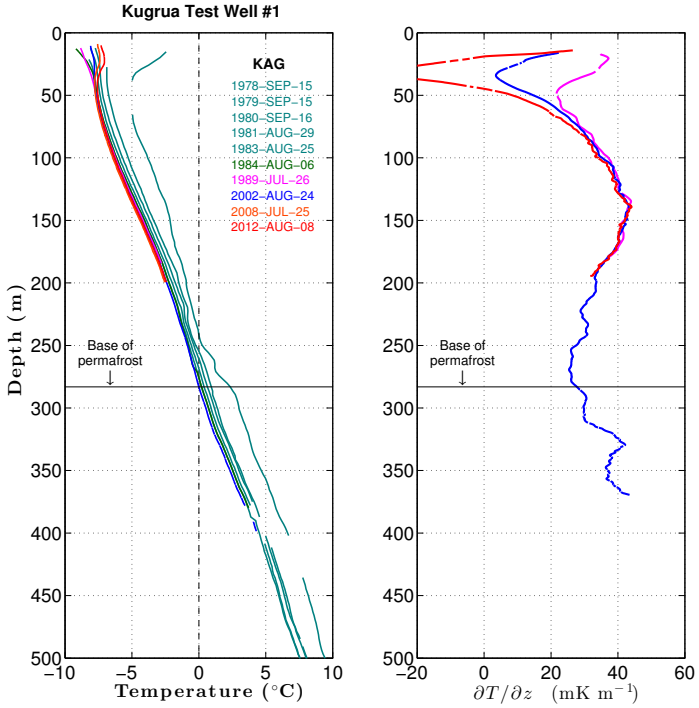

Figure 4.17: Temperature profiles in the Kugrua Test Well No. 1, color-coded by acquisition date (left). Temperature gradients calculated from the 1989, 2002, and 2012 logs are shown in the right panel.

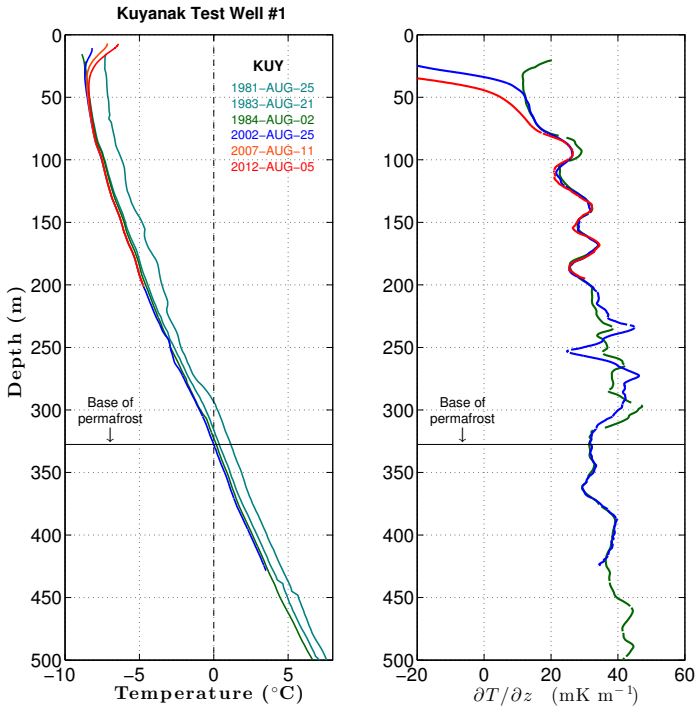

Figure 4.18: Temperature profiles in the Kuyanak Test Well No. 1, color-coded by acquisition date (left). Temperature gradients calculated from the 1984, 2002, and 2012 logs are shown in the right panel.

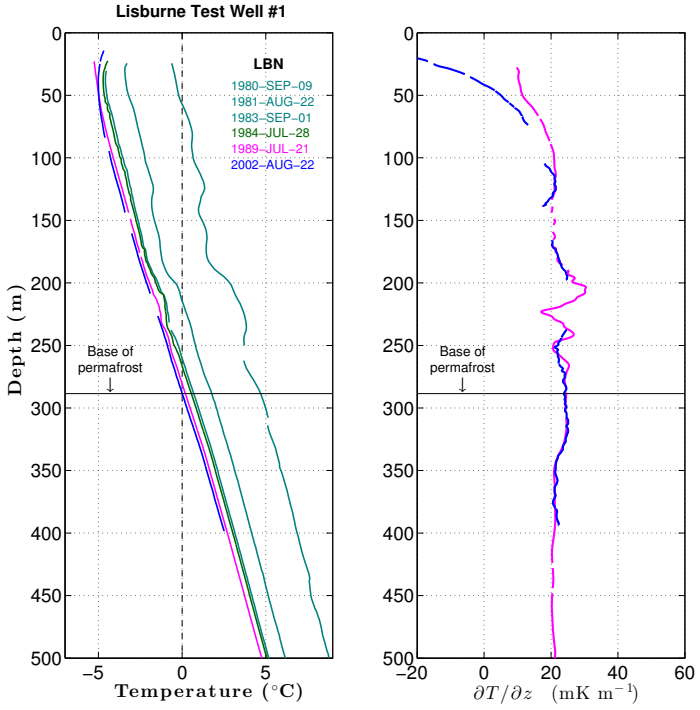

Figure 4.19: Temperature profiles in the Lisburne Test Well No. 1, color-coded by acquisition date (left). Temperature gradients calculated from the 1989 and 2002 logs are shown in the right panel.

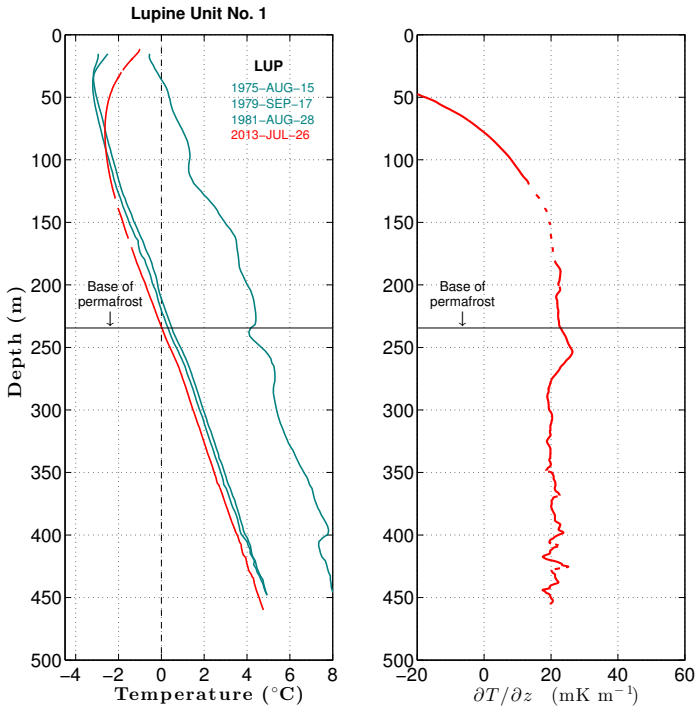

Figure 4.20: Temperature profiles in the Lupine Unit No. 1 well, color-coded by acquisition date (left). The temperature gradient calculated from the 2013 log is shown in the right panel.

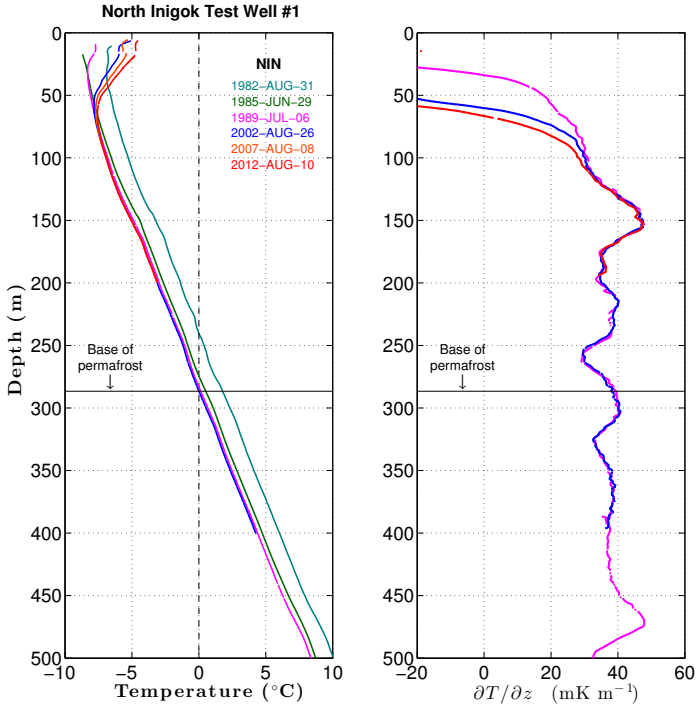

Figure 4.21: Temperature profiles in the North Inigok Test Well No. 1, color-coded by acquisition date (left). Temperature gradients calculated from the 1989, 2002, and 2012 logs are shown in the right panel.

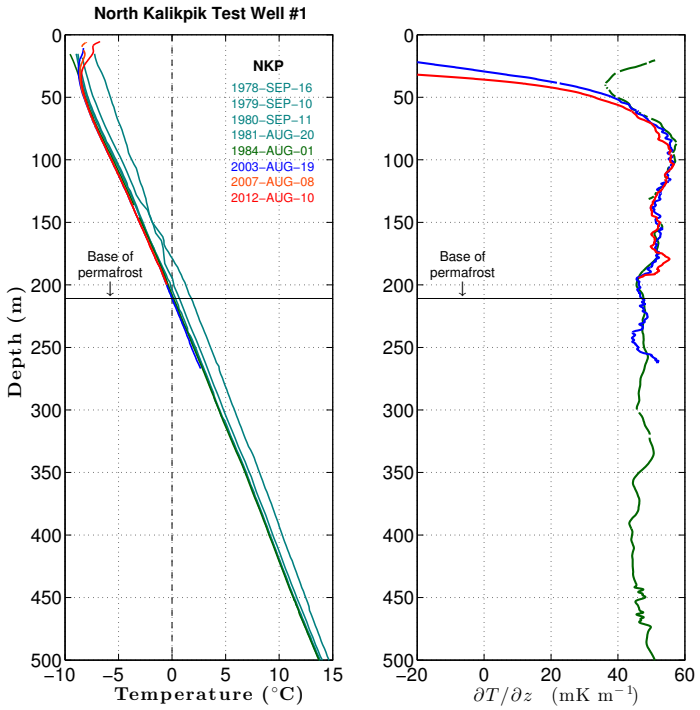

Figure 4.22: Temperature profiles in the North Kalikpik Test Well No. 1, color-coded by acquisition date (left). Temperature gradients calculated from the 1984, 2003, and 2012 logs are shown in the right panel.

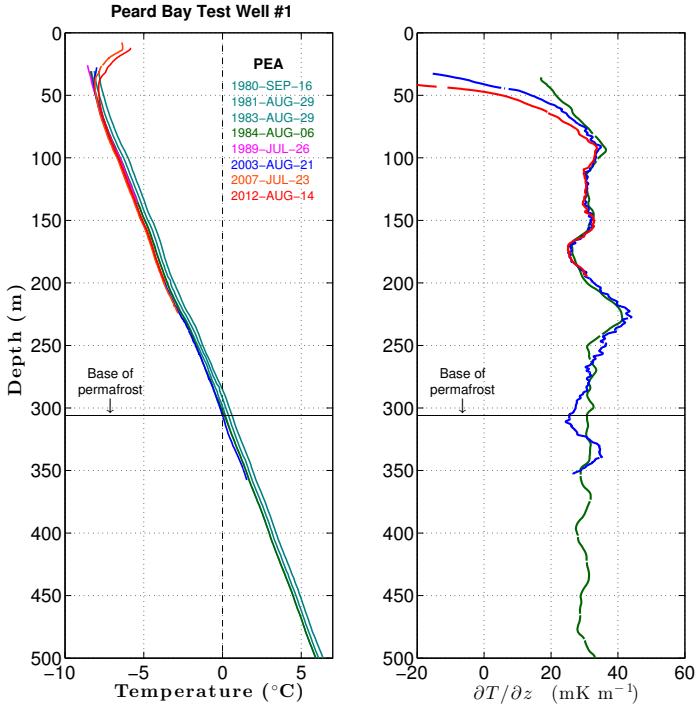

Figure 4.23: Temperature profiles in the Peard Bay Test Well No. 1, color-coded by acquisition date (left). Temperature gradients calculated from the 1984, 2003, and 2012 logs are shown in the right panel.

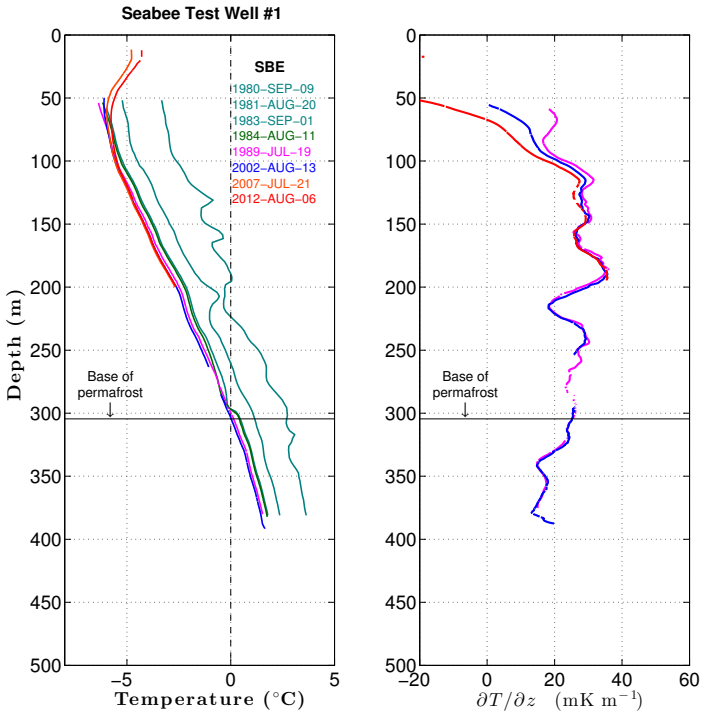

Figure 4.24: Temperature profiles in the Seabee Test Well No. 1, color-coded by acquisition date (left). Temperature gradients calculated from the 1989, 2002, and 2012 logs are shown in the right panel.

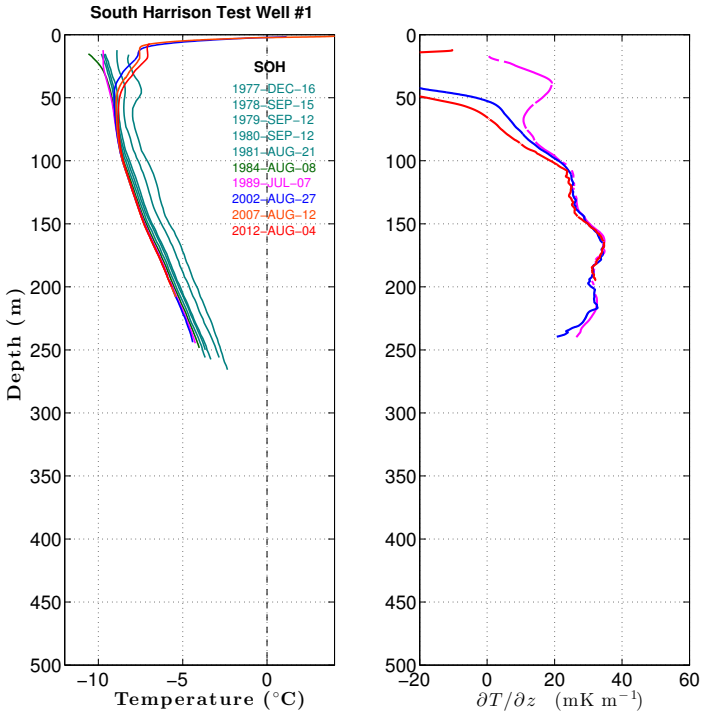

Figure 4.25: Temperature profiles in the South Harrison Test Well No. 1, color-coded by acquisition date (left). Temperature gradients calculated from the 1989, 2002, and 2012 logs are shown in the right panel.

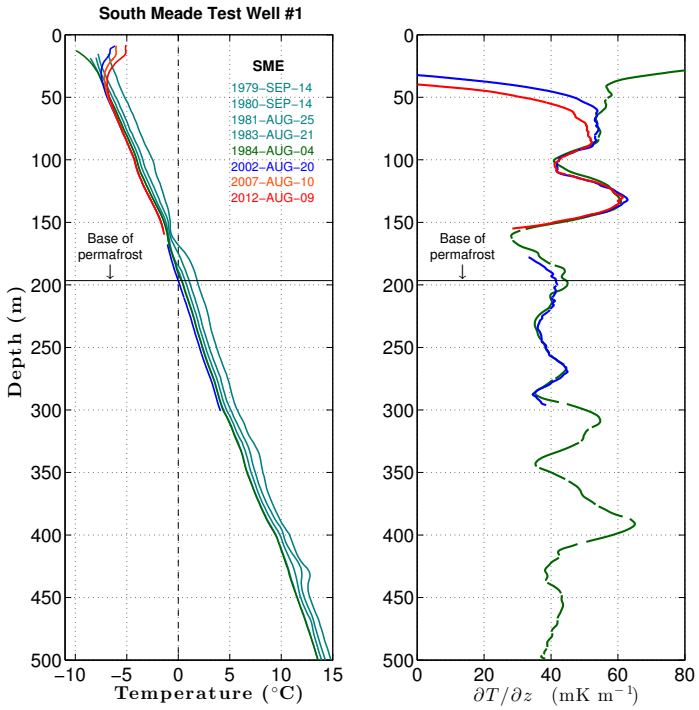

Figure 4.26: Temperature profiles in the South Meade Test Well No. 1, color-coded by acquisition date (left). Temperature gradients calculated from the 1984, 2002, and 2012 logs are shown in the right panel.

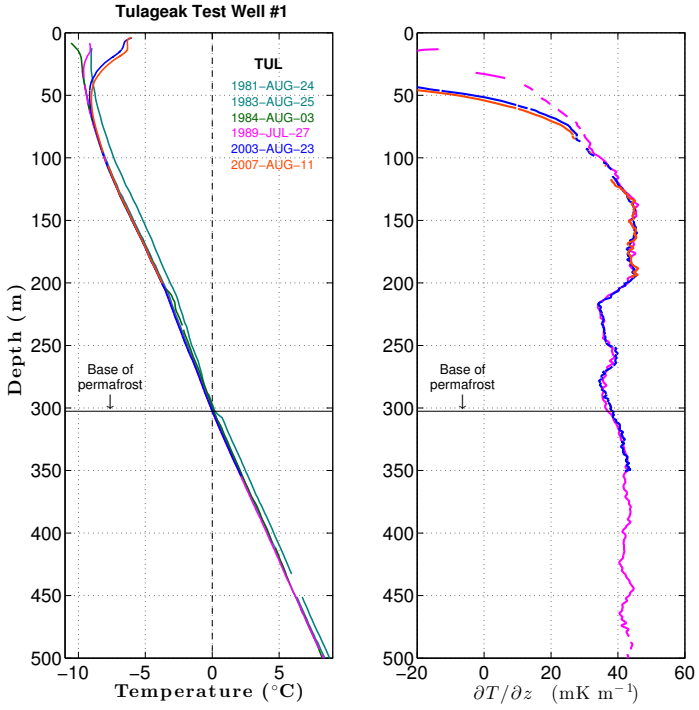

Figure 4.27: Temperature profiles in the Tulageak Test Well No. 1, color-coded by acquisition date (left). Temperature gradients calculated from the 1989, 2003, and 2007 logs are shown in the right panel.

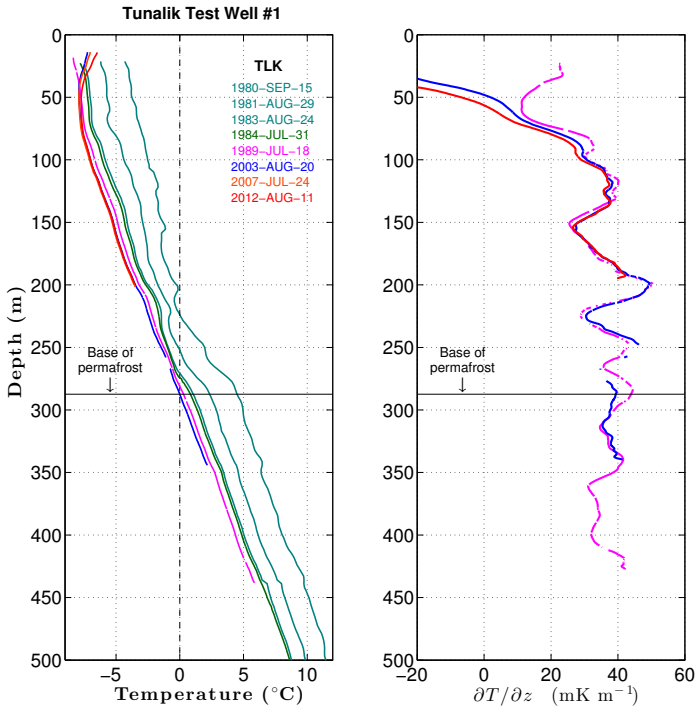

Figure 4.28: Temperature profiles in the Tunalik Test Well No. 1, color-coded by acquisition date (left). Temperature gradients calculated from the 1989, 2003, and 2012 logs are shown in the right panel.

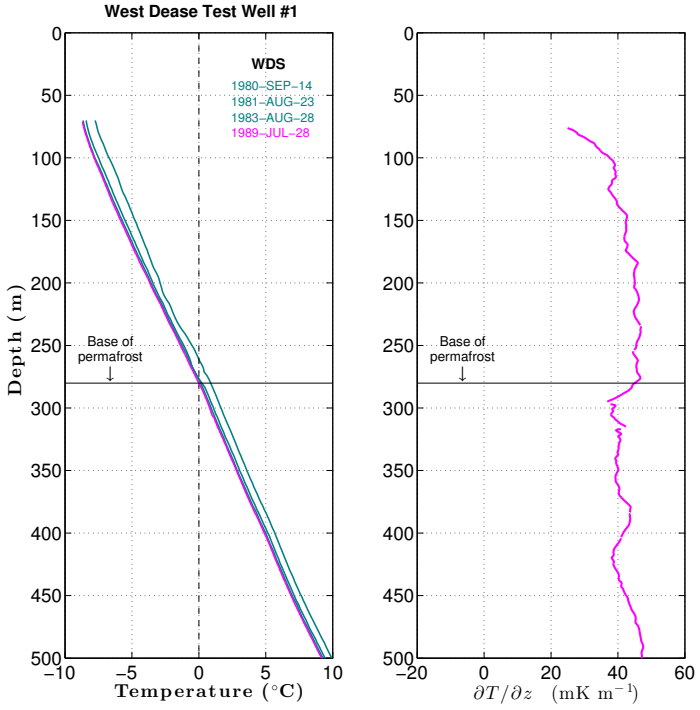

Figure 4.29: Temperature profiles in the West Dease Test Well No. 1, color-coded by acquisition date (left). Temperature gradient calculated from the 1989 log is shown in the right panel.

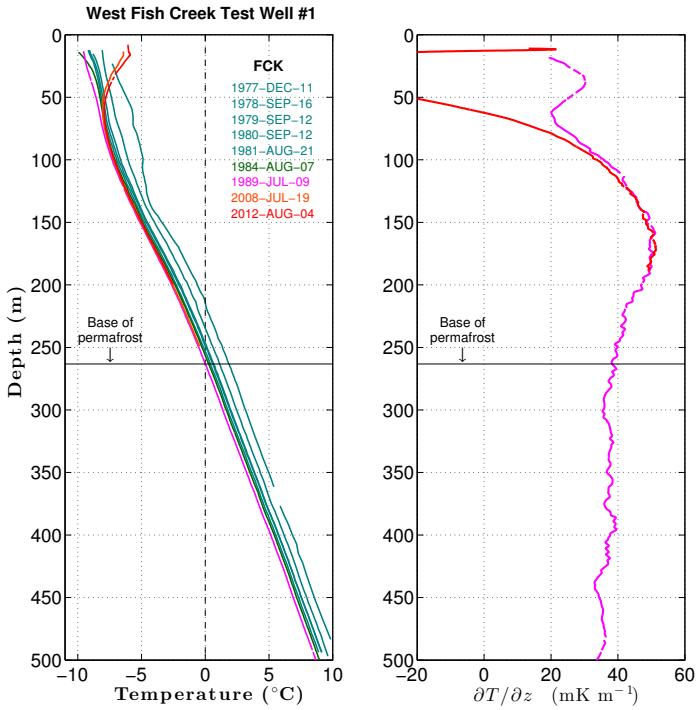

Figure 4.30: Temperature profiles in the West Fish Creek Test Well No. 1, color-coded by acquisition date (left). Temperature gradients calculated from the 1989 and 2012 logs are shown in the right panel.

cessation of drilling, temperatures in the well and surrounding rock gradually return to the undisturbed predrilling condition. As these wells were drilled to much greater depths (up to 6 km) than the portion that has remained accessible for temperature logging, all the logs were acquired from the upper zone that was warmed by drilling. As a result, the DOI/GTN-P temperature profiles exhibit a gradual cooling over time (left panels, **Figures 4.8–4.30**).

Although the transfer of heat within a well during drilling is a complicated process, the recovery of a well from the drilling disturbance can be approximated by a simple relationship for times not too soon after well completion. If t is the time since the drill bit first reached a given depth z and s is the duration of the drilling disturbance at that depth (i.e., the duration of fluid circulation), then the temperature at depth z and time t can be approximated by,

$$T(z,t) = T_o(z) + \frac{\bar{q}_l}{4\pi K}\left[\ln\left(\frac{t}{t-s}\right) - \frac{a^2}{2\kappa s}\left(\frac{s}{t}\right)^2 + O\left(\frac{s}{t}\right)^3\right] \tag{4.12}$$

where $T_o(z)$ is the undisturbed predrilling temperature, K is the thermal conductivity of the surrounding rock, κ is the rock's thermal diffusivity, a is the borehole radius, and $\bar{q}_l$ is the mean heat-flux from the drilling fluid into the surrounding rock per unit length of borehole [*Lachenbruch and Brewer*, 1959]. The validity of this expression is restricted to times $t \gg s$. If we let $\tau \equiv (t/s)$ represent dimensionless time, Eq. (4.12) can be re-expressed as,

$$T(z,\tau) = T_o(z) + \frac{\bar{q}_l}{4\pi K}\left[\ln\left(1+\frac{1}{\tau}\right) - \frac{1}{2F_s\tau^2} + O(\tau^{-3})\right] \tag{4.13}$$

where $F_s \equiv (\kappa s/a^2)$ is the dimensionless source-function Fourier number. For the DOI/GTN-P temperature logs, τ is large enough that the term of order τ^{-3} is negligible and can be ignored. The second term in brackets takes into account the finite dimension of a well and is only important when the product $F_s\tau^2$ is small. Most of the DOI/GTN-P monitoring wells were drilled over a few months and have associated Fourier numbers F_s in the range 100–300 while the remaining wells took roughly a year to drill and have F_s values exceeding 1500. Given these large Fourier numbers, the second term in brackets (Eq. 4.13) is small and can be safely ignored under the conditions for which the equation is valid ($t \gg s$).

Figure 4.31 shows the recovery of temperatures from the drilling disturbance in one of the DOI/GTN-P monitoring wells (Atigaru Test Well No. 1). The temperatures do indeed recover in the manner predicted by Eq. (4.13) for $\tau > 8$. The right panel of **Figure 4.31** shows the evolution of the thermal drilling disturbance,

$$\Delta T_d(z,\tau) = T(z,\tau) - T_o(z) \tag{4.14}$$

over time. For the last log obtained in the Atigaru well (13 August 2007), the drilling disturbance had dissipated to the extent that temperatures were within 0.03–0.05 K of the undisturbed predrilling condition. **Table 4.2** lists the drilling disturbance values (ΔT_d) for all the DOI/GTN-P wells during the 1989, 2002–2003, 2007–2008, and 2012–2013 field campaigns. With the exception of the Tunalik test well, the drilling disturbances remaining in the DOI/GTN-P monitoring wells were of order 0.1 K or less by the early 2000s. For all but five of the wells (AWU, LBN, NIN, SBE, TLK), ΔT_d was of order 0.1 K or less substantially earlier (i.e., by 1989).

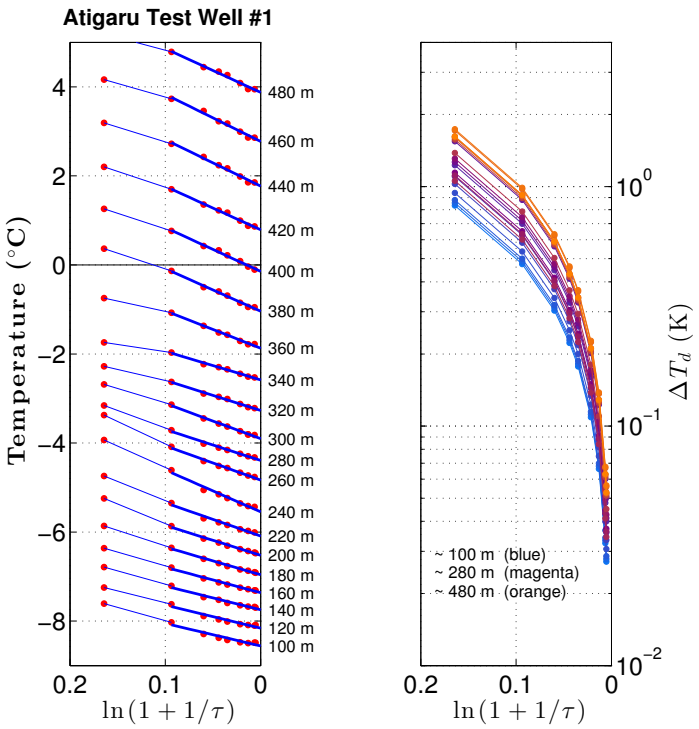

Figure 4.31: Recovery of temperatures from the thermal drilling disturbance at fixed depths in the Atigaru Test Well No. 1 (left). In this case, the earliest log was obtained at dimensionless time $\tau = 5.6$, or $\ln(1 + 1/\tau) = 0.16$. Complete thermal recovery occurs as $\ln(1 + 1/\tau)$ approaches zero ($\tau \to \infty$). A least-squares fit to the temperature data for times $\tau > 8$ provides values for the undisturbed temperature profile $T_o(z)$ and the factor $\bar{q}_l/(4\pi K)$ (dark blue lines). With these values, the evolution of the thermal drilling disturbance ΔT_d (right panel) can be found using Eqs. (4.13) and (4.14).

4.4.3 Latent heat effects

Many of the wells display an abnormally slow recovery for intervals within the permafrost layer, particularly at small dimensionless times τ. The Echooka, J. W. Dalton, and Seabee test wells are good examples (**Figure 4.13**, **Figure 4.15**, **Figure 4.24**), as is the 250 m depth in the Atigaru well (**Figure 4.8**). This slow recovery is attributable to latent heat effects. While drilling a deep borehole through permafrost, interstitial ice within the permafrost zone generally thaws in the vicinity of the well. Once the well is completed, the thawed interstitial ice releases its latent heat upon refreezing, retarding the cooling process as the permafrost returns to its predrilling state. Permafrost intervals showing a delayed recovery are likely to have appreciable amounts of interstitial ice. An extensive discussion of latent heat effects in the cold permafrost found on the Arctic Slope can be found in *Lachenbruch et al.* [1982]. In warm permafrost (mean annual surface temperature $> -2°C$),

Table 4.2: Drilling disturbance ΔT_d remaining in the DOI/GTN-P monitoring wells at the time of the 1989, 2002–2003, 2007–2008, and 2012–2013 field campaigns. The corresponding dimensionless times τ are also listed.

Borehole	USGS Code	Drilling Duration (days)	1989		2002–2003		2007–2008		2012–2013	
			τ	ΔT_d (K)	τ	ΔT_d (K)	τ	ΔT_d (K)	τ	ΔT_d (K)
Atigaru Test Well #1	ATI	60	76	0.07–0.13	156	0.03–0.06	186	0.03–0.05	–	–
Awuna Test Well #1	AWU	412	8	0.20–0.33	20	0.09–0.14	25	0.07–0.11	29	0.06–0.10
Drew Point Test Well #1	DRP	54	78	0.05–0.09	173	0.02–0.04	200	0.02–0.04	–	–
East Simpson Test Well #1	ESN	44	87	0.07–0.11	195	0.03–0.05	236	0.03–0.04	278	0.03–0.04
East Teshekpuk Test Well #1	ETK	56	87	0.05–0.09	179	0.02–0.04	205	0.02–0.04	–	–
Echooka Unit #1	EB1	160	–	–	–	–	–	–	94	0.04–0.05
Ikpikpuk Test Well #1	IKP	442	9	0.09–0.16	20	0.04–0.07	24	0.04–0.06	28	0.03–0.05
J. W. Dalton Test Well #1	JWD	86	43	0.10–0.16	103	0.04–0.07	–	–	–	–
Koluktak Test Well #1	KOL	24	127	0.04	326	0.01–0.02	401	0.01	477	0.01
Kugrua Test Well #1	KAG	98	43	0.13–0.16	91	0.06–0.07	113	0.05–0.06	129	0.04–0.05
Kuyanak Test Well #1	KUY	42	–	–	186	0.03–0.05	229	0.03–0.04	273	0.02–0.03
Lisburne Test Well #1	LBN	344	11	0.35–0.40	25	0.12–0.18	–	–	–	–
Lupine Unit #1	LUP	309	–	–	–	–	–	–	46	0.07-0.09
North Inigok Test Well #1	NIN	45	68	0.33–0.38	175	0.13–0.15	215	0.10–0.12	256	0.09–0.10
North Kalikpik Test Well #1	NKP	40	–	–	233	0.04–0.05	269	0.03–0.04	315	0.03
Peard Bay Test Well #1	PEA	73	53	0.10–0.11	123	0.04–0.05	143	0.04	168	0.03
Seabee Test Well #1	SBE	257	14	0.19–0.26	33	0.08–0.11	40	0.07–0.09	47	0.06–0.08
South Harrison Test Well #1	SOH	67	69	0.14–0.15	140	0.07–0.08	167	0.06	195	0.05
South Meade Test Well #1	SME	341	–	–	26	0.06–0.11	32	0.05–0.09	37	0.04–0.08
Tulageak Test Well #1	TUL	22	140	0.03–0.05	373	0.01–0.02	439	0.01	–	–
Tunalik Test Well #1	TLK	407	10	0.53–0.67	22	0.24–0.29	26	0.20–0.26	30	0.17–0.22
West Dease Test Well #1	WDS	36	96	0.05–0.08	–	–	–	–	–	–
West Fish Creek Test Well #1	FCK	67	68	0.15–0.16	–	–	171	0.06	193	0.05–0.06

latent heat effects in the surficial layer at the top of permafrost can strongly modulate the response of the underlying ground to climate change [*Riseborough*, 1990; *Romanovsky et al.*, 2010]. These effects are much less important on the cold Arctic Slope.

4.4.4 Temperature gradients

Temperature gradients $\partial T/\partial z$ calculated from select temperature profiles are shown in the right panels of **Figures 4.8–4.30** for all of the DOI/GTN-P monitoring wells. Except for the upper 100 m where climate-change effects are large, the gradients primarily reflect thermal conductivity variations with depth; thermal profiles undisturbed by latent heat effects were used wherever possible to find the gradients. A 10 m averaging interval was used for the gradient calculations, 2–3 times greater than the spatial scales at which the wavelet denoising and deconvolution operate. In most cases, the thermal gradient determined in this way shows good agreement among logs for any given well. Depths below 100 m where the gradient $\partial T/\partial z$ between logs is disparate indicate intervals where

one or more of the temperature profiles is less certain. Unlike nearby Prudhoe Bay, a significant change in the temperature gradient is not observed at the base of permafrost in the NPR-A wells or in the Lupine or Echooka test wells; the strong gradient contrast at the base of permafrost in Prudhoe Bay has been attributed to the high porosity ($\sim 39\,\%$) of the saturated coarse-grained materials found there [*Lachenbruch et al.*, 1982].

4.4.5 Borehole fluid convection

The fluid in a monitoring well is expected to freely convect wherever the temperature gradient exceeds a value given by the sum of a lapse rate term and the critical potential-temperature gradient,

$$\frac{\partial T}{\partial z} > \frac{g\alpha T}{c_\mathrm{p}} + \left(\frac{\partial \theta}{\partial z}\right)_\mathrm{crit}. \tag{4.15}$$

Here, α is the coefficient of thermal expansion for the borehole fluid, c_p is its specific heat, g is the gravitational acceleration, and T is temperature expressed in Kelvin. The critical potential-temperature gradient,

$$\left(\frac{\partial \theta}{\partial z}\right)_\mathrm{crit} = \frac{\nu\kappa}{\alpha g a^4}\left(Ra_\mathrm{c}\gamma^4\right), \tag{4.16}$$

accounts for the effects of viscous drag within the fluid and the boundary conditions at the wall of the borehole; ν is the kinematic viscosity of the fluid, κ is its thermal diffusivity, a is the borehole radius, $\gamma \equiv (a/L)$ is the aspect ratio for convective cells of height L, and Ra_c is the critical Rayleigh number. *Charlson and Sani* [1970, 1971] found that the minimum $(Ra_\mathrm{c}\gamma^4)$ value at which convection will occur is 71 for perfectly insulating side walls and 220 for perfectly conducting walls. Using the thermal properties of the DOI/GTN-P borehole fluid (diesel oil), the radius of the boreholes (12–17 cm), and assuming thermally conducting sidewalls (a reasonable assumption for these wells), the lapse rate term is $1.44\,\mathrm{mK\,m^{-1}}$ while the critical potential-temperature gradient is much smaller, 0.007–$0.028\,\mathrm{mK\,m^{-1}}$. Thus, the viscosity of the fluid and resistive drag on the walls is small enough that the onset of convection in these wells is predominantly determined by the lapse rate term. Considering both terms, free convection is expected to occur at all depths where the temperature gradient exceeds $1.47\,\mathrm{mK\,m^{-1}}$. Except for the climate-induced gradient reversal near the surface, the temperature gradients in these wells exceed the value necessary for the onset of convection by more than an order of magnitude. Thus the

form of the convective flow is expected to be fully turbulent. Analysis of the temperature logs confirms that the borehole fluid is undergoing turbulent convection. Random temperature fluctuations as large as ± 10 mK associated with the turbulent eddies constitutes the primary source of noise in the post-1999 temperature logs.

During the spring and early summer, temperature gradients typically exceed 100 mK m^{-1} in the upper $\sim$ 10 m of permafrost. As a result, convection of the borehole fluid can become so intense that the temperatures within the monitoring wells become nearly isothermal during this period at shallow depths. **Figure 4.32** shows temperatures in the Koluktak test well monitored by a thermistor string located 5–13 m below the surface. Strong positive temperature gradients develop near-surface by early March as the permafrost chills. By early June, the isothermal zone extends down to 10 m in this well and then warms in response to summer heating. By early- to mid-August, near-surface gradients weaken, shallow convection ceases, and the isothermal zone vanishes. As most of the DOI/GTN-P temperature logs have been acquired at about the convective transition period, many of the logs show an isothermal section in the upper $\sim$ 10 m while others do not.

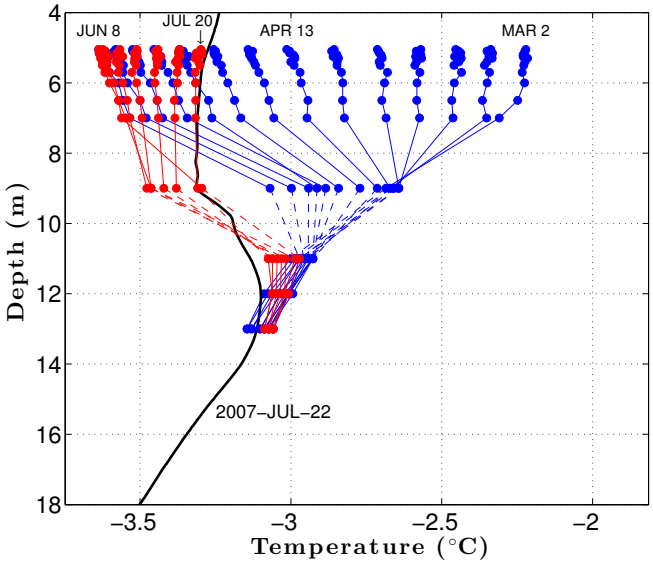

Figure 4.32: Temperatures in the Koluktak Test Well No. 1 measured by a thermistor string extending over the 5–13 m depths from 2 March through 20 July (2007); thermistor string temperatures are displayed once per week. The thermistor string was removed from the well and a standard borehole temperature log acquired on 22 July 2007 (black line). The thermistor string data confirm the development of a nearly-isothermal zone in the upper 10 m of the well due to intense convection during the spring and early summer.

4.4.6 Climate change effects

Although the temperatures in this dataset have not been corrected for the thermal drilling disturbance, measurements acquired during the last 25 yr when the disturbance has been small demonstrate the magnitude of permafrost warming experienced on the Arctic Slope of Alaska since the late 1980s. **Figure 4.33** shows the last four temperature logs acquired in the Awuna test well as an example. Correcting the logs for the drilling disturbance is a high priority as it will give a clearer picture of how near-surface temperatures in permafrost have evolved in this region since the onset of the monitoring program in 1973. A preliminary analysis of the well log data indicates a spatially variable warming has occurred across with the Arctic Slope of Alaska, with temperature increases ranging 2–3 K at the 20-m depth since the late 1980s.

4.5 Summary

A 40 yr dataset of borehole temperature measurements from continuous permafrost in arctic Alaska has been assembled for the period 1973–2013. The data represent the true temperatures in the wellbores and surrounding rocks at the time of the measurements; they have not been corrected to remove the thermal disturbance caused by drilling the

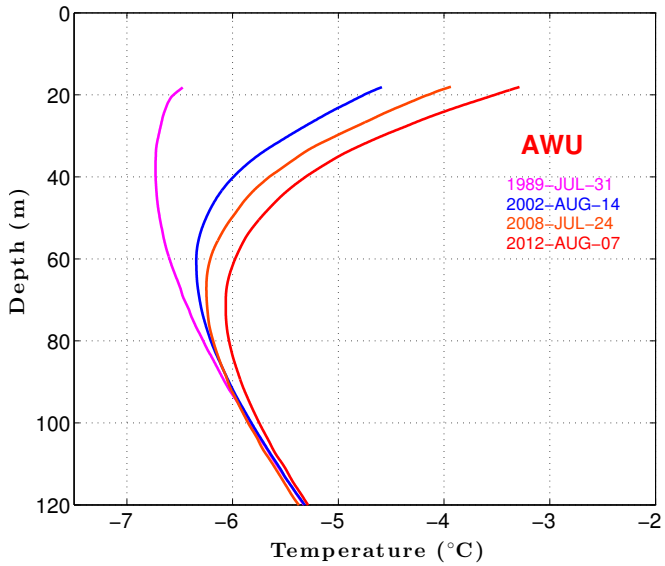

Figure 4.33: Upper portion of the last four temperature logs from the Awuna Test Well No. 1. Near-surface permafrost temperatures have warmed substantially at this site since the late 1980s in response to climate change. Seasonal effects in the upper 18 m have been removed to more clearly show the climate signal.

wells. With a few exceptions, the drilling disturbance is estimated to have been of order 0.1 K or less by 1989. Thus, most of the temperature measurements acquired during the last 25 yr are little affected by the drilling disturbance. The data contribute to ongoing efforts to monitor changes in the thermal state of permafrost in both hemispheres by the Global Terrestrial Network for Permafrost (GTN-P), one of the primary subnetworks of the Global Terrestrial Observing System (GTOS). In addition, the data will be useful for refining our basic understanding of the physical conditions in near-surface materials on the Arctic Slope of Alaska, including the thickness of permafrost and its ice content, as well as provide important information for validating predictive models used for climate impact assessments. The dataset may also prove useful for testing the validity of borehole recovery models used to describe how the thermal disturbance caused by drilling diminishes over time. Such models are often used to ascertain undisturbed rock temperatures from a series of temperature logs perturbed by drilling effects. Very few high-quality datasets are available for testing such models, particularly in permafrost terrain. The fully processed borehole temperature data are available online from the ACADIS repository at http://dx.doi.org/10.5065/D6N014HK.

4.6 References

Beltrami, H., and Mareschal, J.C. (1992), Ground temperature histories for central and eastern Canada from geothermal measurements: Little Ice Age signature, *Geophys. Res. Lett.*, 19, 689–692.

Charlson, G.S., and Sani, R.L. (1970), Thermoconvective instability in a bounded cylindrical fluid, *Int. J. Heat Mass Transfer*, 13, 1479–1496.

Charlson, G.S., and Sani, R.L. (1971), On thermoconvective instability in a bounded cylindrical fluid layer, *Int. J. Heat Mass Transfer*, 14, 2157–2160.

Clow, G.D. (2008), USGS Polar Temperature Logging System, description and measurement uncertainties, *USGS Techniques and Methods 2–E3*, U.S. Geological Survey, 24 pp., available at: http://pubs.usgs.gov/tm/02e03.

Clow, G.D. (2013), USGS permafrost temperatures acquired from the DOI/GTN-P Deep Borehole Array in arctic Alaska, 1973-continuing, Advanced Cooperative Arctic Data and Information Service (ACADIS), Boulder, Colorado USA, http://dx.doi.org/10.5065/D6N014HK.

Gryc, G. (1988), Geology and exploration of the National Petroleum Reserve in Alaska, 1974 to 1982, *USGS Professional Paper 1399*, U.S. Geological Survey, 940 pp.

International Permafrost Association (IPA) (2010), IPA-IPY thermal state of permafrost (TSP) snapshot borehole inventory, National Snow and Ice Data Center, Boulder, Colorado USA, http://dx.doi.org/10.7265/N57D2S25.

Jeffries, M.O., Richter-Menge, J., and Overland, J.E. (eds.) (2012), Arctic Report Card: Update for 2012, National Oceanic and Atmospheric Administration, http://www.arctic.noaa.gov/report12.

Jeffries, M.O., Overland, J.E., and Perovich, D.K. (2013), The Arctic shifts to a new normal, *Physics Today*, 35–40.

Lachenbruch, A.H., and Brewer, M.C. (1959), Dissipation of the temperature effect of drilling a well in arctic Alaska, *USGS Bulletin 1083-C*, U.S. Geological Survey, 73–109.

Lachenbruch, A.H., and Marshall, B.V. (1986), Changing climate: geothermal evidence from permafrost in the alaskan Arctic, *Science*, 234, 689–696.

Lachenbruch, A.H., Sass, J.H., Marshall, B.V., and Moses, T.H., Jr. (1982), Permafrost, heat flow, and the geothermal regime at Prudhoe Bay, Alaska, *J. Geophys. Res.*, 87, 9301–9316.

Lachenbruch, A.H., Sass, J.H., Lawver, L.A., Brewer, M.C., Marshall, B.V., Munroe, R.J., Kennelly, J.P., Galanis, S.P, Jr., and Moses, T.H., Jr. (1988a), Temperature and depth of permafrost on the Arctic Slope of Alaska, in *Geology and Exploration of the National Petroleum Reserve in Alaska, 1974 to 1982*, USGS Professional Paper 1399, U.S. Geological Survey, 645–656.

Lachenbruch, A.H., Cladouhos, T.T, and Saltus, R.W. (1988b), Permafrost temperature and the changing climate, in *Proceedings of the Fifth International Conference on Permafrost*, Trondheim, Norway, 2–5 August 1988, vol. 3, 9–17.

Mareschal, J.C., and Beltrami, H. (1992), Evidence for recent warming from perturbed geothermal gradients: examples from eastern Canada, *Clim. Dyn.*, 6, 135–153.

Nielsen, S.B., and Balling, N. (1984), Accuracy and resolution in continuous temperature logging, *Tectonophysics*, 103, 1–10.

Nielsen, S.B., and Beck, A.E. (1989), Heat flow density values and paleoclimate determined from stochastic inversion of four temperature-depth profiles from the Superior Province of the Canadian Shield, *Tectonophysics*, 164, 345–359.

Osterkamp, T.E., and Jorgenson, J.C. (2006), Warming of permafrost in the Arctic National Wildlife Refuge, Alaska, *Permafrost Periglac.*, 17, 65–69.

Osterkamp, T.E., and Romanovsky, V.E. (1999), Evidence for warming and thawing of discontinuous permafrost in Alaska, *Permafrost Periglac.*, 10, 17–37.

Riseborough, D.W. (1990), Soil latent heat as a filter of the climate signal in permafrost, in *Proceedings of the Fifth Canadian Permafrost Conference*, Collection Nordicana No. 54, Université Laval, Québec, 199–205.

Romanovsky, V.E., Smith, S.L., and Christiansen, H.H. (2010), Permafrost thermal state in the polar Northern Hemisphere during the International Polar Year 2007–2009: a synthesis, *Permafrost Periglac.*, 21, 106–116.

Saltus, R.W., and Clow, G.D. (1994), Deconvolution of continuous borehole temperature logs: algorithms and accuracies, *USGS Open-File Report 94–254*, U.S. Geological Survey, Reston, Virginia USA, 42 pp..

Sass, J.H., Lachenbruch, A.H., Munroe, R.J., Greene, G.W., and Moses, T.H., Jr. (1971), Heat flow in the western United States, *J. Geophys. Res.*, 76, 6376–6413.

Sessa, R., and Dolman, H. (eds.) (2008), Terrestrial essential climate variables for climate change assessment, mitigation and adaption, *GTOS 52*, Global Terrestrial Observing System, Food and Agricultural Organization of the United Nations, Rome.

Smith, S., and Brown, J. (2009), Assessment of the status of the development of the standards for the Terrestrial Essential Climate Variables - T7 - Permafrost and seasonally frozen ground, *GTOS 62*, Global Terrestrial Observing System, Food and Agricultural Organization of the United Nations, Rome.

Smith, S.L., Burgess, M.M., Risenborough, D., and Nixon, F.M. (2005), Recent trends from Canadian permafrost thermal monitoring sites, *Permafrost Periglac.*, 16, 19–30.

Smith, S.L., Romanovsky, V.E., Lewkowicz, A.G., Burn, C.R., Allard, M., Clow, G.D., Yoshikawa, K., and Throop, J. (2010), Thermal state of permafrost in North America - a contribution to the International Polar Year, *Permafrost Periglac.*, 21, 117–135.

Steinhart, J.S., and Hart, S.R. (1968), Calibration curves for thermistors, *Deep-Sea Res.*, 15, 497–503.

Strang, G., and Nguyen, T. (1996), *Wavelets and Filter Banks*, Wellesley-Cambridge Press, Wellesley, Massachusetts USA, 490 pp.

Swartz, J.H. (1954), A geothermal measuring circuit, *Science*, 120, 573-574.

Taylor, A.E., Wang, K., Smith, S.L., Burgess, M.M., and Judge, A.S. (2006), Canadian arctic permafrost observatories: detecting climate change through inversion of subsurface time series, *J. Geophys. Res.*, 111, doi:10.1029/2004JB003208.

Urban, F.E., and Clow, G.D. (2014), DOI/GTN-P climate and active-layer data acquired in the National Petroleum Reserve–Alaska and the Arctic National Wildlife Refuge, 1998–2011, *USGS Data Series 812*, U.S. Geological Survey, http://dx.doi.org/10.3133/ds812.

CHAPTER 5

A GREEN'S FUNCTION APPROACH FOR ASSESSING THE THERMAL DISTURBANCE CAUSED BY DRILLING DEEP BOREHOLES IN ROCK OR ICE

5.1 Abstract

A knowledge of subsurface temperatures in sedimentary basins, fault zones, volcanic environments, and polar ice sheets is of interest for a wide variety of geophysical applications*. However, the process of drilling deep boreholes in these environments to provide access for temperature and other measurements invariably disturbs the temperature field around a newly created borehole. Although this disturbance dissipates over time, most temperature measurements are made while the temperature field is still disturbed. Thus, the measurements must be 'corrected' for the drilling-disturbance effect if the undisturbed temperature field is to be determined. This paper provides compact analytical solutions for the thermal drilling disturbance based on 1-D (radial) and 2-D (radial and depth) Green's functions in cylindrical coordinates. Solutions are developed for three types of boundary conditions at the borehole wall: (1) prescribed temperature, (2) prescribed heat flux, and (3) a prescribed convective condition. The boundary condition at the borehole wall is allowed to vary both with depth and time. Inclusion of the depth dimension in the 2-D solution allows vertical heat-transfer effects to be quantified in situations where they are potentially important, that is near the earth's surface, at the bottom of a well, and when considering

*This chapter was originally published as: Clow, G.D. (2015), A Green's function approach for assessing the thermal disturbance caused by drilling deep boreholes in rock or ice, *Geophys. J. Int.*, **230**, 1877–1895, doi:10.1093/gji/ggv415.

finite drilling rates. The 2-D solution also includes a radial- and time-dependent boundary condition at the earth's surface to assess the impact of drilling-related infrastructure (drilling pads, mud pits, permanent shelters) on the subsurface temperature field. Latent-heat effects due to the melting and subsequent refreezing of interstitial ice while drilling a borehole through ice-rich permafrost can be included in the Green's function solution as a moving-plane heat source (or sink) located at the solid-liquid interface. Synthetic examples are provided illustrating the 1-D and 2-D Green's function solutions. The flexibility of the approach allows the investigation of thermal drilling effects in rock or ice for a wide variety of drilling technologies. Numerical values for the required radial Green's functions $\mathbf{G}_R$ are available through the Advanced Cooperative Arctic Data and Information Service at doi:10.5065/D64F1NS6.

5.2 Introduction

A variety of technologies are currently used to drill deep ($>$ 500 m) boreholes in rock or ice. These include the use of rotary drills with either direct or reverse fluid circulation, coiled tubing drills with downhole hydraulic motors, hot-water drills designed to rapidly melt a hole through ice, and cable-suspended electromechanical and electrothermal drills used to core through the polar ice sheets. An inevitable consequence of deep drilling is that temperatures in the vicinity of a new borehole are always disturbed, the magnitude of the disturbance depends on the size of the hole and the drilling method. For most technologies, the thermal disturbance is primarily due to heat exchange between the drilling fluid and the material surrounding the hole. Other sources include: frictional heating at the drill bit (most drills), direct injection of heat at the bottom of the hole (electrothermal drills), frictional heating between the drill rods and the surrounding rock (rotary drills), and heat generated by downhole motors (electromechanical and coiled tubing drills).

Although temperatures around a well eventually return to the undisturbed state, for commercial, regulatory, or logistical reasons, borehole-temperature measurements can only be made relatively soon after a hole is drilled in most circumstances. Thus, the measured temperatures must be 'corrected' if the undisturbed temperature distribution in the surrounding rock or ice is to be found. Undisturbed formation temperatures are of interest for a wide range of geophysical applications, including regional heat-flow studies, model-

ing hydrocarbon maturation in sedimentary basins, assessment of geothermal-reservoir potential, interpretation of electric well logs, prediction of gas-hydrate stability zones, permafrost characterization, and climate-change studies.

Several methods have been proposed for correcting borehole-temperature measurements for the thermal drilling disturbance. The earliest class of methods treated the borehole as an infinitely long line-source that exchanged heat with the formation at a constant rate during the drilling phase [*Bullard*, 1947; *Lachenbruch and Brewer*, 1959]. *Štulc* [1995] later extended the method to consider intermittently drilled boreholes, a somewhat common situation. The main disadvantage of line-source methods is that they are only valid for large shut-in times when the thermal recovery is insensitive to the details of the drilling process, the finite dimension of the hole, and the contrast of thermal properties between the formation and the borehole fluid. The approximate limit of validity is $t_s > 5s$ where s is the duration of the heat source (provided by fluid circulation, frictional heating, or direct heat injection) and t_s is the 'shut-in' time, that is the time since the hole was completed and the perturbing heat sources were terminated.

A second class of methods uses cylindrical-source models that were developed to better simulate thermal recovery at the small shut-in times relevant for the acquisition of most borehole-temperature logs. The first models in this class assumed the thermal properties of the fluid inside the borehole to be identical to those of the surrounding medium [*Middleton*, 1979; *Leblanc et al.*, 1981]. This limitation was subsequently removed with the development of new analytical models incorporating different thermal properties inside and outside a borehole. Due to the mathematical complexity of the cylindrical-source problem with composite media, analytical solutions became available only for simple boundary conditions (constant temperature change or constant heat flux) and these were restricted to conditions occurring near the bottom of the hole [*Lee*, 1982; *Shen and Beck*, 1986]. Numerical cylindrical-source models were developed in parallel to simulate the thermal recovery at any depth in a borehole [*Lee*, 1982; *Nielsen et al.*, 1990]. Numerical models also allowed for the use of time-dependent boundary conditions (BCs) at the borehole wall during drilling [e.g., *Nielsen et al.*, 1990]. More recently, *Fomin et al.* [2003] presented an approximate analytical solution based on the generalized integral-balance method [*Volkov et al.*, 1988] that is less restrictive than previous analytical solutions. In addition, *Fomin et al.* [2003]

utilized a convective (Robin) BC at the borehole wall following Newton's law of cooling instead of the commonly used temperature or heat-flux BC. A third class of methods is represented by the spherical-source model advanced by *Ascencio et al.* [1994]. This model attempts to simulate radial and vertical heat flow near the bottom of a well by assuming a spherically symmetric source at the bottom of the hole. This model was specifically developed to aid in the interpretation of bottom hole temperatures and is inappropriate for conditions higher up in a borehole.

Despite the large number of drilling-disturbance models currently available, accurately determining undisturbed formation temperatures remains a technical challenge, especially for small shut-in times [*Andaverde et al.*, 2005; *Bassam et al.*, 2010; *Espinoza-Ojeda et al.*, 2011; *Wong-Loya et al.*, 2012]. Modern numerical methods are capable of simulating all the principal heat flow mechanisms involved in the thermal recovery of a borehole and surrounding medium from the drilling disturbance. However, given the large number of parameters that must typically be specified in these models, it is often difficult to gain physical insight into which variables are most important and the interaction between them. In addition, the values for many of these parameters are often poorly known. Analytic solutions provide a clearer view of the principal physical controls, their evaluation is generally faster and potentially more accurate than solving the heat-transfer problem numerically, and are essential for testing complex numerical codes. The main difficulty with analytical models is finding the solution, which can be a significant challenge for all but the simplest cases.

Given the continued value of analytic solutions, the aim of this paper is to present a general solution for the thermal recovery of the medium outside a borehole that encompasses a broad range of situations. Green's functions (GFs) are used to solve the transient thermal problem which leads to solutions in a very compact form. Although heat transfer is predominantly radial for the drilling-disturbance problem, vertical effects can also be important near the earth's surface, at the bottom of a well, and when considering finite-drilling rates [*Lachenbruch and Brewer*, 1959; *Shen and Beck*, 1986]. To connect with earlier work and to treat vertical heat-transfer effects, both 1-D (pure radial) and 2-D (radial and depth) cylindrical-source solutions are presented. Three boundary conditions are considered at the borehole wall, all of which can be time- and depth-dependent: (i) prescribed temperature, (ii) prescribed heat flux, and (iii) a prescribed convective condition.

This flexibility is intended to allow the investigation of drilling effects for a wide range of drilling technologies, none of which are likely to result in a steady BC at the borehole wall for the entire drilling cycle (e.g., **Figure 5.1**). With this approach, it is assumed the BC at the borehole wall can be specified from borehole-temperature monitoring experiments, determined using geophysical inverse methods [e.g., *Nielsen et al.*, 1990], or through the use of an auxiliary model such as an engineering wellbore thermal simulator [*Garcia et al.*, 1998; *Espinosa et al.*, 2000; *Szarka and Bobok*, 2012]. The primary difficulty with the Green's function (GF) approach is finding the appropriate Green's function. Once the GF has been found, it is relatively straightforward to solve the thermal problem for different initial conditions, boundary conditions, and heat-production functions.

5.3 General temperature solution

To consider boreholes drilled in rock or moving ice, we begin with the advection-diffusion equation,

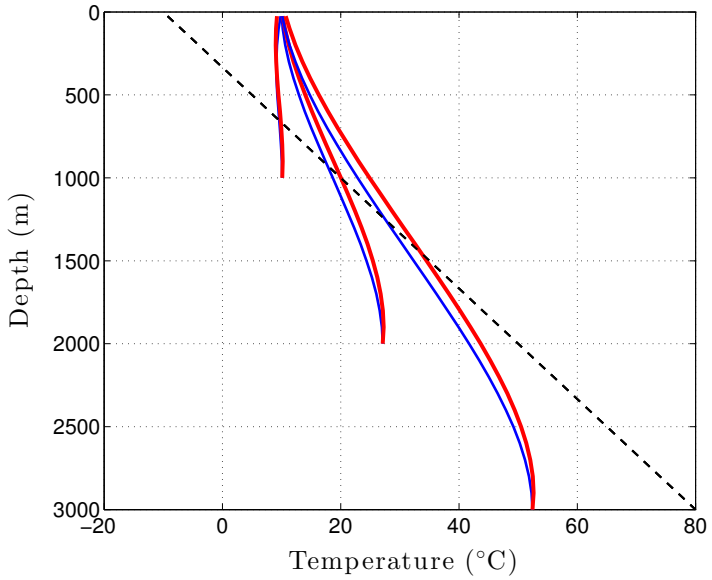

Figure 5.1: Fluid temperatures inside the drill pipe (blue lines) and in the annulus between the pipe and the formation (red lines) for a hypothetical well drilled to 3000 m with a rotary drill based on the *Szarka and Bobok* [2012] wellbore model. Solid lines show the temperatures when the drill has penetrated to 1000, 2000, and 3000 m. Temperatures in the annulus are relatively constant for the first 1000 m of drilling and then steadily increase as the drill penetrates to depths warmer than the fluid injection temperature (+10°C in this simulation). Fluid circulation continues for 6 hours after drilling is completed to condition the well. Dashed line shows the undisturbed formation temperature.

$$\rho c_p \frac{\partial T(\mathbf{r},t)}{\partial t} \;=\; \nabla \cdot K \nabla T(\mathbf{r},t) \;-\; \rho c_p \mathbf{v}(\mathbf{r}) \cdot \nabla T(\mathbf{r},t) \;+\; g(\mathbf{r},t) \tag{5.1}$$

describing heat-transfer in the medium surrounding the hole. Here T is temperature, t is time, $\mathbf{r}$ is the vector location, ρ is the density of the medium, c_p is its specific heat, K is the thermal conductivity, and $\mathbf{v}$ is the velocity. The first term on the right hand side of eq. (5.1) represents heat diffusion, the second term represents heat advection, and the third term $g(\mathbf{r},t)$ represents any heat production sources that may be present. Potential heat sources include the decay of radioactive isotopes in rock, strain heating in ice, and latent-heat effects associated with the melting and refreezing of interstitial ice while drilling boreholes through permafrost. The advection term can be ignored when the rate of temperature change due to the drilling disturbance satisfies $(\partial T/\partial t) \gg \mathbf{v} \cdot \nabla T$. Using the *Dansgaard and Johnsen* [1969] model to describe the horizontal and vertical velocities in an ice sheet, $\mathbf{v} \cdot \nabla T$ is found to be less than 10^{-10} K s^{-1} except near ice streams and within 10% of the edge of the Greenland and Antarctic Ice Sheets. Thus in most circumstances, ice advection can be ignored during the time of interest (first few decades after a borehole is drilled) and the transient drilling disturbance can be treated as a pure conduction problem. If we further assume the medium outside the borehole is homogeneous and isotropic, the solution to (5.1) can be compactly expressed in terms of a Green's function $G(\mathbf{r},t \mid \mathbf{r}',t')$,

$$\begin{aligned} T(\mathbf{r},t) \;=\; & \int_V G(\mathbf{r},t \mid \mathbf{r}',t')|_{t'=0}\, F(\mathbf{r}')\, dV' + \kappa \int_{t'=0}^{t} \sum_{i=1}^{s} \int_{S_i} G(\mathbf{r},t \mid \mathbf{r}',t')|_{\mathbf{r}'=\mathbf{r}_i} \frac{f_i(\mathbf{r}',t')}{K_i}\, ds_i'\, dt' \\ & + \frac{\kappa}{K} \int_{t'=0}^{t} \int_V G(\mathbf{r},t \mid \mathbf{r}',t')\; g(\mathbf{r}',t')\, dV' dt', \end{aligned} \tag{5.2}$$

when a prescribed heat flux or convective condition occurs on the bounding surfaces S_i of volume V [*Özişik*, 1980]. The first term on the right hand side of (5.2) describes the thermal effect of the initial condition $F(\mathbf{r})$, the second term is the thermal effect due to the boundary conditions $f_i(\mathbf{r},t)$ on surfaces S_i, and the third term is the effect of the heat-production function $g(\mathbf{r},t)$; κ is the thermal diffusivity. The Green's function $G(\mathbf{r},t \mid \mathbf{r}',t')$ is the thermal response at location $\mathbf{r}$ and time t due to an instantaneous heat source released at time t' at location $\mathbf{r}'$. It can also be interpreted as the *weighting function* acting on $g(\mathbf{r}',t')$ needed to find the thermal effect at $(\mathbf{r},t)$ due to the heat-production function. Similarly, $G(\mathbf{r},t \mid \mathbf{r}',t')|_{t'=0}$ is the weighting function acting on $F(\mathbf{r}')$ needed to find the thermal effect at $(\mathbf{r},t)$ due to the initial temperature field, and $G(\mathbf{r},t \mid \mathbf{r}',t')|_{\mathbf{r}'=\mathbf{r}_i}$ is the weighting function

acting on $f_i(\mathbf{r}', t')$ needed to find the thermal effect at $(\mathbf{r}, t)$ due to the boundary condition on surface S_i. The second term in (5.2) takes a slightly different form for any boundaries S_j having a prescribed temperature condition,

$$\begin{aligned} T(\mathbf{r},t) &= \int_V G(\mathbf{r},t\,|\mathbf{r}',t')|_{t'=0}\, F(\mathbf{r}')\, dV' + \kappa \int_{t'=0}^{t} \sum_{j=1} \int_{S_j} \left.\frac{\partial G}{\partial n_j}\right|_{\mathbf{r}'=\mathbf{r}_j} f_j(\mathbf{r}',t')\, ds_j'\, dt' \\ &+ \frac{\kappa}{K} \int_{t'=0}^{t} \int_V G(\mathbf{r},t\,|\mathbf{r}',t')\; g(\mathbf{r}',t')\, dV' dt'. \end{aligned} \tag{5.3}$$

To complete the mathematical description of the transient thermal problem, the initial condition is,

$$T(\mathbf{r},t)|_{t=0} = F(\mathbf{r}), \tag{5.4}$$

while the three BCs considered in this paper are,

$$T(\mathbf{r},t)|_{S_i} = f_i(\mathbf{r},t) \qquad \text{Dirichlet, prescribed temperature (T-BC)} \tag{5.5}$$

$$K_i \left.\frac{\partial T}{\partial n_i}\right|_{S_i} = f_i(\mathbf{r},t) \qquad \text{Neumann, prescribed heat flux (Q-BC)} \tag{5.6}$$

$$h_i\, T|_{S_i} + K_i \left.\frac{\partial T}{\partial n_i}\right|_{S_i} = h_i\, T_f = f_i(\mathbf{r},t). \qquad \text{Robin, convective condition (C-BC)} \tag{5.7}$$

For the convective BC, we specify the heat-transfer coefficient h_i across the fluid boundary-layer adjacent to boundary S_i and the fluid temperature T_f outside the boundary layer. **Figure 5.2** illustrates the problem domain for the drilling-disturbance problem. Surface S_1 refers to the borehole wall while S_2 refers to the earth's surface.

5.3.1 One-dimensional radial temperatures

Before presenting the complete 2-D solution to the drilling-disturbance problem, we consider just the radial aspects. For simplicity, the initial condition $F(\mathbf{r}, t)$ and heat-production function $g(\mathbf{r}, t)$ are assumed to be axisymmetric about the borehole. Without the vertical and azimuthal dependencies, the problem reduces to a 1-D semi-infinite problem in cylindrical coordinates. To provide greater insight into the interaction between variables, we express the Green's function and associated temperature solution in terms of dimensionless variables. To accomplish this, we define a dimensionless radial coordinate by,

$$\zeta = \left(\frac{r}{a}\right), \tag{5.8}$$

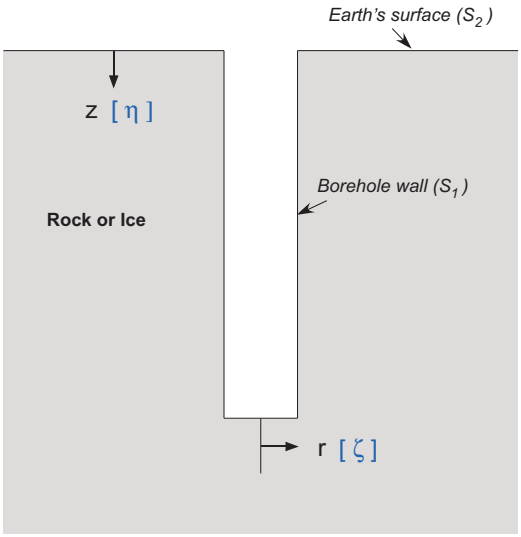

Figure 5.2: Illustration of the problem domain, boundary surfaces S_1 and S_2, and the coordinate system convention; ζ is the dimensionless radial distance while η is dimensionless depth.

and dimensionless time by,

$$\tau \;=\; \left(\frac{\kappa\, t}{a^2}\right), \tag{5.9}$$

where a is the borehole radius. A dimensionless version of the radial Green's function (indicated in boldface) is defined by,

$$\mathbf{G}_R(\zeta, \tau \,|\, \zeta', \tau') \;=\; a^2\, G_R(\zeta, \tau \,|\, \zeta', \tau')\,. \tag{5.10}$$

Given the single boundary surface (the borehole wall), the temperature solution at radial location ζ and time τ can be expressed as a linear combination of three terms,

$$T(\zeta, \tau) \;=\; T_{\mathrm{ic}}(\zeta, \tau) \;+\; T_{\mathrm{bc}}(\zeta, \tau) \;+\; T_{\mathrm{g}}(\zeta, \tau)\,, \tag{5.11}$$

in which T_{ic} is the thermal effect of the initial temperature field, T_{bc} is the effect of the boundary condition at the borehole wall, and T_{g} is the heat-production effect. Based on the general 3-D temperature equations (5.2) and (5.3), these terms are,

$$T_{\text{ic}}(\zeta,\tau) \;=\; \int_{\zeta'=1}^{\infty} \mathbf{G}_R(\zeta,\tau\,|\,\zeta',\tau')|_{\tau'=0}\; F(\zeta')\,\zeta' d\zeta' \tag{5.12}$$

$$T_{\text{bc}}(\zeta,\tau) \;=\; \begin{cases} \displaystyle\int_{\tau'=0}^{\tau} \left[\frac{\partial \mathbf{G}_R}{\partial \zeta'}\right]_{\zeta'=1} f_1(\tau')\,d\tau' & \text{T-BC} \\ \displaystyle a\int_{\tau'=0}^{\tau} \mathbf{G}_R(\zeta,\tau\,|\,\zeta',\tau')\big|_{\zeta'=1}\,\frac{f_1(\tau')}{K}d\tau' & \text{Q-BC, C-BC} \end{cases} \tag{5.13}$$

$$T_{\text{g}}(\zeta,\tau) \;=\; \frac{a^2}{K}\int_{\tau'=0}^{\tau}\int_{\zeta'=1}^{\infty} \mathbf{G}_R(\zeta,\tau\,|\,\zeta',\tau')\,g(\zeta',\tau')\,\zeta' d\zeta'\,d\tau' \tag{5.14}$$

for the 1-D radial problem in dimensionless coordinates.

The radial Green's function $\mathbf{G}_R(\zeta,\tau\,|\,\zeta',\tau')$ appearing in the temperature terms (5.12)–(5.14) can be found using the procedure outlined in *Özişik* [1980] by (i) solving the homogeneous version of eq. (5.1) for the semi-infinite 1-D radial problem without advection using separation of variables, (ii) expressing the solution in the form of eq. (5.12) so that $\mathbf{G}_R(\zeta,\tau\,|\,\zeta',\tau')|_{\tau'=0}$ can be identified ($T = T_{\text{ic}}$ since T_{g} and T_{bc} are zero for the homogeneous version of the problem), and (iii) replacing τ with $(\tau-\tau')$ in $\mathbf{G}_R(\zeta,\tau\,|\,\zeta',\tau'))|_{\tau'=0}$ to find $\mathbf{G}_R(\zeta,\tau\,|\,\zeta',\tau')$. Following this procedure, the radial GF is found to be,

$$\mathbf{G}_R(\zeta,\tau\,|\,\zeta',\tau') \;=\; \int_{\chi=0}^{\infty} \frac{1}{N(\chi)}\,e^{-\chi^2(\tau-\tau')}\,R_o(\chi,\zeta)\,R_o^*(\chi,\zeta')\,\chi\,d\chi, \tag{5.15}$$

where χ is a dimensionless integration parameter. *Özişik* [1980] provides expressions for the radial function R_o and normalization integral N for each of the three boundary conditions (5.5)–(5.7) in terms of radial coordinate r. Dimensionless versions of these functions involving combinations of Bessel functions of the first and second kind, $J_\nu(\chi\zeta)$ and $Y_\nu(\chi\zeta)$, are given in **Table 5.1**. To incorporate the effects of convective heat transfer, the dimensionless Biot number $Bi = (h_i\,a/K)$ appears in the $R_o(\chi,\zeta)$ and $N(\chi)$ expressions for the convective BC.

If the temperature is prescribed at the borehole wall, the derivative $\partial\mathbf{G}_R/\partial\zeta'$ must also be known to find the temperature at (ζ,τ). Defining a new radial function,

$$R_1(\chi,\zeta) \;=\; Y_1(\chi\zeta)\,J_o(\chi) \;-\; J_1(\chi\zeta)\,Y_o(\chi)\,, \tag{5.16}$$

the derivative is,

Table 5.1: Radial function $R_o(\chi,\zeta)$ and associated normalization integral $N(\chi)$ for the three types of boundary condition at the borehole wall.

BC Type	$R_o(\chi,\zeta)$	$N(\chi)$
Prescribed temperature	$J_o(\chi\zeta)\,Y_o(\chi) - Y_o(\chi\zeta)\,J_o(\chi)$	$J_o^2(\chi) + Y_o^2(\chi)$
Prescribed heat flux	$J_o(\chi\zeta)\,Y_1(\chi) - Y_o(\chi\zeta)\,J_1(\chi)$	$J_1^2(\chi) + Y_1^2(\chi)$
Convective condition	$J_o(\chi\zeta)\,[\chi Y_1(\chi) + Bi\,Y_o(\chi)]$	$[\chi J_1(\chi) + Bi\,J_o(\chi)]^2$
	$-Y_o(\chi\zeta)\,[\chi J_1(\chi) + Bi\,J_o(\chi)]$	$+\,[\chi Y_1(\chi) + Bi\,Y_o(\chi)]^2$

$$\frac{\partial \mathbf{G}_R}{\partial \zeta'} \;=\; \int_{\chi=0}^{\infty} \frac{1}{N(\chi)}\, e^{-\chi^2(\tau-\tau')}\, R_o(\chi,\zeta)\, R_1^*(\chi,\zeta')\, \chi^2\, d\chi\,. \tag{5.17}$$

Given the complexity of the integrands, (5.15) and (5.17) must be integrated numerically to find the radial Green's function $\mathbf{G}_R$ and its derivative $\partial\mathbf{G}_R/\partial\zeta'$. Because of the Bessel functions, $R_o(\chi,\zeta)$ oscillates rapidly when $\chi > 1/\zeta$, posing a considerable challenge for accurately determining the integrals when the time difference $\Delta\tau = (\tau - \tau')$ is small; when $\Delta\tau$ is large, the exponential time term in the integrands effectively damps the oscillations. Performing the integration in a piecewise fashion between the zeros of $R_o(\chi,\zeta)$ can be used to successfully resolve the integration difficulties for small $\Delta\tau$.

As expected, in the small-time limit ($\Delta\tau < 0.1$) the radial GF is greatest in the immediate vicinity of ζ (**Figure 5.3**). As the time difference $\Delta\tau = (\tau - \tau')$ increases, $\mathbf{G}_R$ becomes increasingly broad, reflecting the fact that the temperature at location ζ depends on $F(\zeta')$ and $g(\zeta',\tau')$ over an increasingly large range of radial distances. The Green's function $\mathbf{G}_R(\zeta,\tau\,|\,\zeta',\tau')$ for the convective condition at the borehole wall reduces to the prescribed temperature GF in the limit $Bi \gg 1$ (compare **Figure 5.3a** and **Figure 5.3c**) and to the prescribed heat-flux GF when $Bi \ll 1$ (**Figure 5.3b** and **Figure 5.3d**). Evaluating $\mathbf{G}_R(\zeta,\tau\,|\,\zeta',\tau')$ at $\tau' = 0$ provides the GF term appearing in the initial-condition effect T_{ic} (eq. 5.12, **Figure 5.4**). The GF term appearing in the boundary-condition effect T_{bc} (eq. 5.13) exhibits a maximum when $\Delta\tau \approx (\zeta^2/6)$ regardless of the type of BC (**Figure 5.5**). Thus, the thermal response at radial location ζ is most sensitive to the BCs occurring on the borehole wall at a time $\Delta\tau \approx (\zeta^2/6)$ prior to the evaluation time τ. Although the GF term appearing in T_{bc} for the prescribed temperature and convective BCs are quite different, $[\partial\mathbf{G}_R/\partial\zeta']_{\zeta'=1}$ versus $\mathbf{G}_R|_{\zeta'=1}$, the two terms have the same shape in the limit $Bi \gg 1$ (**Figure 5.5a** and

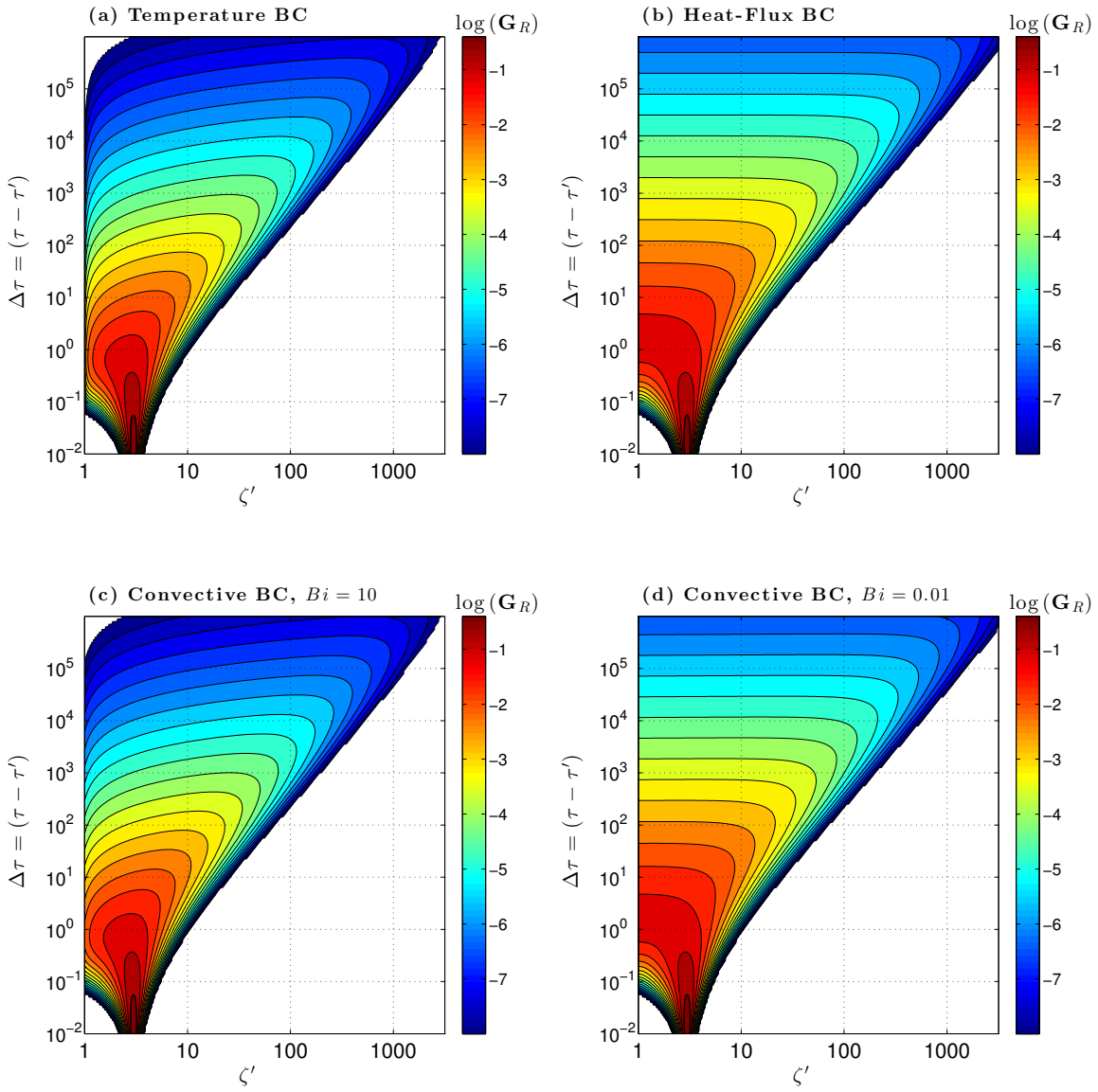

Figure 5.3: Radial Green's function $\mathbf{G}_R(\zeta, \tau \,|\, \zeta', \tau')$ at radial location $\zeta = 3$. Panel (a) shows $\mathbf{G}_R$ for a prescribed temperature condition at the borehole wall, (b) shows $\mathbf{G}_R$ for a prescribed heat-flux BC, while (c) and (d) show $\mathbf{G}_R$ for a convective BC with Biot numbers $Bi = 10$ and $Bi = 0.01$, respectively.

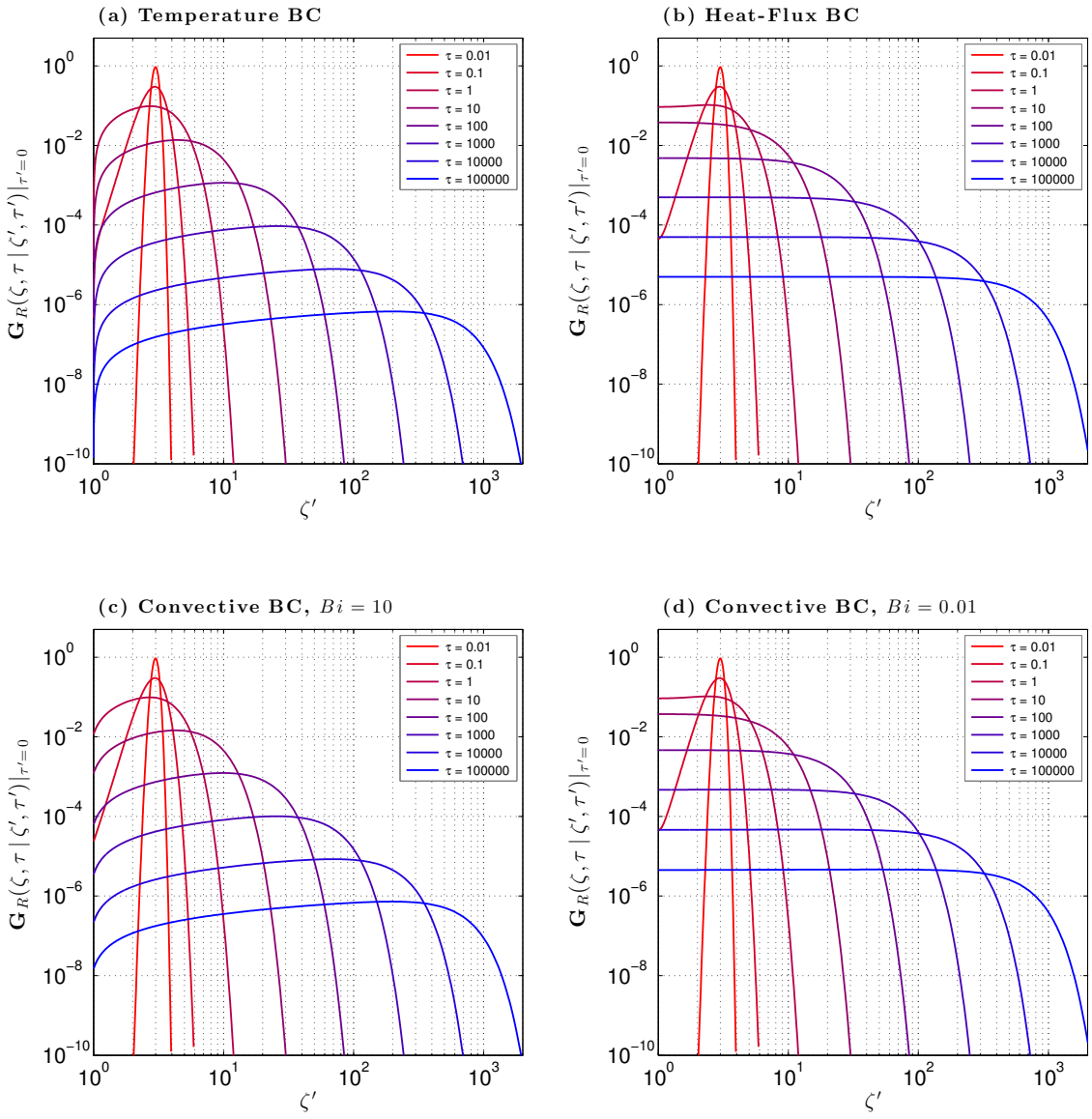

Figure 5.4: Radial Green's function term $\mathbf{G}_R(\zeta, \tau \mid \zeta', \tau')|_{\tau'=0}$ appearing in the initial condition effect T_{ic} (eq. 5.12) at radial location $\zeta = 3$ and times τ ranging from 0.01 to 10^5. Panel (a) shows the Green's function for a prescribed temperature condition at the borehole wall, (b) shows the GF for a prescribed heat-flux BC, while (c) and (d) show the GF for a convective BC with Biot numbers $Bi = 10$ and $Bi = 0.01$, respectively.

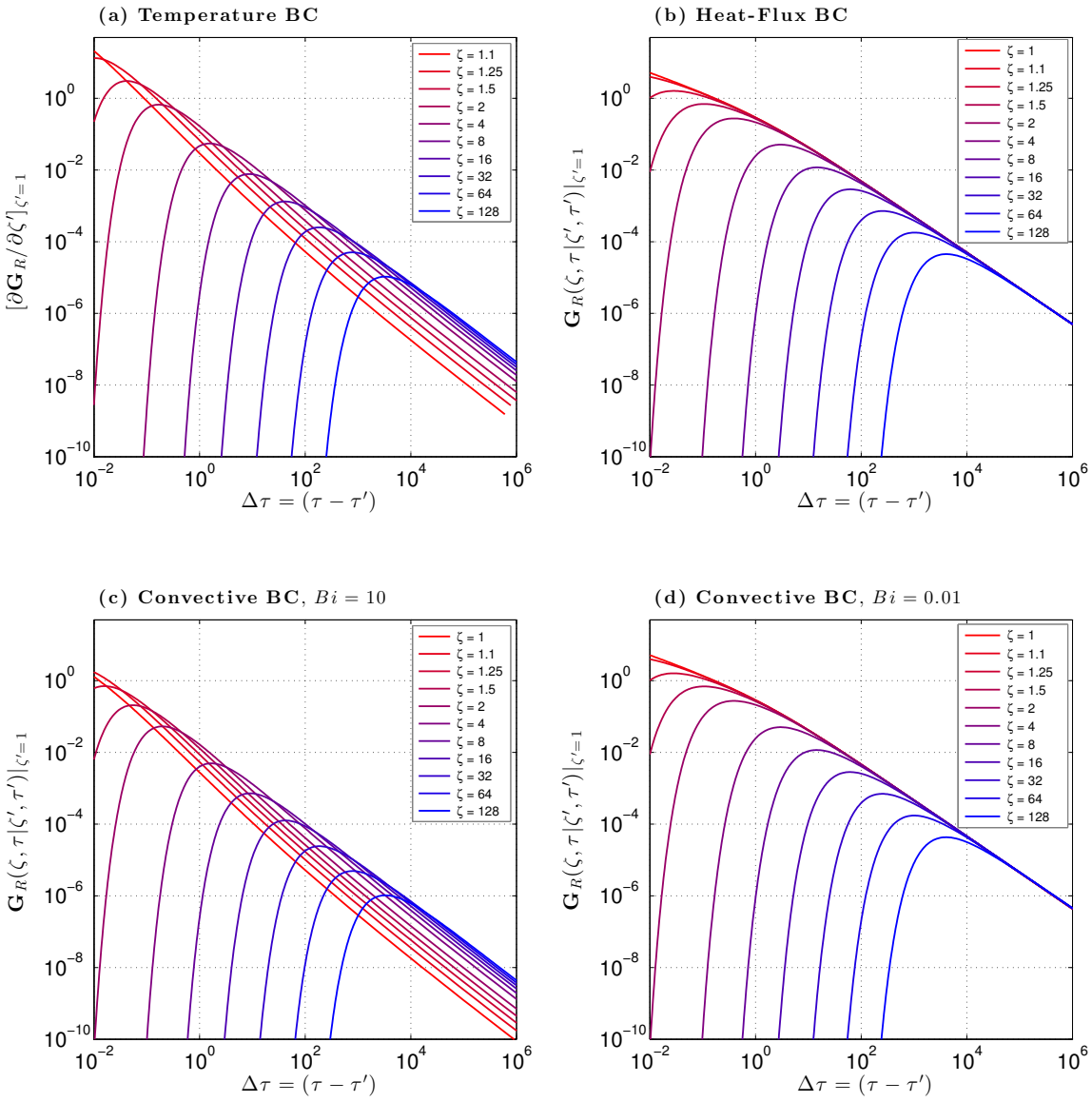

Figure 5.5: Radial Green's function term appearing in the boundary condition effect T_{bc} (eq. 5.13) at radial locations $\zeta \in (1, 128)$. Panel (a) shows $[\partial \mathbf{G}_R/\partial\zeta']_{\zeta'=1}$ for a prescribed temperature condition at the borehole wall, (b) shows $\mathbf{G}_R(\zeta, \tau \,|\, \zeta', \tau')|_{\zeta'=1}$ for a prescribed heat-flux BC, while (c) and (d) show $\mathbf{G}_R(\zeta, \tau \,|\, \zeta', \tau')|_{\zeta'=1}$ for a convective BC with Biot numbers $Bi = 10$ and $Bi = 0.01$, respectively.

Figure 5.5c) while the magnitudes differ by a factor of Bi.

5.3.2 One-dimensional vertical temperatures

The vertical aspects of the drilling disturbance are treated as a 1-D semi-infinite problem with a single boundary at the earth's surface where a prescribed temperature condition is assumed to occur. The development of the vertical solution is very similar to that used to find the 1-D radial solution in Section 5.3.1. For the radial problem, the borehole radius a is the natural length scale. The vertical dimension lacks such a clear-cut scale. We simply let L be the vertical length scale, allowing it to be set by the depth of the annual thermal wave, the total depth of the borehole, or by a convenient scaling number such as 10 m. The dimensionless vertical coordinate is then defined by,

$$\eta \;=\; \left(\frac{z}{L}\right), \tag{5.18}$$

the ratio of the vertical and radial length scales by,

$$\alpha \;=\; \left(\frac{L}{a}\right), \tag{5.19}$$

and a dimensionless version of the vertical GF (indicated in boldface) by,

$$\mathbf{G}_Z(\eta,\tau\,|\,\eta',\tau') \;=\; L\;G_Z(\eta,\tau\,|\,\eta',\tau')\,. \tag{5.20}$$

Dimensionless time τ is defined in the same way as for the radial problem (eq. 5.9). With a single boundary, the temperature solution at dimensionless depth η and time τ is,

$$T(\eta,\tau) \;=\; T_{\rm ic}(\eta,\tau) \;+\; T_{\rm bc}(\eta,\tau) \;+\; T_{\rm g}(\eta,\tau), \tag{5.21}$$

where

$$T_{\rm ic}(\eta,\tau) \;=\; \int_{\eta'=0}^{\infty} \mathbf{G}_Z(\eta,\tau\,|\,\eta',\tau')|_{\tau'=0}\,F(\eta')\,d\eta' \tag{5.22}$$

$$T_{\rm bc}(\eta,\tau) \;=\; \frac{1}{\alpha^2}\int_{\tau'=0}^{\tau} \left.\frac{\partial \mathbf{G}_Z}{\partial \eta'}\right|_{\eta'=0} f_2(\tau')\,d\tau' \qquad \text{T-BC} \tag{5.23}$$

$$T_{\rm g}(\eta,\tau) \;=\; \frac{a^2}{K}\int_{\tau'=0}^{\tau}\int_{\eta'=0}^{\infty} \mathbf{G}_Z(\eta,\tau\,|\,\eta',\tau')\;g(\eta',\tau')\,d\eta' d\tau'. \tag{5.24}$$

Following the procedure outlined by *Özişik* [1980], the vertical GF is found to be,

$$\mathbf{G}_Z(\eta,\tau\,|\,\eta',\tau') \;=\; \int_{\chi=0}^{\infty} \frac{1}{N(\chi)}\, e^{-\left(\frac{\chi}{\alpha}\right)^2(\tau-\tau')}\, Z(\chi,\eta)\, Z^*(\chi,\eta')\, d\chi. \tag{5.25}$$

Consideration of the homogeneous problem shows that the depth function and normalization integral are $Z(\chi,\eta) = \sin(\chi\eta)$ and $N(\chi) = \pi/2$, respectively, for a prescribed temperature BC. With these simple functions, (5.25) can be solved analytically for the Green's function,

$$\mathbf{G}_Z(\eta,\tau|\eta',\tau') = \frac{\alpha}{2\sqrt{\pi}(\tau-\tau')^{1/2}}\left\{\exp\left[-\frac{\alpha^2(\eta-\eta')^2}{4(\tau-\tau')}\right] - \exp\left[-\frac{\alpha^2(\eta+\eta')^2}{4(\tau-\tau')}\right]\right\} \tag{5.26}$$

(**Figure 5.6**) and its spatial derivative,

$$\frac{\partial \mathbf{G}_Z}{\partial \eta'} = \frac{\alpha^3}{4\sqrt{\pi}(\tau-\tau')^{3/2}}\left\{(\eta-\eta')\exp\left[-\frac{\alpha^2(\eta-\eta')^2}{4(\tau-\tau')}\right] + (\eta+\eta')\exp\left[-\frac{\alpha^2(\eta+\eta')^2}{4(\tau-\tau')}\right]\right\}. \tag{5.27}$$

5.3.3 Two-dimensional temperatures

We now develop the general 2-D solution to the drilling-disturbance problem in cylindrical coordinates. Given the existence of two boundary surfaces, the complete solution is a superposition of four terms,

$$T(\zeta,\eta,\tau) \;=\; T_{\text{ic}}(\zeta,\eta,\tau) \;+\; T_{\text{bc1}}(\zeta,\eta,\tau) \;+\; T_{\text{bc2}}(\zeta,\eta,\tau) \;+\; T_{\text{g}}(\zeta,\eta,\tau), \tag{5.28}$$

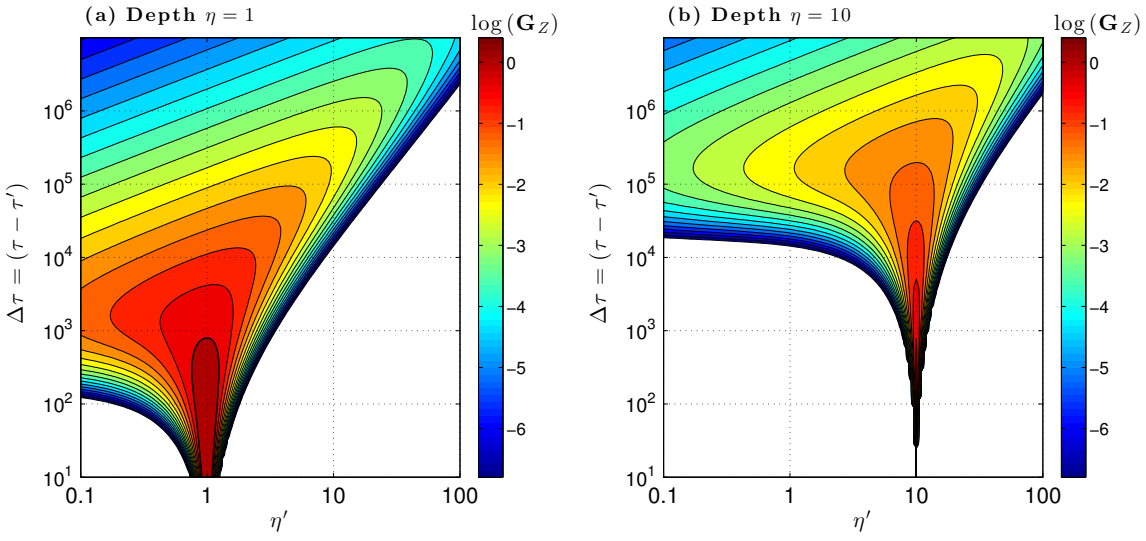

Figure 5.6: Vertical Green's function $\mathbf{G}_Z(\eta,\tau\,|\,\eta',\tau')$ for sample depths $\eta = 1$ (a) and $\eta = 10$ (b). The ratio of the vertical and radial length scales α is assumed to be 100 in this example.

that involve a 2-D Green's function $\mathbf{G}_{RZ}(\zeta,\eta,\tau\,|\,\zeta',\eta',\tau')$. For the axisymmetric cylindrical coordinate system, $\mathbf{G}_{RZ}$ can be obtained very simply as the product of the 1-D GFs derived in Sections 5.3.1 and 5.3.2, $\mathbf{G}_{RZ} = \mathbf{G}_R \cdot \mathbf{G}_Z$, with the restriction that the heat-transfer coefficient h_i must be a constant for any surface S_i having a convective BC [*Beck et al.*, 1992]. Starting with eqs (5.2) and (5.3), transforming to dimensionless coordinates, and separating the 2-D GF into its 1-D components, the four terms in (5.28) are,

$$T_{\mathrm{ic}}(\zeta,\eta,\tau) = \int_{\zeta'=1}^{\infty} \mathbf{G}_R(\zeta,\tau\,|\,\zeta',\tau')|_{\tau'=0} \int_{\eta'=0}^{\infty} \mathbf{G}_Z(\eta,\tau\,|\,\eta',\tau')|_{\tau'=0}\, F(\zeta',\eta')\, d\eta'\, \zeta' d\zeta' \tag{5.29}$$

$$T_{\mathrm{bc1}}(\zeta,\eta,\tau) = \begin{cases} \displaystyle\int_{\tau'=0}^{\tau} \left[\frac{\partial \mathbf{G}_R}{\partial \zeta'}\right]_{\zeta'=1} \int_{\eta'=0}^{\infty} \mathbf{G}_Z(\eta,\tau\,|\,\eta',\tau')\, f_1(\eta',\tau')\, d\eta'\, d\tau' & \text{T-BC} \\ \displaystyle\frac{a}{K}\int_{\tau'=0}^{\tau} \mathbf{G}_R(\zeta,\tau|\zeta',\tau')|_{\zeta'=1} \int_{\eta'=0}^{\infty} \mathbf{G}_Z(\eta,\tau|\eta',\tau')\, f_1(\eta',\tau') d\eta' d\tau' & \text{Q-BC, C-BC} \end{cases} \tag{5.30}$$

$$T_{\mathrm{bc2}}(\zeta,\eta,\tau) = \frac{1}{\alpha^2}\int_{\tau'=0}^{\tau} \left[\frac{\partial \mathbf{G}_Z}{\partial \eta'}\right]_{\eta'=0} \int_{\zeta'=1}^{\infty} \mathbf{G}_R(\zeta,\tau\,|\,\zeta',\tau')\, f_2(\zeta',\tau')\, \zeta' d\zeta'\, d\tau' \qquad \text{T-BC} \tag{5.31}$$

$$T_{\mathrm{g}}(\zeta,\eta,\tau) = \frac{a^2}{K}\int_{\tau'=0}^{\tau} \int_{\zeta'=1}^{\infty} \mathbf{G}_R(\zeta,\tau\,|\,\zeta',\tau') \int_{\eta'=0}^{\infty} \mathbf{G}_Z(\eta,\tau\,|\,\eta',\tau')\, g(\zeta',\eta',\tau')\, d\eta'\, \zeta' d\zeta' d\tau'. \tag{5.32}$$

Equations (5.28)–(5.32) provide the general solution to the 2-D temperature-transient problem in cylindrical coordinates.

5.4 One-dimensional radial disturbance

5.4.1 Green's function-based thermal disturbance

In this section we focus on the radial aspects of the drilling disturbance, the dominant mode of the thermal disturbance in most situations. The initial condition $F(\zeta,\eta)$ is set at a time prior to the onset of drilling and is thus equivalent to the undisturbed temperature field. Unless a borehole is drilled in a very special topographic location (e.g., the top of a mountain), the initial temperature distribution is unlikely to have a significant radial dependence. We are thus reasonably safe assuming that the initial temperature field is independent of ζ and can be regarded as a constant (F_η) at any depth η. The radial temperature disturbance caused by drilling is then defined by the difference between the temperature at time τ and the initial undisturbed value,

$$\Delta T_{\mathrm{d}}(\zeta,\tau) \;=\; T(\zeta,\tau) \;-\; F_\eta\,. \tag{5.33}$$

To proceed, we assume the BC at the borehole wall (surface S_1) can be expressed in one of the following forms for the three types of BCs,

$$f_1(\tau) \;=\; \left[\begin{array}{lcll} T(\tau)|_{S_1} & = & F_\eta + \Delta T_\star\,\theta(\tau) & \text{T-BC} \\ q(\tau)|_{S_1} & = & q_\star\,\vartheta(\tau) & \text{Q-BC} \\ h\,T_f(\tau) & = & h\left[F_\eta + \Delta T_\star\,\varphi(\tau)\right]. & \text{C-BC} \end{array}\right. \tag{5.34}$$

Thus for a prescribed temperature BC, the temperature change at the borehole wall is given by the product of a scaling temperature $\Delta T_\star$ that describes the characteristic magnitude of the change and a dimensionless function $\theta(\tau)$ that encapsulates the time-dependence. Similarly, $q_\star$ is a scaling heat flux while $\vartheta(\tau)$ and $\varphi(\tau)$ are dimensionless functions describing the time-dependence of the heat flux and convective BCs. The thermal effect due to boundary condition $f_1(\tau)$ then consists of two components, one due to the initial temperature field and the other due to the drilling disturbance,

$$T_{\mathrm{bc}}(\zeta,\tau) \;=\; T_{\mathrm{bco}}(\zeta,\tau) \;+\; T_{\mathrm{bc}\Delta}(\zeta,\tau). \tag{5.35}$$

Referring to eq. (5.13), the portion due to the initial temperature F_η is,

$$T_{\mathrm{bco}}(\zeta,\tau) \;=\; \left[\begin{array}{ll} F_\eta \displaystyle\int_{\tau'=0}^{\tau} \left[\frac{\partial \mathbf{G}_R}{\partial \zeta'}\right]_{\zeta'=1} d\tau' & \text{T-BC} \\ 0 & \text{Q-BC} \\ Bi\;F_\eta \displaystyle\int_{\tau'=0}^{\tau} \mathbf{G}_R(\zeta,\tau\,|\,\zeta',\tau')|_{\zeta'=1}\,d\tau'. & \text{C-BC} \end{array}\right. \tag{5.36}$$

Next, we separate the heat-production function into its short- and long-term components,

$$g(\zeta,\tau) \;=\; g_s(\zeta,\tau) \;+\; g_l(\zeta,\tau). \tag{5.37}$$

Here, the short-term component $g_s(\zeta,\tau)$ operates on timescales less than or comparable to that associated with the drilling disturbance (τ_d) while the timescale for the long-term component $g_l(\zeta,\tau)$ is much greater than τ_d. Radiogenic heating in rock and basal shear heating in ice are examples of sources that would contribute to g_l while latent-heat effects

in permafrost would contribute to g_s. The thermal effect due to the heat-production term (5.14) can then be separated into its short- and long-term components,

$$T_{\mathrm{g}}(\zeta,\tau) \;=\; T_{\mathrm{gs}}(\zeta,\tau) \;+\; T_{\mathrm{gl}}(\zeta,\tau). \tag{5.38}$$

With the BC in the form of (5.34), we are able to examine the solution to simple steady-state problems using the general 1-D radial temperature solution (5.11)–(5.14). This examination yields the following useful relationship that holds for all three types of boundary condition,

$$F_\eta \;=\; T_{\mathrm{ic}}(\zeta,\tau) \;+\; T_{\mathrm{bco}}(\zeta,\tau) \;+\; T_{\mathrm{gl}}(\zeta,\tau)\,. \tag{5.39}$$

Substituting (5.34)–(5.39) into the 1-D radial temperature solution, the radial drilling disturbance is found to consist of two terms, one due to the thermal effect of the disturbance at the borehole wall and the other due to the effect of short-term heat production,

$$\Delta T_{\mathrm{d}}(\zeta,\tau) \;=\; T_{\mathrm{bc}\Delta}(\zeta,\tau) \;+\; T_{\mathrm{gs}}(\zeta,\tau)\,. \tag{5.40}$$

As expected, the drilling disturbance is independent of all terms related to the initial condition and to long-term heat production. The thermal effect due to the disturbance at the wall is given by,

$$T_{\mathrm{bc}\Delta}(\zeta,\tau) \;=\; \begin{cases} \Delta T_\star \displaystyle\int_{\tau'=0}^{\tau} \left[\frac{\partial \mathbf{G}_R(\zeta,\tau|\zeta',\tau')}{\partial\zeta'}\right]_{\zeta'=1} \theta(\tau')\,d\tau' & \text{T-BC} \\ \left(\dfrac{a\,q_\star}{K}\right) \displaystyle\int_{\tau'=0}^{\tau} \mathbf{G}_R(\zeta,\tau\,|\,\zeta',\tau')|_{\zeta'=1}\;\vartheta(\tau')\,d\tau' & \text{Q-BC} \\ Bi\;\Delta T_\star \displaystyle\int_{\tau'=0}^{\tau} \mathbf{G}_R(\zeta,\tau\,|\,\zeta',\tau')|_{\zeta'=1}\;\varphi(\tau')\,d\tau'. & \text{C-BC} \end{cases} \tag{5.41}$$

A borehole drilled into ice-rich permafrost may constitute a situation for which the short-term heat-production term $g_s(\zeta,\tau)$ is important. In this case, it is common for the interstitial ice to melt near the borehole while it is being drilled and then refreeze during the recovery phase. The phase change can be treated as a moving-plane heat source (or sink) located at the solid-liquid interface [*Özişik*, 1980]. For the 1-D radial case, the moving source can be expressed by,

$$g_s(\zeta,\tau) \;=\; \frac{\kappa\, S_r \phi\, \rho_i L_f}{a^2}\,\frac{\partial\sigma}{\partial\tau}\,\delta[\zeta-\sigma(\tau)], \tag{5.42}$$

where ϕ is the porosity, ρ_i is the density of ice, L_f is the latent heat of fusion for ice, S_r is the fractional saturation of the pores, $\sigma(\tau)$ is the location of the phase boundary (in dimensionless radial coordinates), and δ is the Dirac delta function. Substituting $g_s(\zeta, \tau)$ into (5.14), the short-term heat production effect for permafrost is,

$$T_{\mathrm{gs}}(\zeta, \tau) \;=\; \frac{\kappa\, S_r \phi\, \rho_i L_f}{K} \int_{\tau'=0}^{\tau} \mathbf{G}_R(\zeta, \tau \,|\, \zeta', \tau')|_{\zeta'=\sigma(\tau')} \; \frac{\partial \sigma(\tau')}{\partial \tau}\, \sigma(\tau')\, d\tau'. \tag{5.43}$$

This expression can also be used to estimate the thermal effect of the moving-phase boundary at the edge of hot-water holes drilled into glaciers and ice sheets by letting $S_r \phi = 1$. The remaining unknown, the location of the phase-boundary $\sigma(\tau)$, can be found from the condition that on the interface,

$$T_{\mathrm{m}} \;=\; F_\eta \;+\; T_{\mathrm{bc}\Delta}(\sigma, \tau) \;+\; T_{\mathrm{gs}}(\sigma, \tau), \tag{5.44}$$

where T_{m} is the melting temperature.

When the short-term heat production effect T_{gs} is negligible, eqs (5.40) and (5.41) show that the *magnitude* of the radial drilling disturbance ΔT_{d} is directly related to $\Delta T_\star$ for the prescribed temperature BC, to $(a\, q_\star / K)$ for the prescribed heat-flux BC, and to $(Bi\, \Delta T_\star)$ for the convective BC. The *dissipation* of the disturbance ΔT_{d} over time is directly related to the integral of the dimensionless functions $\theta(\tau)$, $\vartheta(\tau)$, $\varphi(\tau)$ over time, weighted by the appropriate GF (or $\partial \mathbf{G}_R / \partial \zeta'$ for a prescribed temperature BC). These relationships are more complicated in situations where a significant heat-production term $g_s(\zeta, \tau)$ exists such as in ice-rich permafrost.

5.4.2 Applications

We illustrate the radial drilling disturbance with three synthetic examples, all of which involve time-dependent BCs. For the pure radial models presented in this section, we let $\tau = 0$ when the drill bit first reaches the depth of interest. During the recovery phase, the time since borehole completion is $\delta\tau = (\tau - \tau_s)$ where τ_s is the duration of drilling and circulation.

5.4.2.1 Uniformly drilled borehole

The first example (model UNI) focuses on conditions at the 500-m depth while drilling a 23.2-cm diameter borehole to 3000 m using a conventional rotary drill with direct fluid

circulation. Drilling at a uniform rate (50 m day^{-1}), the borehole is completed in 60 days. To estimate the fluid temperatures in the annulus between the drill pipe and the borehole wall, we use the *Szarka and Bobok* [2012] wellbore model for the entire drilling process. Necessary parameters include the temperature of the fluid entering the drill pipe at the surface (T_e), the pumping rate p, the formation surface temperature F_o, and the formation temperature gradient Γ. For this example, these parameters are set to $T_e = 10°\text{C}$, $p = 378$ liters min^{-1}, $F_o = -10°\text{C}$, and $\Gamma = 30$ K km^{-1}. Fluid temperatures at 500 m are initially 3.38 K warmer than the undisturbed formation temperature F_η when the drill bit first passes through this zone, they cool slightly over the next 2 days as drilling continues through formation rock cooler than T_e, and then they warm substantially, ultimately becoming 11.30 K warmer than the formation temperature on day 60 when drilling is completed and circulation ends (**Figure 5.1**). The temperature difference $T_f(\tau) - F_\eta$ is then used to define $\Delta T_\star \, \varphi(\tau)$ during the drilling phase assuming a convective BC at the borehole wall (**Figure 5.7a**). Although the value selected for the scaling temperature $\Delta T_\star$ is somewhat arbitrary, we set it here to the maximum fluid temperature differential ($T_f - F_\eta = 11.30$ K). During the recovery phase ($\tau > \tau_s$), the time-dependent function $\varphi(\tau)$ is set according to the condition that the heat flux at the borehole wall is approximately zero once the fluid circulation is terminated.

In this example the short-term heat production term $g_s(\zeta, \tau)$ is assumed to be zero, in which case the radial drilling disturbance is due solely to conditions at the borehole wall [$\Delta T_\text{d}(\zeta, \tau) = T_{\text{bc}\Delta}(\zeta, \tau)$]. The thermal disturbance can then be found from the time-integral of $\varphi(\tau)$ weighted by the radial Green's function $\mathbf{G}_R|_{\zeta'=1}$ (eq. 5.41). With a Biot number $Bi = 10$, the disturbance at the wall for model UNI drops rapidly from its peak value (11.30 K) at the termination of drilling and then follows a logarithmic decline with time (**Figure 5.8**); the transition to logarithmic behavior occurs at roughly $(\delta\tau/\tau_s) = 10$. The disturbance at the wall diminishes to 1, 0.1, and 0.01 K at approximately $(\delta\tau/\tau_s) = 1.0$, 13, 140, respectively. For a 23.2-cm diameter petroleum well, these times correspond to 50, 670, 6960 days after borehole completion assuming a nominal thermal diffusivity of $\kappa = 1 \times 10^{-6}$ m^2 s^{-1}; the corresponding times for the thermal disturbance to reach these levels would be 22 times less for a 5-cm diameter hole due to the presence of a^2 in the definition of dimensionless time τ (eq. 5.9).

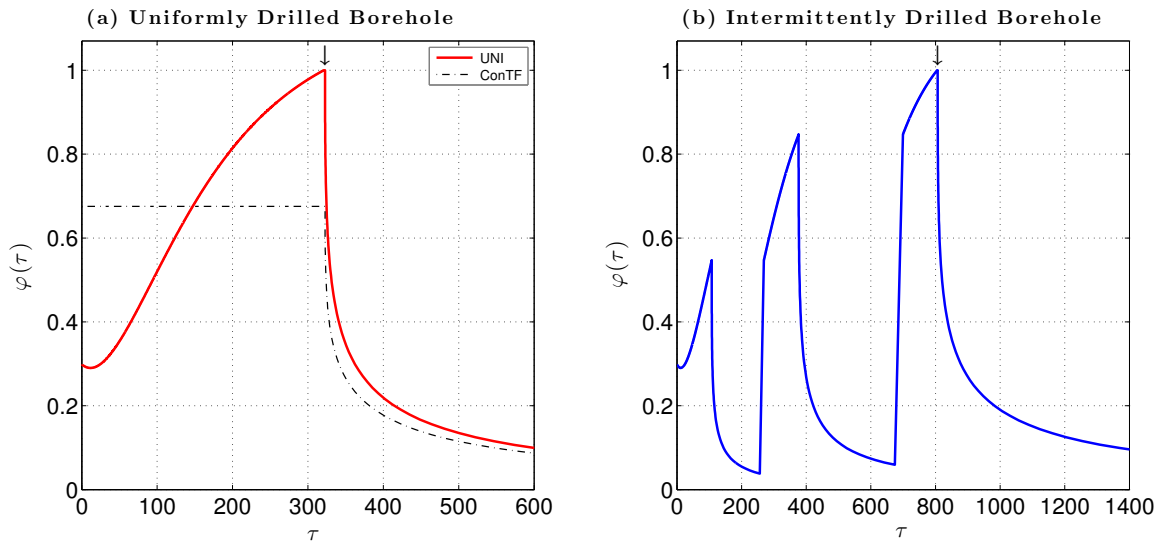

Figure 5.7: Dimensionless function $\varphi(\tau)$ describing the time dependence of the convective BC in the uniformly drilled (model UNI) and intermittently drilled (model INT) radial disturbance examples. Panel (a) shows $\varphi(\tau)$ for model UNI based on fluid temperatures from the *Szarka and Bobok* [2012] wellbore model (red line). Also shown is an equivalent 'constant temperature' model (ConTF, dashed line) in which $\varphi(\tau)$ during drilling is a constant equal to the mean φ-value of model UNI during this phase. Panel (b) shows $\varphi(\tau)$ for model INT. Borehole completion occurs at dimensionless time $\tau_s = 323$ for model UNI and $\tau_s = 806$ for model INT (arrows).

It is often assumed that temperatures at the borehole wall are nearly constant during the drilling phase. To examine the impact of this assumption, the thermal disturbance for an equivalent 'constant temperature' model (ConTF) was determined. For model ConTF, $\Delta T_\star\, \varphi(\tau)$ is a constant set to yield the same mean fluid temperature T_f as model UNI during the drilling phase; during recovery, $\varphi(\tau)$ is again set to the condition that the heat flux is approximately zero once circulation has ended (**Figure 5.7a**). The ratio of the thermal disturbance calculated with models UNI and ConTF shows that the drilling disturbance is significantly different between the two models (up to a factor of 2) at the onset of the recovery phase due to the timing difference of heat deposition in the formation (**Figure 5.8b**). Strong differences persist between the models until $(\delta\tau/\tau_s) \sim 1$ and then diminish to near-zero by $(\delta\tau/\tau_s) \sim 10$.

For a convective BC, temperatures at the borehole wall are controlled by the efficiency of heat transfer across the fluid boundary layer adjacent to the wall and by heat conduction into the medium surrounding the hole. This control is incorporated into the

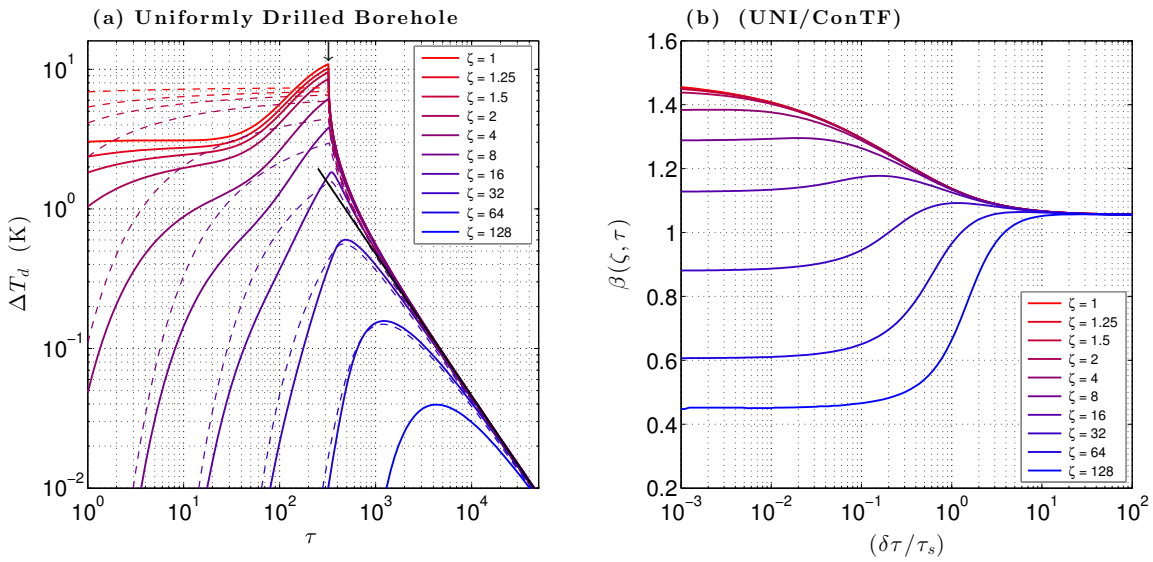

Figure 5.8: Panel (a) shows the drilling disturbance at 500 m for a uniformly drilled 3000 m borehole (model UNI, solid lines) assuming a convective BC with Biot number $Bi = 10$. Dashed lines show the disturbance for the 'constant' temperature model (model ConTF). Diagonal line indicates a logarithmic decline with time. Panel (b) shows the ratio β of the drilling disturbance during the recovery phase calculated with time-dependent model UNI to that determined with the constant temperature model ConTF.

GF solution through the dimensionless Biot number Bi. Large Bi values are expected to produce wall temperatures close to the mean fluid temperature T_f and large drilling disturbances as a consequence. This dependence on the Biot number is confirmed when model UNI is used to calculate the drilling disturbance for a wide range of Bi numbers (**Figure 5.9a**). The magnitude of the thermal disturbance reveals three different regimes: (i) when $Bi < 0.1$, the magnitude of the drilling disturbance is linearly dependent on the Biot number (**Figure 5.9b**). In this regime, conductive heat transfer in the formation is much more effective than convective heat transfer across the fluid boundary layer. (ii) When $Bi > 10$, the drilling disturbance is both large and insensitive to the Biot number. In this regime, convective heat transfer in the fluid is much more efficient than conductive heat transfer in the formation. The prescribed temperature BC corresponds to this regime in the limit $Bi \to \infty$. (iii) A transitional regime ($0.1 < Bi < 10$) occurs when both convective and conductive heat transfer provide important controls on the wall temperature. As the thermal conductivity is roughly the same (order of magnitude level) for most geophysical applications, the primary controls on the Biot number are the heat-transfer coefficient of

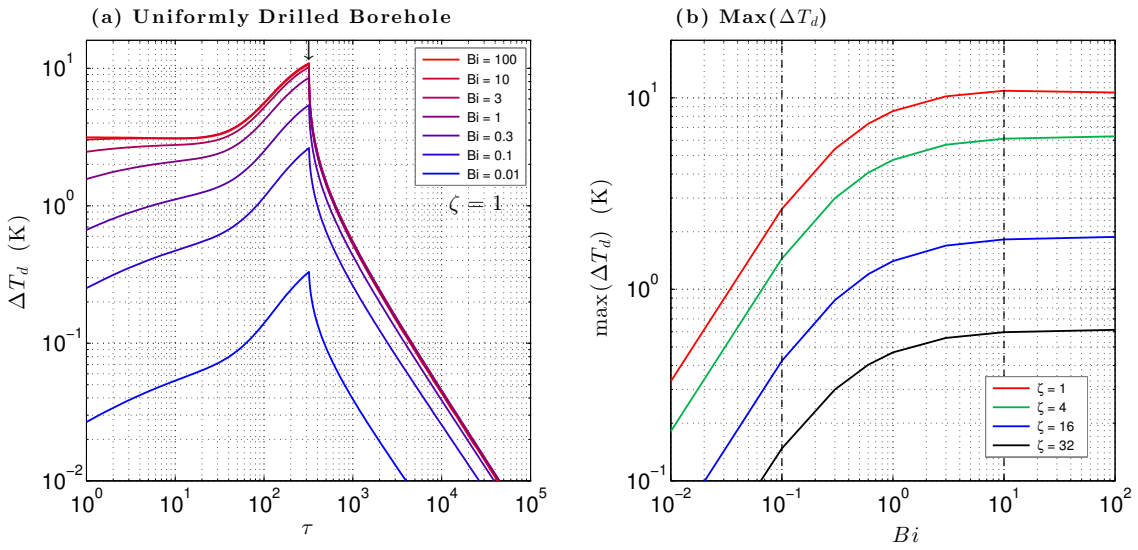

Figure 5.9: Sensitivity of the drilling disturbance at the borehole wall to the Biot number for model UNI (a). Panel (b) shows the magnitude of the drilling disturbance as a function of Bi. The behavior indicates the existence of 3 regimes in the Green's function solution: (i) small Biot number ($Bi < 0.1$), (ii) large Biot number ($Bi > 10$), and (iii) transitional ($0.1 < Bi < 10$).

the fluid (h) and the borehole radius a. Thus, the small Biot number regime ($Bi < 0.1$) is likely to occur when fluid flow is laminar (or stagnant) and/or the borehole diameter is very small. Conversely, the large Biot number regime ($Bi > 10$) is associated with fully turbulent fluid flow and/or very large borehole diameters.

5.4.2.2 Intermittently drilled borehole

The second radial example is provided by model INT which is used to illustrate the radial drilling disturbance for an intermittently drilled borehole. Model INT is the same as UNI except that the drilling is accomplished in three distinct phases separated by two suspension periods, resulting in a more complicated BC (**Figure 5.7b**). The suspensions extend the time before the borehole is completed to $\tau_s = 806$. **Figure 5.10a** shows the drilling disturbance for the intermittent drilling model along with the uniformly drilled borehole (model UNI) modified to the have the same completion time. Although the intermittent and uniform models produce very different thermal disturbances during the drilling phase, close to the borehole wall ($\zeta < 2$) the disturbances are very similar (within a few percent) during the recovery phase (**Figure 5.10b**). In contrast, the effect of the drilling suspensions is strongly experienced farther from the borehole during the recovery

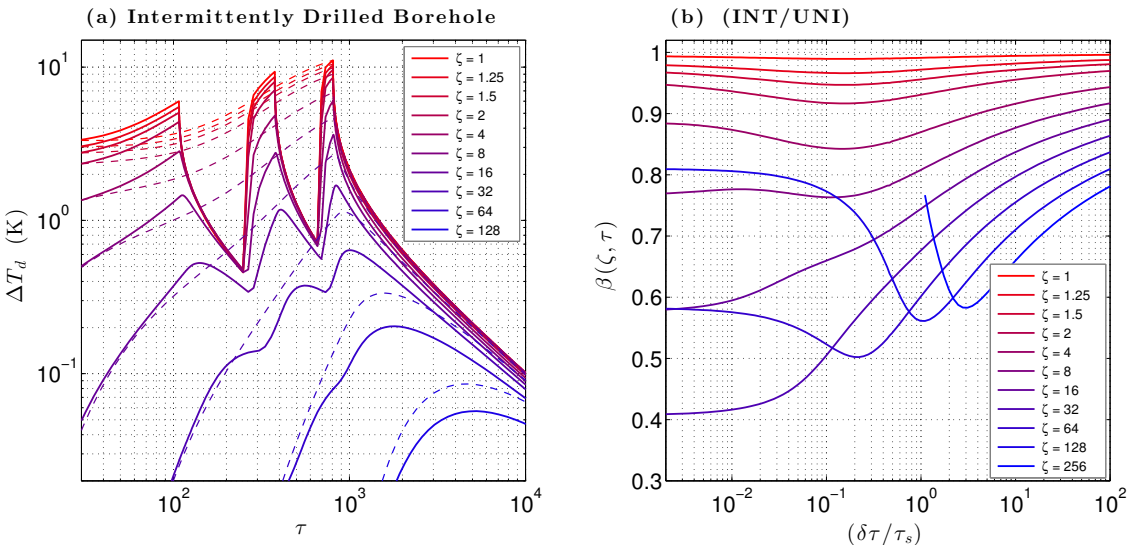

Figure 5.10: Panel (a) shows the drilling disturbance at 500 m for an intermittently drilled borehole (model INT) using a convective BC with $Bi = 10$ (solid lines). Dashed lines show the disturbance for a uniformly drilled borehole (model UNI) modified to have the same completion time ($\tau_s = 806$). Panel (b) shows the ratio β of the drilling disturbance during the recovery phase calculated with the intermittent model INT to that determined with the uniform model UNI.

due to the delay in propagation of the boundary signal away from the hole. The thermal disturbance of the intermittently drilled borehole is half that of the uniformly drilled hole in the radial zone $\zeta = 16$ to 64, at least for recovery times $(\delta\tau/\tau_s) < 1$. The difference between the models is smaller at greater radial distances as the details of the changes at the borehole wall tend to be filtered by the intervening material. Although the two models converge at large times, differences of 10–20% still exist at $(\delta\tau/\tau_s) \sim 100$ for radial distances $\zeta > 8$.

5.4.2.3 Borehole drilled in ice-rich permafrost

The final radial example (model PERMA) involves drilling a 3000-m borehole through ice-rich permafrost at a uniform rate. We use the same drilling and formation parameters as those used for radial model UNI, although here we focus on the 200-m depth where the undisturbed formation temperature is -4°C. In addition, the dimensionless function $\varphi(\tau)$ is modified slightly from model UNI so that temperatures at the borehole wall remain at the melting point during the phase transition. In this example, the melting temperature is assumed to be 0°C, the porosity ϕ is 30%, the pores are fully saturated ($S_r = 1$), the thermal

diffusivity is $\kappa = 1 \times 10^{-6}$ m^2 s^{-1}, and the thermal conductivity is $K = 2.2$ W m^{-1} K^{-1}. **Figure 5.11a** shows the temperature components (F_η, $T_{\mathrm{bc}\Delta}$, T_{gs}) shortly after the drill has passed the 200-m depth and the relatively warm drilling fluid has caused interstitial ice to melt near the borehole. The sum of the components ($T = F_\eta + T_{\mathrm{bc}\Delta} + T_{\mathrm{gs}}$) is equal to the melting temperature T_{m} at the phase boundary as required by eq. (5.44). In addition, the shape of the source term $T_{\mathrm{gs}}(\zeta, \tau)$ guarantees that the difference between the conductive heat fluxes on the liquid and solid sides of the phase-change interface equals the latent-heat flux there,

$$q_c^{\mathrm{liq}} - q_c^{\mathrm{solid}} \;=\; \frac{\kappa\, S_r \phi\, \rho_i L_f}{a} \left(\frac{\partial \sigma}{\partial \tau} \right). \tag{5.45}$$

With the drilling and formation parameters utilized in this example, the zone of melting continues to expand until $\tau = 370$ which occurs shortly after the drilling and circulation phases have concluded ($\tau_s = 361$). At this time, the melt extends from the borehole wall to radial distance $\zeta = 7.5$ (**Figure 5.11b**). Interstitial water then refreezes as temperatures at the borehole wall cool. It takes approximately $2\tau_s$ for all the interstitial water to refreeze, substantially increasing the duration of the thermal disturbance (**Figure 5.11c**). Comparing the drilling disturbance for ice-rich permafrost with (model PERMA) and without (model PERMA-noLH) latent-heat effects confirms the importance of the ice phase-change for this material. During the recovery phase, liberation of latent heat amplifies the drilling disturbance by up to a factor of 4 at $(\delta\tau/\tau_s) \sim 2$ (**Figure 5.11d**). Although the amplification diminishes with time, the drilling disturbance including latent-heat effects is still up to 50% larger at $(\delta\tau/\tau_s) = 10$ and 25% larger at $(\delta\tau/\tau_s) = 100$ than it is if latent-heat effects are neglected.

5.5 Two-dimensional drilling disturbance

5.5.1 Green's function-based thermal disturbance

The development of expressions for the 2-D drilling disturbance is very similar to that used for the 1-D radial disturbance in Section 5.4. Once again, the initial temperature field is assumed to be independent of radial position so that $F(\zeta, \eta) = F(\eta)$. The drilling disturbance is then defined by the difference between the temperature $T(\zeta, \eta, \tau)$ and the initial temperature field,

$$\Delta T_{\mathrm{d}}(\zeta, \eta, \tau) \;=\; T(\zeta, \eta, \tau) \;-\; F(\eta). \tag{5.46}$$

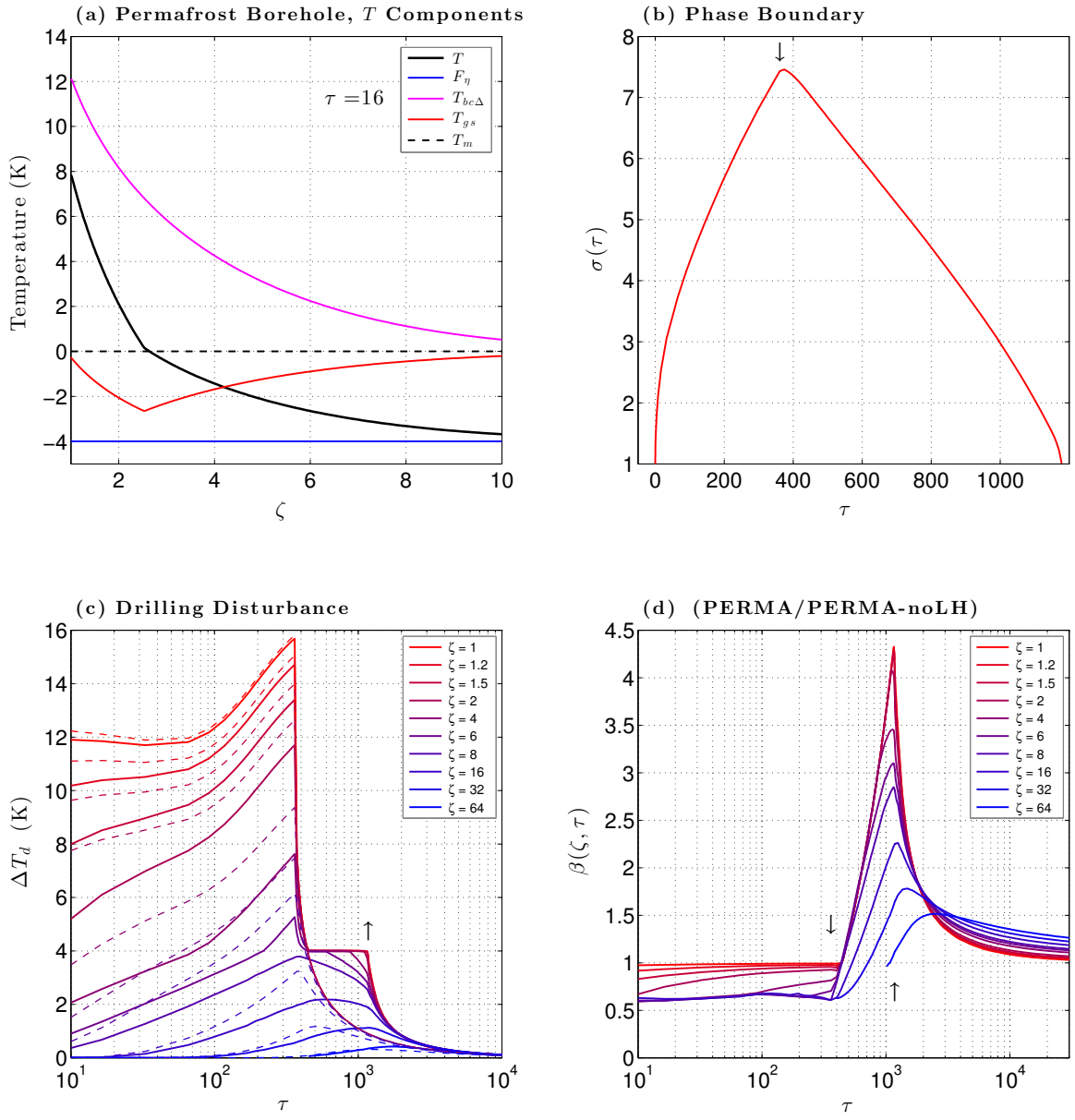

Figure 5.11: Latent-heat effects in ice-rich permafrost (model PERMA). Panel (a) shows the temperature distribution $T(\zeta,\tau)$ at $\tau = 16$ shortly after drilling begins (black line), and its components F_η, $T_{\mathrm{bc}\Delta}(\zeta,\tau)$, and $T_{\mathrm{gs}}(\zeta,\tau)$. Dashed line shows the melting temperature T_{m}. The migration of the phase-change interface $\sigma(\tau)$ is shown in (b). Panel (c) shows the drilling disturbance with the inclusion of latent-heat effects ($\Delta T_{\mathrm{d}} = T_{\mathrm{bc}\Delta} + T_{\mathrm{gs}}$). Also shown is the disturbance if latent-heat effects are ignored ($\Delta T_{\mathrm{d}} = T_{\mathrm{bc}\Delta}$, dashed lines, model PERMA-noLH). The ratio of the drilling disturbance with latent-heat effects to that if latent-heat effects are neglected is shown in (d). Down-arrows in all panels indicate the completion of the drilling and circulation phases ($\tau = 361$) while up-arrows indicate when the interstitial water has completely refrozen ($\tau = 1178$).

Boundary conditions at the borehole wall (surface S_1) and earth's surface (S_2) are given by,

$$f_1(\eta,\tau) \;=\; \begin{cases} T(\eta,\tau)|_{S_1} = F(\eta) \;+\; \Delta T_{1\star}\,\theta(\eta,\tau) & \text{T-BC} \\ q(\eta,\tau)|_{S_1} \;= q_\star \vartheta(\eta,\tau) & \text{Q-BC} \\ hT_f(\eta,\tau) \;= h\,[F(\eta) \;+\; \Delta T_{1\star}\varphi(\eta,\tau)] & \text{C-BC} \end{cases} \tag{5.47}$$

$$f_2(\zeta,\tau) \;=\; T(\zeta,\tau)|_{S_2} = F_o \;+\; \Delta T_{2\star}\,\omega(\zeta,\tau) \qquad \text{T-BC} \tag{5.48}$$

where $\Delta T_{1\star}$ is the characteristic magnitude of the temperature change at the borehole wall, $q_\star$ is the scaling heat flux at the wall, and θ, ϑ, φ are dimensionless functions describing the time- and depth-dependencies of boundary condition $f_1(\eta,\tau)$. Construction of drilling pads, mud pits, and permanent drilling structures disrupt the natural landscape and thereby create a thermal disturbance on the surface near many boreholes. This drilling-related disturbance results from a change in the surface energy balance in the area near the borehole due to a change in surface albedo, change in cold-season snow depth, and other factors. Terms appearing in boundary condition $f_2(\zeta,\tau)$ include the initial surface temperature $F_o = F(0)$ and the characteristic temperature change $\Delta T_{2\star}$ of the disturbed area. Dimensionless function $\omega(\zeta,\tau)$ describes the variation of the surface disturbance with radial position and time. With BCs in the form of eqs (5.47) and (5.48), the thermal effect due to the BCs consists of two components,

$$T_{\text{bc1}}(\zeta,\eta,\tau) \;=\; T_{\text{bc1o}}(\zeta,\eta,\tau) \;+\; T_{\text{bc1}\Delta}(\zeta,\eta,\tau) \tag{5.49}$$

$$T_{\text{bc2}}(\zeta,\eta,\tau) \;=\; T_{\text{bc2o}}(\zeta,\eta,\tau) \;+\; T_{\text{bc2}\Delta}(\zeta,\eta,\tau) \tag{5.50}$$

where the part due to the initial temperature field is,

$$T_{\text{bc1o}}(\zeta,\eta,\tau) \;=\; \begin{cases} \displaystyle\int_{\tau'=0}^{\tau} \left[\frac{\partial \mathbf{G}_R}{\partial \zeta'}\right]_{\zeta'=1} \int_{\eta'=0}^{\infty} \mathbf{G}_Z(\eta,\tau\,|\,\eta',\tau')\; F(\eta')\, d\eta'\, d\tau' & \text{T-BC} \\ 0 & \text{Q-BC} \\ Bi \displaystyle\int_{\tau'=0}^{\tau} \mathbf{G}_R(\zeta,\tau|\zeta',\tau')|_{\zeta'=1} \int_{\eta'=0}^{\infty} \mathbf{G}_Z(\eta,\tau|\eta',\tau') F(\eta')\, d\eta' d\tau' & \text{C-BC} \end{cases} \tag{5.51}$$

$$T_{\text{bc2o}}(\zeta,\eta,\tau) \;=\; \frac{F_o}{\alpha^2} \int_{\tau'=0}^{\tau} \left[\frac{\partial \mathbf{G}_Z}{\partial \eta'}\right]_{\eta'=0} \int_{\zeta'=1}^{\infty} \mathbf{G}_R(\zeta,\tau\,|\,\zeta',\tau')\; \zeta' d\zeta' d\tau'. \qquad \text{T-BC} \tag{5.52}$$

Once again the heat-production term is separated into its short- and long-term components ($g = g_s + g_l$), resulting in a two-component thermal effect,

$$T_{\text{g}}(\zeta,\eta,\tau) \;=\; T_{\text{gs}}(\zeta,\eta,\tau) \;+\; T_{\text{gl}}(\zeta,\eta,\tau). \tag{5.53}$$

Consideration of simple 2-D steady-state problems then yields the following relationship that holds for all three types of BCs,

$$F(\eta) \;=\; T_{\mathrm{ic}}(\zeta,\eta,\tau) \;+\; T_{\mathrm{bc1o}}(\zeta,\eta,\tau) \;+\; T_{\mathrm{bc2o}}(\zeta,\eta,\tau) \;+\; T_{\mathrm{gl}}(\eta). \tag{5.54}$$

Substitution of (5.47)–(5.54) into the general 2-D temperature solution (5.28)–(5.32) yields the 2-D drilling disturbance which is now found to consist of three terms,

$$\Delta T_{\mathrm{d}}(\zeta,\eta,\tau) \;=\; T_{\mathrm{bc1}\Delta}(\zeta,\eta,\tau) \;+\; T_{\mathrm{bc2}\Delta}(\zeta,\eta,\tau) \;+\; T_{\mathrm{gs}}(\zeta,\eta,\tau). \tag{5.55}$$

The thermal effect due to the heating (or cooling) at the borehole wall ($T_{\mathrm{bc1}\Delta}$) and that due to the drilling-related disturbance on the earth's surface ($T_{\mathrm{bc2}\Delta}$) are given by,

$$T_{\mathrm{bc1}\Delta}(\zeta,\eta,\tau) \;=\; \begin{cases} \Delta T_{1\star} \displaystyle\int_{\tau'=0}^{\tau} \left[\frac{\partial \mathbf{G}_R}{\partial \zeta'}\right]_{\zeta'=1} \int_{\eta'=0}^{\infty} \mathbf{G}_Z(\eta,\tau\,|\,\eta',\tau')\,\theta(\eta',\tau')\,d\eta'\,d\tau' & \text{T-BC} \\ \dfrac{a\,q_\star}{K} \displaystyle\int_{\tau'=0}^{\tau} \mathbf{G}_R(\zeta,\tau|\zeta',\tau')|_{\zeta'=1} \int_{\eta'=0}^{\infty} \mathbf{G}_Z(\eta,\tau|\eta',\tau')\,\vartheta(\eta',\tau')d\eta'd\tau' & \text{Q-BC} \\ Bi\;\Delta T_{1\star} \displaystyle\int_{\tau'=0}^{\tau} \mathbf{G}_R(\zeta,\tau|\zeta',\tau')|_{\zeta'=1} \int_{\eta'=0}^{\infty} \mathbf{G}_Z(\eta,\tau|\eta',\tau')\,\varphi(\eta',\tau')d\eta'd\tau' & \text{C-BC} \end{cases} \tag{5.56}$$

$$T_{\mathrm{bc2}\Delta}(\zeta,\eta,\tau) \;=\; \frac{\Delta T_{2\star}}{\alpha^2} \int_{\tau'=0}^{\tau} \left[\frac{\partial \mathbf{G}_Z}{\partial \eta'}\right]_{\eta'=0} \int_{\zeta'=1}^{\infty} \mathbf{G}_R(\zeta,\tau|\zeta',\tau')\omega(\zeta',\tau')\zeta' d\zeta' d\tau'. \qquad \text{T-BC} \tag{5.57}$$

5.5.2 Two-dimensional applications

To illustrate the potential impact of vertical heat flow in the drilling-disturbance problem, we return to the first example of Section 5.4.2 (model UNI), i.e., drilling a 23.2-cm diameter borehole to 3000 m in 60 days using a conventional rotary drill. A convective condition is assumed to exist at the borehole wall. For the 2-D problem, we let $\tau = 0$ when the drill bit first penetrates the earth's surface. With this convention, drilling is completed and circulation terminated at $\tau_s = 387$ (60 drilling days + 6 hours of fluid circulation for well conditioning). Using $L = 10$ m for the vertical length scale, the maximum borehole depth is $\eta = 300$ and the ratio $\alpha = (L/a)$ is 86. As with other drilling technologies, the function $\varphi(\eta,\tau)$ representing conditions along the borehole wall is a strong function of both depth and time for this rotary drilling example (**Figure 5.12a**). Using the same drilling and formation parameters as model UNI, temperatures outside the wellbore warm

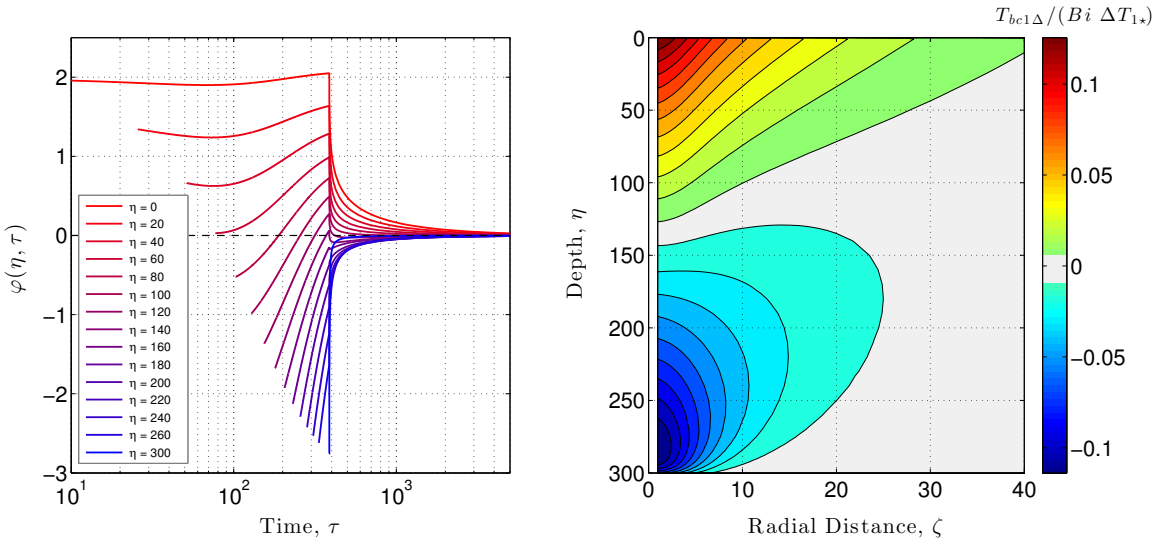

Figure 5.12: Panel (a) shows the dimensionless function $\varphi(\eta,\tau)$ representing conditions along the borehole wall for the 2-D applications presented in Section 5.5.2 based on fluid temperatures estimated with the *Szarka and Bobok* [2012] wellbore model. Drilling and formation parameters are the same as for model UNI (Section 5.4.2). Panel (b) shows a snapshot of the thermal drilling disturbance surrounding the well at $\tau = 390$ shortly after borehole completion ($\tau_s = 387$), assuming a convective BC with Biot number $Bi = 10$.

during drilling between the surface and $\eta = 130$, and cool at greater depths, as a result of the temperature contrast between the circulating drill fluid and the surrounding medium (**Figure 5.12b**). Thereafter, temperatures relax back to the initial state.

To assess the significance of vertical heat-transfer effects, we examine the ratio of the drilling disturbance found using the 2-D formulation (eqs 5.55–5.57) with that considering only the radial effects (eqs 5.40–5.43),

$$\beta_z(\zeta,\eta,\tau) \;=\; \frac{\Delta T_{\mathrm{d}}(\zeta,\eta,\tau)}{\Delta T_{\mathrm{d}}(\zeta,\tau)}. \tag{5.58}$$

Vertical effects are negligible when $\beta_z \approx 1$. Focusing solely on the disturbance due to heating and cooling at the borehole wall, we assume in this section that the boundary at the earth's surface remains undisturbed ($\Delta T_{2\star} = 0$) and the source term $g_s(\zeta,\eta,\tau)$ is zero. In this case, β_z reduces to,

$$\beta_z(\zeta,\eta,\tau) \;=\; \frac{\displaystyle\int_{\tau'=0}^{\tau} \mathbf{G}_R(\zeta,\tau\,|\,\zeta',\tau')|_{\zeta'=1} \left[\int_{\eta'=0}^{\infty} \mathbf{G}_Z(\eta,\tau\,|\,\eta',\tau')\;\varphi(\eta',\tau')\,d\eta'\right] d\tau'}{\displaystyle\int_{\tau'=0}^{\tau} \mathbf{G}_R(\zeta,\tau\,|\,\zeta',\tau')|_{\zeta'=1}\;\varphi(\eta,\tau')\,d\tau'} \tag{5.59}$$

for a convective BC and to similar expressions for the other two types of boundary condition. By inspection, vertical effects arise from the integral of $\varphi(\eta,\tau)$ along the borehole wall weighted by the vertical Green's function G_Z (term in brackets). In the special case where φ is independent of depth, the term in brackets can be solved analytically and (5.59) reduces to,

$$\beta_z(\zeta,\eta,\tau) = \frac{\int_{\tau'=0}^{\tau} \mathbf{G}_R(\zeta,\tau|\zeta',\tau')|_{\zeta'=1}\left[\operatorname{erf}\left(\frac{\alpha\,\eta}{2\sqrt{\tau-\tau'}}\right) - \frac{1}{2}\left\{1+\operatorname{erf}\left[\frac{\alpha\,(\eta-\eta_m)}{2\sqrt{\tau-\tau'}}\right]\right\}\right]\varphi(\tau')d\tau'}{\int_{\tau'=0}^{\tau} \mathbf{G}_R(\zeta,\tau\,|\,\zeta',\tau')|_{\zeta'=1}\;\varphi(\tau')\,d\tau'} \tag{5.60}$$

where η_m is the maximum depth of the borehole. This expression reveals the following limits,

$$\beta_z(\zeta,\eta,\tau) \;=\; \begin{cases} 0 & \text{for } \eta = 0 \\ 1 & \dfrac{4\sqrt{\tau-\tau_o}}{\alpha} \;<\; \eta \;<\; \eta_m - \dfrac{4\sqrt{\tau-\tau_o}}{\alpha} \\ 1/2 & \eta = \eta_m\,. \end{cases} \tag{5.61}$$

Thus strong vertical heat-transfer effects are expected near the earth's surface ($\eta = 0$) due to the presence of the upper boundary and near the bottom of the borehole (η_m) due to the finite depth of drilling; τ_o is the time when the drill reaches depth η. We emphasize that expression (5.60) results strictly from the geometry of the problem encapsulated by the vertical Green's function G_Z and does not consider the additional effect due to φ-variations along the borehole wall. Nevertheless, it indicates where strong vertical effects are likely to occur.

5.5.2.1 Thermal disturbance near the earth's surface

Information contained in temperature profiles at shallow depths is often used in climate studies, either to infer the magnitude of climate changes over the recent past (last few centuries) or to document the rate at which the earth's surface is currently warming. Thus, consideration of vertical heat-transfer effects near the earth's surface is potentially important when correcting borehole-temperature measurements for the drilling disturbance.

Near the earth's surface, β_z values determined with the exact expression (5.59) confirm that vertical heat-transfer effects are small ($\beta_z \approx 1$, **Figure 5.13**) and hence can be ignored at depths η greater than $4\sqrt{\tau-\tau_o}/\alpha$ as suggested by the limits in (5.61). However vertical

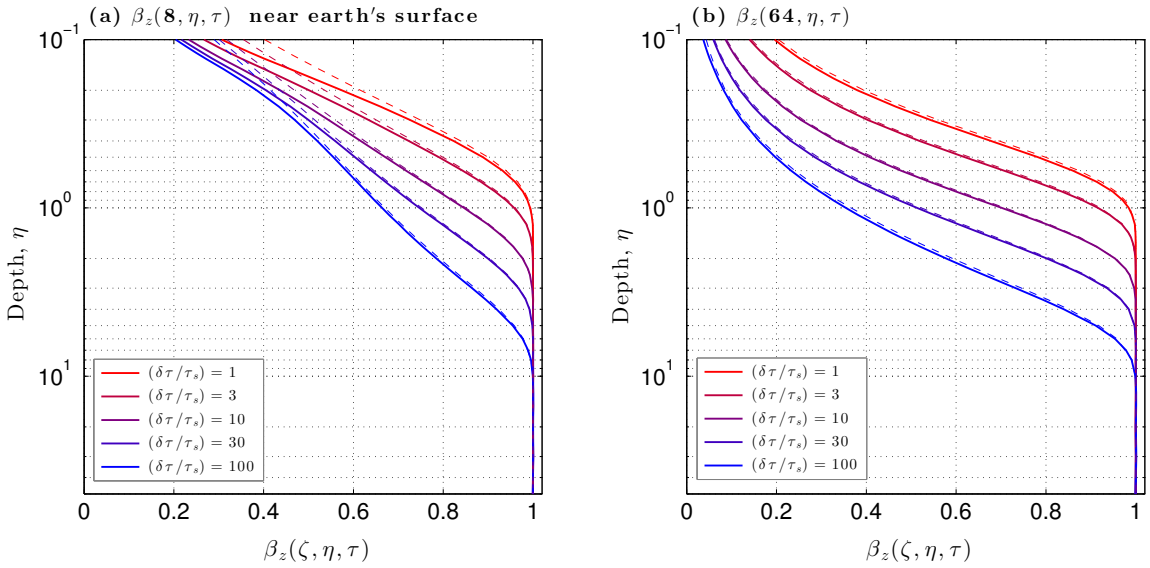

Figure 5.13: Ratio (β_z) of the drilling disturbance found using the 2-D formulation near the earth's surface with that considering only the radial effects. Panels (a) and (b) show β_z profiles at radial distances $\zeta = 8$ and 64, respectively, based on the exact expression (5.59). Dashed lines show β_z profiles calculated with the approximate expression that ignores φ-variations along the borehole wall (eq. 5.60).

effects are substantial at shallower depths, diminishing the drilling disturbance to zero at $\eta = 0$. Profiles of β_z calculated with the expression ignoring vertical φ-variations (eq. 5.60) are within a few percent of those calculated with the exact expression except close to the borehole very near the earth's surface ($\zeta < 16$, $\eta < 0.3$, **Figure 5.13**), demonstrating that the dominant source of vertical heat-transfer effects near the earth's surface is the geometry of the problem domain (i.e., the presence of the upper boundary).

Translating the results to dimensional depths, vertical heat-transfer effects are significant at depths less than 20 m one year after well completion for the 3000 m rotary-borehole example. This is probably of little consequence as the affected depths are entirely embedded within the zone of strong seasonal change. However, large boreholes similar to the one emulated by this example have been used to monitor contemporary climate change for the last 40 years [*Clow*, 2014]. Ten years after these wells were drilled, vertical heat-transfer significantly affected the drilling disturbance from the surface to the 70 m depth. After 40 years, the drilling disturbance was significantly affected to the 140 m depth. As this range of depths encompasses those of interest for climate change studies, the 2-D drilling disturbance equations accounting for vertical heat-transfer effects should be utilized in

these studies.

5.5.2.2 Thermal disturbance near the bottom of a borehole

The situation near the bottom of the example borehole is quite dynamic with $\varphi(\eta, \tau)$ and the duration of fluid circulation varying rapidly with depth (**Figure 5.12a**). As a result, the expression for β_z ignoring φ-variations along the borehole wall (eq. 5.60) provides only a rough approximation to the exact solution (5.59). This is particularly true as time proceeds as the temperature at any location (ζ, η) depends on conditions along a greater extent of the borehole wall (the Green's function $\mathbf{G}_Z$ broadens with time). Results based on the exact expression confirm that vertical heat-transfer effects are important at heights $\Delta\eta = (\eta_m - \eta) < 4\sqrt{\tau - \tau_o}/\alpha$ above the bottom and that they reduce the drilling disturbance by half in the limit $\eta \to \eta_m$ (**Figure 5.14**). Thus for the 3000-m rotary borehole, vertical effects are important up to 5 m above the bottom 15 days ($\delta\tau = 100$) after well completion and up 15 m above the bottom 155 days ($\delta\tau = 1000$) after well completion.

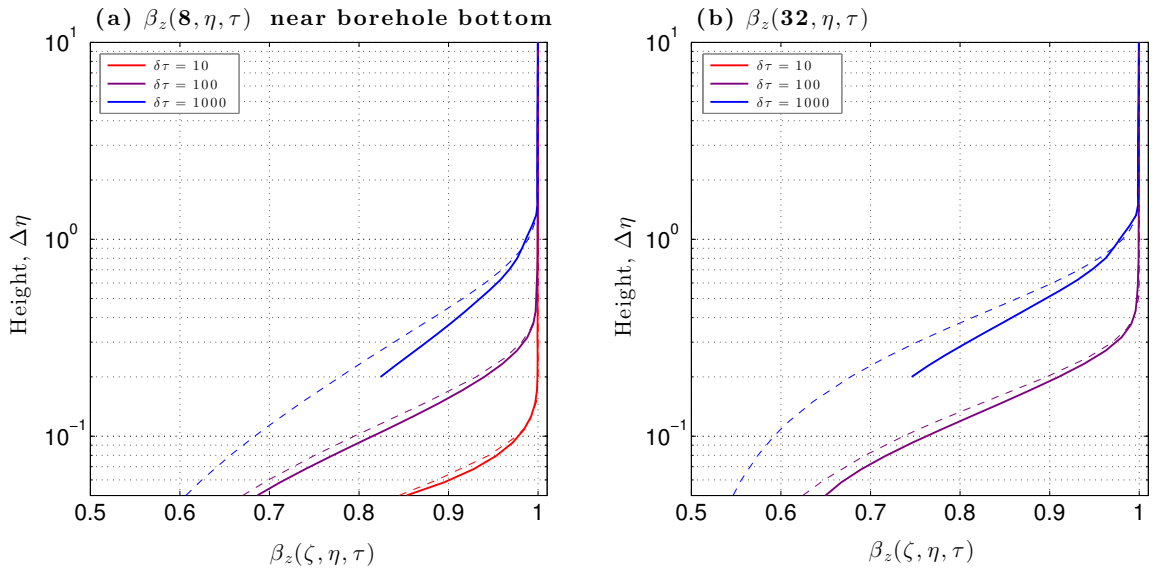

Figure 5.14: Ratio (β_z) of the drilling disturbance found using the 2-D formulation near the bottom of a borehole with that considering only the radial effects. Panels (a) and (b) show β_z as a function of height above bottom at radial distances $\zeta = 8$ and 32, respectively, based on the exact expression (5.59). Also shown are β_z profiles calculated with the expression ignoring φ-variations along the borehole wall (eq. 5.60, dashed lines).

5.6 Summary and conclusions

Analytical solutions for the thermal disturbance caused by drilling deep boreholes in rock or ice have been developed in 1-D (radial) and 2-D (radial and depth) cylindrical coordinates using a Green's function approach. Solutions are developed for three types of boundary conditions at the borehole wall: (i) prescribed temperature (Dirichlet), (ii) prescribed heat flux (Neumann), and (iii) a prescribed convective condition (Robin). These boundary conditions are allowed to be both depth- and time-dependent. Inclusion of the depth dimension in the 2-D solution allows vertical heat-transfer effects to be quantified in situations where they are potentially important, i.e., near the earth's surface, at the bottom of a well, and when considering finite drilling rates. The 2-D solution also includes a radial- and time-dependent boundary condition at the earth's surface to assess the impact of drilling-related infrastructure (drilling pads, mud pits, permanent shelters) on the subsurface temperature field. The drilling disturbance ΔT_d for the full 2-D problem is found to consist of three terms: (i) the thermal effect associated with the boundary condition at the borehole wall, (ii) the effect due to the boundary condition at the earth's surface, and (iii) the effect related to short-term heat production. An example of short-term heat production that may be important in certain situations is provided by the melting and subsequent refreezing of interstitial ice when drilling a borehole through ice-rich permafrost; the thermal contribution of this latent-heat effect to the drilling disturbance is developed. As expected, heat production terms operating on timescales much longer than the drilling disturbance do not contribute to ΔT_d.

Each of the three terms contributing to the 2-D drilling disturbance involves a radial Green's function $\mathbf{G}_R(\zeta, \tau | \zeta', \tau')$ and a vertical Green's function $\mathbf{G}_Z(\eta, \tau | \eta', \tau')$, both of which are developed in this paper. A simple analytical expression is found for $\mathbf{G}_Z$. In contrast, the integral expressions describing $\mathbf{G}_R$ for the three types of boundary condition at borehole wall cannot be solved analytically due to their complexity. Instead, a challenging numerical integration must be performed to evaluate $\mathbf{G}_R$. To eliminate the need to repeat these calculations, numerical values for $\mathbf{G}_R$ are made available through the Advanced Arctic Data and Information Service for all three types of boundary condition considered in this paper [*Clow*, 2015]. The salient equations describing the Green's function and drilling-disturbance solutions are summarized in **Table 5.2**.

Table 5.2: Equations describing the Green's function and drilling-disturbance solutions.

Nomenclature		Equations
Dimensionless coordinates:		
Radial	ζ	eq. (5.8)
Vertical	η	eq. (5.18)
Temporal	τ	eq. (5.9)
Green's functions:		
Radial	$\mathbf{G}_R$, $\partial\mathbf{G}_R/\partial\zeta'$	eqs (5.15) and (5.17)
Vertical	$\mathbf{G}_Z$, $\partial\mathbf{G}_Z/\partial\eta'$	eqs (5.26) and (5.27)
Drilling disturbance:		
1-D drilling disturbance	$\Delta T_\mathrm{d}(\zeta,\tau)$	eq. (5.40)
1-D thermal effect of borehole	$T_{\mathrm{bc}\Delta}(\zeta,\tau)$	eq. (5.41)
1-D latent-heat effect, permafrost	$T_\mathrm{gs}(\zeta,\eta)$	eq. (5.43)
2-D drilling disturbance	$\Delta T_\mathrm{d}(\zeta,\eta,\tau)$	eq. (5.55)
2-D thermal effect of borehole	$T_{\mathrm{bc1}\Delta}(\zeta,\eta,\tau)$	eq. (5.56)
2-D thermal effect of earth's surface	$T_{\mathrm{bc2}\Delta}(\zeta,\eta,\tau)$	eq. (5.57)

With the availability of the Green's functions, calculating the drilling disturbance for a wide range of situations is relatively straightforward as demonstrated by several applications:

(i) The effect of time-varying boundary conditions at the borehole wall, including those due to uniformly drilled and intermittently drilled boreholes using conventional rotary drills. The time-varying boundary condition associated with a uniformly drilled rotary borehole produces a thermal disturbance up to a factor of 2 different from that produced by the often-used 'constant' boundary condition, at least until $(\delta\tau/\tau_\mathrm{s}) \sim 1$ where τ_s is the duration of the drilling and circulation phases and $\delta\tau$ is the time since hole completion. The differences diminish to near-zero by $(\delta\tau/\tau_\mathrm{s}) \sim 10$. Comparison of the thermal disturbance caused by intermittently drilling a borehole with that due to drilling at a uniform rate without suspensions shows strong differences away from the wall. Although these differences diminish with time, differences of 10–20% still exist at $(\delta\tau/\tau_\mathrm{s}) \sim 100$.

(ii) The dependence of the drilling disturbance on the Biot number for a convective BC can be described by 3 regimes related to the relative efficiency of convective heat transfer in the fluid boundary layer adjacent to the wall as compared to conductive

heat transfer in the material surrounding the borehole. When the Biot number is small ($Bi < 0.1$), the drilling disturbance is linearly dependent on the Biot number. These conditions are associated with laminar (or stagnant) fluid flow and/or very small borehole diameters. The drilling disturbance is greatest when $Bi > 10$. This regime is associated with fully turbulent fluid flow and/or very large diameter boreholes. In this regime, ΔT_{d} is insensitive to the Biot number. The prescribed temperature BC corresponds to this case in the limit $Bi \to \infty$. A transitional regime ($0.1 < Bi < 10$) occurs when convective heat transfer in the borehole fluid and conductive heat transfer in the formation are both important for controlling the temperature at the borehole wall.

(iii) Latent-heat effects that occur when drilling a borehole through ice-rich permafrost strongly moderate the drilling disturbance away from the borehole wall during the drilling phase. During recovery, liberation of latent heat as interstitial ice refreezes amplifies the drilling disturbance by up to a factor of 4 at $(\delta\tau/\tau_s) \sim 2$ for typical permafrost conditions, and by 1.5 at $(\delta\tau/\tau_s) = 10$. A 25% amplification is still present at $(\delta\tau/\tau_s) = 100$.

(iv) Vertical heat-transfer effects are important near the earth's surface and near the bottom of a borehole, significantly reducing the drilling disturbance from that predicted by expressions based solely on radial heat transfer. Near the earth's surface, all depths $\eta < 4\sqrt{\tau - \tau_o}/\alpha$ are affected by vertical heat-transfer while near the bottom of a hole all depths $\eta > \eta_m - 4\sqrt{\tau - \tau_o}/\alpha$ are affected; τ_o is the time the drill reaches dimensionless depth η, η_m is the maximum depth of the hole, and α is the ratio of the vertical and radial length scales.

The flexibility of the Green's function approach is expected to allow the investigation of thermal drilling effects in rock or ice over both the drilling and recovery phases for a wide variety of drilling technologies, including conventional rotary drills, coiled tubing drills, hot-water drills, electromechanical drills, and electrothermal drills. One limitation of the current work is that the medium outside the borehole is assumed to be homogeneous and isotropic. Future work utilizing Galerkin-based Green's functions may remove this restriction.

5.7 References

Andaverde, J., Verma, S.P., and Santoyo, E. (2005), Uncertainty estimates of static formation temperatures in boreholes and evaluation of regression models, *Geophys. J. Int.*, 160, 1112–1122.

Ascencio, F., García, A., Rivera, J., and Arellano, V. (1994), Estimation of undisturbed formation temperatures under spherical-radial heat flow conditions, *Geothermics*, 23, 317–326.

Bassam, A., Santoyo, E., Andaverde, J., Hernández, J.A., and Espinoza-Ojeda, O.M. (2010), Estimation of static formation temperatures in geothermal wells by using an artificial neural network approach, *Comput. Geosci.*, 36, 1191–1199.

Beck, J.V., Cole, K.D., Haji-Sheikh, A., and Lithouhi, B. (1992), *Heat Conduction Using Green's Functions*, Hemisphere Publishing Corp., 523 pp.

Bullard, E.C. (1947), The time necessary for a borehole to attain temperature equilibrium, *Mon. Not. R. Astr. Soc. Geophys. Supp.*, 5, 127–130.

Clow, G.D. (2014), Temperature data acquired from the DOI/GTN-P Deep Borehole Array on the Arctic Slope of Alaska, 1973–2013, *Earth Syst. Sci. Data*, 6, 201–218.

Clow, G.D. (2015), Radial Green's functions used to correct borehole temperature measurements for the thermal disturbance caused by drilling, UCAR/NCAR–CISL–ACADIS, dataset, doi:10.5065/D64F1NS6.

Dansgaard, W., and Johnsen, S.J. (1969), A flow model and a time scale for the ice core from Camp Century, Greenland, *J. Glaciol.*, 8, 215–223.

Espinosa, G., Garcia, A., Hernández, I., and Santoyo, E. (2000), Comparative study of thermal behavior during drilling of geothermal wells using mud and air-water as drilling fluids, in *Proceedings World Geothermal Congress 2000*, pp. 4017–4022, Kyushu - Tohoku, Japan, May 28 – June 10, 2000.

Espinoza-Ojeda, O.M., Santoyo, E., and Andaverde, J. (2011), A new look at the statistical assessment of approximate and rigorous methods for the estimation of stabilized formation temperatures in geothermal and petroleum wells, *J. Geophys. Eng.*, 8, 233–258.

Fomin, S., Chugunov, V., and Hashida, T. (2003), Analytical modelling of the formation temperature stabilization during the borehole shut-in period, *Geophys. J. Int.*, 155, 469–478.

Garcia, A., Hernandez, I., Espinosa, G., and Santoyo, E. (1998), TEMLOPI: a thermal simulator for estimation of drilling mud and formation temperatures during drilling of geothermal wells, *Comput. Geosci.*, 24, 465–477.

Lachenbruch, A.H., and Brewer, M.C. (1959), Dissipation of the temperature effect of drilling a well in arctic Alaska, *USGS Bulletin 1083-C*, U.S. Geological Survey, 73–109,

Leblanc, Y., Pascoe, L.J., and Jones, F.W. (1981), The temperature stabilization of a borehole, *Geophysics*, 46, 1301–1303.

Lee, T.-C. (1982), Estimation of formation temperature and thermal property from dissipation of heat generated by drilling, *Geophysics*, 47, 1577–1584.

Middleton, M.F. (1979), A model for bottom-hole temperature stabilization, *Geophysics*, 44 1458–1462.

Nielsen, S.B., Balling, N., and Christiansen, H.S. (1990), Formation temperatures determined from stochastic inversion of borehole observations, *Geophys. J. Int.*, 101, 581–590.

Özişik, M.N. (1980), *Heat Conduction*, John Wiley & Sons, 687 pp.

Shen, P.Y., and Beck, A.E. (1986), Stabilization of bottom hole temperature with finite circulation and fluid flow, *Geophys. J. R. Astr. Soc.*, 86, 63–90.

Štulc, P. (1995), Return to thermal equilibrium of an intermittently drilled hole: theory and experiment, *Tectonophysics*, 241, 35–45.

Szarka, Z., and Bobok, E. (2012), Determination of the temperature distribution in the circulating drilling fluid, *Geosci. Eng.*, 1, 37–47.

Volkov, I.K., Chugunov, V.A., and Salamatin, A.N. (1988), Generalization of the method of integral correlations and its application to some heat transfer problems, *J. Sov. Math.*, 41, 1013–1029.

Wong-Loya, J.A., Andaverde, J., and Santoyo, E. (2012), A new practical method for the determination of static formation temperatures in geothermal and petroleum wells using a numerical method based on rational polynomial functions, *J. Geophys. Eng.*, 9, 711–728.

CHAPTER 6

ESTIMATING SUBSURFACE THERMAL EFFECTS CAUSED BY DRILL PADS, RESERVE PITS, AND THE OCEAN

6.1 Introduction

In Chapter 5 we alluded to potential subsurface thermal effects caused by drilling infrastructure in the form of drill pads, reserve pits, and permanent shelters. For the wells drilled in the NPR-A, no permanent structures other than the well heads were left after drilling was completed [*Schindler*, 1988]. To further rehabilitate the environment, materials were scraped from the thicker drill pads into the reserve pits after which the pads were seeded with a grass mix of Tundra Bluegrass, Arctared Fescue, Nugget Bluegrass, and annual rye. Despite these efforts, most or all of the original reserve pit still exists at most of the sites. In addition, the revegetation efforts were largely unsuccessful at the coastal sites, leaving a drill pad with a very different albedo from its surroundings during the summer and much thinner snow cover during the rest of the year due to wind scouring (**Figure 6.1**). As a result of this 'landscape' change, mean-annual temperatures immediately beneath the coastal drill pads tend to be colder than the nearby undisturbed tundra. In contrast, the reseeded vegetation for some of the inland sites tends to be much taller than the adjacent undisturbed tundra allowing it to capture and retain more snow during autumn, winter, and spring. Thicker snow cover leads to warmer mean-annual temperatures beneath these inland drill pads. The reserve pits are also expected to produce a warming effect, behaving in a similar way to shallow lakes which are warmer than the surrounding tundra on an annual average [*Lachenbruch et al.*, 1962]. Finally, many of the coastal wells are relatively close to the Beaufort Sea. Using a simplified model, *Lachenbruch* [1957] showed that the relatively warm temperatures of the Arctic Ocean ($\sim 0^{\circ}$C) should affect subsurface permafrost temperatures up to several hundred meters inland of a stationary shoreline.

Figure 6.1: Drew Point Test Well No. 1 on the Beaufort Sea coast, arctic Alaska. The ocean is moving inland approximately 19 m a^{-1} at this site [*Barnhart et al.*, 2014].

However, coastal erosion rates along the NPR-A section of the Beaufort Sea have been relatively high with a mean value of 5.6 m a^{-1} during 1955–2002 [*Jones et al.*, 2008]. Erosion rates along this coast have been accelerating due to an increased exposure to relatively warm ocean water and were up to 13.6 m a^{-1} by 2002–2007 [*Barnhart et al.*, 2014; *Jones et al.*, 2009a]. This rapid transgression is expected to reduce the effect of the ocean on inland permafrost temperatures.

Given the shape of the drill pads, reserve pits, and the Beaufort Sea coastline, a cartesian coordinate system is a more natural system in which to estimate the thermal effects than the cylindrical system used in Chapter 5. Here, a cartesian system is used to develop a general 3-D temperature solution to investigate the subsurface thermal disturbance associated drill pads, reserve pits, and the transgressing Arctic Ocean. The temperature logs acquired in the DOI/GTN-P boreholes can then be 'corrected' for these effects if they are sufficiently large.

6.2 Three-dimensional temperature solution

The development of a 3-D temperature solution in cartesian coordinates closely follows that used for the 2-D cylindrical solution presented in Chapter 5. The origin of the local coordinate system is located on the surface at the well head. The problem domain is infinite in the $\hat{x}$- and $\hat{y}$-directions parallel to the surface, and semi-infinite in the $\hat{z}$-direction (depth). A single boundary condition (BC) occurs at the earth's surface which is assumed to be a Type 1 BC (prescribed temperature). The complete 3-D temperature solution can be found from the superposition of three terms,

$$T(x,y,z,t) \;=\; T_{\rm ic}(x,y,z,t) \;+\; T_{\rm bc}(x,y,z,t) \;+\; T_{\rm g}(x,y,z,t), \tag{6.1}$$

in which $T_{\rm ic}$ is the thermal effect of the initial temperature field $F(x,y,z)$, $T_{\rm bc}$ is the effect of the BC at the earth's surface $f(x,y,t)$, and $T_{\rm g}$ is the heat-production effect [*Özişik*, 1980]; $T_{\rm bc}$ corresponds to $T_{\rm bc2}$ in *Clow* [2015]. For convenience, the solution is best expressed using dimensionless coordinates,

$$\zeta \;=\; \left(\frac{x}{L}\right), \quad \nu \;=\; \left(\frac{y}{L}\right), \quad \eta \;=\; \left(\frac{z}{L}\right), \quad \tau \;=\; \left(\frac{t}{t^\star}\right) \tag{6.2}$$

where L and $t^\star$ are scaling lengths and times, respectively. We also define a useful dimensionless parameter,

$$\alpha \;=\; \frac{L}{\sqrt{\kappa\, t^\star}}, \tag{6.3}$$

where κ is the thermal diffusivity. Assuming the diffusivity and thermal conductivity K are approximately constant within the problem domain, the three components of the general temperature solution can be expressed in terms of 2-D and 3-D Green's functions (GFs), $\mathbf{G}_{XY}$ and $\mathbf{G}_{XYZ}$,

$$T_{\rm ic}(\zeta,\nu,\eta,\tau) = \int_0^\infty \int_{-\infty}^{\infty} \int_{-\infty}^{\infty} \mathbf{G}_{XYZ}(\zeta,\nu,\eta,\tau|\zeta',\nu',\eta',\tau')|_{\tau'=0}\, F(\zeta',\nu',\eta')\, d\zeta'\, d\nu'\, d\eta' \tag{6.4}$$

$$T_{\rm bc}(\zeta,\nu,\eta,\tau) = \frac{1}{\alpha^2} \int_{\tau'=0}^{\tau} \left[\frac{\partial \mathbf{G}_Z}{\partial \eta'}\right]_{\eta'=0} \int_{-\infty}^{\infty} \int_{-\infty}^{\infty} \mathbf{G}_{XY}(\zeta,\nu,\tau\,|\zeta',\nu',\tau')\, f(\zeta',\nu',\tau') d\zeta' d\nu' d\tau' \tag{6.5}$$

$$T_{\rm g}(\zeta,\nu,\eta,\tau) = \frac{L^2}{K\,\alpha^2} \int_{\tau'=0}^{\tau} \int_0^\infty \int_{-\infty}^{\infty} \int_{-\infty}^{\infty} \mathbf{G}_{XYZ}(\zeta,\nu,\eta,\tau|\zeta',\nu',\eta',\tau')\, g(\zeta',\nu',\eta',\tau') d\zeta' d\nu' d\eta' d\tau'. \tag{6.6}$$

An advantage of the cartesian coordinate system is that the 2-D and 3-D GFs can be obtained from simple products of 1-D Green's functions [*Beck et al.*, 1992]. Thus, $G_{XY} =$

$G_X\, G_Y$ and $G_{XYZ} = G_X\, G_Y\, G_Z$. The 1-D GFs depend on the boundary conditions. For those described here, the 1-D GFs are,

$$\mathbf{G}_X(\zeta,\tau\,|\,\zeta',\tau') \;=\; \frac{\alpha}{\left[4\pi\,(\tau-\tau')\right]^{1/2}}\;\exp\left[-\frac{\alpha^2(\zeta-\zeta')^2}{4(\tau-\tau')}\right] \tag{6.7}$$

$$\mathbf{G}_Y(\nu,\tau\,|\,\nu',\tau') \;=\; \frac{\alpha}{\left[4\pi\,(\tau-\tau')\right]^{1/2}}\;\exp\left[-\frac{\alpha^2(\nu-\nu')^2}{4(\tau-\tau')}\right] \tag{6.8}$$

$$\mathbf{G}_Z(\eta,\tau\,|\,\eta',\tau') \;=\; \frac{\alpha}{\left[4\pi\,(\tau-\tau')\right]^{1/2}}\left\{\exp\left[-\frac{\alpha^2(\eta-\eta')^2}{4(\tau-\tau')}\right]-\exp\left[-\frac{\alpha^2(\eta+\eta')^2}{4(\tau-\tau')}\right]\right\} \tag{6.9}$$

with

$$\left.\frac{\partial\mathbf{G}_Z}{\partial\eta'}\right|_{\eta'=0} \;=\; \frac{\alpha^3\,\eta}{\sqrt{4\pi}\,(\tau-\tau')^{3/2}}\;\exp\left[-\frac{\alpha^2\,\eta^2}{4(\tau-\tau')}\right] \tag{6.10}$$

[*Özişik*, 1980; *Clow*, 2015].

6.3 Drill pads and reserve pits

To simulate the thermal effect of a drill pad or reserve pit, the boundary condition $f(x,y,t)$ in Eq. (6.5) must be specified. The dependence of f on x, y, and t can be as complicated as desired. To estimate the magnitude of the effect, we assume the pad or pit is instantaneously created at time $t = 0$ and that it can be approximated by a $\Delta x \times \Delta y$ rectangle centered at (x_0, y_0). Once created, the temperature difference between the pad (or pit) and the surrounding terrain is $\Delta T_\star\,\theta(t)$ where $\Delta T_\star$ is the characteristic temperature difference and $\theta(t)$ is a dimensionless function describing the time dependence. We retain the time dependence as the pad may trap more snow some winters than others, or the pit may remain ice-covered longer some years than others. With these provisions, the boundary condition can be described by a function utilizing dimensionless variables,

$$f(\zeta,\nu,\tau) \;=\; \Delta T_\star\,\theta(\tau)\,\Pi\left(\frac{\zeta-\zeta_o}{\Delta\zeta}\right)\;\Pi\left(\frac{\nu-\nu_o}{\Delta\nu}\right), \tag{6.11}$$

where Π is the rectangular or normalized boxcar function. Substituting f into Eq. (6.5), the subsurface thermal effect of a drill pad or reserve pit is,

$$T_{\rm bc}(\zeta,\nu,\eta,\tau) = \frac{\Delta T_\star}{\alpha^2}\int_{\tau'=0}^{\tau}\theta(\tau')\left[\frac{\partial\mathbf{G}_Z}{\partial\eta'}\right]_{\eta'=0}\left[\int_{\zeta'=\zeta_o-\Delta\zeta/2}^{\zeta_o+\Delta\zeta/2}\mathbf{G}_X(\zeta,\tau|\zeta',\tau')\,d\zeta'\int_{\nu'=\nu_o-\Delta\nu/2}^{\nu_o+\Delta\nu/2}\mathbf{G}_Y(\nu,\tau|\nu',\tau')\,d\nu'\right]d\tau'. \tag{6.12}$$

Three different drill-pad designs were used in the NPR-A, thick pads, thin pads, and insulated pads. Material for the thin pads came entirely from the reserve pits. No attempt was made to push this material back into the pit upon completion of the drilling, leaving the original reserve pit completely intact. Material for the thick pads was imported from other sources to avoid the ice-rich materials generally found in the reserve pits. At the conclusion of drilling, at least some of this material was pushed back into the reserve pit to reduce the height of the pad and obscure the boundary of the pit. This action moved the edge of the remaining reserve pit further from the well head. A few of the deeper wells utilized insulating foam in the drill pad to accommodate year-round or multiyear drilling. Only a small amount of material from immediately around the well head was pushed into the reserve pit during environmental rehabilitation in these cases. Although the exact geometry varied amongst the NPR-A wells, the Koluktak Test Well serves as an approximate example of the drill-pad dimensions and the placement of the well head near the reserve pit (**Figure 6.2**). For the Koluktak (KOL) well, the main part of the drill pad is 161 m $\times$ 61 m and the center of the pad is 30 m from the well head. Koluktak utilized the thin-pad design so the original reserve pit is completely intact; the edge of the 78 m $\times$ 86 m reserve pit is 15 m from the well head.

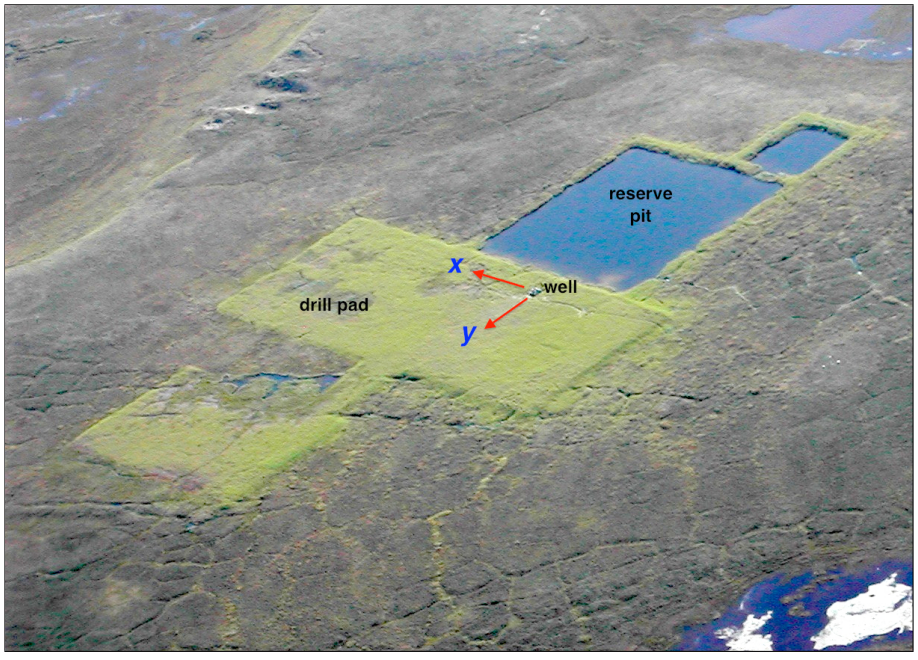

Figure 6.2: Koluktak Test Well No. 1, National Petroleum Reserve–Alaska.

To avoid the possible influence of seasonal effects, a common practice in the permafrost community is to report temperature changes observed in boreholes at the 20-m depth. Cross-sections of the normalized pad disturbance $(T_{\mathrm{bc}}/\Delta T_\star)$ for the KOL well indicate temperatures may be significantly disturbed at the 20-m depth at this time, 35 years after well completion, depending on the magnitude of $\Delta T_\star$ (**Figure 6.3**). For the drill-pad effect, we assume the vegetation on the pad reached its equilibrium height within a few years of well completion so we can treat the function $\theta(\tau)$ as a constant ($\theta = 1$). Unlike the drilling disturbance discussed in Chapter 5, the disturbance associated with the drill pad becomes stronger and penetrates to greater depth with increasing time. At the borehole, the shape of the drill-pad disturbance profile mimics that due to a change in climate coincident with drill pad completion (**Figure 6.4**a). For the thermal disturbance shown in **Figure 6.3** and **Figure 6.4**a, the thermal diffusivity κ was assumed to be $1.0 \times 10^{-6}\mathrm{m}^2\ \mathrm{s}^{-1}$, a typical value for earth materials. However, κ is poorly known for the fine-grained permafrost found in the NPR-A. Temperature trends at the 20 and 40-m depths in the KOL borehole show the strong influence κ has on the thermal disturbance due to the pad (**Figure 6.4**b).

The temperature offset between the pad and the surrounding undisturbed tundra ($\Delta T_\star$)

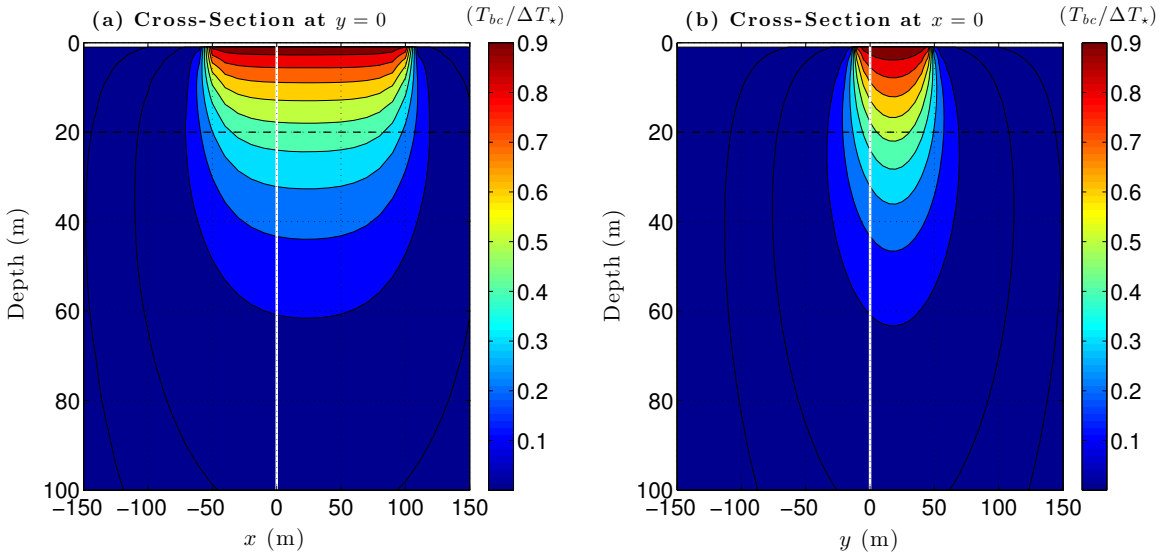

Figure 6.3: Cross-sections of the subsurface thermal effect associated with the Koluktak drill pad, 35 years after the pad was created, assuming $\kappa = 1.0 \times 10^{-6}\mathrm{m}^2\ \mathrm{s}^{-1}$. White vertical lines represent the borehole, located at $x = 0, y = 0$. Dashed horizontal line highlights the depth (20 m) at which permafrost temperature changes are commonly reported.

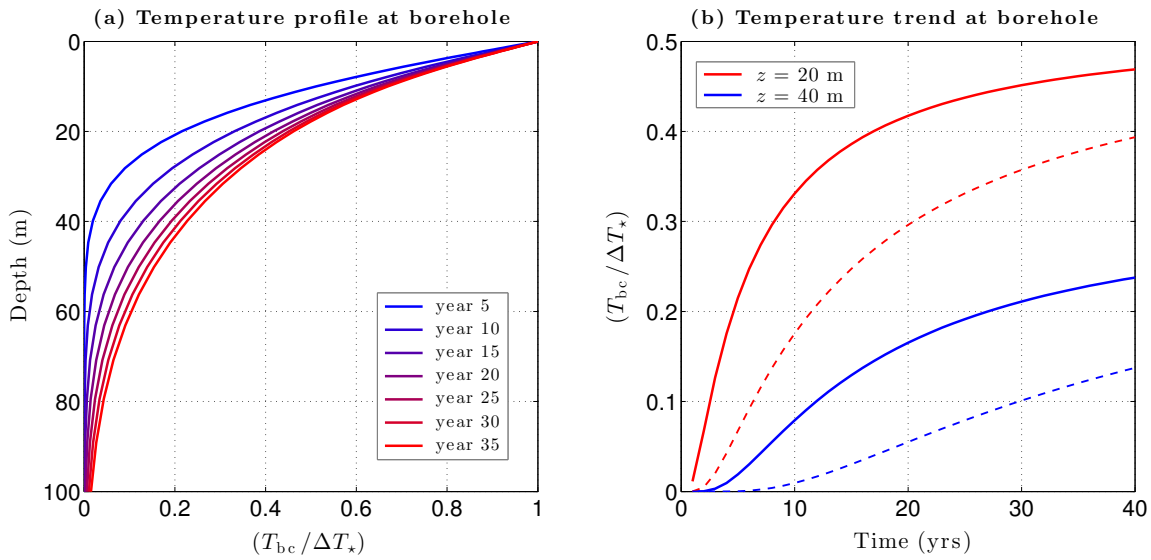

Figure 6.4: Drill-pad disturbance in the Koluktak well. Normalized drill-pad disturbance profiles are shown in panel (a) for $\kappa = 1.0 \times 10^{-6}\text{m}^2\ \text{s}^{-1}$ and $\theta(\tau) = 1$. Panel (b) shows the temperature trends due to the pad disturbance at the 20 and 40-m depths for $\kappa = 1.0 \times 10^{-6}\text{m}^2\ \text{s}^{-1}$ (solid lines) and $0.4 \times 10^{-6}\text{m}^2\ \text{s}^{-1}$ (dashed lines).

is the primary source of uncertainty for the drill-pad effect. At Koluktak in the southern portion of the Arctic Coastal Plain, the pad vegetation is much taller than that of the surrounding tundra. As a result, the pad tends to catch and retain more snow than the tundra during the cold seasons. A limited set of 1-m depth temperatures acquired on the KOL drill pad and in the surrounding terrain shows considerable interannual variability. Analysis of data from the nearby Koluktak climate station [*Urban and Clow*, 2016] confirms this variability is primarily due to year-to-year variability of the cold-season snowpack. During years with a thin tundra snowpack, the pad is about 3 K warmer than the surrounding terrain while during thick tundra snowpack years, the pad is 0.5–1.0 K warmer. Data from the Koluktak climate station show that thin tundra snowpacks occur about 30% of the time. At the Drew Point well (**Figure 6.1**) on the Beaufort Sea coast the reverse is true. Here, the pad vegetation is extremely sparse so the snowpack on the windswept pad tends to be very thin most winters. A pair of climate-monitoring stations operating on the pad and in the nearby tundra for a few years again show considerable variability. On average, pad temperatures at this site tend to be about 4 K colder than the surrounding tundra during the winter. This strong temperature difference is mitigated somewhat during the

snow-free period due to a lower albedo on the drill pad and stronger evaporative cooling over the wet tundra. On an annual average, the 1-m depth pad temperatures are 1–2 K cooler at Drew Point than the surrounding tundra. Koluktak and Drew Point represent the two end members in terms of pad vegetation. Given the frequency of thin tundra snowpacks, and the limited data available regarding the temperature difference between a drill pad and the surrounding tundra, $\Delta T_\star$ appears to be between 0 and 1 K for sites in the southern NPR-A where the pad vegetation is much taller than the tundra. At sites where the pad vegetation is sparse, $\Delta T_\star$ is between 0 and -2 K. Thus, at southern NPR-A sites with tall pad vegetation, the present warming at the 20-m depth due to the drill pad may be as large as 0.4–0.5 K (**Table 6.1**). At sites with sparse pad vegetation, a cooling of up to 0.8–0.9 K may presently occur at 20-m due to the drill pad. We emphasize that these values are probably upper limits.

In contrast to the drill pads, the thermal effect of the reserve pits is always to warm the subsurface. These water-filled depressions essentially act as small lakes. At high northern latitudes, the seasonal ice that forms on lakes is categorized as 'bedfast-ice' if it freezes solid to the bottom of the lake, 'floating-ice' if some liquid water remains beneath the ice throughout the winter, and 'intermittent' if it is bedfast some years and floating during others. Temperatures at the bottom of floating-ice lakes are always warmer than 0°C. Thus, floating-ice lakes on the Arctic Coastal Plain (ACP) can make a large thermal impression on the landscape [*Lachenbruch et al.*, 1962]. Whether a lake is a bedfast-ice lake or a floating-ice lake depends on whether the maximum seasonal ice-cover thickness $Z_{\text{ice}}^{\text{max}}$ exceeds the depth of the lake. During the 1970s and 1980s, $Z_{\text{ice}}^{\text{max}}$ for lakes in the maritime zone along the Beaufort Sea coast was 2.0 ± 0.2 m [*Weeks et al.*, 1981; *Arp et al.*, 2012]. With a warming climate in arctic Alaska over the last few decades [e.g., see *Bieniek et al.*, 2014], the maximum seasonal ice thickness on these lakes had decreased to about 1.5 m by 2010 [*Arp et al.*, 2012]. Unfortunately, ice-thickness data from the inland portion of the ACP are only available back to 1998. But by 2010, $Z_{\text{ice}}^{\text{max}}$ for lakes in this zone was about 1.4 m. *Zhang and Jeffries* [2000] showed that $Z_{\text{ice}}^{\text{max}}$ for lakes in northernmost Alaska depends primarily on snow depth and secondarily on air temperature. Although there is a great deal of interannual variability, data from *Urban and Clow* [2016] show that for any given year the winter snowpack is fairly uniform across the Arctic Coastal Plain in the NPR-A, as is the

Table 6.1: Drill-pad and reserve-pit thermal effects at the 20-m depth in the DOI/GTN-P monitoring wells 35 years after well completion for two thermal diffusivities κ. Also listed are the pad type, the distance of the well head from the edge of the reserve pit Δy, and a classification of the vegetation on the drill pad. Vegetation classification '-' indicates pad vegetation much shorter than surrounding tundra, '+' is much taller than surrounding tundra, and '0' is about the same. The range of T_{bc}^{pad} values are based on $\Delta T_\star \in (-2, 0)$ K for sparse pad vegetation sites and $\Delta T_\star \in (0, +1)$ K for inland sites with tall pad vegetation.

Borehole	Pad Type	Δy (m)	Vegetation on Pad	$\kappa = 0.4 \times 10^{-6}$m^2 s^{-1}		$\kappa = 1.0 \times 10^{-6}$m^2 s^{-1}	
				T_{bc}^{pad} (K)	T_{bc}^{pit} (K)	T_{bc}^{pad} (K)	T_{bc}^{pit} (K)
Tunalik	insul	20	-	[-0.76, 0]	0.38	[-0.92, 0]	0.73
Peard Bay	thin	15	-	[-0.76, 0]	0.60	[-0.92, 0]	1.02
Kugrua	thick	19	-	[-0.76, 0]	0.43	[-0.92, 0]	0.80
South Meade	thick	15	0	0	0.59	0	1.01
Kuyanak	thin	12	-	[-0.76, 0]	0.70	[-0.92, 0]	1.08
Tulageak	thin	11	0	0	0.76	0	1.15
West Dease	thin	11	0	0	0.77	0	1.18
East Simpson #1	thin	15	-	[-0.76, 0]	0.57	[-0.92, 0]	0.95
Ikpikpuk	thick	23	0	0	0.31	0	0.62
Drew Point	thick	35	-	[-0.76, 0]	0.09	[-0.92, 0]	0.26
J.W. Dalton	thick	26	-	[-0.76, 0]	0.21	[-0.92, 0]	0.44
East Teshekpuk	thick	44	0	0	0.03	0	0.09
North Kalikpik	thick	37	-	[-0.76, 0]	0.08	[-0.92, 0]	0.24
Atigaru	thick	36	-	[-0.76, 0]	0.09	[-0.92, 0]	0.24
South Harrison	thick	33	-	[-0.76, 0]	0.08	[-0.92, 0]	0.21
West Fish Creek	thick	34	0	0	0.11	0	0.29
North Inigok	thin	18	0	0	0.45	0	0.80
Koluktak	thin	15	+	[0, 0.38]	0.58	[0, 0.46]	0.95
Seabee	insul	22	-	[-0.76, 0]	0.31	[-0.92, 0]	0.62
Awuna	insul	18†	+	[0, 0.38]	1.56	[0, 0.46]	2.40

†Initially 18 m from the well-head, the edge of the Awuna reserve pit has been eroding towards the well at 0.55 m a^{-1}.

winter air temperature. Given the similarity of the environmental parameters controlling ice thickness in the maritime and inland portions of the ACP, it is likely Z_{ice}^{max} has been following the same trend in the two zones since the 1980s. Based on this reasoning, Z_{ice}^{max} for lakes in the inland portion of the ACP is expected to have been 1.9 ± 0.2 m during the late 1970s and early 1980s.

Information provided by the drilling contractor to the U.S. Geological Survey indicates the depth of the thin-pad NPR-A reserve pits is about 1.4 m, and is 1.5 m for the thick-pad reserve pits. Thus, the reserve pits for both drill-pad designs would have frozen solid each winter in the early 1980s since the mean Z_{ice}^{max} was 1.9–2.0 m across the entire ACP

at that time, with an ± 0.2 m interannual variability, $Z_{\text{ice}}^{\text{max}}$ ranged 1.7–2.2 m. By 2010, the maximum seasonal ice thickness $Z_{\text{ice}}^{\text{max}}$ in the coastal and inland zones would have been comparable to the depth of the reserve pits, 1.4–1.5 m. As a consequence, the reserve pits would have had bedfast ice some winters and floating ice during others, placing them firmly in the 'intermittent' category by 2010. The Awuna well is an exception as its reserve pit is 3.4 m deep. This depth greatly exceeded $Z_{\text{ice}}^{\text{max}}$ even during the early 1980s so the Awuna reserve pit has been a floating-ice lake since its inception. *Arp et al.* [2012] recently provided lake-bed temperature data for bedfast-ice, intermittent-ice, and floating-ice lakes in the NPR-A. From these data we find the reserve pits were $\sim$ 4 K warmer than the surrounding tundra on a mean-annual basis during the early 1980s when they were bedfast-ice lakes. With their transition to intermittent-ice lakes, they would have been 9 K warmer than the surrounding permafrost by 2010. The floating-ice reserve pit at Awuna would have been 9.5 K warmer than the surrounding tundra ever since the pit was created in 1980.

To simulate the thermal effect of the reserve pits, we let the boundary condition f increase from 4 K to 9 K within the confines of the pit over the time interval 0 to 35 yrs (f is zero outside the pit). This is accomplished by setting $\Delta T_\star = 9$ K and $\theta(t)$ to a linear function increasing from 0.45 at $t = 0$ to 1.0 at $t = 35$ yrs. The Awuna reserve pit is modeled as a constant 9.5 K warming since its creation. As expected, the resulting normalized reserve-pit disturbance ($T_{\text{bc}}/\Delta T_\star$) is focused beneath the pit and is relatively small at the location of the well (**Figure 6.5**, **Figure 6.6a**). Since the well head is some lateral distance from the reserve pit, the temperature trends are more sensitive to the thermal diffusivity than is the case for the drill-pad disturbance (**Figure 6.6b**). Given the linear increase in the BC function $\theta(t)$, the subsurface warming due to the reserve pits is predicted to have been increasing almost linearly over time. Despite the small normalized reserve-pit disturbance at the well, the absolute disturbance T_{bc} is large due to the magnitude of $\Delta T_\star$. The disturbance is also quite sensitive to the distance of the well head to the edge of the reserve pit (**Figure 6.7**). For the thin-pad reserve pits, the warming at the 20-m depth 35 yrs after the pads were created is on the order of 1 K (**Table 6.1**). For the thick drill pads where some degree of reserve pit infilling occurred during environmental rehabilitation, the 20-m warming varies from 0 to 1 K.

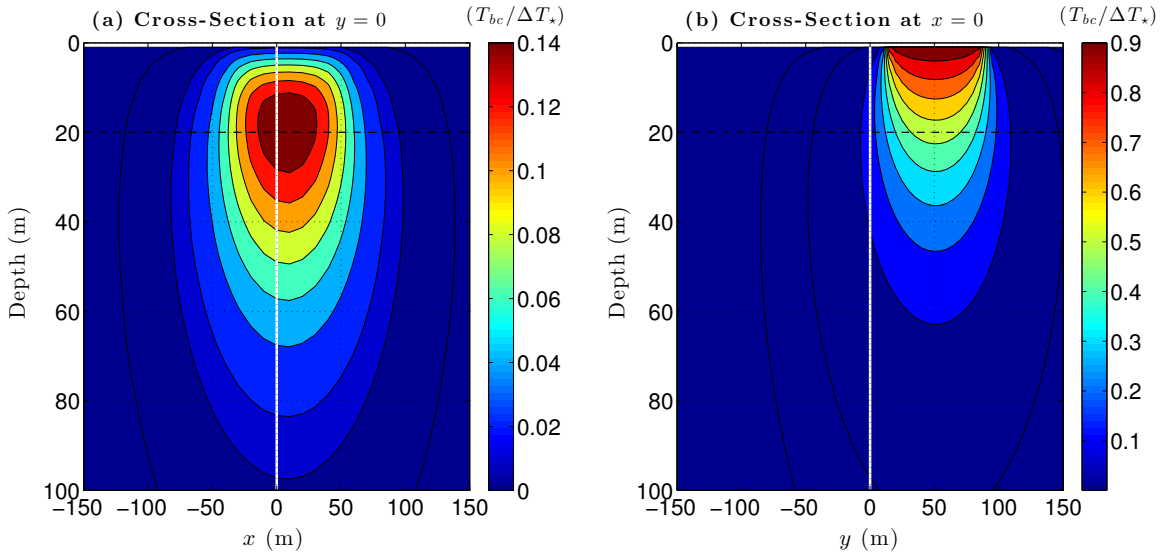

Figure 6.5: Cross-sections of the subsurface thermal effect associated with the Koluktak reserve pit, 35 years after the pit was created, assuming $\kappa = 1.0 \times 10^{-6}\text{m}^2\ \text{s}^{-1}$. White vertical lines represent the borehole, located at $x = 0, y = 0$. Dashed horizontal line highlights the depth (20 m) at which permafrost temperature changes are commonly reported. Note the different temperature scales used in (a) and (b).

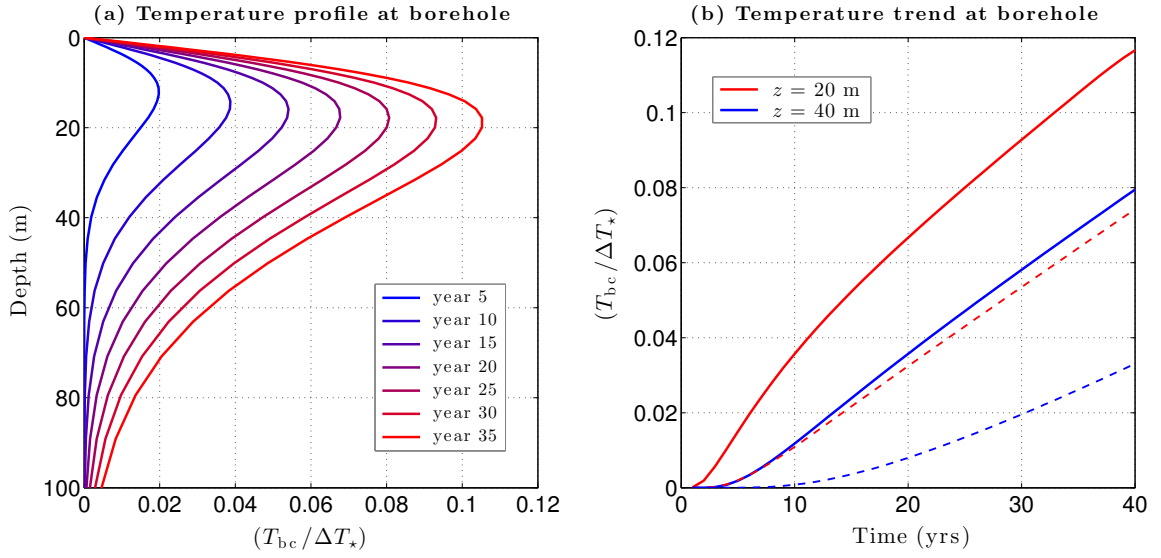

Figure 6.6: Reserve-pit disturbance in the Koluktak well. Normalized reserve-pit disturbance profiles are shown in (a) assuming $\kappa = 1.0 \times 10^{-6}\text{m}^2\ \text{s}^{-1}$. Panel (b) shows the temperature trends due to the reserve-pit disturbance at the 20 and 40-m depths for $\kappa = 1.0 \times 10^{-6}\text{m}^2\ \text{s}^{-1}$ (solid lines) and $0.4 \times 10^{-6}\text{m}^2\ \text{s}^{-1}$ (dashed lines).

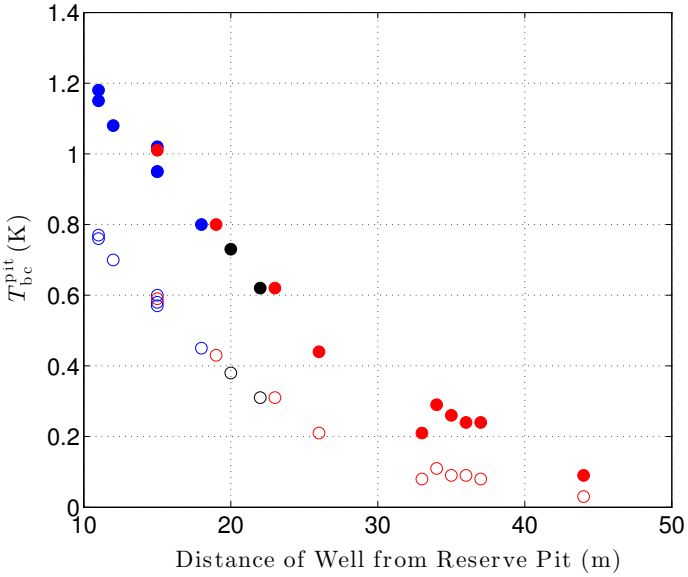

Figure 6.7: Predicted thermal disturbance at the 20-m depth in the NPR-A wells due to the reserve pits, 35 yrs after the pits were created. Solid and open circles are for $\kappa = 1.0 \times 10^{-6}\text{m}^2\ \text{s}^{-1}$ and $\kappa = 0.4 \times 10^{-6}\text{m}^2\ \text{s}^{-1}$, respectively. Blue points indicate thin-pad reserve pits, red indicate thick-pad pits, while black are for insulated-pad reserve pits. Awuna is not shown.

6.4 Ocean transgression

Given the proximity of the ocean to some of the coastal wells in the DOI/GTN-P array, it is pertinent to investigate what effect the ocean may have on the temperature logs acquired in these wells. Surface temperatures along the Beaufort Sea coast were about $-10°$C in the early 1980s, prior to the current climate warming. Mean-annual ocean bottom temperatures close to shore are about $-1°$C, producing a 9 K temperature contrast at the shoreline. *Lachenbruch* [1957] solved this thermal problem for the steady-state case, and for the case where the ocean instantaneously moved to its current position 10,000 years ago at the end of the last ice age. However, comparison of old maps, air photos, and more recent satellite imagery indicate the shore is eroding fairly quickly along most of the Beaufort Sea coast of the NPR-A. To address this, we consider a moving boundary condition of the form,

$$f(x,t) \;=\; \Delta T_\star \, H(vt - x) \tag{6.13}$$

where $\Delta T_\star$ is the temperature difference between the base of the ocean and the land surface (9 K), v is the velocity of the eroding coastline, and H is the Heaviside step function. The

coordinate system is oriented with $\hat{x}$ perpendicular to the coastline. To further simplify the problem, the coastline is assumed to be straight so any y-dependence can be neglected. This is a reasonable assumption along most sections of the Beaufort coast. In terms of dimensionless variables, the moving boundary condition becomes,

$$f(\zeta, \tau) \;=\; \Delta T_\star \, H\left(v\, t^\star \tau - L\, \zeta\right). \tag{6.14}$$

Substituting into Eq. (6.5), the subsurface effect of the moving boundary condition is found to be,

$$T_{\mathrm{bc}}(\zeta, \eta, \tau) \;=\; \frac{\Delta T_\star}{\alpha^2} \int_{\tau'=0}^{\tau} \left[\frac{\partial \mathbf{G}_Z}{\partial \eta'}\right]_{\eta'=0} \int_{\zeta'=-\infty}^{v\, t^\star \tau'/L} \mathbf{G}_X(\zeta, \tau \,|\, \zeta', \tau')\, d\zeta'\, d\tau'. \tag{6.15}$$

The motion of the boundary is encapsulated in the upper integration limit for ζ.

We assume the coast is initially static and far off-shore. The initial condition can then be described by,

$$F(\zeta, \eta) \;=\; \Delta T_\star \, H(-\zeta) \;+\; L\, \Gamma \eta \, H(\zeta), \tag{6.16}$$

where Γ is the onshore permafrost temperature gradient. After substituting F into Eq. (6.4), the thermal effect of the initial condition is ultimately found to be,

$$T_{\mathrm{ic}}(\zeta, \eta, \tau) \;=\; T_s \;+\; \frac{\Delta T_\star}{2} \operatorname{erfc}\left(\frac{\alpha \zeta}{\sqrt{4\tau}}\right) \operatorname{erf}\left(\frac{\alpha\, \eta}{\sqrt{4\tau}}\right) \;+\; \frac{L\, \Gamma}{2} \left[1 + \operatorname{erf}\left(\frac{\alpha \zeta}{\sqrt{4\tau}}\right)\right] \eta\,, \tag{6.17}$$

where T_s is the onshore surface temperature. Ignoring any heat-production terms, the complete solution for the temperature field near the ocean is,

$$\begin{aligned} T(\zeta, \eta, \tau) \;=\; & T_s \;+\; \frac{\Delta T_\star}{2} \operatorname{erfc}\left(\frac{\alpha \zeta}{\sqrt{4\tau}}\right) \operatorname{erf}\left(\frac{\alpha\, \eta}{\sqrt{4\tau}}\right) \;+\; \frac{L\, \Gamma}{2} \left[1 + \operatorname{erf}\left(\frac{\alpha \zeta}{\sqrt{4\tau}}\right)\right] \eta \\ & + \frac{\Delta T_\star}{\alpha^2} \int_{\tau'=0}^{\tau} \left[\frac{\partial \mathbf{G}_Z}{\partial \eta'}\right]_{\eta'=0} \int_{\zeta'=-\infty}^{v\, t^\star \tau'/L} \mathbf{G}_X(\zeta, \tau \,|\, \zeta', \tau')\, d\zeta'\, d\tau'. \end{aligned} \tag{6.18}$$

Letting the ocean move inland for 1000–2000 years to mitigate the effect of the simplified initial condition, the maximum subsurface thermal effect of the ocean at the coastal wells is found to be less than 1 mK at the time of their most recent temperature logs (**Table 6.2**). Wells near a slowly eroding shore (East Simpson, Tulageak) are still far enough away from the coast that the warm ocean has little effect. Wells adjacent to a rapidly eroding section of coast (J.W. Dalton, Drew Point) have now been overridden by the ocean. In these cases, the ocean moved in so quickly that the subsurface temperatures at the well

Table 6.2: Maximum subsurface thermal effect at the coastal wells during their most recent temperature logs due to the transgression of the Arctic Ocean; Δx is the distance of the well from the coast at that time. The velocity of the moving coast at each site is v.

Borehole	v (m a^{-1})	Δx (m)	max($T_{\mathbf{bc}}$) (K)
East Simpson	0.6	427	7.2×10^{-5}
Tulageak	1.2	187	1.8×10^{-4}
Atigaru	3.6	60	2.8×10^{-4}
J.W. Dalton	9.5	100	5.7×10^{-15}
Drew Point	10	155	9.8×10^{-23}

never saw it coming. **Figure 6.8** illustrates the thermal effect of the encroaching ocean at the Tulageak well site at the time of its most recent temperature log.

The situation at the Awuna borehole is unique among the DOI/GTN-P monitoring wells in that the edge of the reserve pit has been eroding towards the well. From repeat photography, the mean erosion rate is estimated to be 0.55 m a^{-1}. Following the methodology used to simulate the ocean transgression, the effect of the eroding reserve pit can be captured by including a time-dependent position for the upper integration limit

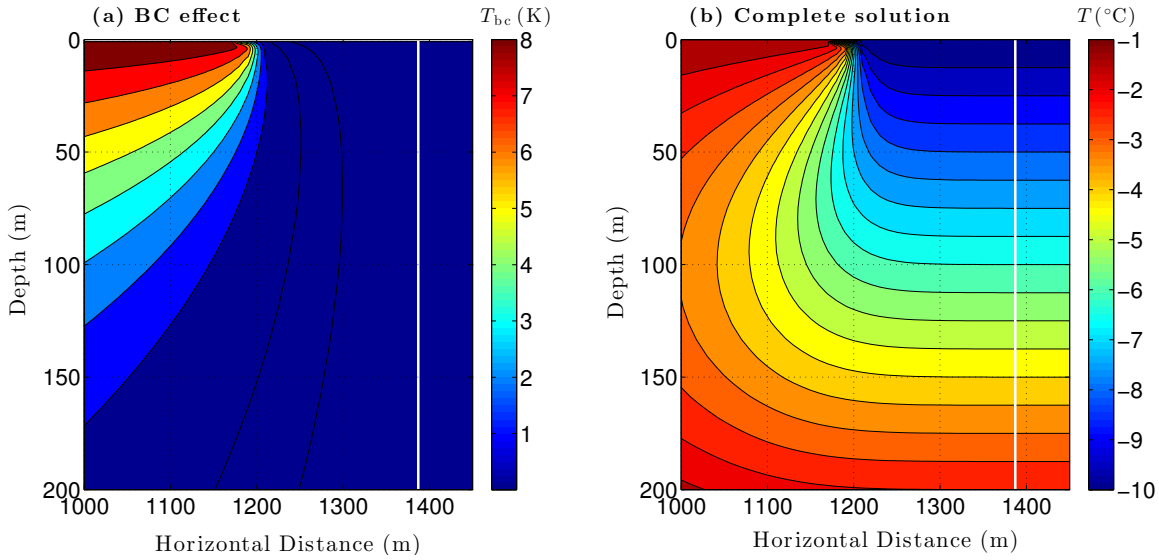

Figure 6.8: Thermal effect of the ocean at the Tulageak well site. The boundary condition effect T_{bc} due to the transgression of the Beaufort Sea at the Tulageak well is shown in (a) during the latest temperature log (2-JUL-2014). Panel (b) shows the complete temperature solution at that time. The well (vertical white lines) was 187 m from the coast ($x = 1200$ m) during 2014. The ocean is moving inland (left to right) at 1.2 m a^{-1} at this site.

(coordinate ν) in Eq. (6.12). The great depth of this reserve pit, combined with the erosion of its edge, leads to a present-day thermal disturbance at the well greatly exceeding 1 K at the 20-m depth (**Table 6.1**).

6.5 Summary

There is a continuum of vegetation states on the NPR-A drill pads, ranging from extremely sparse at several coastal locations (Drew Point, East Simpson, Kuyanak), to being much taller than the surrounding undisturbed tundra in the southern NPR-A (Koluktak, Awuna). The ability of pad vegetation to catch and retain snow in the ever-present arctic winds is the dominant factor controlling the temperature difference between the drill pads and the surrounding vegetation. This leads to a cooling beneath some drill pads and a warming beneath others. Unlike the drilling disturbance discussed in Chapter 5, this effect becomes stronger with time. Based on the few data that exist for the pad-to-tundra temperature offset, the cooling that occurs at the location of the well for sparsely vegetated drill pads likely ranges between -0.9 K and 0 K at the 20-m depth at present. The warming at the well for drill pads with tall vegetation likely ranges between 0 K and +0.5 K at the 20-m depth. The thermal effect of the drill pads is potentially large enough to bias the climate pattern on the Arctic Slope ultimately deduced from the temperature profiles acquired in the DOI/GTN-P monitoring wells. Given the potential size of the drill-pad effect, further effort should be made to measure the pad-to-tundra temperature difference at a range of sites.

Water-filled reserve pits adjacent to the drill pads produce a substantial subsurface warming at all well sites. The strength of this effect has been enhanced by a reduction of the maximum seasonal ice thickness since $\sim$ 1980, another ramification of arctic climate change. Similar to the drill-pad effect, the warming due to the reserve pits increases with time, although at rate that is nearly linear. At present, the reserve pit warming at the 20-m depth in the wells ranges from almost zero to +1.2 K, depending on the distance of the well head from the edge of the reserve pit. The strength of the effect is also sensitive to the thermal diffusivity of the local permafrost. The reserve-pit warming is expected to be a substantial fraction of the total warming observed in many of the wells since the well-monitoring program began. The reserve pit warming at the Awuna well is excep-

tionally large due to its great depth and the erosion of the pit towards the well. In this case, the thermal disturbance due to the reserve pit may be the dominant component of the warming observed in this well.

The thermal effect of the warm ocean near the coastal wells of the DOI/GTN-P array is smaller than our detection limit, 1 mK. Wells near a slowly eroding section of the coast are still too far from the ocean to see the effect. Near rapidly eroding portions of the coast, the ocean is moving inland faster than the thermal diffusion rate so the ocean engulfs the well before the subsurface thermal effects are sensed.

6.6 References

Arp, C.D., Jones, B.M., Lu, Z., and Whitman, M.S. (2012), Shifting balance of thermokarst lake ice regimes across the Arctic Coastal Plain of northern Alaska, *Geophys. Res. Lett.*, 39, L16503, doi:10.1029/2012GL052518.

Barnhart, K.R., Anderson, R.S., Overeem, I., Wobus, C., Clow, G.D., and Urban, F.E. (2014), Modeling erosion of ice-rich permafrost bluffs along the alaskan Beaufort Sea coast, *J. Geophys. Res. Earth Surface*, 119, doi:10.1002/2013JF002845.

Beck, J.V., Cole, K.D., Haji-Sheikh, A., and Lithouhi, B. (1992), *Heat Conduction Using Green's Functions*, Hemisphere Publishing Corp., 523 pp.

Bieniek, P.A., Walsh, J.E., Thoman, R.L., and Bhatt, U.S. (2014), Using climate divisions to analyze variations and trends in Alaska temperature and precipitation, *J. Climate*, 27, 2800–2818.

Clow, G.D. (2015), A green's function approach for assessing the thermal disturbance caused by drilling deep boreholes in rock or ice, *Geophys. J. Int.*, 203, 1877–1895, doi:10.1093/gji/ggv415.

Haugen, R.K., and Brown, J. (1980), Coastal-inland distributions of summer air temperature and precipitation in northern Alaska, *Arctic and Alpine Research*, 12, 403–412.

Jones, B.M., Hinkel, K.M., Arp, C.D., and Eisner, W.R. (2008), Modern erosion rates and loss of coastal features and sites, Beaufort Sea Coastline, Alaska, *Arctic*, 61, 361–372.

Jones, B.M., Arp, C.D., Jorgenson, M.T., Hinkel, K.M., Schmutz, J.A., and Flint, P.L. (2009), Increase in the rate and uniformity of coastline erosion in arctic Alaska, *Geophys. Res. Lett.*, 36, L03503, doi:10.1029/2008GL036205.

Jones, B.M., Arp, C.D., Hinkel, K.M., Beck, R.A., Schmutz, J.A., and Winston, B. (2009), Arctic lake physical processes and regimes with implications for winter water availability and management in the National Petroleum Reserve Alaska, *Environmental Management*, 43, 1071–1084.

Lachenbruch, A.H. (1957), Thermal effects of the ocean on permafrost, *Geol. Soc. America Bull.*, 68, 1515–15329.

Lachenbruch, A.H., Brewer, M.C., Greene, G.W., and Marshall, B.V. (1962), Temperatures in permafrost, in *Temperature – Its Measurement and Control in Science and Industry*, 3, Reinhold Publishing Corp., New York.

Özişik, M.N. (1980), *Heat Conduction*, John Wiley & Sons, 687 pp.

Schindler, J.F. (1988), History of exploration in the National Petroleum Reserve in Alaska, with emphasis on the period from 1975 to 1982, in *Geology and Exploration of the National Petroleum Reserve in Alaska, 1974 to 1982*, USGS Professional Paper 1399, U.S. Geological Survey, 13–72.

Urban, F.E., and Clow, G.D. (2016), DOI/GTN-P climate and active-layer data acquired in the National Petroleum Reserve-Alaska and the Arctic National Wildlife Refuge, 1998–2014, *USGS Data Series 977*, U.S. Geological Survey, http://dx.doi.org/10.3133/ds977.

Weeks, W.F., Gow, A.J., and Schertler, R.J. (1981), Ground-truth observations of ice-covered North Slope lakes imaged by radar, *CRREL Report 81-19*, Cold Regions Research and Engineering Laboratory, Hanover, NH, 17 pp.

Zhang, T., and Jeffries, M.O. (2000), Modeling interdecadal variations of lake-ice thickness and sensitivity to climatic change in northernmost Alaska, *Ann. Glaciol.*, 31, 339–347.

CHAPTER 7

A THERMAL MODEL FOR PERMAFROST ON THE WESTERN ARCTIC SLOPE

7.1 Introduction

Permafrost in the NPR-A primarily consists of fine-grained sedimentary rocks (shales and mudrocks). In contrast to coarse-grained permafrost such as that found to the east in Prudhoe Bay, fine-grained permafrost is a much more complex material due to its ability to retain pore water in the unfrozen state at temperatures well below 0°C. The extent to which it retains unfrozen water depends largely on sediment texture, clay composition, and porosity. As a result, the thermophysical properties of these materials are strongly dependent on both the sediment characteristics and the temperature.

To better understand the properties of fine-grained permafrost and its response to drilling processes and climate change, multidimensional numerical heat-transfer models are developed in this chapter. These models are designed to handle the unique characteristics possessed by fine-grained permafrost, including: unfrozen water and latent-heat effects, moving phase boundaries, temperature-dependent thermophysical parameters, and material inhomogeneities. In these models, permafrost is treated as a matrix of nonvolatile materials (primarily mineral grains) while the pores are filled with unfrozen water, ice, and air.

7.2 Methods

7.2.1 Governing equation

Although substantial quantities of unfrozen water can exist within the pores of fine-grained permafrost, it generally migrates so slowly, if at all, that advective heat-transfer can be neglected. In this case, the differential form of the conservation-of-enthalpy equation is,

$$\frac{\partial(\rho H)}{\partial t} = -\nabla \cdot \mathbf{J} + S, \tag{7.1}$$

where ρ is the bulk density, H is the specific enthalpy, $\mathbf{J} = -K\nabla T$ is the diffusive heat flux, S is a source term, and t is time; K is the bulk thermal conductivity and T is temperature. For coarse-grained permafrost, latent-heat effects can be included as a moving source term [*Özişik*, 1980; *Clow*, 2015]. However for fine-grained permafrost, latent-heat effects are more appropriately included in the enthalpy change term, $\partial(\rho H)/\partial t$.

7.2.2 Thermophysical parameters

7.2.2.1 Unfrozen water content

The freezing of pore water in fine-grained sediments is a complex process occurring over a wide range of temperatures. Several models have been proposed to explain this behavior [see reviews by *Davis*, 2001; *Watanabe and Mizoguchi*, 2002]. Early capillary and hydrodynamic models that examine the bulk free energy of the water-ice system fail to predict the existence of unfrozen water more than a few tenths of a degree below the triple point T_{tr} (273.16 K). A more complete accounting of the free energies on all the interfaces, the bulk free energies of the ice and water, and the free energies related to the intermolecular forces between the molecules in the ice, water, and mineral layers is required to predict the stable existence of unfrozen water at lower temperatures. These effects are incorporated in the 'premelting' model which predicts liquid water at temperatures as low as $\sim 0.9\, T_{\text{tr}}$ [*Davis*, 2001]. Experimental evidence confirms the existence of unfrozen water in fine-grained materials at these low temperatures. For example, experiments by *Watanabe and Mizoguchi* [2002] found that 5% of the water in a silty clay soil is in the liquid state at -20°C and that 20% was unfrozen at -10°C.

For thick permafrost as is found on the Arctic Slope, three effects potentially contribute to a depression of the freezing point: (a) pore-pressure effects, (b) solute (chemical) effects, and (c) soil-texture effects. The freezing point T_f, defined to be the temperature at which ice just begins to form within the pores, is given by the linear combination,

$$T_f \;=\; T_{\text{tr}} - \theta_p - \theta_c - \theta_s \qquad (\text{K}) \tag{7.2}$$

where θ_p, θ_c, and θ_s are the freezing point depressions due to pressure, chemical, and sediment-texture effects, respectively [*Osterkamp and Payne*, 1981].

Beginning with the pressure effect, *Osterkamp and Payne* [1981] found the related freezing point depression is given simply by,

$$\theta_p \;=\; bP \tag{7.3}$$

where b is the Clausius-Clapeyron slope (7.66×10^{-8} K/Pa) and P is the pore pressure. If the water is freely connected with the earth's surface, the pore pressure is equal to the *hydrostatic* pressure $P = \rho_u g z$ where ρ_u is the density of unfrozen water, g is the acceleration of gravity, and z is the depth below surface. However if water is trapped, the pore pressure can be nearly equal to or exceed the *lithostatic* pressure $P = \rho g z$ [*Turcotte and Schubert*, 1982]. On the Arctic Coastal Plain, pore-pressure data from drill-stem tests and well-log calculations indicate pressures are close to hydrostatic in near-surface sedimentary rocks [*Collett et al.*, 1988]. The greatest pressure effects are expected to occur along the Beaufort coast where permafrost is up to 410 m thick [*Clow*, 2014]. Here, the freezing-point depression due to pressure θ_p can be as large as 0.30 K. In the Arctic Foothills, sedimentary horizons tend to be overpressured [*Collett et al.*, 1988]. Thus at sites such as the Awuna well, θ_p may be as large as 0.56 K near the base of permafrost.

Water samples recovered from drill-stem and production tests show that salinities in near-surface (0–1500 m) sedimentary rocks are generally low on the Arctic Slope and that the dominant solute is NaCl [*Collett et al.*, 1988]. Ninety percent of the Nanushuk and Colville water samples reported by *Collett et al.* [1988] had salinities less than 9 parts per thousand (ppt); the median value was 4.9 ppt. The freezing point depression due to NaCl can be estimated using the empirical equation,

$$\theta_c \;=\; 0.0137 + 0.051990\, s + 0.00007225\, s^2 \qquad \text{(K)} \tag{7.4}$$

where the salinity s is expressed in ppt [*Osterkamp and Payne*, 1981]. Based on this equation, the freezing point depression due to chemical solutes is expected to be less than 0.49 K (90% probability) in the NPR-A. The median expected value for θ_c is 0.27 K.

The freezing point depression due to sediment texture is more complicated. Using data from six representative soil samples, *Anderson et al.* [1973] empirically found the unfrozen water content of a fine-grained sediment at atmospheric pressure is related to the temperature (in Celsius) through a power law,

$$w_u \;=\; \alpha\,(-T)^{\beta}, \qquad \text{for } T < 0^{\circ}\text{C} \tag{7.5}$$

where α and β are constants that depend on the sediment type. In the permafrost literature, the unfrozen water content w_u is defined by the ratio of the mass of unfrozen water per-unit-volume to the mass of the sediment in its completely dry state,

$$w_u \;=\; \frac{\rho_u \phi_u}{\rho_g (1-\phi)}. \tag{7.6}$$

Here, ρ_g is the mean density of the mineral grains, ϕ is the sediment porosity, and ϕ_u is the volume fraction of unfrozen water. The volume fractions of the other potential pore constituents are ϕ_i for ice and ϕ_a for air ($\phi = \phi_u + \phi_i + \phi_a$). Using thermodynamic arguments, *Qin et al.* [2009] showed that w_u can be described by an expression of the form,

$$w_u \;=\; -\frac{k_o \rho}{k} \frac{1}{1+b-a} (-T)^{1+b-a} + c$$

where k, k_o, a, b, and c are experimentally determined parameters. This can be restated as,

$$w_u \;=\; A(-T)^B + c,$$

where A and B are constants. Since the amount of unfrozen water is zero in the limit $T \to -\infty$, parameter c should be zero ($B < 0$). Thus, the power law commonly used for w_u (Eq. 7.5) can be derived directly from thermodynamic arguments, placing it on a stronger theoretical footing. A consequence of this relationship is that the unfrozen water content is independent of porosity; to first order it depends only on the temperature and the sediment type. **Figure 7.1** shows the unfrozen water content for the six representative soils ($\mathcal{M} = 1$–6) considered by *Anderson et al.* [1973]. Among these soils, bentonite, illite (Hawaiian clay), kaolinite, and silty clay retain significant amounts of unfrozen water at low temperatures while Fairbanks silt and fine sand hold very little. Naturally occurring sediments often have two or more dominant components. Returning to the definition of unfrozen water content, w_u for binary and more complicated mixtures can be expressed by,

$$w_u \;=\; f_1 w_{u1} + f_2 w_{u2} + f_3 w_{u3} + \cdots \tag{7.7}$$

where $f_i = (m_i/m)$ is the fraction of the total dry mass ($m = \sum m_i$) belonging to the i^{th} material and w_{ui} is its unfrozen water content. Once w_u has been determined, the volume fraction of unfrozen water can be found by rearranging Eq. (7.6),

$$\phi_u \;=\; \frac{(1-\phi)\,\rho_g}{\rho_u}\, w_u\,. \tag{7.8}$$

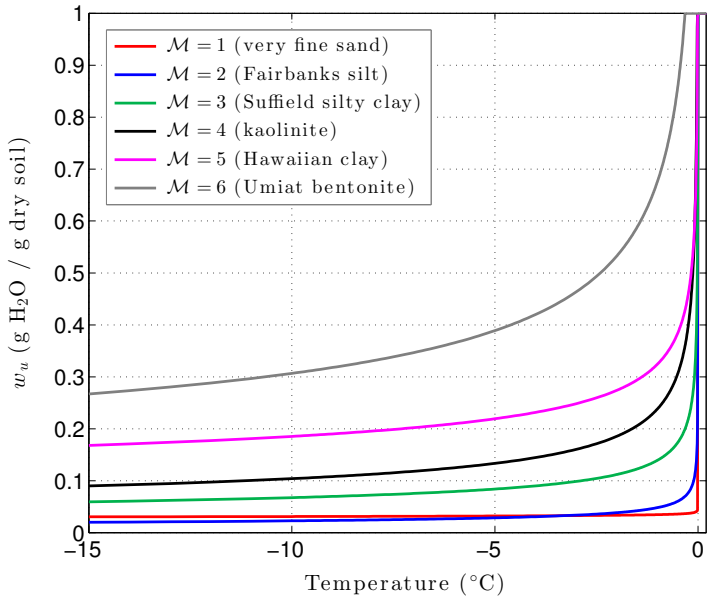

Figure 7.1: Unfrozen water content w_u for six representative soils from *Anderson et al.* [1973]. Hawaiian clay is predominately illite with small amounts of kaolinite [*Wentworth et al.*, 1940].

Unlike w_u, the relative amount of water in the liquid state $[\phi_u/(\phi_u + \phi_i)]$ is very sensitive to the porosity. This sensitivity is shown in **Figure 7.2** for a sediment with the unfrozen water properties of Suffield silty clay ($\mathcal{M} = 3$). The tendency of pore water to remain in the liquid state is so strong for silty clay that no ice forms until temperatures are well below 0°C, especially at porosities less than 30%. With a porosity of 20%, no ice forms in Suffield silty clay until temperatures drop below −3.43°C ($\theta_s = 3.43$) and 71% of the pore water remains in the liquid state at temperatures as cold as −10°C. This tendency is even stronger for kaolinite, illite, and bentonite, all of which have been reported to occur on the Arctic Slope. Thus, the freezing point depression due to sediment texture θ_s potentially can be as large as several degrees for permafrost in the NPR-A, especially if porosities are low and sediment types $\mathcal{M} \geq 3$ are present in significant quantities (**Figure 7.3**). In contrast, the freezing point depression due to sediment texture is weak for soils $\mathcal{M} \leq 2$ or if the porosity is high ($\phi > 0.35$). Under these conditions, the contributions of θ_p, θ_c, and θ_s to the freezing point T_f are roughly comparable.

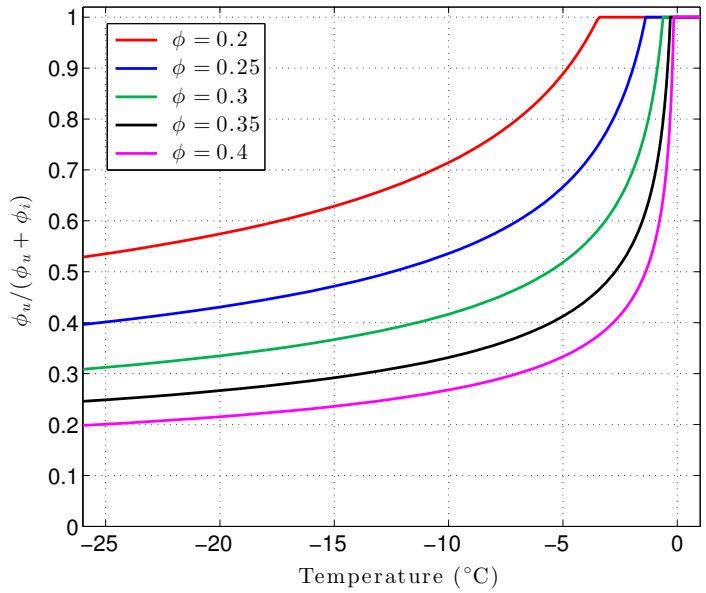

Figure 7.2: Fraction of water in the liquid state for Suffield silty clay ($\mathcal{M} = 3$) with porosities ϕ ranging 20% to 40%, assuming the pores are fully saturated ($\phi_a = 0$).

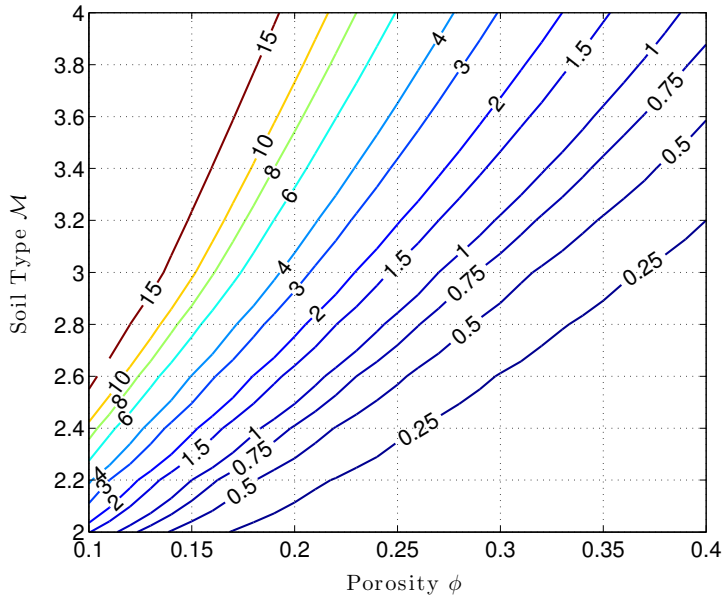

Figure 7.3: Freezing point depression due to sediment texture (θ_s) in kelvin for sediment types $\mathcal{M} = 2$–4 (silt, silty clay, kaolinite).

7.2.2.2 Enthalpy and the volumetric heat capacity

The specific enthalpy is defined by the total heat content per-unit-mass at temperature T,

$$H(T) \;=\; \int_0^T c_p(T')\,dT' + \sum_i L_i$$

where c_p is the specific heat associated with the lattice vibrations of the constituent atoms and $\sum_i L_i$ represents the latent heat associated with any phase changes occurring between absolute zero and temperature T (in Kelvin). For fine-grained permafrost, the amount of latent heat per-unit-volume associated with unfrozen water is,

$$L \;=\; \rho_u \phi_u L_f, \tag{7.9}$$

where L_f is the latent heat of fusion for water. The total enthalpy-per-volume for permafrost is then given by,

$$\rho H(T) \;=\; \rho \int_0^T c_p(T')\,dT' + \rho_u \phi_u L_f. \tag{7.10}$$

The volumetric heat capacity, defined by $C \equiv \rho\,(\partial H/\partial T)$, consists of a lattice-energy term and a latent-heat term,

$$C \;=\; \rho c_p \;+\; \rho_u L_f \frac{\partial \phi_u}{\partial T} \tag{7.11}$$

$$\rho c_p \;=\; (1-\phi)\rho_g c_{pg} + \phi_i \rho_i c_{pi} + \phi_u \rho_u c_{pu} + \phi_a \rho_a c_{pa} \quad \text{(lattice energy)} \tag{7.12}$$

$$\rho_u L_f \frac{\partial \phi_u}{\partial T} \;=\; (1-\phi)\rho_g L_f \frac{\partial w_u}{\partial T}, \qquad \text{(latent heat)} \tag{7.13}$$

where c_{pg}, c_{pi}, c_{pu}, and c_{pa} are the specific heats of the mineral grains, ice, unfrozen water, and air, respectively. For most argillaceous mineral grains, the density ρ_g is about 2650 kg m^{-3} and the specific heat c_{pg} is 890–900 J kg^{-1} K^{-1}. The specific heat of ice is given by,

$$c_{pi}(T) \;=\; 152.32 + 7.11590\,T, \qquad (\text{J kg}^{-1}\,\text{K}^{-1}) \tag{7.14}$$

where T is in Kelvin [*Yen*, 1981]. As noted by *Holten et al.* [2012], the specific heat of liquid water (c_{pu}) has a strong temperature dependence in the supercooled region, possibly due to a liquid–liquid critical point in the vicinity of 227 K. A least-squares fit using an 8$^{\text{th}}$-degree polynomial provides an adequate representation of the data reported by *Angell et*

al. [1982] below 270 K and to the International Association for the Properties of Water and Steam (IAPWS) 2008 values above 273 K (**Figure 7.4**).

Figure 7.5a shows the lattice-energy component (ρc_p) of the heat capacity for argillaceous materials such as those found in the NPR-A. The low specific heat of ice compared to that of unfrozen water causes the lattice-energy term to be smaller when the sediments are in a partially frozen state ($T < T_f$) than when completely thawed. For silty clay, the phase-transition term exceeds the lattice-energy term in the temperature range $-7°\mathrm{C} < T < T_f$ and becomes quite large as T approaches the freezing point, particularly at high porosities (**Figure 7.5b**). Other fine-grained materials behave in a similar way. As a result, for all temperatures encountered in the NPR-A, the total heat capacity C is substantially greater when the sediments are partially frozen than when thawed.

7.2.2.3 Thermal conductivity and diffusivity

Farouki [1981a, b] compared several methods for finding the thermal conductivity of frozen soils and found that for saturated or nearly saturated frozen fine-grained soils, the simple geometric mean gave the best match to available measurements. This method has also been commonly used to find the thermal conductivity of unfrozen aggregates [e.g., *Sass et al.*, 1971]. Ignoring the thermal conductivity of air, the thermal conductivity of saturated permafrost may then be written,

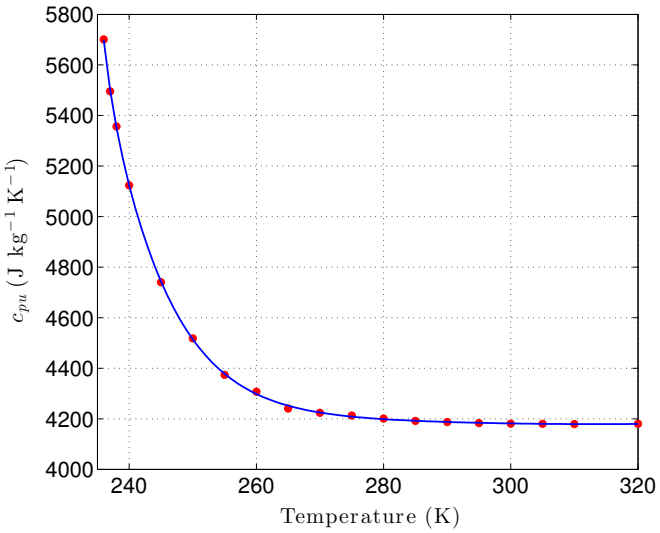

Figure 7.4: Specific heat of liquid water.

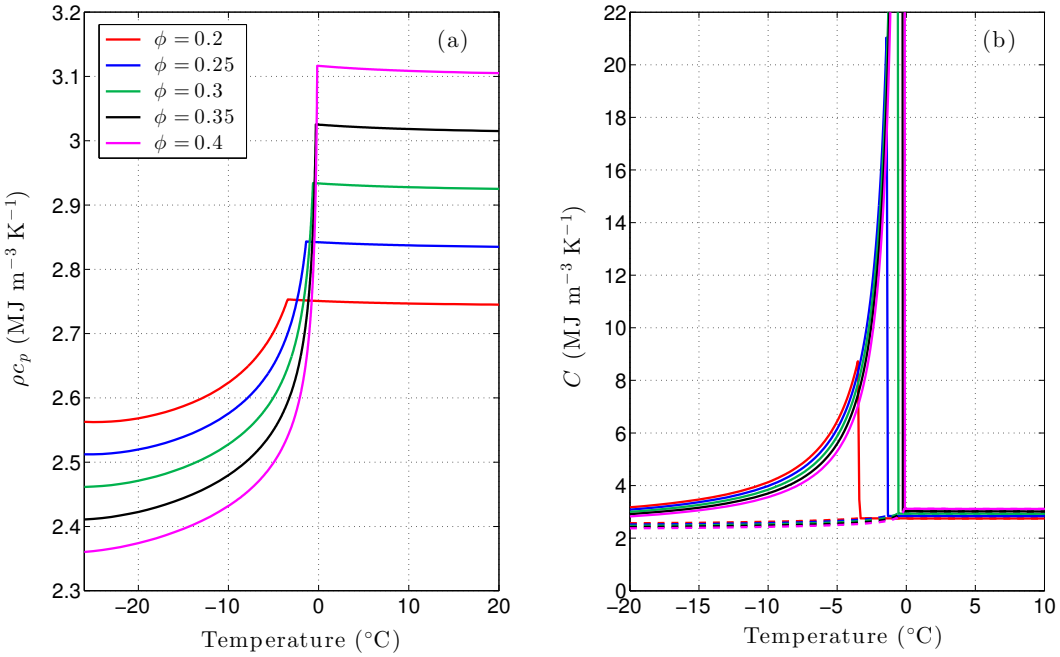

Figure 7.5: Lattice-energy component (ρc_p) of the heat capacity for argillaceous sediment at porosities ϕ ranging 20–40% (a). Panel (b) shows the total volumetric heat capacity C of a silty clay (solid lines) and the lattice-energy component for comparison (dashed lines).

$$\begin{aligned} K &= K_g^{(1-\phi)}\, K_i^{\phi_i}\, K_u^{\phi_u} \qquad \text{for } T < T_f \\ &= K_g^{(1-\phi)}\, K_u^{\phi_u}, \qquad\qquad T \geq T_f \end{aligned} \tag{7.15}$$

where K_g, K_i, and K_u are the mineral grain, ice, and unfrozen-water conductivities. All three components have a temperature dependence. For most silicate grains, the thermal conductivity decreases about 0.25% per kelvin [*Birch and Clark*, 1940]. The thermal conductivity of ice is best described by an exponential function of the form,

$$K_i(T) = a\, e^{-b\,T} \tag{7.16}$$

where $a = 9.828$ W m^{-1} K^{-1}, $b = 0.0057$ K^{-1}, and T is in Kelvin [*Yen*, 1981]. *Huber et al.* [2012] provide a correlating function for the thermal conductivity of water that extrapolates well down to −20°C. This function is a sum of four terms,

$$K_u(\tilde{T}) = \sum_{i=1}^{4} c_i\, \tilde{T}^{d_i} \tag{7.17}$$

where $\tilde{T} = T/(300\text{ K})$ and T is again in Kelvin. Constants c_1–c_4 are 1.6630, −1.7781, 1.1567, −0.432115 W m^{-1} K^{-1} while d_1–d_4 are −1.15, −3.4, −6.0, −7.6.

Figure 7.6 shows the bulk thermal conductivity K of a silty clay assuming the mean grain conductivity K_g^{25} is 1.85 W m^{-1} K^{-1} at 25°C (the superscript is used to designate the reference temperature). Since the thermal conductivity of liquid water (0.5–0.6 W m^{-1} K^{-1}) is much less than that of the matrix, the bulk conductivity K is sensitive to the unfrozen water content. As a result, K is sensitive to the porosity at temperatures exceeding the freezing point T_f and to the in-situ temperature when $T < T_f$. This produces a strong conductivity contrast at high porosities but only a subtle contrast at low porosities. This contrast should be reflected in the temperature gradient at locations where the temperature is near the freezing point.

The thermal diffusivity is a measure of a material's ability to conduct thermal energy relative to its ability to store it. Thus for permafrost, the thermal diffusivity is defined by,

$$\kappa = \frac{K}{C} = \frac{K}{\rho c_p + \rho_u L_f \dfrac{\partial \phi_u}{\partial T}}. \tag{7.18}$$

Figure 7.7 shows the thermal diffusivity for a silty clay assuming a mean grain conductivity K_g^{25} of 1.85 W m^{-1} K^{-1}. Due to the effects of unfrozen water, the thermal diffusivity for fine-grained materials such as silty clay are extraordinarily low in the temperature range typically experienced by permafrost in the NPR-A ($-10°$ to 0°C). Thus, the propagation of heat in fine-grained permafrost in response to temperature changes at a borehole wall

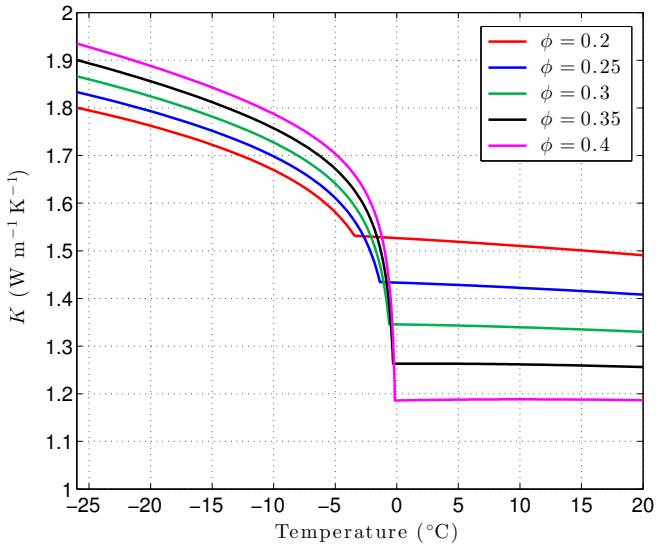

Figure 7.6: Thermal conductivity of a silty clay ($\mathcal{M} = 3$) assuming a grain conductivity K_g^{25} of 1.85 W m^{-1} K^{-1}.

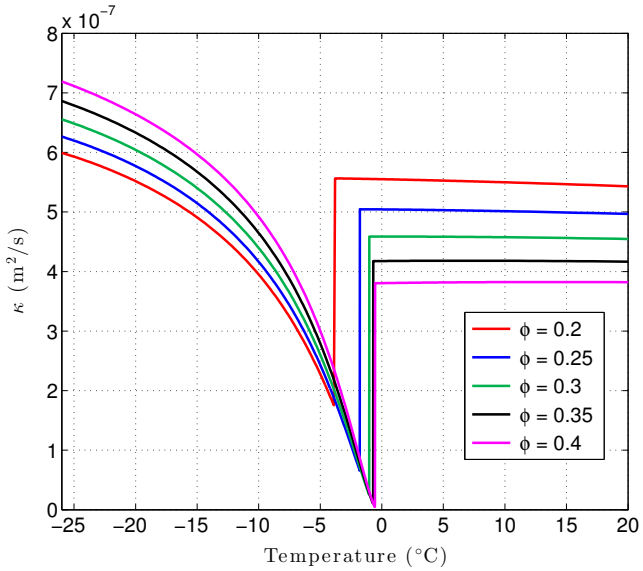

Figure 7.7: Thermal diffusivity of a silty clay ($\mathcal{M} = 3$) assuming a grain conductivity K_g^{25} of 1.85 W m^{-1} K^{-1}.

during drilling, or at the earth's surface due to climate change, is expected to proceed relatively slowly.

7.2.3 Numerical heat-transfer models

The Green's function solutions presented in Chapters 5 and 6 for assessing the thermal disturbance caused by drilling processes and surface modifications (engineering effects) assume the material properties K, ρ, C are homogeneous and independent of temperature. Section 7.2.2 indicates these assumptions are in general not satisfied for fine-grained permafrost. Numerical heat-transfer models potentially allow us to relax the assumptions regarding the material properties and treat permafrost in a more realistic way. In addition to giving a first assessment of the magnitude of the engineering effects, the Green's function solutions provide important analytic solutions for testing the numerical models.

Several standard approaches are used for developing numerical heat-transfer models, including finite-difference, finite-element, and control-volume methods. To date, all numerical heat-transfer models for permafrost have been based on the finite-difference and finite-element schemes [e.g., *Goodrich*, 1978; *Zhang*, 1993; *Noetzli et al.*, 2007; *Marchenko et al.*, 2008]. Although current models incorporate latent-heat effects and unfrozen water, nearly all of them are 1-dimensional, limiting their use for exploring thermal effects near

recently drilled boreholes or in the vicinity of drill pads, reserve pits, lakes, transgressing shorelines, and other local/regional-scale features with strong lateral gradients. The one known 3-dimensional permafrost model assumes the material in the problem domain is homogeneous and isotropic [*Noetzli et al.*, 2007], a severe restriction for the layered sediments of the Arctic Slope. In addition, nearly all the current models ignore the radiogenic heat production (source) term which is important when modeling the thermal field in thick continuous permafrost.

Given the importance of latent-heat effects, large contrasts in thermophysical properties over short distances (**Figures 7.5–7.7**), the likely presence of composite media, and the possibility of one or more moving phase-boundaries, the control-volume (CV) approach was selected for the development of cartesian and cylindrical numerical heat-transfer models for fine-grained permafrost. The CV approach has several advantages in this situation: (a) The numerical scheme can be designed to strictly conserve energy (and mass) in every finite volume. Thus, energy is not artificially created or destroyed at domain boundaries, phase boundaries, or strong material property contrasts [*Minkowycz et al.*, 1988; *Anderson et al.*, 1984]. (b) The expressions tend to be more accurate near boundaries. (c) The accuracy is unaffected by the use of non-uniform grids. (d) Since the governing equations are based on an energy balance, the resulting discretization equations have a specific physical interpretation which is useful during model development and verification.

When applied to internal energy, the starting point for the control-volume method is the integral form of the conservation-of-enthalpy equation (Eq. 7.1),

$$\int_V \frac{\partial}{\partial t}(\rho H)\, dV \;=\; -\int_V \nabla \cdot \mathbf{J}\, dV \;+\; \int_V S\, dV. \tag{7.19}$$

Integrating over a time step Δt, the conservation equation becomes,

$$\int_t^{t+\Delta t} \int_V \frac{\partial}{\partial t}(\rho H)\, dV dt \;=\; -\int_t^{t+\Delta t} \int_V \nabla \cdot \mathbf{J}\, dV dt \;+\; \int_t^{t+\Delta t} \int_V S\, dV dt. \tag{7.20}$$

The first term on the left reduces to,

$$\int_V \Big[(\rho H)^{n+1} - (\rho H)^n \Big]\, dV$$

where the superscripts refer to the time step following standard numerical nomenclature (i.e., $t^{n+1} = t^n + \Delta t$). Using Eq. (7.10), the enthalpy change per volume over a time step is,

$$(\rho H)^{n+1} - (\rho H)^n \;=\; \rho c_p \left(T^{n+1} - T^n\right) + \rho_u L_f \left[\phi_u(T^{n+1}) - \phi_u(T^n)\right].$$

Utilizing a Taylor expansion for ϕ_u, the enthalpy change can be written,

$$\begin{aligned}(\rho H)^{n+1} - (\rho H)^n &= \left[\rho c_p + \rho_u L_f \left.\frac{\partial \phi_u}{\partial T}\right|^{T^n}\right] \left(T^{n+1} - T^n\right) \\ &= C^n \left(T^{n+1} - T^n\right), \end{aligned} \tag{7.21}$$

where C^n is the volumetric heat capacity at time t^n. Substituting into Eq. (7.20), we can restate the enthalpy conservation equation as,

$$\int_V C^n \left(T^{n+1} - T^n\right) dV \;=\; -\int_t^{t+\Delta t} \int_V \nabla \cdot \mathbf{J}\, dV dt \;+\; \int_t^{t+\Delta t} \int_V S\, dV dt. \tag{7.22}$$

To proceed further, the problem domain and coordinate system must be specified.

7.2.3.1 One-dimensional vertical model

For a 1-D vertical problem, we consider a finite problem domain divided into discrete 'control-volumes'. Grid points are located at the centers of the control volumes, and on the upper and lower boundaries. Scalars such as temperature (T) and conductivity (K) are computed at the grid points while heat fluxes (J) are computed at the control-volume interfaces (**Figure 7.8**). Applying the enthalpy conservation equation (Eq. 7.22) to a 1-D vertical control volume, we have,

$$\int_{z_u}^{z_d} C^n \left(T^{n+1} - T^n\right) dz \;=\; \int_t^{t+\Delta t} (J_d - J_u)\, dt + \int_t^{t+\Delta t} \int_{z_u}^{z_d} S(z,t)\, dz\, dt. \tag{7.23}$$

Each integral appearing in Eq. (7.23) is now approximated to find a discretized version of the enthalpy equation. First, the enthalpy change integral is approximated by,

$$\int_{z_u}^{z_d} C^n \left(T^{n+1} - T^n\right) dz \;=\; \Delta z\, C_P^n \left(T_P^{n+1} - T_P^n\right) \tag{7.24}$$

where subscript P is used to denote values at the center of the control volume (grid point P) which are assumed to represent reasonable averages for the entire CV. Second, the heat-flux integral is written as a linear combination of values at either end of the time step,

$$\int_t^{t+\Delta t} (J_d - J_u)\; dt \;=\; \Delta t \left[f(J_d - J_u)^{n+1} \;+\; (1-f)(J_d - J_u)^n\right]. \tag{7.25}$$

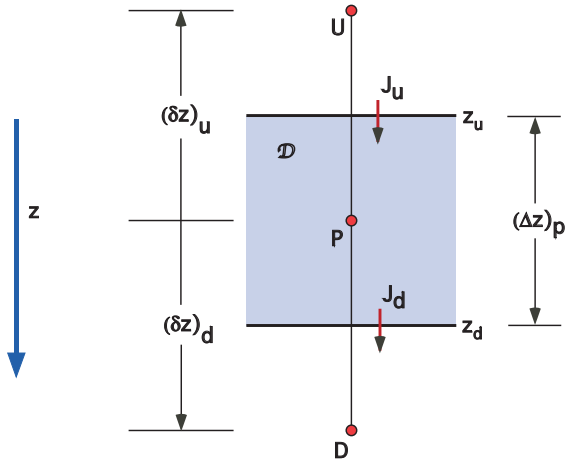

Figure 7.8: Schematic showing the nomenclature associated with a control-volume in the interior of the 1-D vertical model. The control-volume is bounded by interfaces at depths z_u and z_d, through which fluxes J_u and J_d pass. Grid point P is located at the center of the CV. Grid points U and D are located at the center of the adjacent control volumes.

Here, we introduce the explicit/implicit weighting factor f. Setting $f = 0$ produces a fully explicit code while $f = 1$ is fully implicit. Following *Patankar* [1980], the heat fluxes at the interfaces are written as,

$$J_u = -\frac{\tilde{K}_u}{(\delta z)_u}\,(T_P - T_U) \tag{7.26}$$

$$J_d = -\frac{\tilde{K}_d}{(\delta z)_d}\,(T_D - T_P) \tag{7.27}$$

where $\tilde{K}_u$ and $\tilde{K}_d$ are the 'effective' conductivities on the upper and lower interfaces, defined by,

$$\tilde{K}_u = \left[\frac{1}{\dfrac{(1-\varepsilon_u)}{K_U} + \dfrac{\varepsilon_u}{K_P}}\right], \qquad \tilde{K}_d = \left[\frac{1}{\dfrac{(1-\varepsilon_d)}{K_P} + \dfrac{\varepsilon_d}{K_D}}\right], \tag{7.28}$$

with fractional distances,

$$\varepsilon_u = \left(\frac{z_P - z_u}{z_P - z_U}\right), \qquad \varepsilon_d = \left(\frac{z_D - z_d}{z_D - z_P}\right). \tag{7.29}$$

The use of effective conductivities guarantees the heat fluxes exactly balance at the interface between materials with different properties (e.g., composite media). Leaving the source term in a very general form, we let

$$\mathcal{S}_P = \Delta t \int_{z_u}^{z_d} S(z,t)\,dz\,. \tag{7.30}$$

Substituting Eqs (7.24)–(7.27) and (7.30) into Eq. (7.23), the discrete form of the enthalpy balance for the control volume centered on P is,

$$\Delta z\, C_P^n \left(T_P^{n+1} - T_P^n\right) + \Delta t\, f \left[-\frac{\tilde{K}_d}{(\delta z)_d}\left(T_D^{n+1} - T_P^{n+1}\right) + \frac{\tilde{K}_u}{(\delta z)_u}\left(T_P^{n+1} - T_U^{n+1}\right)\right] + \Delta t\,(1-f)\left[-\frac{\tilde{K}_d}{(\delta z)_d}\left(T_D^n - T_P^n\right) + \frac{\tilde{K}_u}{(\delta z)_u}\left(T_P^n - T_U^n\right)\right] \;=\; \mathcal{S}_P. \tag{7.31}$$

This can then be rewritten as,

$$a_P T_P^{n+1} \;=\; a_U T_U^{n+1} + a_D T_D^{n+1} + a'_U T_U^n \;+\; a'_D T_D^n \;+\; a'_P T_P^n \;+\; b \tag{7.32}$$

with discretization coefficients,

$$\left[\begin{array}{lcllcl} a_U &=& \Delta t\, f\, \dfrac{\tilde{K}_u}{(\delta z)_u}, & a'_U &=& \Delta t\,(1-f)\,\dfrac{\tilde{K}_u}{(\delta z)_u} \\ a_D &=& \Delta t\, f\, \dfrac{\tilde{K}_d}{(\delta z)_d}, & a'_D &=& \Delta t\,(1-f)\,\dfrac{\tilde{K}_d}{(\delta z)_d} \\ a_P &=& \Delta z\, C_P^n + (a_U + a_D), & a'_P &=& \Delta z\, C_P^n - (a'_U + a'_D) \\ b &=& \mathcal{S}_P. & & & \end{array}\right. \tag{7.33}$$

These coefficients apply to all the interior control volumes. Consideration of the enthalpy balance shows that the coefficients are slightly different for CVs adjacent to the boundaries. For a control volume adjacent to a boundary with a prescribed temperature (Dirichlet BC), a factor of $(4/3)$ is introduced into the coefficients associated with the boundary and the opposing interface; this factor improves the estimated heat flux at the boundary. Thus, if the temperature on the upper boundary is specified [e.g., $T_U = T_s(t)$], the coefficients for the upper CV become,

$$\left[\begin{array}{lcllcl} a_U &=& \left(\frac{4}{3}\right)\Delta t\, f\, \dfrac{\tilde{K}_u}{(\delta z)_u}, & a'_U &=& \left(\frac{4}{3}\right)\Delta t\,(1-f)\,\dfrac{\tilde{K}_u}{(\delta z)_u} \\ a_D &=& \left(\frac{4}{3}\right)\Delta t\, f\, \dfrac{\tilde{K}_d}{(\delta z)_d}, & a'_D &=& \left(\frac{4}{3}\right)\Delta t\,(1-f)\,\dfrac{\tilde{K}_d}{(\delta z)_d} \\ a_P &=& \Delta z\, C_P^n + (a_U + a_D), & a'_P &=& \Delta z\, C_P^n - (a'_U + a'_D) \\ b &=& \mathcal{S}_P. & & & \end{array}\right. \tag{7.34}$$

When the heat flux is prescribed on a boundary (Neumann BC), the coefficients associated with the boundary are zero, and the specified heat flux appears in discretization coefficient b. Thus, if the heat flux on the lower boundary is specified [e.g., $J_d = q_b(t)$], the discretization coefficients for the lowest CV become,

$$\left[\begin{array}{lcllcl} a_U &=& \Delta t\, f\, \dfrac{\tilde{K}_u}{(\delta z)_u}\,, & a'_U &=& \Delta t\,(1-f)\,\dfrac{\tilde{K}_u}{(\delta z)_u} \\ a_D &=& 0\,, & a'_D &=& 0 \\ a_P &=& \Delta z\, C_P^n \,+\, (a_U + a_D)\,, & a'_P &=& \Delta z\, C_P^n \,-\, (a'_U + a'_D) \\ b &=& \mathcal{S}_P \,-\, \Delta t \left[f\, q_b^{n+1} + (1-f)\, q_b^n \right]. & & & \end{array}\right. \tag{7.35}$$

With the discretization coefficients defined for all of the control volumes, the discretization equation (Eq. 7.32) can be solved recursively at each time step using the TriDiagonal Matrix Algorithm, TDMA [*Patankar*, 1980]. Given their temperature sensitivities, w_u, ϕ_u, K, and C are updated at every time step using the thermophysical model developed in Section 7.2.2. In order for the numerical scheme to remain unconditionally stable, all of the discretization coefficients must be ≥ 0. This consideration leads to the numerical stability condition for the 1-D vertical model,

$$\Delta t \;<\; \frac{\Delta z\, C_P^n}{(1-f)\left[\dfrac{\tilde{K}_u}{(\delta z)_u} + \dfrac{\tilde{K}_d}{(\delta z)_d}\right]}\,. \tag{7.36}$$

For a uniform grid with homogenous physical properties, this reduces to the more familiar form,

$$\Delta t \;<\; \frac{(\Delta z)^2}{2(1-f)\kappa}\,.$$

Once the vertical grid is selected, the time step Δt must be set to satisfy the numerical stability condition (Eq. 7.36). An interesting facet of the model is that the high volumetric heat capacity that occurs below the freezing temperature T_f (**Figure 7.5**) enhances numerical stability. However, the stability will be diminished should a CV completely thaw ($T > T_f$). Thus, the stability condition should be checked periodically during a model run and the time step adjusted accordingly.

7.2.3.2 One-dimensional radial model

Development of a 1-D radial model is very similar to that used for the 1-D vertical model. We begin again with the integral form of the enthalpy conservation equation (Eq. 7.22), approximate the integrals, and derive a discrete form for the energy balance of a control volume; nomenclature for the radial model is shown in **Figure 7.9**. Grid points are

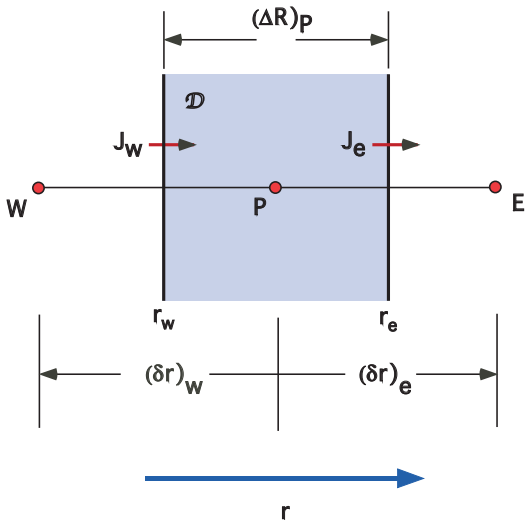

Figure 7.9: Schematic showing the nomenclature associated with a control-volume in the interior of the 1-D radial model. The control-volume is bounded by interfaces at radial distances r_w and r_e, through which fluxes J_w and J_e pass. Grid point P is located at the center of the CV. Grid points W and E are located at the center of the adjacent control volumes.

again located at the centers of the control volumes, and on the inner and outer boundaries.

The resulting discretization equation is,

$$a_P T_P^{n+1} \;=\; a_W T_W^{n+1} + a_E T_E^{n+1} + a'_W T_W^n \;+\; a'_E T_E^n \;+\; a'_P T_P^n \;+\; b \tag{7.37}$$

with discretization coefficients,

$$\left[\begin{array}{lcllcl} a_W &=& \Delta t\, f\, \dfrac{r_w \tilde{K}_w}{(\delta r)_w}\,, & a'_W &=& \Delta t\,(1-f)\, \dfrac{r_w \tilde{K}_w}{(\delta r)_w} \\ a_E &=& \Delta t\, f\, \dfrac{r_e \tilde{K}_e}{(\delta r)_e}\,, & a'_E &=& \Delta t\,(1-f)\, \dfrac{r_e \tilde{K}_e}{(\delta r)_e} \\ a_P &=& \Lambda\, C_P^n \;+\; (a_W + a_E)\,, & a'_P &=& \Lambda\, C_P^n \;-\; (a'_W + a'_E) \\ b &=& \mathcal{S}_P & & & \end{array}\right. \tag{7.38}$$

for the internal control volumes. The spatial factor Λ is defined to be $(r_e^2 - r_w^2)/2$.

Effective conductivities for the radial model are given by,

$$\tilde{K}_w \;=\; \frac{1}{\dfrac{(1-\varepsilon_w)}{K_W} + \dfrac{\varepsilon_w}{K_P}}, \qquad \tilde{K}_e \;=\; \frac{1}{\dfrac{(1-\varepsilon_e)}{K_P} + \dfrac{\varepsilon_e}{K_E}}, \tag{7.39}$$

with fractional distances,

$$\varepsilon_w \;=\; \left(\frac{r_P - r_w}{r_P - r_W}\right), \qquad \varepsilon_e \;=\; \left(\frac{r_E - r_e}{r_E - r_P}\right), \tag{7.40}$$

while the source term integral is,

$$\mathcal{S}_P \;=\; \Delta t \int_{r_w}^{r_e} S(r,t)\, r\, dr. \tag{7.41}$$

Consideration of the enthalpy balance for the control volumes adjacent to the boundaries leads to discretization coefficients that are modified in the same way as for the 1-D vertical case: (1) A factor of $(4/3)$ is introduced into coefficients associated with the boundary and opposing interface when the boundary temperature is prescribed (Dirichlet BC). (2) Coefficients associated with a boundary are set to zero for a Neumann BC and the prescribed heat flux included in the discretization coefficient b (**Table 7.1**). An additional situation that sometimes occurs with the radial geometry is that the problem domain extends to $r = 0$ so that no inner boundary condition exists. In this case, the discretization coefficients for the innermost CV are the same as for the internal CVs (Eq. 7.38).

As with the 1-D vertical model, the discretization equation (Eq. 7.37) can be solved recursively using TDMA once the discretization coefficients have been defined for all the

Table 7.1: Discretization coefficient b for a control volume adjacent to a prescribed heat-flux boundary condition.

Coordinate System	Prescribed Heat Flux	b
R	min(R): $q_a(t)$	$\mathcal{S}_P + \Delta t \left[f\, r_w\, q_a^{n+1} + (1-f)\, r_w\, q_a^n \right]$
	max(R): $q_o(t)$	$\mathcal{S}_P - \Delta t \left[f\, r_e\, q_o^{n+1} + (1-f)\, r_e\, q_o^n \right]$
Z	min(Z): $q_s(t)$	$\mathcal{S}_P + \Delta t \left[f\, q_s^{n+1} + (1-f)\, q_s^n \right]$
	max(Z): $q_b(t)$	$\mathcal{S}_P - \Delta t \left[f\, q_b^{n+1} + (1-f)\, q_b^n \right]$
RZ	min(R): $q_a(t)$	$\mathcal{S}_P + \Delta z\, \Delta t \left[f\, r_w\, q_a^{n+1} + (1-f)\, r_w\, q_a^n \right]$
	max(R): $q_o(t)$	$\mathcal{S}_P - \Delta z\, \Delta t \left[f\, r_e\, q_o^{n+1} + (1-f)\, r_e\, q_o^n \right]$
	min(Z): $q_s(t)$	$\mathcal{S}_P + \Lambda\, \Delta t \left[f\, q_s^{n+1} + (1-f)\, q_s^n \right]$
	max(Z): $q_b(t)$	$\mathcal{S}_P - \Lambda\, \Delta t \left[f\, q_b^{n+1} + (1-f)\, q_b^n \right]$
XYZ	min(X): $q_a(t)$	$\mathcal{S}_P + \Delta y\, \Delta z\, \Delta t \left[f\, q_a^{n+1} + (1-f)\, q_a^n \right]$
	max(X): $q_o(t)$	$\mathcal{S}_P - \Delta y\, \Delta z\, \Delta t \left[f\, q_o^{n+1} + (1-f)\, q_o^n \right]$
	min(Y): $q_c(t)$	$\mathcal{S}_P + \Delta x\, \Delta z\, \Delta t \left[f\, q_c^{n+1} + (1-f)\, q_c^n \right]$
	max(Y): $q_d(t)$	$\mathcal{S}_P - \Delta x\, \Delta z\, \Delta t \left[f\, q_d^{n+1} + (1-f)\, q_d^n \right]$
	min(Z): $q_s(t)$	$\mathcal{S}_P + \Delta x\, \Delta y\, \Delta t \left[f\, q_s^{n+1} + (1-f)\, q_s^n \right]$
	max(Z): $q_b(t)$	$\mathcal{S}_P - \Delta x\, \Delta y\, \Delta t \left[f\, q_b^{n+1} + (1-f)\, q_b^n \right]$

CVs. The radial model is unconditionally stable when the time step satisfies,

$$\Delta t \;<\; \frac{\Lambda\, C_P^n}{(1-f)\left[\dfrac{r_w \tilde{K}_w}{(\delta r)_w} + \dfrac{r_e \tilde{K}_e}{(\delta r)_e}\right]}\,. \tag{7.42}$$

7.2.3.3 Two-dimensional cylindrical model

The 2-D cylindrical model builds on elements of the 1-D vertical and 1-D radial models, using the same nomenclature and boundary conditions. Considering the enthalpy balance of a 2-D cylindrical control volume, the discretization equation can be expressed by,

$$\begin{aligned} a_P T_P^{n+1} \;=\; & a_W T_W^{n+1} + a_E T_E^{n+1} + a_U T_U^{n+1} + a_D T_D^{n+1} \\ & + a'_W T_W^n + a'_E T_E^n + a'_U T_U^n + a'_D T_D^n + a'_P T_P^n + b \end{aligned} \tag{7.43}$$

with internal CV discretization coefficients,

$$\left[\begin{array}{lcllcl} a_W &=& \Delta z\,\Delta t\, f\,\dfrac{r_w \tilde{K}_w}{(\delta r)_w}\,, & a'_W &=& \Delta z\,\Delta t\,(1-f)\,\dfrac{r_w \tilde{K}_w}{(\delta r)_w} \\ a_E &=& \Delta z\,\Delta t\, f\,\dfrac{r_e \tilde{K}_e}{(\delta r)_e}\,, & a'_E &=& \Delta z\,\Delta t\,(1-f)\,\dfrac{r_e \tilde{K}_e}{(\delta r)_e} \\ a_U &=& \Lambda\Delta t\, f\,\dfrac{\tilde{K}_u}{(\delta z)_u}\,, & a'_U &=& \Lambda\Delta t\,(1-f)\,\dfrac{\tilde{K}_u}{(\delta z)_u} \\ a_D &=& \Lambda\Delta t\, f\,\dfrac{\tilde{K}_d}{(\delta z)_d}\,, & a'_D &=& \Lambda\Delta t\,(1-f)\,\dfrac{\tilde{K}_d}{(\delta z)_d} \\ a_P &=& \Lambda\Delta z\, C_P^n \;+\; (a_W + a_E) \;+\; (a_U + a_D) & & & \\ a'_P &=& \Lambda\,\Delta z\, C_P^n \;-\; (a'_W + a'_E) \;-\; (a'_U + a'_D) & & & \\ b &=& \mathcal{S}_P. & & & \end{array}\right. \tag{7.44}$$

Here, the source term integral is given by,

$$\mathcal{S}_P \;=\; \Delta t \int_{z_u}^{z_d}\int_{r_w}^{r_e} S(r,z,t)\, r\, dr\, dz. \tag{7.45}$$

Discretization coefficients for the control volumes adjacent to the boundaries are modified in the same way as for the 1-D vertical and 1-D radial models; expressions for coefficient b on the four boundaries are listed in **Table 7.1**.

For the 2-D model, the line-by-line method utilizing TDMA alternately between the radial and vertical directions can be used to efficiently solve the discretization equation

(Eq. 7.43). Considering the requirement that all discretization coefficients must be ≥ 0 for the scheme to be stable, the numerical stability condition for the 2-D cylindrical model is,

$$\Delta t \; < \; \frac{\Lambda \, \Delta z \, C_P^n}{(1-f)\left\{\Delta z\left[\dfrac{r_w \tilde{K}_w}{(\delta r)_w} + \dfrac{r_e \tilde{K}_e}{(\delta r)_e}\right] + \Lambda\left[\dfrac{\tilde{K}_u}{(\delta z)_u} + \dfrac{\tilde{K}_d}{(\delta z)_d}\right]\right\}}. \tag{7.46}$$

7.2.3.4 Three-dimensional cartesian model

Extending the 1-D vertical model to three dimensions in the cartesian coordinate system, the enthalpy balance for a control volume can be written as,

$$\begin{aligned} a_P T_P^{n+1} &= a_W T_W^{n+1} + a_E T_E^{n+1} + a_S T_S^{n+1} + a_N T_N^{n+1} + a_U T_U^{n+1} + a_D T_D^{n+1} \\ &+ a'_W T_W^n + a'_E T_E^n + a'_S T_S^n + a'_N T_N^n + a'_U T_U^n + a'_D T_D^n + a'_P T_P^n + b \end{aligned} \tag{7.47}$$

where grid points W and E lie along the x-axis while S and N lie along the y-axis. Discretization coefficients for the internal CVs are,

$$\left[\begin{array}{lcll} a_W &=& \Delta y\,\Delta z\,\Delta t\, f\,\dfrac{\tilde{K}_w}{(\delta x)_w} & a'_W \;=\; \Delta y\,\Delta z\,\Delta t\,(1-f)\,\dfrac{\tilde{K}_w}{(\delta x)_w} \\ a_E &=& \Delta y\,\Delta z\,\Delta t\, f\,\dfrac{\tilde{K}_e}{(\delta x)_e} & a'_E \;=\; \Delta y\,\Delta z\,\Delta t\,(1-f)\,\dfrac{\tilde{K}_e}{(\delta x)_e} \\ a_S &=& \Delta x\,\Delta z\,\Delta t\, f\,\dfrac{\tilde{K}_s}{(\delta y)_s} & a'_S \;=\; \Delta x\,\Delta z\,\Delta t\,(1-f)\,\dfrac{\tilde{K}_s}{(\delta y)_s} \\ a_N &=& \Delta x\,\Delta z\,\Delta t\, f\,\dfrac{\tilde{K}_n}{(\delta y)_n} & a'_N \;=\; \Delta x\,\Delta z\,\Delta t\,(1-f)\,\dfrac{\tilde{K}_n}{(\delta y)_n} \\ a_U &=& \Delta x\,\Delta y\,\Delta t\, f\,\dfrac{\tilde{K}_u}{(\delta z)_u} & a'_U \;=\; \Delta x\,\Delta y\,\Delta t\,(1-f)\,\dfrac{\tilde{K}_u}{(\delta z)_u} \\ a_D &=& \Delta x\,\Delta y\,\Delta t\, f\,\dfrac{\tilde{K}_d}{(\delta z)_d} & a'_D \;=\; \Delta x\,\Delta y\,\Delta t\,(1-f)\,\dfrac{\tilde{K}_d}{(\delta z)_d} \\ a_P &=& \Delta x\,\Delta y\,\Delta z\,C_P^n \;+\; (a_W + a_E) \;+\; (a_S + a_N) \;+\; (a_U + a_D) & \\ a'_P &=& \Delta x\,\Delta y\,\Delta z\,C_P^n \;-\; (a'_W + a'_E) \;-\; (a'_S + a'_N) \;-\; (a'_U + a'_D) & \\ b &=& \mathcal{S}_P, & \end{array}\right. \tag{7.48}$$

with the source-term integral defined by,

$$\mathcal{S}_P \;=\; \Delta t \int_{z_u}^{z_d}\int_{y_s}^{y_n}\int_{x_w}^{x_e} S(x,y,z,t)\,dx\,dy\,dz. \tag{7.49}$$

Effective conductivities $\tilde{K}_s$ and $\tilde{K}_n$ are defined in a completely analogous way to their x-axis counterparts, $\tilde{K}_w$ and $\tilde{K}_e$.

Once again, the discretization coefficients for the CVs adjacent to the boundaries are modified in the same way as for the 1-D models. With all the coefficients defined, the discretization equation (Eq. 7.47) can be solved using the line-by-line method with TDMA. For the full 3-D cartesian model, the numerical stability condition takes the form,

$$\Delta t < \frac{\Delta x\,\Delta y\,\Delta z\,C_P^n}{(1-f)\left\{\Delta y\Delta z\left[\frac{\tilde{K}_w}{(\delta x)_w}+\frac{\tilde{K}_e}{(\delta x)_e}\right]+\Delta x\Delta z\left[\frac{\tilde{K}_s}{(\delta y)_s}+\frac{\tilde{K}_n}{(\delta y)_n}\right]+\Delta x\Delta y\left[\frac{\tilde{K}_u}{(\delta z)_u}+\frac{\tilde{K}_d}{(\delta z)_d}\right]\right\}}. \tag{7.50}$$

This condition must be satisfied in each CV for the scheme to remain unconditionally stable.

7.3 Numerical examples

7.3.1 Drilling disturbance revisited

As shown in Chapter 5, latent-heat effects strongly modify the recovery of temperatures near a well drilled through permafrost. Here, we consider the drilling of the Tunalik Test Well #1 in the western NPR-A using the 2-D cylindrical control-volume model. This 34-cm diameter well took 418 days of continuous drilling, ultimately reaching a total depth of 6198 m. To simulate the dissipation of the drilling disturbance surrounding this well, we select the following values for necessary parameters: porosity $\phi = 0.33$, sediment type $\mathcal{M} = 2.66$ (66% silty clay, 34% silt), mean grain conductivity $K_g^{25} = 1.7$ W m^{-1} K^{-1}, pore water salinity $s = 4.9$ ppt, and geothermal flux $q_b = 58$ W m^{-2}. With these values, the freezing point T_f is -0.73°C which puts the base of ice-rich permafrost (B-IRP) at this location at 271 m. **Figure 7.10** shows a snapshot of the temperature field and drilling disturbance surrounding the well 332 days after borehole completion. High heat-capacity values indicate locations where pore water is refreezing in significant quantities (**Figure 7.10b**). On day 332, refreezing is occurring at the 70–220 m depths near the borehole wall; several meters away from the borehole, pore water is refreezing slightly above the B-IRP (271 m). As expected, the drilling disturbance ΔT_d is much greater above the B-IRP as latent-heat effects retard the cooling of temperatures following the heat input caused by drilling. Also apparent is a minimum in the drilling disturbance at about 255 m near the borehole wall. *Lachenbruch et al.* [1982] predicted a drilling disturbance minimum should occur at or very near the B-IRP. The availability of the 2-D heat-transfer model allows us to

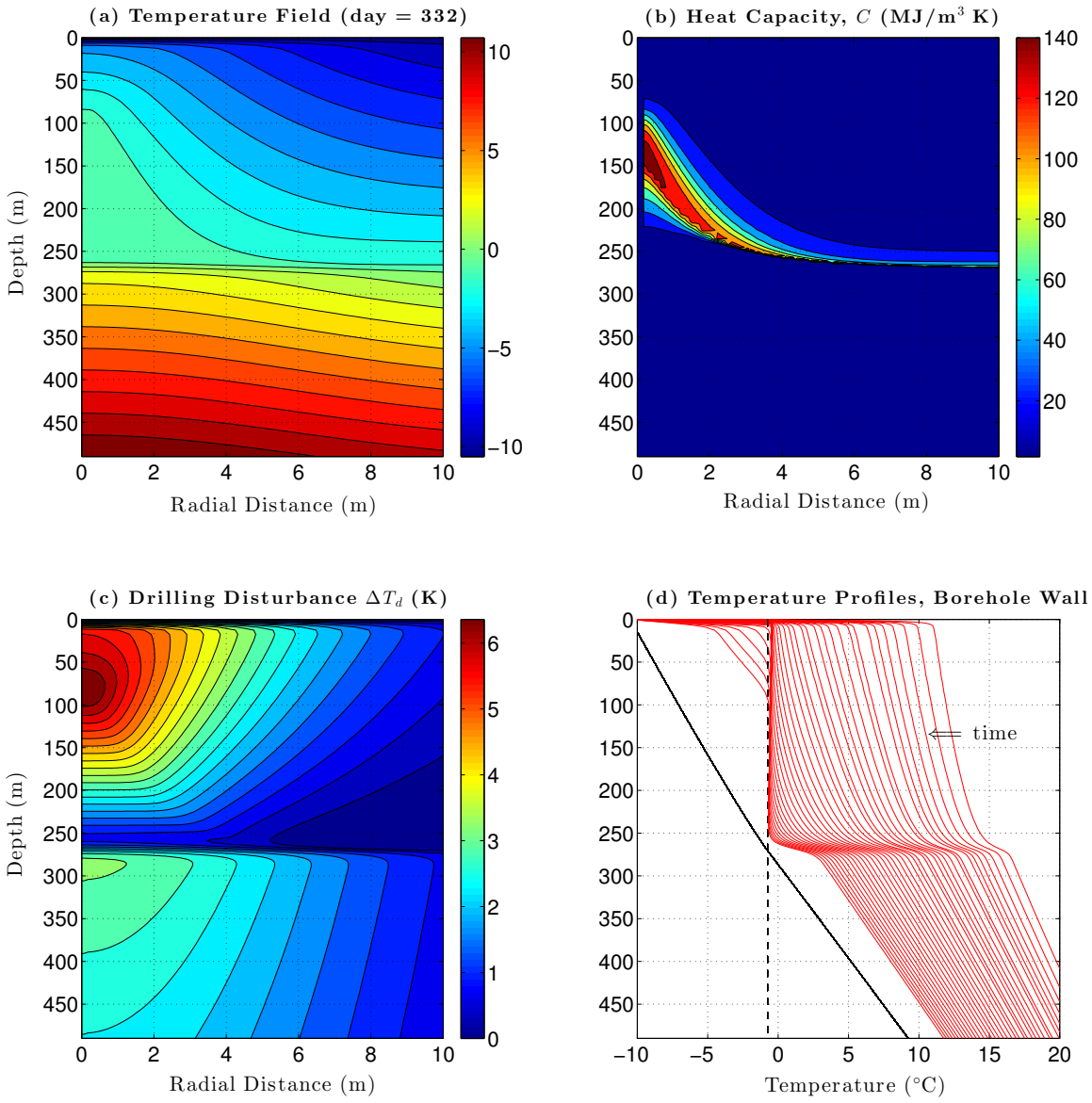

Figure 7.10: Snapshot of the simulated temperature field (a), volumetric heat capacity (b), and drilling disturbance ΔT_d (c), 332 days after the completion of the Tunalik Test Well. Panel (d) shows the evolution of temperatures along the borehole wall from 4 to 332 days after well completion. Solid black line in (d) is the undisturbed formation temperature while the dashed line indicates the freezing point, T_f.

examine this prediction in more detail. For fine-grained permafrost, the minimum drilling disturbance initially occurs several tens of meters above the B-IRP (**Figure 7.11**). Over time, the minimum disturbance migrates downwards as the freezing front moves down the borehole wall. A reduction of the drilling disturbance near the earth's surface is also apparent as predicted by the 2-D Green's function solution proposed by *Clow* [2015].

7.3.2 Reserve pit disturbance

Given the lateral offset of the reserve pits from the well-heads, the magnitude of the reserve-pit disturbance T_{bc}^{pit} at the wells is expected to be sensitive to the thermal diffusivity of the intervening material (Chapter 6). The thermal diffusivity, in turn, depends on the temperature, sediment texture, and porosity. Here we explore the sensitivity of T_{bc}^{pit} to sediment type and porosity using the 3-D cartesian control-volume model. The reserve pit is assumed to have dimensions similar to that found at the Peard Bay Test Bay (110 m $\times$ 106 m); the edge of the reserve pit is 15 m from the well-head. For these tests, the local surface temperature T_s is fixed at -10°C, the geothermal flux at 40 mW m^{-2}, and the grain conductivity at 1.2 W m^{-1} K^{-1}. The reserve pit is instantaneously created at year 0; initially 4 K warmer than the surrounding terrain, the reserve pit warms at a linear rate until it is

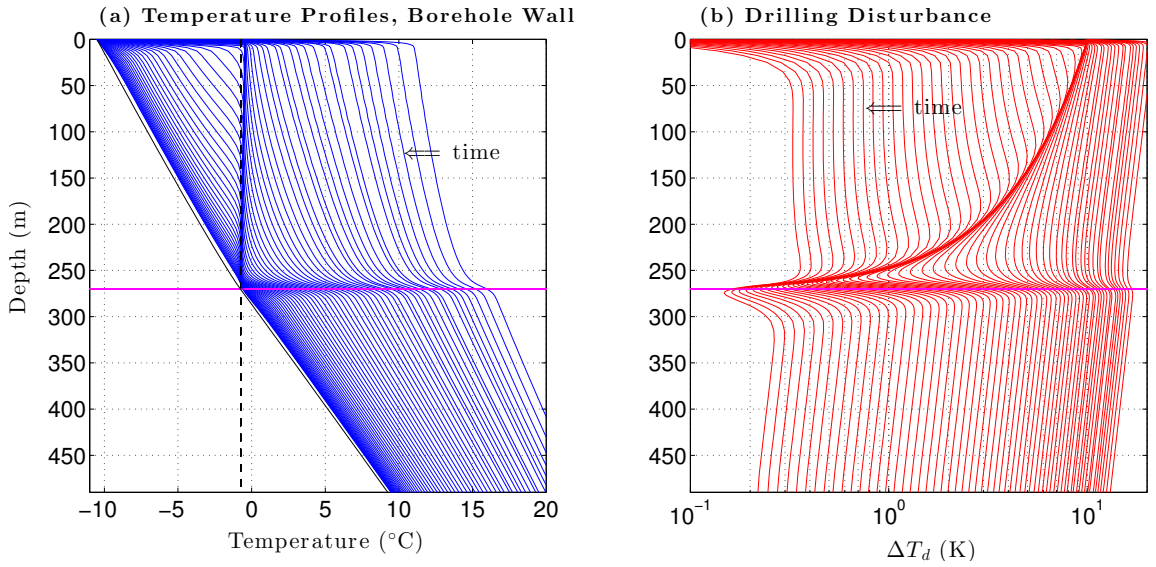

Figure 7.11: Evolution of temperatures and the associated drilling disturbance along the borehole wall for the Tunalik Test Well from 4 to 5900 days after borehole completion. Horizontal magenta lines indicate the base of ice-rich permafrost (B-IRP). Dashed line in (a) indicates the freezing point T_f.

9 K warmer than T_s by year 35 (see discussion in Chapter 6).

Sensitivity tests confirm the magnitude of the reserve-pit disturbance is largely controlled by the thermal diffusivity (**Figure 7.12**). Thus, reserve pits created in fine sand or silt ($\mathcal{M}$ = 1–2) are expected to produce the greatest thermal disturbance T_{bc}^{pit} at the well-heads while those created in silty clay or kaolinite-rich sediments ($\mathcal{M}$ = 3–4) should have the least. In general, low porosities reduce the disturbance slightly. An exception to this behavior occurs when the materials are always warmer than their freezing point temperature T_f. As discussed in Section 7.2.2, silty clays and kaolinite-rich sediments tend to have large freezing point depressions, especially at low porosities. At a porosity of 15%, silty clays and kaolinite are always above the freezing point in these simulations. This accounts for the moderately high thermal diffusivity κ and thermal disturbance T_{bc}^{pit} at $\phi = 0.15$ for sediments $\mathcal{M} \geq 2.9$ (**Figure 7.12**). The nonlinearity of the heat capacity beneath the reserve pit leads to an additional short rapid-rise in the thermal disturbance curves at $T_{bc}^{pit} \approx 0.55$ K at the 20-m depth and at $T_{bc}^{pit} \approx 0.2$ K at the 40-m depth (**Figure 7.12**).

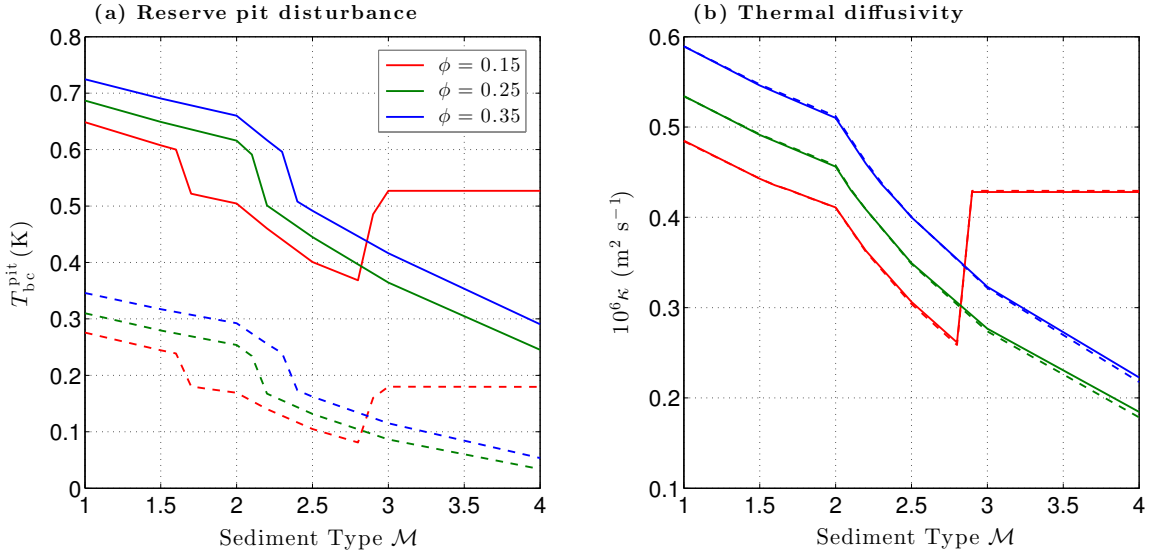

Figure 7.12: Sensitivity of the reserve pit disturbance to sediment type and porosity. T_{bc}^{pit} is shown in (a) assuming the pit was created 35 years earlier. Solid and dashed lines show the disturbance at the 20- and 40-m depths at the well location, respectively. The well-head is 15 m from the edge of the reserve pit in these simulations. Panel (b) shows the thermal diffusivity of the material between the reserve pit and the well-head.

7.3.3 Climate change sensitivities

The sequence of temperature logs acquired in each DOI/GTN-P borehole represents the local response of permafrost to changing boundary conditions at both the borehole wall and at the earth's surface. In this example, we focus on just the climate effects by exploring the response of fine-grained permafrost to a 1 K/decade climate warming for a period of 50 years using the 1-D vertical model. The surface temperature is initially $-9°$C while the geothermal flux and grain conductivity are fixed at $q_b = 50$ W m^{-2} and $K_g^{25} = 1.85$ W m^{-1} K^{-1}, respectively.

Numerical simulations show that the thermal response of high-porosity ($\phi = 0.40$) permafrost strongly depends on the sediment type (**Figure 7.13a**). This is almost entirely due to the sensitivity of the heat capacity and thermal diffusivity to the unfrozen water content of the different sediment types; C and κ vary by a factor of 4 for sediment types $\mathcal{M} = 1$–4 (**Figure 7.13c, d**). Hence, the climate warming is predicted to penetrate to much greater depths by year 50 for silt and fine sand than it is for kaolinite or silty clay. The simulations also reveal the extent to which the thermal properties change as the surface warms. For sediment types tending to have higher unfrozen water contents ($\mathcal{M} \geq 3$), the heat capacity increases by a factor of two at shallow depths during the 50-yr simulation while the thermal diffusivity decreases by a factor of two. The thermal conductivity also changes but to a lesser extent (**Figure 7.13b**).

At low porosities, the thermal response becomes more complicated due to the large freezing point depression that occurs for some sediment types (**Figure 7.3**). This is apparent in the low-porosity ($\phi = 0.20$) simulations shown in **Figure 7.14**; all other parameters are identical to those used for the high-porosity simulations. In the low-porosity case, the entire temperature profile for kaolinite ($\mathcal{M} = 4$) is warmer than its freezing point while the profiles for the other sediment types are below their freezing points, at least down to 130 m. Comparison of the thermal responses for kaolinite in **Figure 7.13** and **Figure 7.14** demonstrates the importance of the porosity to the response, especially for sediment types $\mathcal{M} \geq 3$. These sediment types may be on either side of their freezing points for conditions encountered in the NPR-A, depending on the porosity.

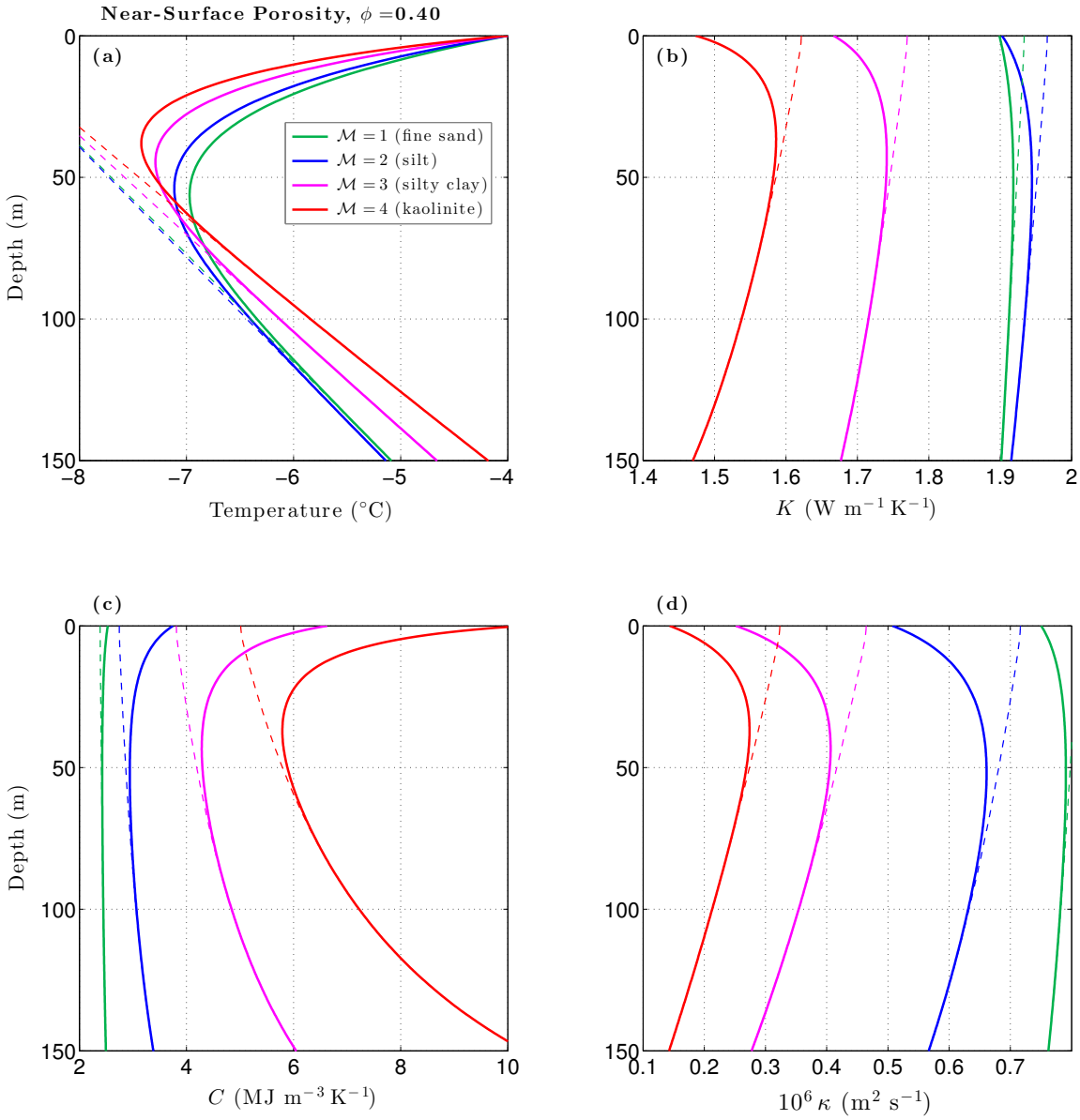

Figure 7.13: Response of high-porosity ($\phi = 0.40$) permafrost to a 1 K/decade warming for 50 years for sediment types $\mathcal{M} = 1$–4 (a). The initial surface temperature was -9°C, the geothermal heat flux $q_b = 50$ W m^{-2}, and the grain conductivity $K_g^{25} = 1.85$ W m^{-1} K^{-1}. Panel (b) shows the thermal conductivity, (c) the volumetric heat capacity, and (d) the thermal diffusivity. Dashed lines show the initial values.

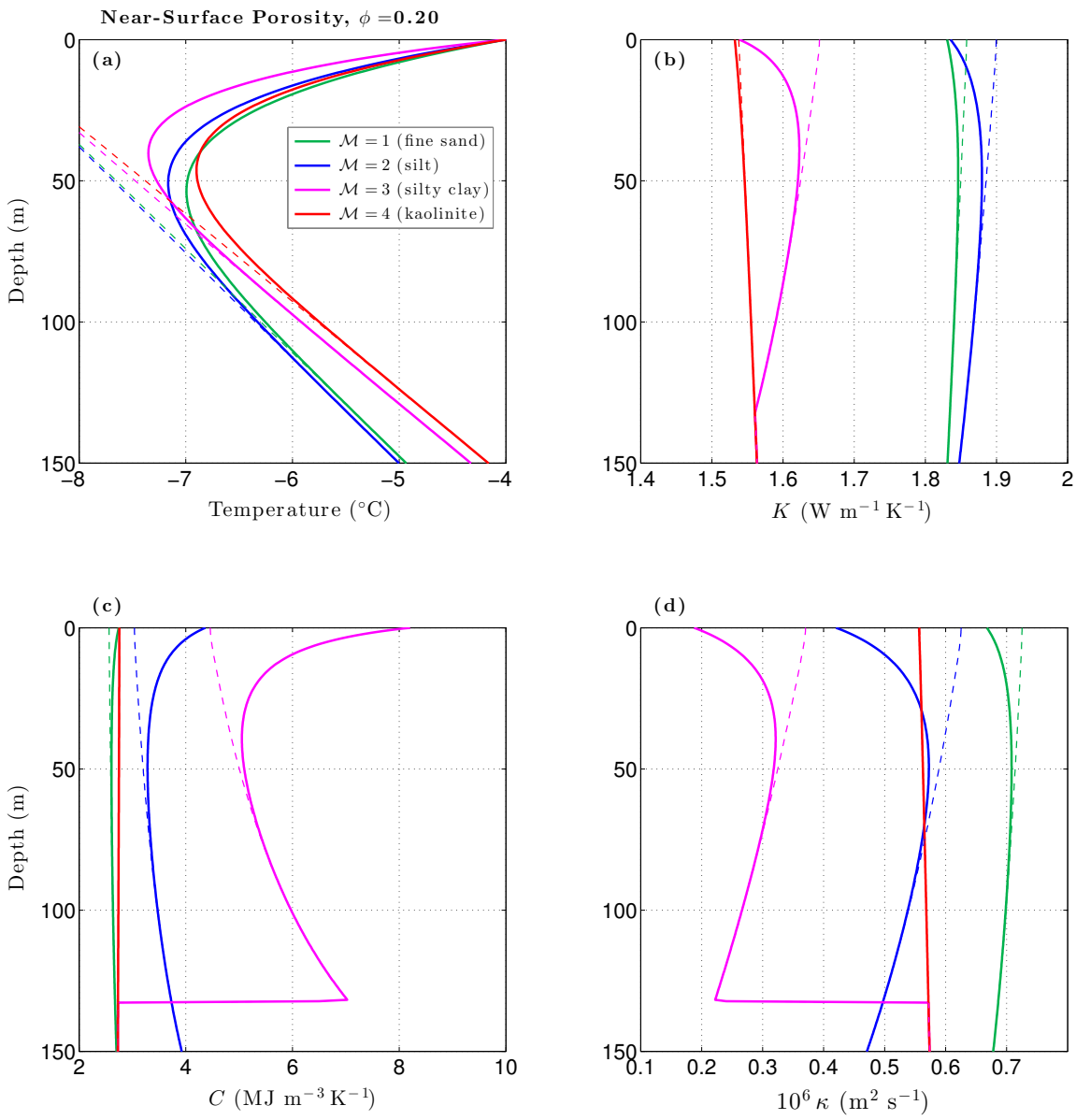

Figure 7.14: Response of low-porosity ($\phi = 0.20$) permafrost to a 1 K/decade warming for 50 years.

7.4 Summary and conclusions

The thermophysical properties of fine-grained permafrost are strongly dependent on sediment type, porosity, and temperature. This is primarily due to the ability of fine-grained sediments to retain significant amounts of unfrozen water within the pores at temperatures well below 0°C. The volumetric heat capacity and thermal diffusivity are particularly sensitive to the sediment type, varying by a factor of 4 for sediment types $\mathcal{M} =$

1–4 (fine sand, silt, silty clay, kaolinite). As a result, the thermal response of fine-grained permafrost to climate change strongly depends on the sediment type. An additional complication is that order of magnitude changes in C and κ are expected as fine-grained sediments warm or cool through their freezing points. At the temperatures experienced in the NPR-A, this transition is more likely to occur in low-porosity sediments; a transition through the freezing point will produce a nonlinear response to climate change. Even without a transition through the freezing point, C and κ are sufficiently sensitive to temperature that they can change by a factor of two within a few decades with a 1 K/decade climate warming, thereby altering the response of permafrost on a relatively short timescale. As the sequence of temperature logs acquired in any of the DOI/GTN-P boreholes represents the response of local permafrost to changing boundary conditions at the borehole wall and at the earth's surface, the thermal properties at the site must be at least approximately known before the logs can be properly interpreted for climate change.

7.5 References

Anderson, D.A., Tannehill, J.C., and Pletcher, R.H. (1984), *Computational Fluid Mechanics and Heat Transfer*, Hemisphere Publishing Corp., 599 pp.

Anderson, D. M., Tice, A.R., and McKim, H.L. (1973), The unfrozen water and the apparent specific heat capacity of frozen soils, in *Proceedings of the Second International Conference on Permafrost*, National Academy of Sciences, 289–295.

Angell, C.A., Oguni, M., and Sichina, W.J. (1982), Heat capacity of water at extremes of supercooling and superheating, *J. Phys. Chem.*, 86, 998–1002.

Birch, F., and Clark, H. (1940), The thermal conductivity of rocks and its dependence on temperature and composition, *Am. J. Sci.*, 238, 529–558.

Brigaud, F., and Vasseur, G. (1989), Mineralogy, porosity and fluid control on thermal conductivity of sedimentary rocks, *Geophysical Journal*, 98, 525–542.

Clow, G.D. (2014), Temperature data acquired from the DOI/GTN-P Deep Borehole Array on the Arctic Slope of Alaska, 1973–2013, *Earth Syst. Sci. Data*, 6, 201–218, doi:10.5194/essd-6-201-2014.

Clow, G.D. (2015), A green's function approach for assessing the thermal disturbance caused by drilling deep boreholes in rock or ice, *Geophys. J. Int.*, 203, 1877–1895, doi:10.1093/gji/ggv415.

Collett, T.S, Bird, K.J., Kvenvolden, K.A., and Magoon, L.B. (1988), Geologic interrelations relative to gas hydrates within the North Slope of Alaska, *USGS Open-File Report 88-389*, U.S. Geological Survey, 150 pp.

Davis, N. (2001), *Permafrost - A Guide to Frozen Ground in Transition*, Univ. of Alaska Press, Fairbanks, 351 pp.

Deming, D., Sass, J.H., and Lachenbruch, A.H. (1996), Heat flow and subsurface temperature, North Slope of Alaska, in *Thermal Evolution of Sedimentary Basins in Alaska*, USGS Bulletin 2142, U.S. Geological Survey, 21–44.

Farouki, O.T. (1981a), The thermal properties of soils in cold regions, *Cold Reg. Sci. Technol.*, 5, 67–75.

Farouki, O.T. (1981b), Thermal properties of soils, *CRREL Monograph 81-1*, U.S. Army Cold Regions Research and Engineering Laboratory, Hanover, NH.

Goodrich, L.E. (1978), Efficient numerical technique for one-dimensional thermal problems with phase change, *Int. J. Heat Mass Transfer*, 21, 615–621.

Herrin, J.M., and Deming, D. (1996), Thermal conductivity of U.S. coals, *J. Geophys. Res.*, 101, 25381–25386.

Holten, V., Bertrand, C.E., Anisimov, M.A., and Sengers, J.V. (2012), Thermodynamics of supercooled water, *J. Chem. Phys.*, 136, doi:10.1063/1.3690497.

Huber, M.L., Perkins, R.A., Friend, D.G., Sengers, J.V., Assael, M.J., Metaxa, I.N., Miyagawa, K., Hellmann, R., and Vogel, E. (2012), New international formulation for the thermal conductivity of H_2O, *J. Phys. Chem Ref. Data*, 41, doi:10.1063/1.4738955.

Lachenbruch, A.H., Sass, J.H., Marshall, B.V., and Moses, T.H., Jr. (1982), Permafrost, heat flow, and the geothermal regime at Prudhoe Bay, Alaska, *J. Geophys. Res.*, 87, 9301–9316.

Marchenko, S., Romanovsky, V., and Tipenko, G. (2008), Numerical modeling of spatial permafrost dynamics in Alaska, in *Proceedings of the Ninth International Conference on Permafrost*, Institute of Northern Engineering, University of Alaska, Fairbanks, 1125–1130

Minkowycz, W.J., Sparrow, E.M., Schneider, G.E., and Pletcher, R.H. (1988), *Handbook of Numerical Heat Transfer*, John Wiley & Sons, Inc., 1024 pp.

Noetzli, J., Gruber, S., Kohl, T., Slzmann, N., and Haeberli, W. (2007), Three-dimensional distribution and evolution of permafrost temperatures in idealized high-mountain topography, *J. Geophys. Res.*, 112, F02S13, doi:10.1029/2006JF000545.

Osterkamp, T.E., and Payne, M.W. (1981), Estimates of permafrost thickness from well logs in northern Alaska, *Cold Reg. Sci. Technol.*, 5, 13–27.

Osterkamp, T.E. (1987), Freezing and thawing of soils and permafrost containing unfrozen water and brine, *Water Resour. Res.*, 23, 2279–2285.

Özişik, M.N. (1980), *Heat Conduction*, John Wiley & Sons, New York, 687 p.

Patankar, S.V. (1980), *Numerical Heat Transfer and Fluid Flow*, Hemisphere Publishing Corp., 197 pp.

Qin, Y., Li, G., and Qu, G. (2009), A formula for the unfrozen water content and temperature of frozen soils, *Cold Regions Engineering 2009*, 155–161, doi:10.1061/41072(359)18.

Sass, J.H., Lachenbruch, A.H., and Munroe, R.J. (1971), Thermal conductivity of rocks from measurements on fragments and its application to heat-flow determinations, *J. Geophys. Res.*, 76, 3391–3401.

Turcotte, D.L., and Schubert, G. (1982), *Geodynamics, Applications of Continuum Physics to Geological Problems*, John Wiley & Sons, 450 pp.

Watanabe, K., and Mizoguchi, M. (2002), Amount of unfrozen water in frozen porous media saturated with solution, *Cold Reg. Sci. Technol.*, 34, 103–110.

Wentworth, C.K, Wells, R.C., and Allen, V.T. (1940), Ceramic clay in Hawaii, *The American Mineralogist*, 25, 1–33.

Yen, Y.-C. (1981), Review of thermal properties of snow, ice, and sea ice, *CRREL Report 81-10*, U.S. Army Cold Regions Research and Engineering Laboratory, Hanover, NH.

Zhang, T. (1993), *Climate, Seasonal Snow Cover and Permafrost Temperatures in Alaska North of the Brooks Range*, Ph.D. dissertation, Univ. of Alaska, Fairbanks, 232 pp.

CHAPTER 8

THERMOPHYSICAL PROPERTIES OF PERMAFROST ON THE WESTERN ARCTIC SLOPE

8.1 Introduction

The response of fine-grained permafrost to a temperature change at the earth's surface, or at a borehole wall, depends on its thermophysical properties (ice content, heat capacity, thermal conductivity and diffusivity). As shown in Chapter 7, these properties are sensitive to the porosity and texture of the permafrost, and to the thermal conductivity of the grains. Rocks in the upper 2–3 km of the NPR-A consist primarily of fine-grained shales, claystones, and siltstones, limited sections of sandstone, gravel, and coal, and in the uppermost sections, small fragments of carbonaceous material and wood. In order of oldest to youngest, the major rock units present in the upper kilometer are the Torok Formation, the Nanushuk Group, and the Colville Group (**Figure 8.1**); permafrost in the NPR-A is 200–400 m thick, depending on location [*Lachenbruch et al.*, 1987]. The upper 3/4's of the Torok Formation is a thick relatively uniform sequence of marine shale and siltstone with minor amounts of thin-bedded sandstone [*Bird*, 1987]. These sediments were deposited in a deep trough that formed during the uplift of the Brooks Range to the south. Conformably overlying the Torok are the fluvial-deltaic deposits of the Nanushuk Group [*Huffman et al.*, 1988]. The lower Nanushuk consists primarily of marine mudstones and shales. These grade upward into transitional facies, and then into nonmarine facies. The Nanushuk sequence relates to the northeastward buildout of the Corwin delta on the western Arctic Slope (west of 156°W, **Figure 8.2**) and to the northward buildout of the Umiat delta on the central Arctic Slope (156°–149°W). The Corwin delta was a relatively muddy system deposited into a slowly subsiding basin with low wave energy and restricted circulation. Due to the large amount of intergranular material (clay, silt, mud) and diagenic effects,

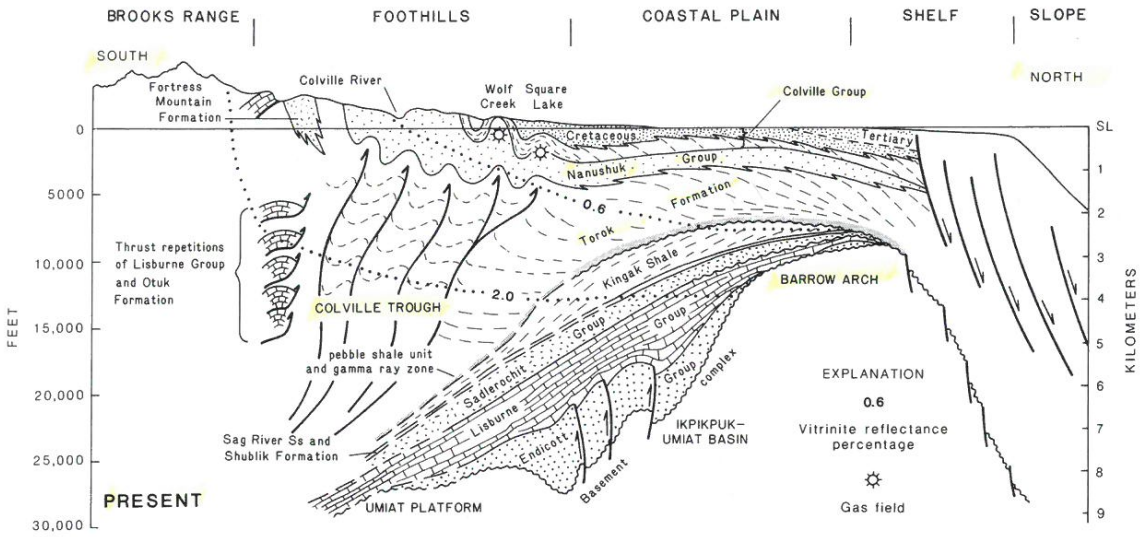

Figure 8.1: North-south geologic cross section through the eastern NPR-A from *Bird* [1987].

the porosity and permeability of the Nanushuk Group in the western region is generally low. The Nanushuk Group of the central Arctic Slope is more complicated. The Umiat delta does not appear to have extended north of Umiat (Seabee well) to any great extent. Sediments north of Umiat represent a coastal barrier shoreline supplied by sediments from the Umiat delta, and occasionally the Corwin River, by longshore currents. The porosity and sand content tend to be greater in this high-energy environment than to the west. Above the Nanushuk lies the Colville Group, a sequence of prodelta claystones and soft clay shales with minor interbedded siltstones, sandstones, and gravels. *Bartsch-Winkler and Huffman* [1981] describe the petrography of the Nanushuk Group and the Torok Formation, although they focus on the sandstones. They found a significant quantity of matrix material filling the interstitial spaces consisting of unsorted silt and clay particles of quartz, chlorite, sericite, and unidentifiable material. The most common authigenic clay is kaolinite, followed by chlorite and sericite.

Above the Colville Group is a thin veneer of unconsolidated marine and nonmarine clastic sediments known as the Gubik Formation covering most of the Arctic Coastal Plain. These sediments were deposited during a series of six marine transgressions and regressions that postdate the opening of the Bering Strait between 3 and 3.5 Ma [*Brouwers*, 1994; *Carter and Galloway*, 2005]. These deposits extend to a maximum altitude of about 40 m above present sea level. Where present, the Gubik is generally 10–15 m thick but locally

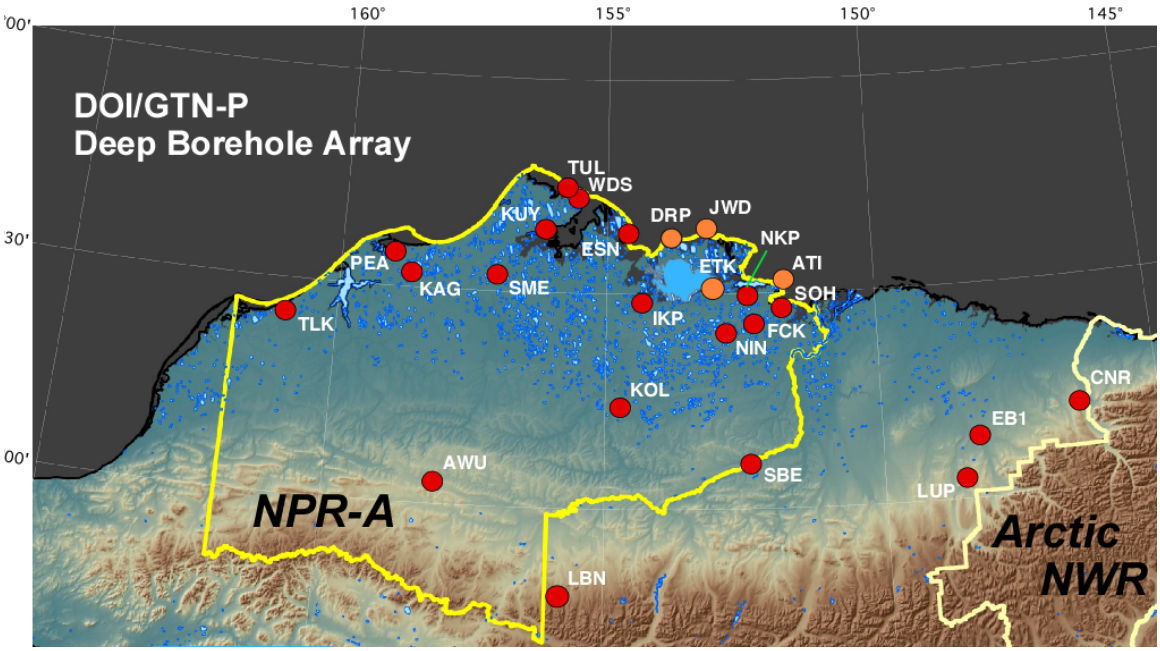

Figure 8.2: Location of the DOI/GTN-P boreholes used to monitor the thermal state of permafrost on the Arctic Slope of Alaska. The Seabee Test Well (SBE) is located at Umiat, Alaska. The Colville River forms the eastern boundary of the NPR-A.

can be as thick as 60 m [*Black*, 1964; *Repenning*, 1983]. In the eastern portion of the NPR-A (south of Teshekpuk Lake), the upper portion of the Gubik consists of an eolian sand sheet deposited during the latter part of the Wisconsin Ice Age (36–12 ka). The source for the sand was the Colville River delta which was subaerially exposed at that time when sea level was at least 100 m lower than today. Prevailing northeasterly winds carried the sand back onto the coastal plain. Present-day ridges of the sand sheet consist of stabilized linear dunes up to 30 m high [*Carter*, 1981].

Aside from the relatively thin Gubik Formation, the permafrost zone at the Awuna, Tulageak, and West Dease wells consist entirely of Torok shales and siltstones (**Table 8.1**). Rocks of the Nanushuk Group span the permafrost zone below the Gubik at all the other western NPR-A wells while Colville rocks span most of the permafrost section at the eastern well sites.

In addition to the geologic descriptions provided by *Bird* [1987], *Huffman et al.* [1988], and others, several other sources of information are valuable for assessing the properties of permafrost in the NPR-A. (1) A description of the cuttings acquired during drilling operations provides a qualitative description of the materials at the well sites, although

Table 8.1: Depth to the top of the Torok formation, Nanushuk group, and Colville group at the DOI/GTN-P well sites measured relative to the height of the kelly bushing H^{kb} on the drill rig [*Bird*, 1988]; ^{e}- estimated from regional trends, dash - unit is not present.

Borehole	USGS code	H^{kb} (m)	Torok (m)	Nanushuk (m)	Colville (m)
Awuna	AWU	7.9	8	—	—
Tunalik	TLK	9.1	1905	30^{e}	—
Peard Bay	PEA	8.5	753	24^{e}	—
Kugrua	KAG	7.6	710	24^{e}	—
South Meade	SME	6.1	759	24^{e}	—
Tulageak	TUL	5.2	30^{e}	—	—
West Dease	WDS	5.8	24^{e}	—	—
Kuyanak	KUY	5.2	381	23^{e}	—
East Simpson #1	ESN	4.9	820	90	24
Ikpikpuk	IKP	6.1	899	30^{e}	—
Koluktak	KOL	8.2	1283	23^{e}	—
Seabee	SBE	9.1	395	85	30
Drew Point	DRP	7.0	975	375	24^{e}
J.W. Dalton	JWD	5.5	1262	811	64
East Teshekpuk	ETK	6.7	945	483	30^{e}
North Kalikpik	NKP	6.4	1058	730	30^{e}
Atigaru	ATI	6.1	1341	1058	30^{e}
South Harrison	SOH	6.1	1286	981	30^{e}
West Fish Creek	FCK	6.4	1193	777	30^{e}
North Inigok	NIN	9.1	995	585	30^{e}

in most cases cuttings from the upper 30–150 m were not examined. These descriptions suggest a much more varied lithology for the eastern NPR-A wells than for those on the western Arctic Slope. (2) A limited set of rock cores have been acquired at depths less than 1 km since petroleum exploration began in the NPR-A during the 1940s. *Bartsch-Winkler and Huffman* [1981] report porosity measurements for some of these cores. (3) A suite of nonthermal geophysical logs were acquired in many of the NPR-A wells at the conclusion of drilling. These have been used to infer the porosity of the Torok Formation [*Nelson and Bird*, 2005], the bulk density of the main stratigraphic units [*Gutman et al.*, 1982], and for a few wells, the depth to the base of ice-bearing permafrost [*Osterkamp and Payne*, 1981; *Collett et al.*, 1988]. (4) The sharp temperature gradient contrast typically observed near the base of coarse-grained permafrost does not occur in the NPR-A temperature logs. Thus, the gradient contrast cannot be used to infer the porosity as was done for the nearby

Prudhoe Bay oil field to the east [*Lachenbruch et al.*, 1982]. However, some of the NPR-A temperature logs do exhibit latent-heat effects during the early portion of the drilling disturbance recovery. *Lachenbruch et al.* [1987] used the observed latent-heat effect to infer the maximum depth of ice-rich permafrost at several of the NPR-A wells.

Of the full suite of thermophysical properties, the three most fundamental for assessing the thermal response of permafrost are the sediment porosity ϕ, the sediment texture $\mathcal{M}$, and the grain or matrix conductivity K_g. From these three basic quantities, all the other thermophysical properties can be determined if the temperature is also known, including: the volume fractions of unfrozen water ϕ_u and of ice ϕ_i, the bulk density ρ, the volumetric heat capacity C, the bulk thermal conductivity K, and the thermal diffusivity κ. In this chapter, we attempt to constrain the possible values for ϕ, $\mathcal{M}$, and K_g at each of the well sites. To allow intercomparison between sites, the porosity is specified at a common reference level, i.e., the near-surface just below the Gubik Formation, and the grain conductivity at a reference temperature of 25°C. Values at these reference points will be referred to as ϕ_0 and K_g^{25}. The first step in finding the properties is to estimate the range of possible porosities at each site from the reported bulk-density measurements and the limited set of rock-core porosities. Next, the base of ice-rich permafrost (B-IRP) is identified (where possible) using the earliest temperature logs and the predicted thermal response of fine-grained permafrost near the borehole wall to the large heat input caused by drilling operations (e.g., **Figs 7.10, 7.11**). The depth of the B-IRP, in conjunction with the equilibrium temperature profile, yields the freezing point depression T_f and constraints on the sediment texture $\mathcal{M}$. The recent warming in arctic Alaska provides the second boundary-condition experiment we are able to exploit. Time and depth derivatives calculated from the sequence of DOI/GTN-P temperature logs allow us to estimate K_g^{25} and further constrain the porosity ϕ_0 at the well sites. Finally, the full suite of thermophysical properties (ϕ_u, ϕ_i, ρ, C, K, κ) is determined for each well from ϕ_0, $\mathcal{M}$, and K_g^{25}.

8.2 Porosity constraints

A limited set of information is available to constrain porosities within the permafrost zone of the NPR-A. (1) *Bartsch-Winkler and Huffman* [1981] report laboratory porosity measurements made on Nanushuk core samples from nine wells drilled during the first phase

(pre-1975) of petroleum exploration in the NPR-A. Most of these samples were acquired at relatively shallow depths, i.e., within 1000 m of the surface. In cases where multiple samples were obtained in a given well, porosities often show little variation with depth within the Nanushuk Group. (2) *Nelson and Bird* [2005] provided a few additional porosity measurements for Nanushuk (and Torok) core samples, although they tend to come from depths greater than 1 km. They also reported porosities at the top of the Torok Formation for all the DOI/GTN-P wells based on a linear fit to sonic-log derived porosities across the Torok. Large discrepancies exist between the linear fit at the top of the Torok and the actual sonic-derived porosities there, and in some cases, between core-sample porosities and sonic-derived porosities at the same depth. Thus, the porosities at top of the Torok provided by *Nelson and Bird* [2005] must be viewed with caution. (3) Using compensated formation density (gamma-gamma) logs, *Gutman et al.* [1982] determined the minimum, mean, and maximum bulk densities for large stratigraphic units at many of the DOI/GTN-P well sites. As their study was part of a large-scale gravity investigation, they treated the Nanushuk Group, Colville Group, and Gubik Formation as a single 'density' unit (#9 in their terminology) and the Torok as another (# 8). Given the coarseness of these units, their tabulated density values typically pertain to depth intervals much larger than that of the permafrost zone. Although the gamma-gamma density data show large lateral variations, they too show little variation with depth within the uppermost stratigraphic units (Torok and higher). *Gutman et al.* [1982] attribute this insensitivity to overpressuring throughout the NPR-A; overpressuring would have reduced the maximum effective stress experienced by these rocks, reducing the degree of compaction.

For nearly all of the DOI/GTN-P wells with permafrost consisting of Torok or Nanushuk rocks, the lower limit of core-sample porosities measured in nearby wells can be used as a lower bound on the near-surface porosity ϕ_0, assuming the density is insensitive to depth. The upper bound for ϕ_0 is established by assuming the minimum density values reported by *Gutman et al.* [1982] occur within the permafrost zone. These density values are converted to porosity using the permafrost model described in Chapter 7. Core-derived porosities are unavailable for the northeastern NPR-A where permafrost consists primarily of Colville rocks. In addition, Unit #9 densities are available only for half of the DOI/GTN-P wells in this area. For the northeastern wells, the lower and upper bounds on ϕ_0 are

estimated from the mean and minimum bulk densities, where available. Otherwise, the ϕ_0 bounds are taken from the nearest wells with similar lithology (based on the drill cutting description) where the densities are available. **Table 8.2** summarizes the upper and lower bounds for the likely near-surface porosity ϕ_0 at each of the well sites.

8.3 Base of ice-rich permafrost

Due to the freezing point depression caused by pressure, solute, and soil texture effects, only a portion of the permafrost zone is likely to contain ice (Chapter 7). To clarify the terminology, *permafrost* is defined to be any soil or rock that remains colder than 0°C for at least two consecutive years. Thus, permafrost is defined strictly on the basis of temperature. *Ice-bearing permafrost* is soil or rock interpreted to contain ice on the basis of nonthermal geophysical logs. This definition relies on the large change in mechanical and electrical properties that occurs at the water-ice transition. Sonic velocity and electrical resistivity logs are typically used to find the base of ice-bearing permafrost. *Ice-rich permafrost* is soil or rock interpreted to contain ice based on latent-heat effects or temperature gradient changes apparent in high-resolution temperature logs. For the fine-grained permafrost of the NPR-A, the effects of interstitial ice are subtle and difficult to detect. After examining DIL (dual induction laterlog) and BHCS (borehole compensated sonic) logs from 150 wells in northern Alaska, *Osterkamp and Payne* [1981] were able to identify the base of ice-bearing permafrost (B-IBP) in only three NPR-A wells (**Table 8.3**). *Collett et al.* [1988] re-examined

Table 8.2: Upper and lower bounds for the likely near-surface porosity ϕ_0 at each of the DOI/GTN-P well sites in the NPR-A.

Borehole	ϕ_0 (%)	Borehole	ϕ_0 (%)
Awuna	8–16	Koluktak	17–24
Tunalik	11–17	Seabee	13–19
Peard Bay	11–20	Drew Point	28–35
Kugrua	11–20	J.W. Dalton	28–35
South Meade	11–17	East Teshekpuk	25–28
Tulageak	9–18	North Kalikpik	25–28
West Dease	10–21	Atigaru	24–29
Kuyanak	20–26	South Harrison	22–27
East Simpson #1	28–31	West Fish Creek	25–29
Ikpikpuk	30–36	North Inigok	25–29

these logs and identified ice-bearing permafrost in six of the NPR-A wells. These two studies agreed only at a single well site (Atigaru), attesting to the difficulty of interpreting geophysical logs for the presence of ice in fine-grained materials. It's worth noting that the detection limit for ice with nonthermal logs is unknown [*Collett et al.*, 1988]. Hence, the reported depths should be viewed as minimum values. Using temperature logs from the DOI/GTN-P boreholes, *Lachenbruch et al.* [1987] identified the bottom of an ice-rich layer in seven of the NPR-A wells (**Table 8.3**). As the ice-rich layer they identified may coincide with a high porosity zone, it has remained unclear whether the bottom of this layer corresponds with the actual base of ice-rich permafrost (B-IRP).

Simulations with a 2-D cylindrical permafrost model (Chapter 7) suggest several features in the thermal field surrounding a well as it recovers from the drilling disturbance that should be useful for identifying the base of ice-rich permafrost and the associated freezing point T_f, including: (1) a clustering of temperatures near T_f in the logs acquired soon after well completion, (2) a change in the temperature gradient near the B-IRP, and (3) a minimum in the drilling disturbance near the B-IRP.

Criterion (1). Temperatures surrounding the wellbore rapidly cool after drilling until they encounter T_f. This occurs first at the top of the well where the ambient temperatures

Table 8.3: Base of ice-bearing permafrost (B-IBP) and base of an ice-rich layer (B-IRL) from previous studies; OP81 [*Osterkamp and Payne*, 1981], C88 [*Collett et al.*, 1988], L87 [*Lachenbruch et al.*, 1987].

Borehole	B-IBP (m)		B-IRL (m)
	OP81	C88	L87
Peard Bay			270
Kugrua	207		
South Meade			160
Tulageak		169	
West Dease			260
East Simpson #1			280
Drew Point	247		250
J.W. Dalton		270	
North Kalikpik		120	
Atigaru	293	293	330
South Harrison		274	
West Fish Creek		116	140

are the coldest. The freezing front then propagates down the wellbore with time, eventually reaching the B-IRP. For most of the NPR-A wells, the propagation of the freezing front down the wellbore occurs fairly rapidly, descending from the surface to within 10–20 m of the B-IRP within a few months. Once the permafrost cools to T_f, further cooling occurs at a much slower rate due to the high heat capacity near the freezing point (**Fig. 7.5**). Once past this sticking point, permafrost is able to cool more rapidly again. The expression of this process in the temperature field is that borehole temperature profiles appear to 'hang' near T_f while the freezing front propagates down the wellbore (**Figure 8.3a**). If T_f can be identified in the temperature logs, the base of ice-rich permafrost is simply given by the depth at which T_f occurs in the equilibrium temperature profile (i.e., the profile corrected for the drilling disturbance). Given how rapidly the freezing front moves down the wellbore compared to the infrequency of temperature logging, very few of the DOI/GTN-P logs captured the situation when temperatures near the wellbore were close to the freezing point. The 13-Sep-1979 log in the J.W. Dalton well is one of the rare exceptions (**Figure 8.4**).

Criterion (2). The second method for identifying the B-IRP utilizes the change in the temperature gradient $\partial T/\partial z$ expected to occur near this depth. Due to the tendency for temperatures to persist near T_f for some time, a maximum occurs in the temperature gradient near the B-IRP (**Figure 8.3b**). The maximum gradient initially occurs a few meters above the B-IRP and then drifts downward, ultimately reaching depths a few meters below the B-IRP (**Figure 8.3c**). An additional characteristic of the temperature gradient is that it is relatively uniform below the B-IRP as long as the material properties do not vary too much. Above the B-IRP, the gradient is expected to exhibit large variations associated with varying ice contents as the porosity fluctuates with depth in the sediments (**Figure 8.5**). Gradient variations with depth are particularly diagnostic of the B-IRP in the fine-grained mudrocks of the NPR-A.

Criterion (3). The drilling disturbance ΔT_d is predicted to have a minimum in the general vicinity of the B-IRP. Initially quite broad and located several tens of meters above the B-IRP, the ΔT_d minimum becomes more distinct as it propagates downward with time (**Figure 8.3d**). Ultimately, it reaches a depth several meters below the B-IRP. In practice, the calculation of ΔT_d involves considerably more processing of the temperature logs than does the temperature gradient. Thus, it tends to be a less reliable indicator of the B-IRP

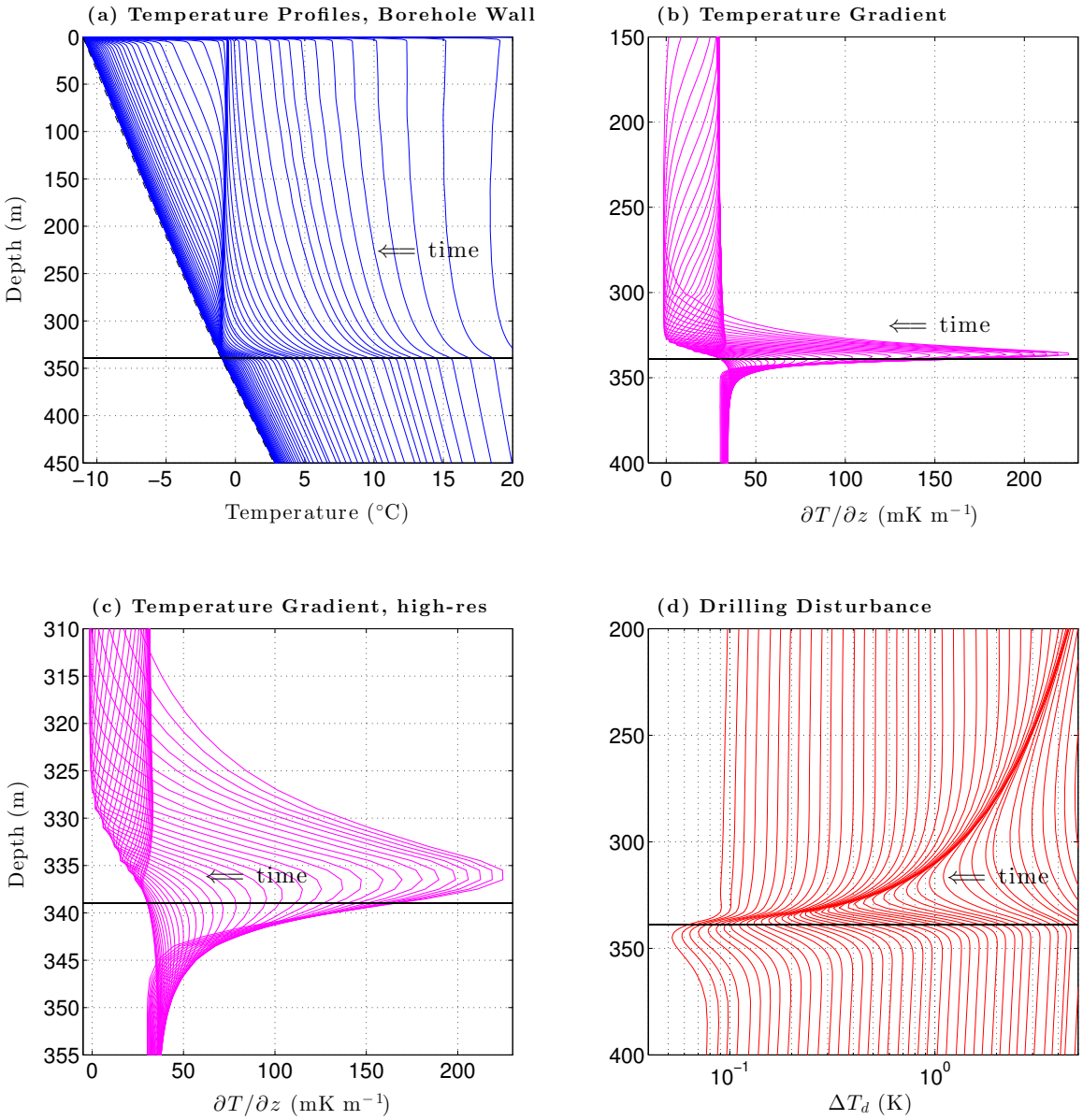

Figure 8.3: Evolution of temperatures, gradients, and drilling disturbance following the drilling of one of the DOI/GTN-P boreholes (East Simpson #1) in the NPR-A. Panel (a) shows the simulated temperatures along the borehole wall, (b) shows the temperature gradient at the wall, (c) is a higher-resolution version of (b), and (d) shows the drilling disturbance. Black horizontal line indicates the base of ice-rich permafrost at this well (339 m) while the dashed line in (a) is the equilibrium temperature profile. The freezing point at the B-IRP is -1.05°C in this simulation. The freezing point occurs at slightly warmer temperatures at shallower depths due to a weakening of the pressure effect.

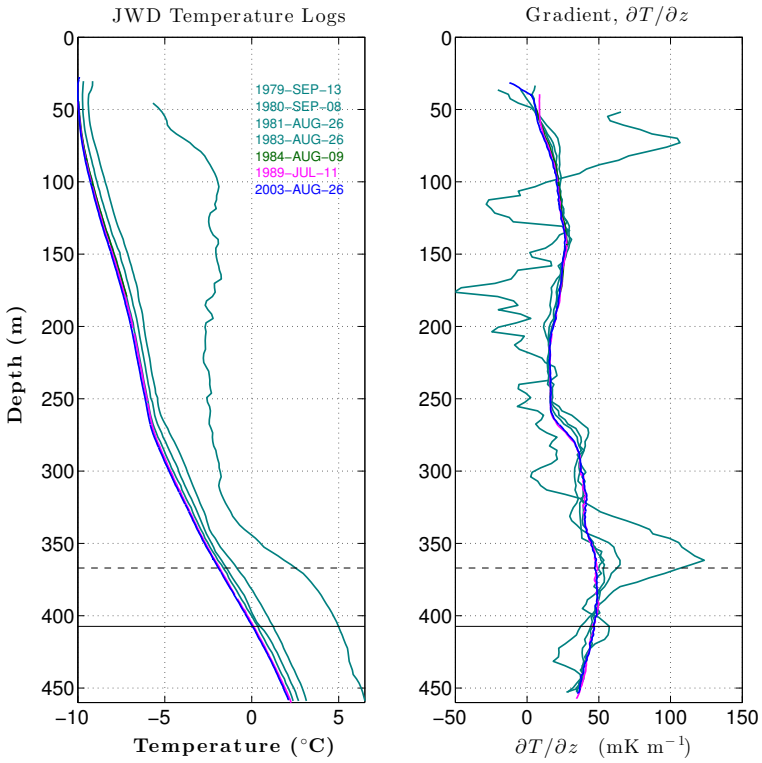

Figure 8.4: Temperature logs and gradients from the J.W. Dalton well, NPR-A. A maximum in the temperature gradient occurs at 362 and 365 m in the Sep-1979 and Sep-1980 logs, respectively. The base of permafrost is located at 407.3 m (solid line), the base of ice-rich permafrost at 367 m (dashed line), and the freezing point is -1.96°C. Temperatures along the borehole wall were at or near the freezing point over the 100–310 m depth range during the Sep-1979 log.

than is the gradient-based method. Still, it can be used to confirm an interpretation based on Criterion (1) or (2) when the ΔT_d profiles are sufficiently clean (**Figure 8.6**).

Based on the above criteria, the following procedure was used in an attempt to find the B-IRP at each of the DOI/GTN-P well sites in the NPR-A: (1) The early temperature logs, gradients, and drilling-disturbance profiles were inspected for signs of latent-heat effects. If latent-heat effects were apparent, Criteria 1–3 were used to identify the approximate location of the B-IRP. (2) The 2-D permafrost model was then used to simulate the thermal recovery of the permafrost surrounding the well from the drilling disturbance. The 2-D simulation provided an estimate of how far above or below the B-IRP the maximum temperature gradient and minimum drilling disturbance were expected to be at the time of each acquired log. This information was then used to refine the B-IRP value. In most cases, the uncertainty of the refined B-IRP is ± 3 m. For some well sites, the 2-D simulation

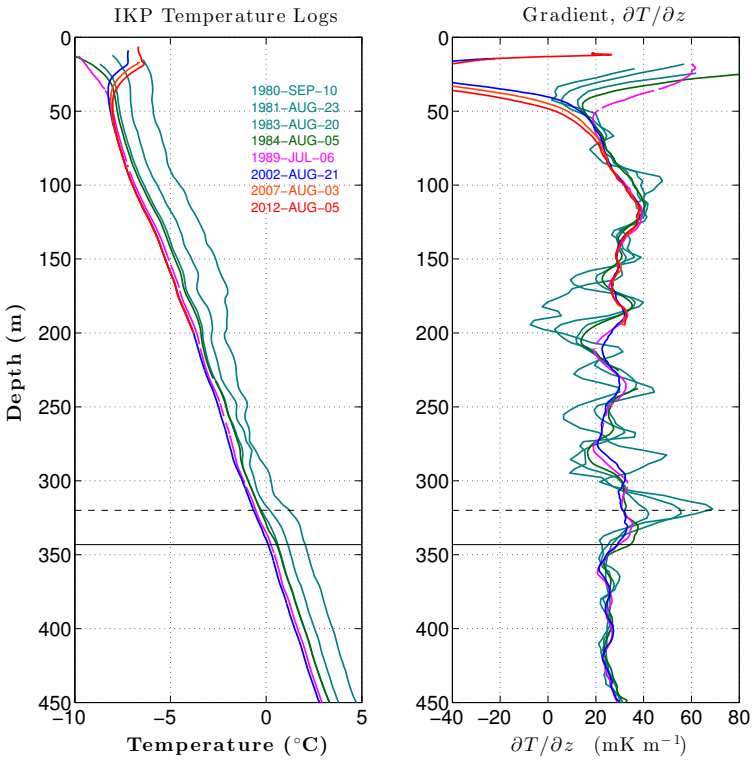

Figure 8.5: Temperature logs and gradients from the Ikpikpuk well, NPR-A. A maximum in the temperature gradient occurs at 318, 321, and 323 m in the Sep-1980, Aug-1981, and Aug-1983 logs, respectively. The base of permafrost is located at 343.2 m (solid line), the base of ice-rich permafrost at 321 m (dashed line), and the freezing point is -0.71°C. As in most of the NPR-A wells, the temperature gradient is much less variable below the B-IRP.

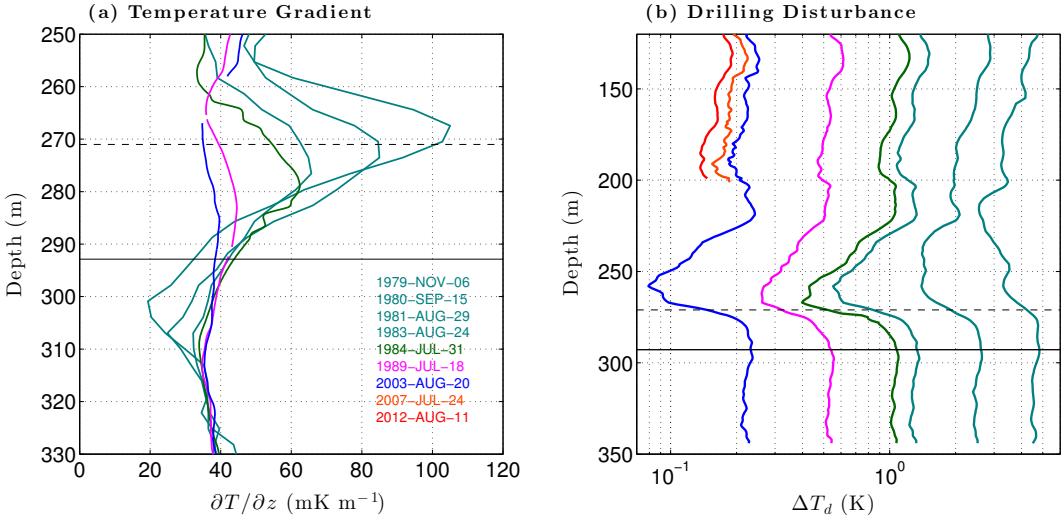

Figure 8.6: Temperature gradient near the B-IRP calculated from the Tunalik temperature logs (a). Panel (b) shows the evolution of the drilling disturbance. The B-IRP at Tunalik is estimated to be at 272 m (dashed line) while the base of permafrost is at 292.9 m (solid line).

revealed that even the earliest temperature log was acquired too late for a detectable signal of the B-IRP to still be present. This explains why no latent-heat effects are apparent in the Tulageak, South Harrison, and North Inigok temperature logs even though these effects are present in logs from nearby wells with similar lithologies. Finally, the early temperature logs from the East Teshekpuk well were found to be of too poor quality to allow the B-IRP to be identified.

With the above procedure, the base of ice-rich permafrost and the associated freezing point were identified in 14 of the DOI/GTN-P wells, limits were placed on the B-IRP in a 15th well, and it was determined that no ice occurs at any depth in a 16th well (**Table 8.4**). In all cases, the B-IRP was found to be considerably deeper than the base of ice-bearing permafrost identified using nonthermal geophysical logs [*Osterkamp and Payne*, 1981; *Collett et al.*, 1988], and with the exception of the West Dease well, 10–60 m deeper than the base of the ice-rich layer identified by *Lachenbruch et al.* [1987]. The B-IRP found using Criteria 1–3 exhibits considerable variability across the NPR-A, even at short length scales. Separated by only 21 km, the B-IRP deepens from 180 m at the North Kalikpik well to 363 m at Atigaru in the northeastern NPR-A. In contrast, the freezing point T_f is much more uniform, particularly within similar rock types. Based on the geologic description provided by *Huffman et al.* [1988], the Nanushuk Group can be separated into three subunits (Corwin, Umiat, and CU) depending on the sediment source; CU is transitional containing sediments derived from both the Corwin and Umiat deltas. For the western wells where permafrost consists primarily of Corwin-delta Nanushuk mudrocks, the freezing point T_f occurs within the narrow range, -0.71°C to -0.84°C. Given the more variable lithology, the freezing point has a wider range (-0.71°C to -1.70°C) at the transitional Nanushuk-*CU* wells. At West Dease, the freezing point of the Torok rocks is -1.63°C, near the lower end of the range found for Nanushuk-*CU* rocks into which the Torok grades. At the Seabee well, the freezing point of the Umiat-delta Nanushuk rocks is about -0.15°C, consistent with the high sand content there. The eastern wells whose permafrost consists primarily of Colville rocks can be separated into two subunits (A, B) based on their thermophysical properties. The freezing point of Colville-*A* rocks (-1.53°C to -1.96°C) overlaps the low end for Nanushuk-*CU* rocks while Colville-*B* has a much lower freezing point, close to -5°C. No evidence was found for interstitial ice at any depth

Table 8.4: Base of ice-rich permafrost (B-IRP) and the associated freezing point T_f from interpretation of the DOI/GTN-P temperature logs (this study). 'Criteria' refers to the methods used to identify the B-IRP. 'Rock Unit' is the unit present at the B-IRP. ⊘ indicates the temperature logs were acquired too late after drilling was completed to provide reliable information about the B-IRP. ⊖ indicates the quality of the logs is too poor to identify the B-IRP. The accessible portion of the Koluktak well isn't deep enough to definitively locate the B-IRP. P_d is the base of permafrost.

Well	Rock Unit	P_d (m)	B-IRP (m)	T_f(°C)	Criteria
Awuna	Torok *(foothills)*	290.5	no ice	—	—
Tunalik	Nanushuk *(Corwin)*	292.8	272	−0.71	2,3
Peard Bay	Nanushuk *(Corwin)*	306.3	280	−0.75	2
Kugrua	Nanushuk *(Corwin)*	285.5	255	−0.79	2,3
South Meade	Nanushuk *(Corwin)*	199.1	176	−0.84	1,2,3
Tulageak	Torok *(coastal)*	301.5	⊘	⊘	⊘
West Dease	Torok *(coastal)*	279.7	244	−1.63	2,3
Kuyanak	Nanushuk *(CU)*	329.9	283	−1.70	2
East Simpson #1	Nanushuk *(CU)*	366.3	339	−1.05	2,3
Ikpikpuk	Nanushuk *(CU)*	343.2	321	−0.71	2
Koluktak	Nanushuk *(CU)*	—	>213	>-2.2	—
Seabee	Nanushuk *(Umiat)*	305.7	299	−0.15	1
Drew Point	Colville *(A)*	322.2	281	−1.90	2,3
J.W. Dalton	Colville *(A)*	407.4	367	−1.96	1,2,3
East Teshekpuk	Colville *(A)*	258.5	⊖	⊖	⊖
North Kalikpik	Colville *(A)*	211.6	180	−1.53	2
Atigaru	Colville *(A)*	402.8	363	−1.73	2
South Harrison	Colville *(B)*	—	⊘	⊘	⊘
West Fish Creek	Colville *(B)*	261.2	156	−4.76	1,2,3
North Inigok	Colville *(B)*	289.2	⊘	⊘	⊘

in the Awuna well (Arctic Foothills), possibly due to the low porosity of the Torok rocks at this site.

8.4 Sediment texture constraints

Only unique combinations of the porosity ϕ and sediment texture $\mathcal{M}$ can yield the observed freezing point T_f at the pressures encountered near the base of ice-rich permafrost. This constraint can be used to establish the relationship between $\mathcal{M}$ and ϕ_0 for the rock units sampled near the B-IRP at each well site. The porosity at the B-IRP is assumed to be given by $\phi = \phi_0 + (\partial\phi/\partial z)\times$(B-IRP) where $\partial\phi/\partial z$ is taken to be the mean of the values provided by *Nelson and Bird* [2005] for the NPR-A. The compaction limit for the

porosity (7% for Torok-*foothills*, 9% for Torok-*coastal*, 11% for Nanushuk and Colville) is provided by the mean lower limit of the available core porosity measurements. **Figure 8.7** shows the resulting relationship for the rock units sampled at the well sites within the porosity limits established in Section 8.2. All the Colville-*A* group samples are found to have a similar $\mathcal{M}$ - ϕ_0 relationship, as do the samples from the Nanushuk-*Corwin* group. The texture-porosity relationship for the Colville-*B* and transitional Nanushuk-*CU* groups appear to be more varied based on our limited sampling.

8.5 Transient analysis constraints

The response of shallow permafrost to the recent warming in arctic Alaska provides another means for constraining the material properties at the NPR-A wells sites. We begin with the differential form of the 3-D heat-diffusion (HD) equation for fine-grained permafrost,

$$C \frac{\partial T(\mathbf{r},t)}{\partial t} = \nabla \cdot K \nabla T(\mathbf{r},t) + S(\mathbf{r},t) \tag{8.1}$$

where C is the volumetric heat capacity,

$$C = \rho c_p + \rho_u L_f \frac{\partial \phi_u}{\partial T}. \tag{8.2}$$

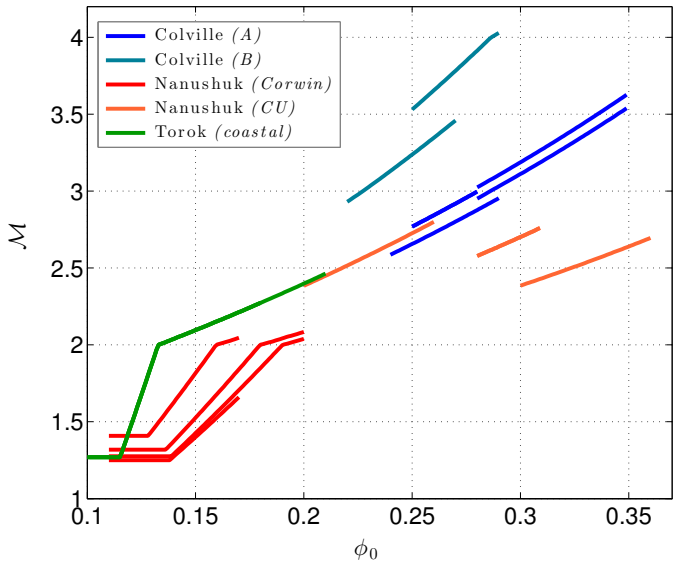

Figure 8.7: Relationship between the sediment texture ($\mathcal{M}$) and the near-surface porosity (ϕ_0) at well sites where the B-IRP and freezing point T_f have been determined.

In shallow permafrost, the heat-production function S is essentially zero and can be ignored. In addition, for times exceeding the drilling duration by a factor of 5–10, radial heat-flow components associated with the drilling disturbance are small. Lateral heat transfer due to the reserve pits and drill pads are, however, large in the upper few tens of meters at the wells (**Figure 8.8**). Below $\sim$ 50 m (the exact depth depending on the local thermal properties), the lateral terms in the heat-diffusion equation are small compared to the vertical terms. In this case, the HD equation reduces to,

$$0 \;=\; C\,\frac{\partial T}{\partial t} \;-\; K\,\frac{\partial^2 T}{\partial z^2} \;-\; \frac{\partial K}{\partial z}\frac{\partial T}{\partial z}. \tag{8.3}$$

Since the sequence of temperature logs acquired in a DOI/GTN-P monitoring well provides all the information necessary to evaluate the temperature derivatives in Eq. (8.3), we can search through possible materials to find those combinations of C and K that satisfy this equation. As the temperature derivatives calculated from the logs are not entirely error-free, it is unlikely the HD equation can be satisfied exactly. With this in mind, our strategy for finding viable solutions is based on minimizing the norm of the residuals,

$$\delta(z) \;=\; \check{C}\,\frac{\partial T}{\partial t} \;-\; \check{K}\,\frac{\partial^2 T}{\partial z^2} \;-\; \frac{\partial \check{K}}{\partial z}\frac{\partial T}{\partial z}, \tag{8.4}$$

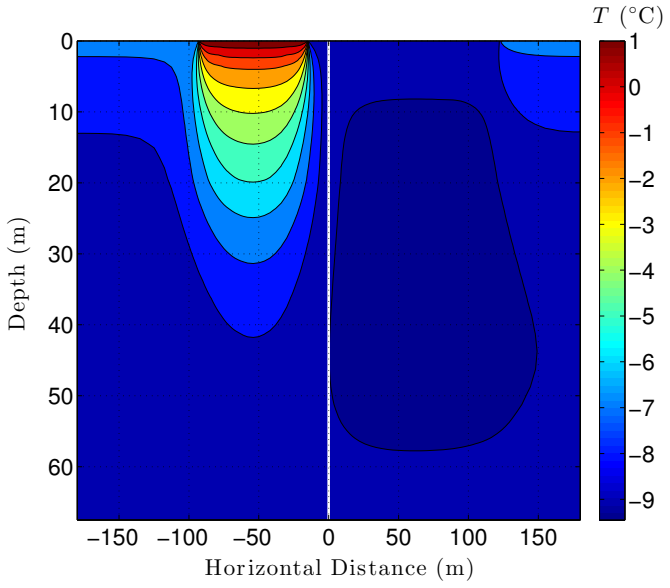

Figure 8.8: Cross-section of the simulated temperature field through the East Simpson No. 1 reserve pit and drill pad during 2015. Vertical white line represents the borehole.

where the trial values $\check{C}$ and $\check{K}$ depend on ϕ_0, $\mathcal{M}$, and K_g^{25}. A comparison of the gradient $\partial T/\partial z$ computed from multiple temperature logs reveals the magnitude of the uncertainty of this derivative, and similarly for the curvature $\partial^2 T/\partial z^2$. The derivative uncertainties are also expressed by the oscillation of the residuals δ with depth (**Figure 8.9**). The standard deviation of the residuals provides an estimate of its uncertainty $\tilde{u}_\delta$, and of the heat-diffusion terms (the symbol ˜ is used to indicate an 'estimate' of the true value).

A measure of the total misfit to the HD equation for a trial combination of properties is given by the 2-norm,

$$\Delta \;=\; ||\delta||_2 \;=\; \left(\sum_i^N \delta_i^2\right)^{1/2} . \tag{8.5}$$

Considering the uncertainties present in the δ_i, the smallest 2-norm among all possible combinations of $\check{C}$ and $\check{K}$ is estimated to be,

$$\tilde{\text{min}}(\Delta) \;=\; \tilde{u}_\delta \sqrt{N-1}\,. \tag{8.6}$$

The uncertainty of the misfit Δ arising from the uncertainty of the individual heat-diffusion terms is very similar,

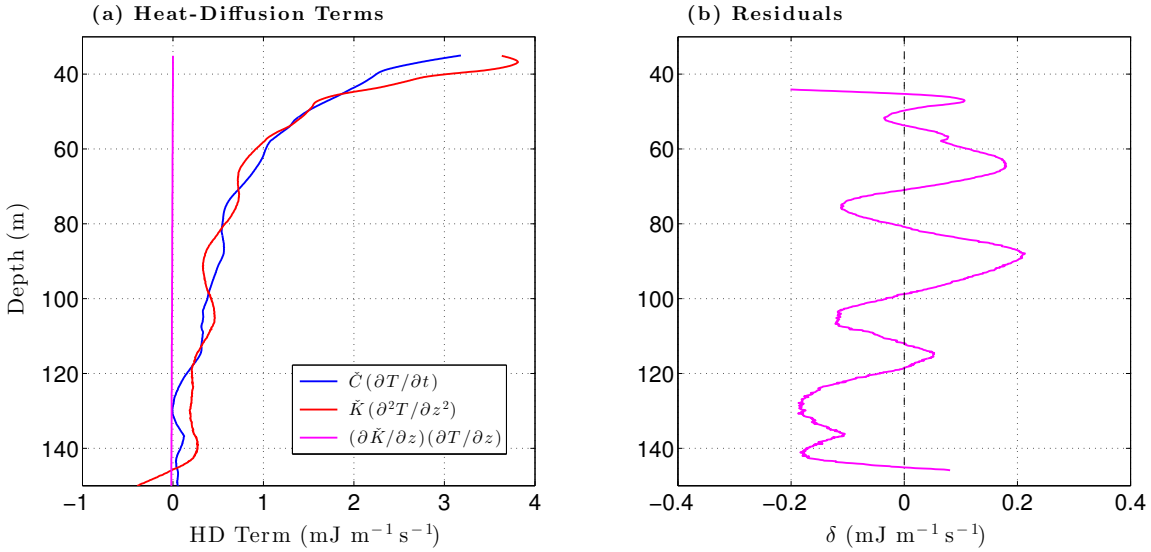

Figure 8.9: Heat-diffusion terms and transient-analysis residuals for the Kugrua well. Heat-diffusion terms in Eq. (8.4) calculated for Kugrua are shown in (a) assuming $\phi_0 = 13.7\%$ and $K_g^{25} = 1.38$ W m^{-1} K^{-1}; the sediment texture $\mathcal{M}$ is specified by the $\mathcal{M}$ - ϕ_0 relationship determined from the depth of the B-IRP. As with all the NPR-A wells, the HD term involving the conductivity gradient $\partial K/\partial z$ is much smaller than the transient or the curvature terms. Panel (b) shows the residuals δ for this trial combination of properties.

$$\tilde{u}_{\Delta} \;=\; \tilde{u}_{\delta}\,\sqrt{N}. \tag{8.7}$$

Since Δ is uncertain, the true value for $\min(\Delta)$ and its location in (C, K)-space, or equivalently in $(\phi_0, \mathcal{M}, K_g^{25})$-space, are unknown. However, it can be shown that the variable

$$t \;=\; \frac{\left[\tilde{\min}(\Delta) - \min(\Delta)\right]\,\sqrt{\nu+1}}{\tilde{u}_{\Delta}} \tag{8.8}$$

has a t distribution with ν degrees of freedom [*Bowker and Lieberman*, 1972]. From this distribution, the upper (one-sided) limit for the true value of $\min(\Delta)$ is,

$$U_{\min(\Delta)} \;=\; \tilde{\min}(\Delta) \;+\; \tilde{u}_{\Delta}\left(\frac{t_{\alpha;\nu}}{\sqrt{\nu+1}}\right), \tag{8.9}$$

at the $100\,(1-\alpha)\%$ confidence level; $t_{\alpha;\nu}$ is the $100\,\alpha$ percentage point of the t distribution with ν degrees of freedom. The $100\,(1-\alpha)\%$ confidence limits for properties $(\phi_0, \mathcal{M}, K_g^{25})$ are those whose associated misfit values Δ satisfy,

$$\Delta \;\leq\; U_{\min(\Delta)}\,. \tag{8.10}$$

The heat-diffusion equation applies to a specific instant in time. Thus, each temperature log can be considered a single realization of a multidecadal experiment. In this vein, we consider the normalized misfit functional for the j^{th} temperature log in a given well,

$$X_j \;=\; \left(\frac{\Delta_j}{u_{\Delta_j}}\right) \tag{8.11}$$

and define a stacked misfit of M logs by,

$$\hat{\Delta} \;=\; \frac{1}{M}\sum_{j}^{M} X_j. \tag{8.12}$$

Each log of the stack is given equal weight. Because the uncertainty of X_j is 1, the smallest expected value for $\min(\hat{\Delta})$ is also 1 and the uncertainty of the stacked misfit is,

$$u_{\hat{\Delta}} \;=\; \frac{1}{\sqrt{M}}\,. \tag{8.13}$$

By analogy with the case for a single log, the upper (one-sided) limit for the true value of $\min(\hat{\Delta})$ is,

$$U_{\min(\hat{\Delta})} \;=\; \tilde{\min}(\hat{\Delta}) \;+\; \tilde{u}_{\hat{\Delta}}\left(\frac{t_{\alpha;\nu}}{\sqrt{\nu+1}}\right). \tag{8.14}$$

For the stack, the $100\,(1-\alpha)\%$ confidence limits for properties $(\phi_0, \mathcal{M}, K_g^{25})$ are those whose associated stacked misfit values satisfy $\hat{\Delta} \;\leq\; U_{\min(\hat{\Delta})}$ (**Figure 8.10**).

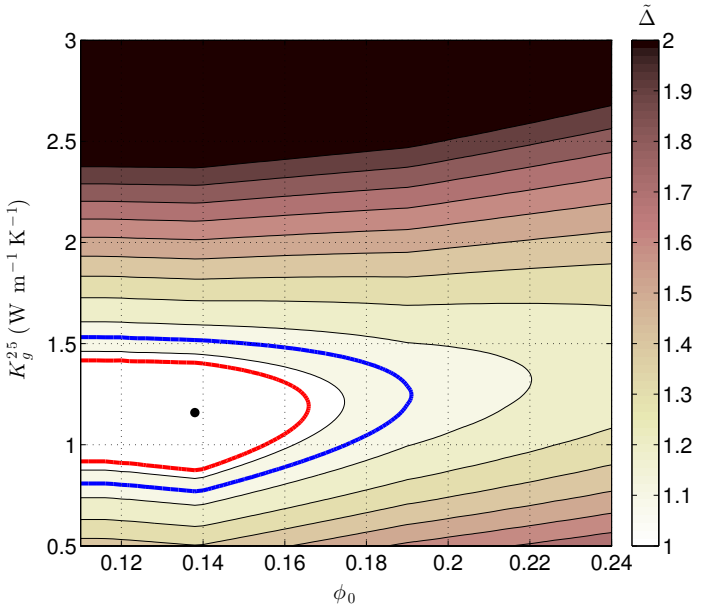

Figure 8.10: Stacked normalized misfit $\hat{\Delta}$ for the Peard Bay Test Well based on the 2003, 2007, 2012 temperature logs. Red and blue lines show the 75% and 90% confidence limits for K_g^{25} and ϕ_0. Black dot shows the location of the $\hat{\Delta}$ minimum. Subsequent analysis shows that no ice exists near 280 m when $\phi_0 < 13.8\%$, contrary to the latent-heat analysis which placed the B-IRP at this depth (Section 8.3). On this basis, solutions with $\phi_0 < 13.8\%$ are implausible. The 75% confidence limits for ϕ_0 and K_g^{25} are then 13.8–16.8% and 0.88–1.40 W m^{-1} K^{-1}, respectively, for the Peard Bay well. The 75% confidence limits for $\mathcal{M}$ (1.28–1.65) are given by the $\mathcal{M}$ - ϕ_0 relationship for this site.

Stacked misfit functionals $\hat{\Delta}$ were calculated for the majority of the DOI/GTN-P wells using the logs containing the strongest climate-induced temperature transients (1995–present). These logs also satisfy the requirement that radial effects due to the drilling disturbance be small. To avoid lateral heat-flow components associated with the drill pads and reserve pits, the temperature data used in the analysis were restricted to depths greater than 35–55 m, depending on the thermal diffusivity and the configuration of the reserve pit and drill pad. To further enhance the sensitivity of the analysis, data from depths greater than 150–160 m were not used since the transient climate signal could not be detected ($\partial T/\partial t \simeq 0$) in the temperature logs beyond these depths. The 75% confidence intervals for ϕ_0, $\mathcal{M}$, and K_g^{25} resulting from the analysis are given in **Table 8.5**. Given the uncertainties, all parameter values within these intervals are viewed as equally likely. The 75% confidence intervals further constrain the ϕ_0 and $\mathcal{M}$ values found in Sections 8.2 and 8.4. Low borehole-fluid levels prevented the acquisition of shallow temperature data

Table 8.5: 75% confidence intervals for the porosity, sediment texture, and grain conductivity at the DOI/GTN-P well sites resulting from the temperature transient analysis. Depth interval indicates the depths over which the analysis was performed and to which the derived material properties apply. Superscript† indicates sites where the $\mathcal{M}$ - ϕ_0 relationship is based on the nearest well of the same rock subunit. ⊘ indicates sites lacking the shallow temperature measurements needed to reliably perform a transient analysis.

Well Code	Depth Interval (m)	Rock Unit	ϕ_0 (%)	$\mathcal{M}$	K_g^{25} (W m^{-1} K^{-1})
AWU	38–160	Torok *(foothills)*	8.0–10.4	2.3	2.01–2.35
TLK	40–160	Nanushuk *(Corwin)*	13.8–16.8	1.25–1.63	0.58–1.25
PEA	44–155	Nanushuk *(Corwin)*	13.8–16.6	1.28–1.65	0.88–1.40
KAG	43–147	Nanushuk *(Corwin)*	13.6–16.3	1.32–1.74	1.22–1.50
SME	35–145	Nanushuk (*Corwin)*	12.8–14.9	1.41–1.80	0.74–1.12
TUL†	46–150	Torok *(coastal)*	11.4–12.5	1.27–1.76	1.04–1.26
WDS	⊘	Torok (*coastal)*			
KUY	35–160	Nanushuk *(CU)*	20.0–23.5	2.38–2.62	0.59–1.56
ESN	40–140	Nanushuk *(CU)*	28.0–31.0	2.58–2.91	1.40–2.08
IKP	38–155	Nanushuk *(CU)*	30.0–35.9	2.39–2.68	0.64–0.99
KOL†	50–160	Nanushuk *(CU)*	17.0–20.4	2.00–2.16	1.13–1.44
SBE	⊘	Nanushuk *(Umiat)*			
DRP	⊘	Colville *(A)*			
JWD	⊘	Colville *(A)*			
ETK†	35–160	Colville *(A)*	25.0–29.7	2.77–3.13	0.76–1.30
NKP	35–160	Colville *(A)*	25.0–29.0	2.77–3.07	0.62–1.29
ATI	35–160	Colville *(A)*	24.0–28.5	2.59–2.92	0.76–1.42
SOH	40–160	Colville *(B)*	22.0–24.8	2.93–3.22	2.23–3.35
FCK	55–160	Colville *(B)*	25.0–27.8	3.53–3.89	2.66–3.61
NIN†	54–150	Colville *(B)*	25.0–27.7	3.53–3.88	2.32–3.08

in several of the wells (West Dease, Seabee, Drew Point, J.W. Dalton). In these cases, a transient analysis could not be reliably performed.

For the most part, the rock subunits defined for NPR-A permafrost occupy distinct places in ($\phi_0, \mathcal{M}, K_g^{25}$)-space (**Figure 8.11**). An exception is the Torok-*coastal* and Nanushuk-*Corwin* subunits of the western NPR-A which are found to have essentially the same ($\phi_0, \mathcal{M}, K_g^{25}$) values. Treated as a single group, the Torok-*coastal*/Nanushuk-*Corwin* rocks above $\sim$ 150 m have low porosities ($<$ 17%), low mean grain conductivities (0.6–1.5 W m^{-1} K^{-1}), and the unfrozen water characteristics of a Fairbanks-silt/very-fine-sand mixture leading to a relatively high freezing temperature. The low mean grain conductivities are consistent with the drill cutting reports which describe these subunits as mudrocks with

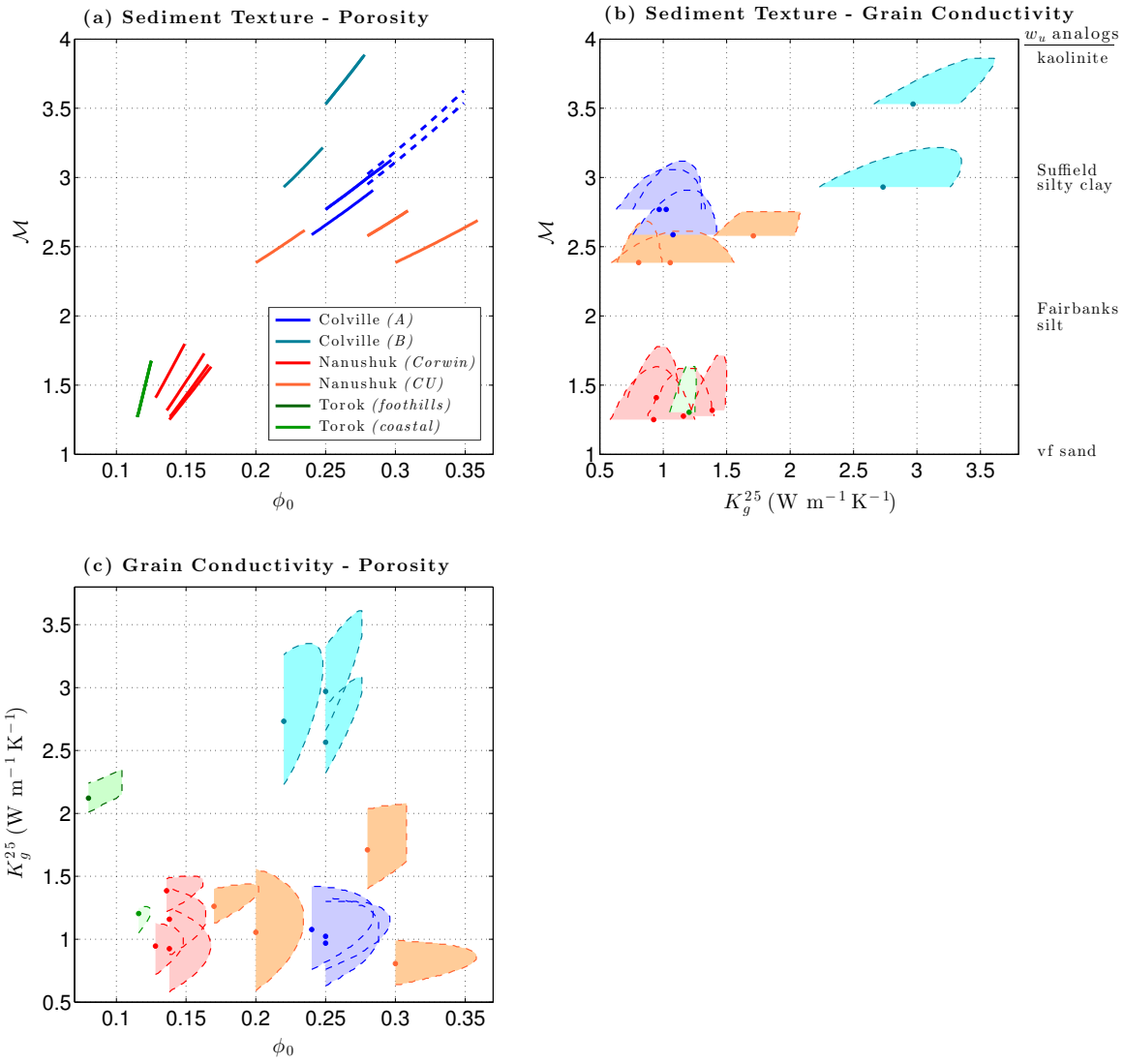

Figure 8.11: Relationship between the sediment texture and near-surface porosity at the DOI/GTN-P well sites in the NPR-A (a). The relationship for the Drew Point and J.W. Dalton wells derived from the B-IRP analysis are shown by dashed lines as they could not be further constrained by a transient analysis. Colored patches in (b) show the joint 75% confidence intervals for sediment texture and grain thermal conductivity; dashed lines delineate values with the largest misfits within the 75% confidence intervals. Panel (c) shows the joint 75% confidence intervals for grain conductivity and near-surface porosity.

substantial amounts of interbedded coal. The thermal conductivity of many clays (illite, smectite, mixed clays) is about 1.85 W m^{-1} K^{-1} [*Brigaud and Vasseur*, 1989] while that of coal is much lower, 0.29 W m^{-1} K^{-1} for a coal sample from the NPR-A [*Herrin and Deming*, 1996]. The mean grain conductivities of the transitional Nanushuk-*CU* subunit are also low. The sediment texture of this subunit best matches a mixture of Fairbanks silt and Suffield silty clay. What's distinctive about the Nanushuk-*CU* is its broad porosity range (17–36%). Higher up in the stratigraphic sequence, Colville-*A* has near-surface porosities of 24–30%, a sediment texture close to that of Suffield silty clay, and a low mean grain conductivity (0.6–1.4 W m^{-1} K^{-1}) similar to that of several other permafrost subunits in the NPR-A. In this case, a contributing factor to the low conductivity may be the presence of small wood fragments; wood has a thermal conductivity on the order of 0.1 W m^{-1} K^{-1}. Although Colville-*B* has a porosity range similar to that of Colville-*A*, its other properties are quite different. The mean grain conductivities for Colville-*B* are much higher (2.5–3.5 W m^{-1} K^{-1}), most likely due to a higher quartz sand content, and its unfrozen water properties resemble a mixture of kaolinite and Suffield silty clay leading to a low freezing temperature (about $-5°C$).

The availability of ϕ_0, $\mathcal{M}$, and K_g^{25} allows the other thermophysical properties to be determined using the permafrost model presented in Chapter 7. **Figures 8.12–8.13** show the bulk density ρ, volume fraction of ice ϕ_i, volumetric heat capacity C, thermal conductivity K, and thermal diffusivity κ, for the DOI/GTN-P monitoring wells in the NPR-A. Within the upper 150 m, Torok and Nanushuk-*Corwin* rocks have the highest densities while the transitional Nanushuk-*CU* rocks have the lowest. Associated with their low densities, Nanushuk-*CU* rocks are predicted to have the highest ice contents, $\sim$ 20% in some cases. The volume fraction of ice tends to be low ($<$ 10%) for Torok, Nanushuk-*Corwin*, and Colville-*B* rocks. Despite their low ice contents, Colville-*B* rocks have the highest heat capacity in the upper 150 m of all the permafrost subunits since Colville-*B* permafrost temperatures are closer to the freezing point than for any other subunit. In most cases, the volumetric heat capacity of Nanushuk and Colville rocks is very sensitive to depth. In contrast, the bulk thermal conductivity is fairly uniform with depth. The bulk conductivity is highest for the Torok-*foothills* and Colville-*B* subunits and lowest for the Nanushuk-*Corwin* and Colville-*A* subunits. With the exception of the Awuna well

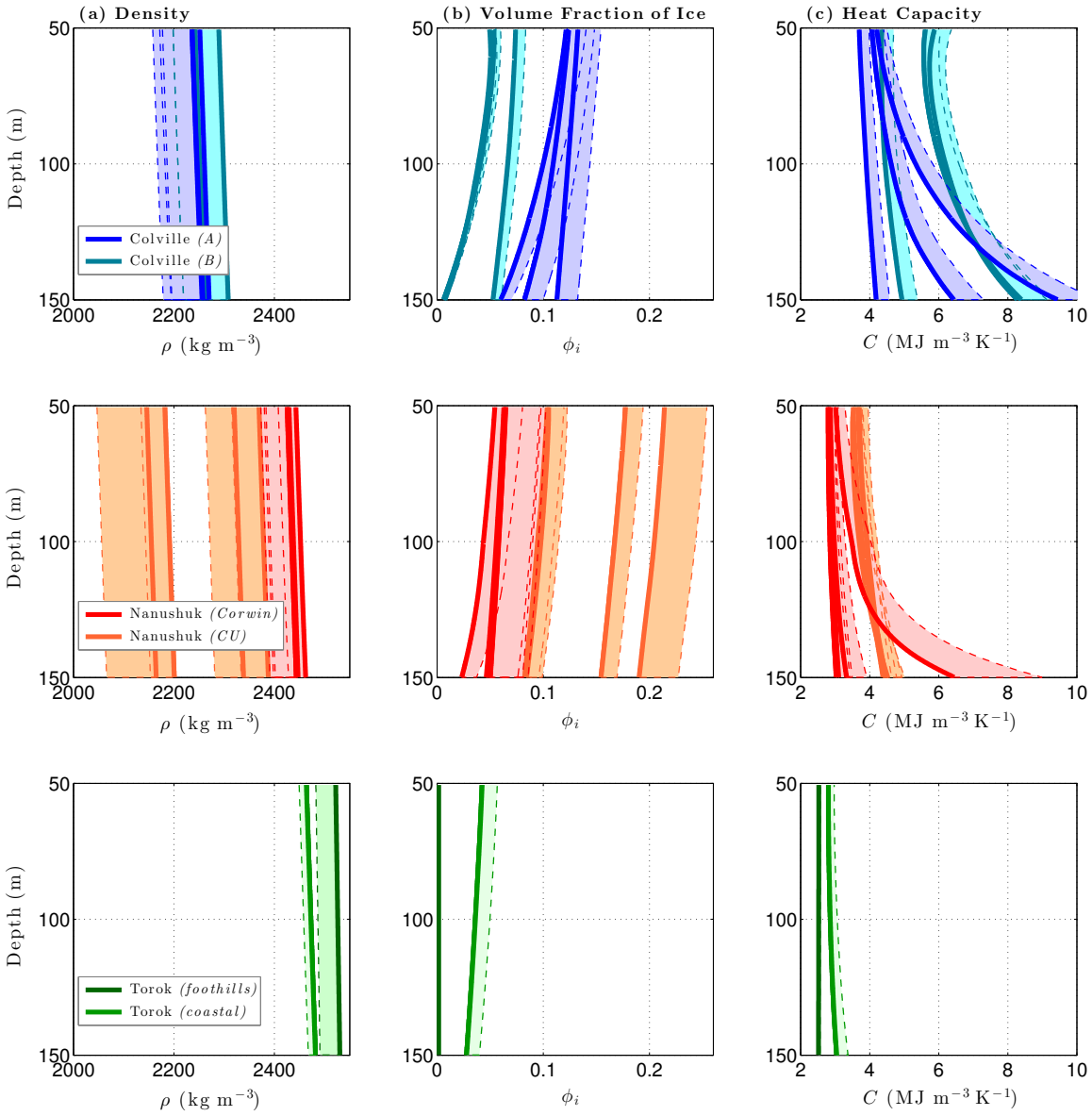

Figure 8.12: Bulk density ρ for the DOI/GTN-P well sites (a). Patches show the 75% confidence interval, solid lines show values corresponding to the best fit (smallest misfit $\hat{\Delta}$), while dashed lines delineate values for the largest misfits within the 75% confidence interval. Panel (b) shows the volume fraction of ice ϕ_i while (c) shows the volumetric heat capacity.

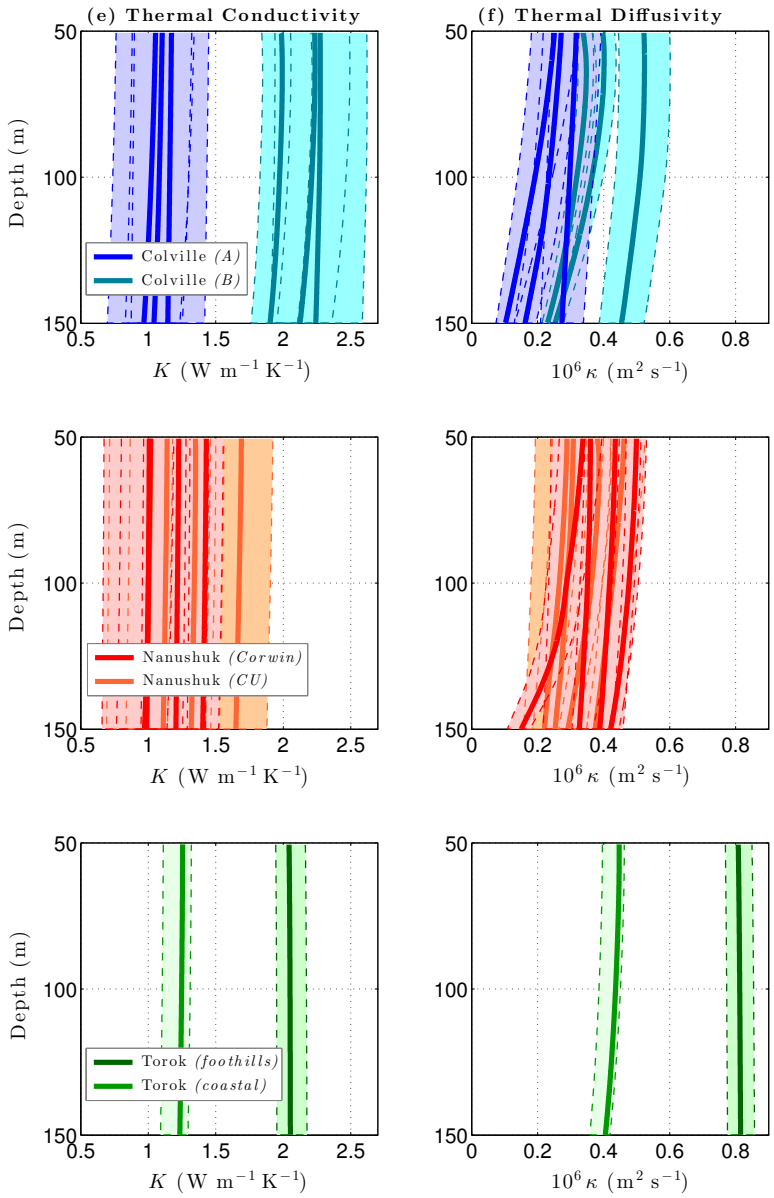

Figure 8.13: Thermal conductivity K and diffusivity κ for the DOI/GTN-P well sites.

(Torok-*foothills*), bulk thermal diffusivities are low ($< 0.5 \times 10^{-6}$ m^2 s^{-1}) in the NPR-A. Colville-*A* rocks have exceptionally low thermal diffusivities, as do the rocks at some of the Nanushuk-*CU* sites (0.1–0.3 $\times 10^{-6}$ m^2 s^{-1}).

Lachenbruch et al. [1982] noted that a large change in the temperature gradient occurs near the base of coarse-grained permafrost in Prudhoe Bay due to the thermal conductivity difference between ice and water held in the pore spaces. Several have noted the lack of a comparable gradient change in the NPR-A temperature logs. Although more muted

than for coarse-grained permafrost, the permafrost model (Chapter 7) does predict that a gradient change should exist near the B-IRP for the fine-grained permafrost of the NPR-A. **Figure 8.14** illustrates the situation at the Peard Bay well. Due to the unfrozen water properties of fine-grained permafrost, the temperature gradient is predicted to gradually decrease above the B-IRP upon approaching the surface where temperatures are colder and the ice content is higher. However, the gradient is predicted to decrease by no more than 6% at this site due to the ice/water conductivity difference. In contrast, the observed temperature gradient variations at Peard Bay are on the order of $\pm$30%, no doubt due to lithologic variations within the mudrocks. Thus, the gradient change predicted by the ice/water conductivity difference is masked by the lithologic variations. The situation is similar at all the other NPR-A well sites, explaining the absence of the predicted gradient change near the B-IRP for these wells.

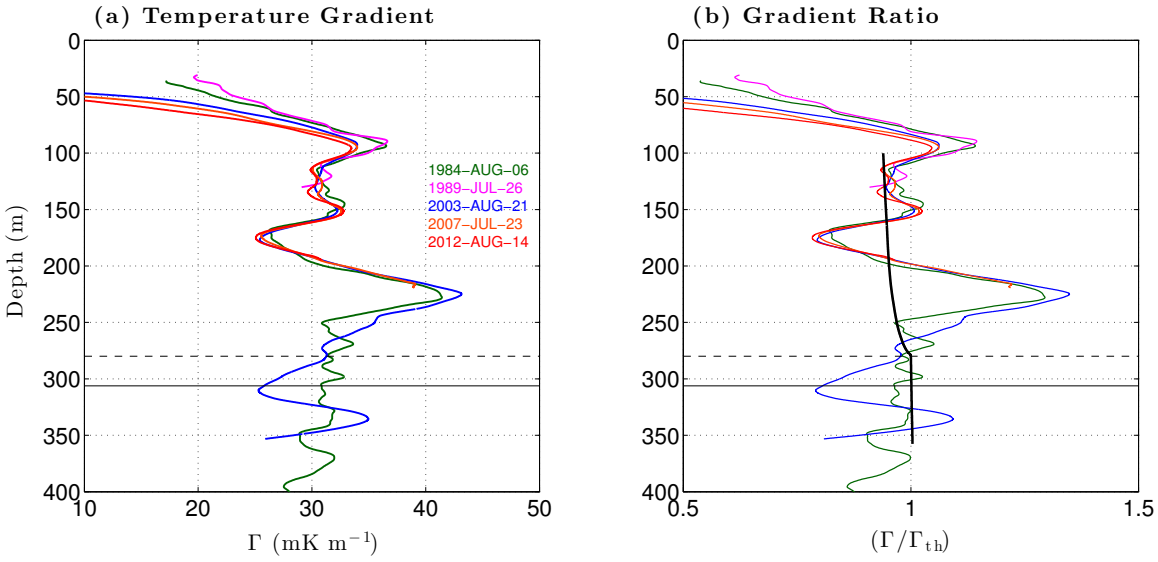

Figure 8.14: Temperature gradient $\Gamma = \partial T/\partial z$ determined from the Peard Bay temperature logs after most of the drilling disturbance had dissipated (a). Solid horizontal line shows the base of permafrost while the dashed line shows the base of ice rich permafrost (B-IRP). Panel (b) shows the ratio of Γ to that below the B-IRP where the ice is thawed. Black near-vertical line shows the $\Gamma/\Gamma_{\text{th}}$ ratio predicted by the bulk thermal conductivity found from the transient analysis.

8.6 Summary and conclusions

Two boundary condition experiments have been exploited to find the thermophysical properties of permafrost in the NPR-A. The first experiment was the heating and subsequent cooling of permafrost near the DOI/GTN-P wellbores caused by drilling operations. Analysis of the latent-heat effects present in the early temperature logs yields the location of the base of ice-rich permafrost (B-IRP) for most of the well sites. The depth of the B-IRP is found to be quite variable in the NPR-A, even over distances as short as 20 km. In contrast, the temperature at which permafrost first begins to freeze (T_f) is much more uniform. In the western NPR-A, the freezing point for Nanushuk-*Corwin* rocks is $-0.7°$C to $-0.8°$C. The Colville-*B* unit in the eastern NPR-A has the lowest freezing point, about $-5°$C. Most of the other NPR-A permafrost units have freezing points ranging from $-1°$C to $-2°$C. The Seabee well (Arctic Foothills) has by far the highest sandstone content of any of the NPR-A wells and an associated freezing point of $-0.15°$C. The freezing point depression provides a relationship between the sediment texture $\mathcal{M}$ and the porosity ϕ_0 for each of the rock units.

The second boundary-condition experiment is provided by the recent climatic warming that began in this region about 1990. Analysis of the transient response of permafrost to this warming constrains the possible values for three fundamental material properties (porosity, sediment texture, grain thermal conductivity) in the approximate depth range 50–150 m at the well sites. As expected from geologic reports, permafrost porosities are found to be low ($< 17\%$) in the western NPR-A. Porosities are both higher and more variable in the eastern NPR-A. Mean grain conductivities are generally low (0.6–1.5 W m^{-1} K^{-1}) for the NPR-A mudrocks. Colville-*B* in the eastern NPR-A has a significantly higher grain conductivity (2.5–3.5 W m^{-1} K^{-1}) than the other permafrost units, most likely due to a higher sand content. Sediment textures range from kaolinite/Suffield-silty-clay mixtures (Colville-*B*) to Fairbanks-silt/very-fine-sand mixtures (Nanushuk-*Corwin*). These textures produce the observed freezing point depressions, T_f.

Using the determined $(\phi_0, \mathcal{M}, K_s^{25})$ values, the main thermophysical properties of interest can be determined within the approximate 50–150 m depth range at the well sites. Torok and Nanushuk-*Corwin* rocks are found to have the highest densities while the transitional Nanushuk-*CU* rocks have the lowest. The volume fraction of ice tends to be low

($< 10\%$) for most of the permafrost in the NPR-A (below 40 m), explaining the difficulty of detecting interstitial ice using nonthermal geophysical logs. The exceptions are Colville-*A* rocks which are predicted to have ice contents as high as 15% and some Nanushuk-*CU* rocks with ice contents up to 18–25%. Colville-*B* rocks have the highest heat capacities, primarily due to the proximity of near-surface permafrost temperatures to the freezing point of these rocks. Except for the Torok unit, the heat capacity of permafrost in the NPR-A is fairly sensitive to depth. Paralleling the grain conductivities, bulk thermal conductivities are generally low (< 1.5 W m^{-1} K^{-1}) in the NPR-A. Bulk conductivities are higher for Torok-*foothills* and Colville-*B* rocks. Thermal diffusivities are generally very low in the NPR-A ($0.1–0.5 \times 10^{-6}$ m^2 s^{-1}); the Awuna well in the Arctic Foothills is the sole exception with a diffusivity near 0.8×10^{-6} m^2 s^{-1}. The availability of the thermophysical properties will improve our ability to understand the past, present, and future response of permafrost to climate change in this region.

8.7 References

Bartsch-Winkler, S., and Huffman, C. (1981), Petrography of the Nanushuk group and Torok formation, *USGS Open-File Report 81-1222*, U.S. Geological Survey, 65 pp.

Bird, K.J. (1987), The framework geology of the North Slope of Alaska as related to oil-source rock correlations, in *Alaska North Slope Geology*, Vol. 1, Tailleur, I., and Weimer, P. (eds), Pacific Section, Society of Economic Paleontologists and Mineralogists, Bakersfield, 121–143.

Bird, K.J. (1988), Alaskan North Slope stratigraphic nomenclature and data summary for government-drilled wells, in *Geology and Exploration of the National Petroleum Reserve in Alaska, 1974 to 1982*, USGS Professional Paper 1399, U.S. Geological Survey, 317–353.

Black, R.F. (1964), Gubik formation of Quaternary age in northern Alaska, *USGS Professional Paper 302-C*, U.S. Geological Survey, 59–90.

Bowker, A.H., and Lieberman, G.J. (1972), *Engineering Statistics*, 2nd Edition, Prentice-Hall, Inc., 641 pp.

Brigaud, F., and Vasseur, G. (1989), Mineralogy, porosity and fluid control on thermal conductivity of sedimentary rocks, *Geophysical Journal*, 98, 525–542.

Brouwers, E.M. (1994), Late pliocene paleoecologic reconstructions based on ostracode assemblages from the Sagavanirktok and Gubik formations, Alaskan North Slope, *Arctic*, 47, 16–33.

Carter, L.D. (1981), A Pleistocene sand sea on the alaskan Arctic Coastal Plain, *Science*, 211, 381–383.

Carter, L.D., and Galloway, J.P. (2005), Engineering geologic maps of northern Alaska, Harrison Bay Quadrangle, *USGS Open-File Report 2005-1194*, U.S. Geological Survey.

Clow, G.D. (2014), Temperature data acquired from the DOI/GTN-P Deep Borehole Array on the Arctic Slope of Alaska, 1973–2013, *Earth Syst. Sci. Data*, 6, 201–218, doi:10.5194/essd-6-201-2014.

Collett, T.S, Bird, K.J., Kvenvolden, K.A., and Magoon, L.B. (1988), Geologic interrelations relative to gas hydrates within the North Slope of Alaska, *USGS Open-File Report 88-389*, U.S. Geological Survey, 150 pp.

Gutman, S.I., Goldstein, A., and Guldenzopf, E.C. (1982), Gravity and magnetic investigations of the National Petroleum Reserve in Alaska, Tetra Tech Report No. 8201, 88 pp.

Herrin, J.M., and Deming, D. (1996), Thermal conductivity of U.S. coals, *J. Geophys. Res.*, 101, 25381–25386.

Huffman, A.C., Ahlbrandt, T.S., and Bartsch-Winkler, S. (1988), Sedimentology of the Nanushuk group, North Slope, in *Geology and Exploration of the National Petroleum Reserve in Alaska, 1974 to 1982*, USGS Professional Paper 1399, 281–298.

Lachenbruch, A.H., Sass, J.H., Marshall, B.V., and Moses, T.H., Jr. (1982), Permafrost, heat flow, and the geothermal regime at Prudhoe Bay, Alaska, *J. Geophys. Res.*, 87, 9301–9316.

Lachenbruch, A.H., Sass, J.H., Lawver, L.A., Brewer, M.C., Marshall, B.V., Munroe, R.J., Kennelly, J.P., Jr., Galanis, S.P., and Moses, T.H., Jr. (1987), Temperature and depth of permafrost on the alaskan Arctic Slope, in *Alaska North Slope Geology*, Vol. 2, Tailleur, I., and Weimer, P. (eds), Pacific Section, Society of Economic Paleontologists and Mineralogists, Bakersfield, 545–558.

Nelson, P.H., and Bird, K.J. (2005), Porosity-depth trends and regional uplift calculated from sonic logs, National Petroleum Reserve in Alaska, *USGS Scientific Investigations Report 2005-5051*, U.S. Geological Survey, 23 pp.

Osterkamp, T.E., and Payne, M.W. (1981), Estimates of permafrost thickness from well logs in northern Alaska, *Cold Reg. Sci. Technol.*, 5, 13–27.

Repenning, C.A. (1983), New evidence for the age of the Gubik formation alaskan North Slope, *Quaternary Res.*, 19, 356–372.

CHAPTER 9

PERMAFROST TEMPERATURES AND CHANGING CLIMATE, AN EXAMPLE FROM THE ARCTIC SLOPE OF ALASKA

9.1 Introduction

The primary purpose of the DOI/GTN-P Deep Borehole Array is to monitor the thermal state of permafrost as it responds to arctic climate change. After correcting for the drilling disturbance, the observed temperature changes in these wells are due to a mixture of climate-change effects and local landscape-change effects related to the reserve pits and drill pads. Our task is to disentangle these effects to isolate the portion that's due to climate alone. This is complicated because the reserve pits and drill pads are also responding to climate change. As demonstrated in Chapter 6, the magnitude of the thermal disturbance at the monitoring wells due to the reserve pits and drill pads depends on the thermal properties of the materials in the upper few tens of meters. In Chapter 8 we found the average thermophysical properties in the approximate depth range 50–150 m at each of the well sites. To separate the landscape effects from the climate effects, we now need to estimate the thermal properties above 50 m where the reserve pits and drill pads have their greatest impact.

Because of the nature of permafrost in northern Alaska, we cannot simply extrapolate the thermal properties from below 50 m all the way to the surface. The porosity of the upper 10–20 m of surficial materials is likely to be quite different from that of the underlying rock units. These surficial deposits consist of the unconsolidated Gubik Formation at elevations lower than 40 m (Chapter 8) and colluvium at many of the higher elevation sites. Soil-moisture data acquired by the DOI/GTN-P Climate Network [*Urban and Clow*, 2016] indicate the porosity of shallow sediments across the NPR-A is 40–42%, typical of

many silty clay soils. In addition, segregation ice (masses of pure ice outside the soil pore structure) is common in the upper few meters of fine-grained permafrost and can form as deep as 30 m [*Davis*, 2001]. The total volume of segregation ice has been estimated to be 10% in the upper few meters of the Arctic Coastal Plain [*Brown*, 1967] but locally can be much higher. *Barnhart et al.* [2014] report 30–70% of the upper few meters consist of segregation ice at Drew Point on the Beaufort coast. Even in the foothills, shallow geotechnical holes reveal massive amounts of segregation ice to depths of at least 9 m at the Awuna well site [*Husky Oil NPR Operations*, 1983a]. The combination of high porosity, saturated conditions, and the existence of segregation ice leads to relatively high total ice contents in the surficial materials at most of the well sites. With segregation-ice volumes ranging 10–30%, the total ice content is 46–58%. With the exception of the Colville-*B* and and Torok-*foothills* units (Chapter 8), such high ice volumes are expected to produce bulk conductivities much higher than those of the underlying rocks. In the northeastern NPR-A, a 10–50 m thick aeolian sand sheet of late Wisconsin age covers the area. This quartz-rich sand sheet is also likely to have a substantially different thermal conductivity than the underlying units.

An additional factor limiting our ability to extrapolate the thermal properties from 50–150 m upwards is the inhomogeneity of the deposits. With few exceptions, permafrost in the NPR-A consists of sequences of fine-grained sediments whose properties vary substantially on vertical scales of 50 m or less. Thus, the average properties at 50–150 m may be a poor predictor of what occurs above 50 m. The Tunalik well site is a good example. The drill cuttings description for this well shows alternating layers of coal, claystone, dolomite, and sandstone [*Husky Oil NPR Operations*, 1983b]. These materials are expected to produce wide variations in the bulk thermal conductivity over 20–50 m depth intervals (**Figure 9.1**).

In this chapter, we assimilate information from a local climate network along with the temperature logs and drill-cutting descriptions (where available) to establish the shallow thermal properties. Average thermophysical properties over the 50–150 m depth range provide additional guidance. We refer to this step as the site 'calibration' process. Once a site has been successfully calibrated, we are then able to separate the landscape effects from the climate effects. We then apply this methodology to the East Simpson well site in order to determine how much permafrost has warmed there purely due to climate change.

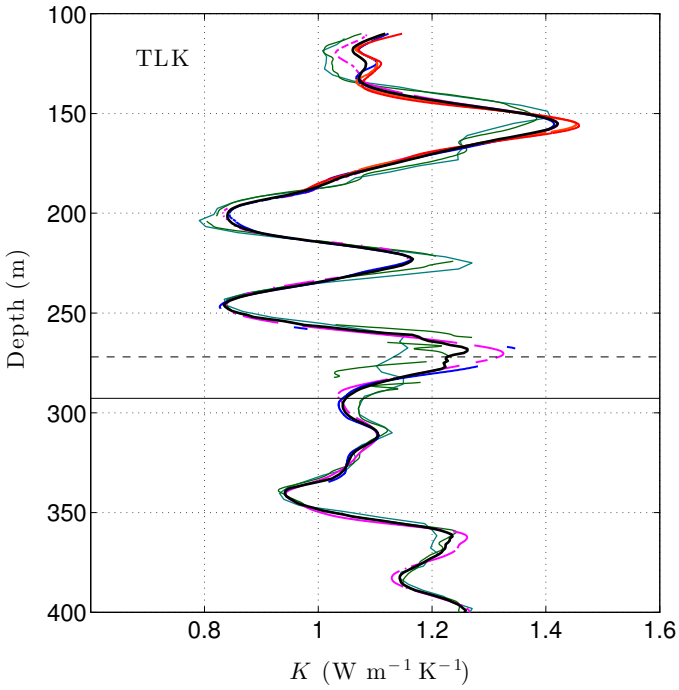

Figure 9.1: Bulk thermal conductivity profile at the Tunalik well determined from the drilling-corrected temperature logs assuming the geothermal flux is $q_b = 40$ mW m^{-2}. The bulk conductivity varies widely between coal, claystone, dolomite, and sandstone layers. Dashed line shows the base of ice-rich permafrost while the solid line is the depth of the 0°C isotherm.

9.2 NPR-A meteorological information

In 1998, the USGS began installing a network of climate stations in arctic Alaska to better understand changes occurring on federal lands under U.S. Department of the Interior management. These stations continually monitor air- and ground-temperatures, winds, radiation, snow depth, and soil moisture. Ground-temperature measurements are made at 10 depths spanning 5 to 120 cm. The shallower ground-temperature sensors record the seasonal freeze-thaw cycle within the 'active layer' while the deeper sensors monitor temperatures in perpetually frozen permafrost; maximum active-layer depths typically reach 30–50 cm by the end of summer in the NPR-A. By 2005, the coverage of the 16-element DOI/GTN-P Climate Network had substantially improved with the installation of the final stations. Many of these stations are located in the vicinity of DOI/GTN-P boreholes. Although air temperatures are very similar at climate-station/borehole pairs, shallow ground temperatures, soil moisture, and snow depths are often different as these

variables vary substantially over lateral distances as small as 10 m on the Arctic Slope. Because of swampy conditions around the borehole sites, many of the climate stations are located a kilometer or more from their corresponding boreholes. Still, the ground temperatures measured at the climate stations provide a rough check on our interpretation of the borehole data and other valuable information.

A significant issue with the records from the DOI/GTN-P climate stations is the large number of data gaps (5–15% of the record) resulting from damage caused by indigenous wildlife, primarily bears and wolverines. Trends calculated from these short incomplete records produce incoherent results. To circumvent this, four regional climate series were constructed utilizing all the available data from four primary stations located in the NPR-A near the Tunalik, Drew Point, West Fish Creek, and Seabee boreholes. These stations are representative of conditions on the Chukchi Sea coast, Beaufort Sea coast, northeastern NPR-A portion of the Arctic Coastal Plain, and Arctic Foothills, respectively. Missing data gaps were filled by analyzing cross-correlations with other stations in the climate network. **Figure 9.2** shows the resulting mean-annual air and 120-cm ground-temperature time series for the four areas. Because of the unique conditions in the Arctic Foothills, correlations with other stations were too poor to fill the missing data gaps in the ground-temperature record for this area.

The mean-annual climate series reveal the following for the western Arctic Slope: (a) The air-temperature series for the four areas in the NPR-A are in general well-correlated with each other. In addition, for the period of overlap (1999–2012) the air-temperature records are well-correlated with the recently developed 1920–2012 air-temperature record developed for the North Slope by *Bieniek et al.* [2014]. (b) The interannual variability is large as is characteristic of the Arctic. Air temperatures vary $\sim$ 1.2 K (1σ) interannually while ground temperatures vary about 0.6 K in the eastern NPR-A and 0.9 K near the Chukchi coast. (c) The ground-temperature series do not follow the air-temperature series in detail. This is because several factors in addition to air temperature influence temperatures in the ground, including: soil moisture, the timing of when the seasonal snowpack begins to form in the autumn (a delayed snowpack allows the ground to chill more readily), and the mean thickness of the winter snowpack. Thus, for example, mean-annual air temperatures were cold across the NPR-A during 1999 while ground temperatures were relatively

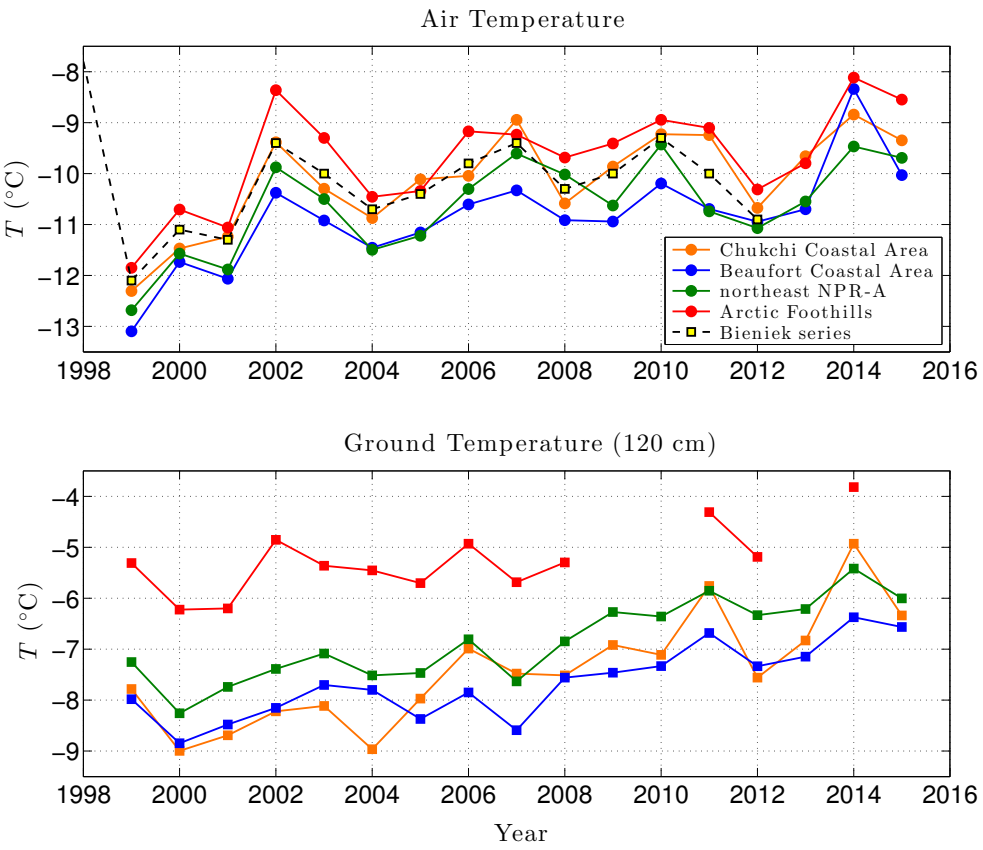

Figure 9.2: Mean-annual air and 120-cm ground temperatures for four areas in the NPR-A based on data from the DOI/GTN-P Climate Network [*Urban and Clow*, 2016]. The recent portion of the North Slope air-temperature record developed by *Bieniek et al.* [2014] is shown for comparison.

warm (**Figure 9.2**). (d) There is a distinct north-south gradient in both air and ground temperatures from the Beaufort coast to the Arctic Foothills with the coast being colder (**Figure 9.3**). Average air temperatures along the Chukchi coast are currently warmer than both the Beaufort coast and the northeastern NPR-A site on the Arctic Coastal Plain. In contrast, ground temperatures at the Chukchi site appear to be as cold as on the Beaufort coast. We view the latter result with caution as the ground temperature sensor at the Chukchi site has been subject to periodic frost heaving. The extent to which frost heaving has affected the ground-temperature data from this site is currently unknown. (e) Because of the insulating effects of the seasonal snowpack, mean-annual ground temperatures tend to be warmer than mean-annual air temperatures. This effect is substantial on the Arctic Slope. At the Beaufort coast and northeastern NPR-A sites, the temperature offset ΔT_{ag}

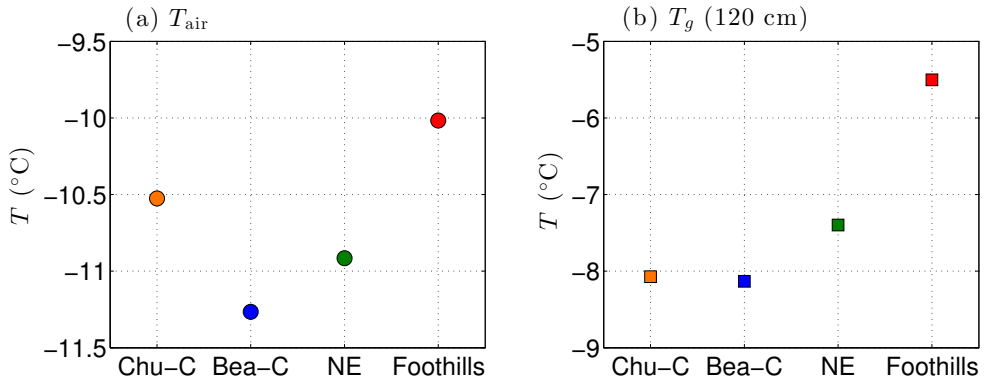

Figure 9.3: Average air and 120-cm ground temperatures over the period 1999–2008 at the Chukchi coast (Chu-C), Beaufort coast (Bea-C), northeast NPR-A (NE), and Arctic Foothills (Foothills) sites.

between 3-m air temperatures and 120-cm ground temperatures is 3.1–3.5 K (**Figure 9.4**). At the Arctic Foothills site where the seasonal snowpack is deeper, the offset is 4.5 K. Thus, the effect of the north-south air-temperature gradient on the ground is enhanced 1–1.5 K by deepening snow towards and into the Arctic Foothills. Again, the low ΔT_{ag} value at the Chukchi site must be viewed with caution due to periodic frost heaving of the ground-temperature sensor which may lead to a spurious value.

In addition to the above observations, a progressive warming is also apparent in the mean-annual DOI/GTN-P climate series over the period of record (1999–2015). Linear least-squares fits confirm that air temperature trends have been strongly positive in each of the four NPR-A focus areas since 1999 (**Table 9.1**, **Figure 9.5**). The similarity of the

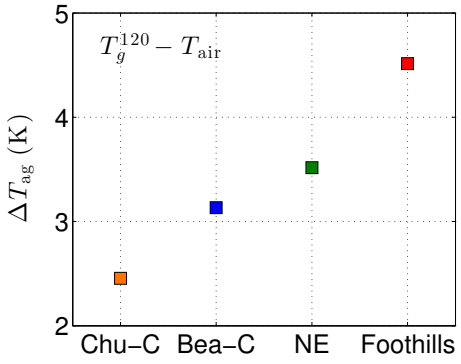

Figure 9.4: Average offset ΔT_{ag} between 120-cm ground temperatures and 3-m air temperatures over the period 1999–2008 at the Chukchi coast (Chu-C), Beaufort coast (Bea-C), northeast NPR-A (NE), and Arctic Foothills (Foothills) sites.

air-temperature trends in the four areas suggests the possibility that air temperatures have been warming uniformly across the NPR-A. To test this hypothesis, we use a two-sided procedure described by *Bowker and Lieberman* [1972] for testing whether two normally-distributed parameters are equal. Application of the test to the trends for every pair of areas indicates the air-temperature trends are the same in all four focus areas at the 75% significance level (there is a 25% chance that we would reject the hypothesis even if it is in fact true). Operating characteristic (OC) curves [*Bowker and Lieberman*, 1972] define the likelihood of accepting the hypothesis that the trends are equal when in fact they differ by an amount Δ_{trend}. We define the 'detection limit' to be the value of Δ_{trend} on the OC curve where we are just as likely to accept the hypothesis as reject it if the difference in trends is in fact Δ_{trend} (**Figure 9.6**). Based on the OC curves developed for each hypothesis test, the

Table 9.1: Temperature trends (K decade^{-1}) and their standard errors at the Chukchi coast (Chu-C), Beaufort coast (Bea-C), northeastern NPR-A (NE), and Arctic Foothills sites over the period 1999–2015.

	air (3 m)		ground (10 cm)		ground (120 cm)	
Area	$\partial T/\partial t$	σ	$\partial T/\partial t$	σ	$\partial T/\partial t$	σ
Chu-C	1.33	0.36	1.86	0.34	1.75	0.34
Bea-C	1.43	0.35	1.44	0.20	1.19	0.20
NE	1.16	0.37	1.41	0.20	1.36	0.20
Foothills	1.20	0.41	0.95	0.29	1.00	0.32

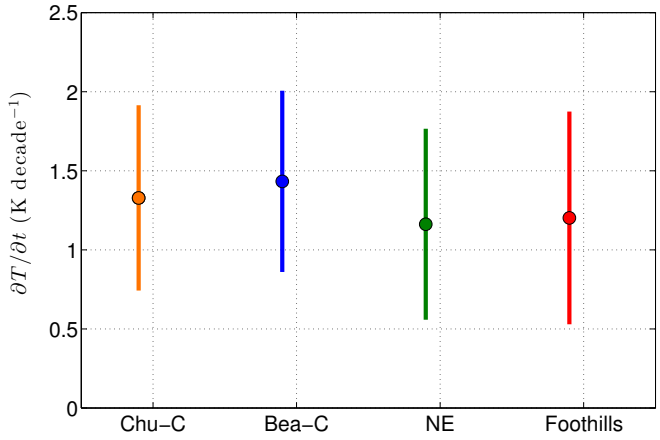

Figure 9.5: Air-temperature trends at the Chukchi coast (Chu-C), Beaufort coast (Bea-C), northeastern NPR-A (NE), and Arctic Foothills sites over the period 1999–2015. Vertical lines show the 90% confidence intervals.

detection limit for determining whether pairs of air-temperature trends are equal is found to range 0.54–0.58 K decade^{-1} (**Table 9.2**). We conclude that mean-annual air temperatures have been warming at 1.28 K decade^{-1} on the western Arctic Slope since 1999. Statistical tests indicate this warming has been uniform across the coastal areas, coastal plain, and foothills to within our current detection limit (0.56 K decade^{-1}).

Ground temperature trends are also found to be strongly positive at all four focus areas in the NPR-A, both in the active layer (10 cm) and below it where the permafrost is frozen year-round (**Table 9.1**, **Figure 9.7**). Hypothesis tests indicate the temperature trends are essentially the same at the 10-cm (active layer) and 120-cm (permafrost) depths in each area. Intercomparison of the 120-cm ground-temperature trends between the different

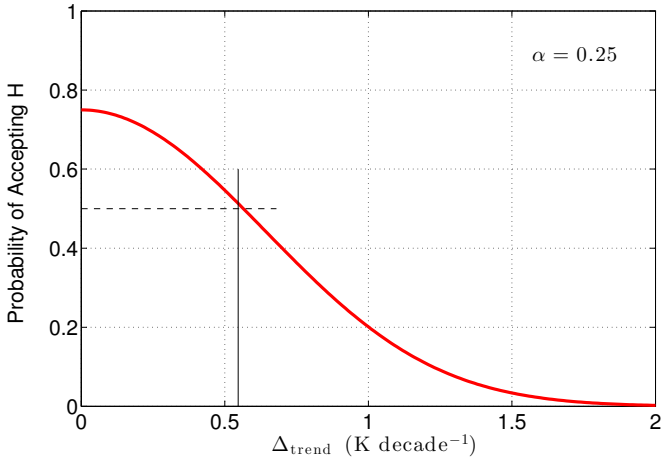

Figure 9.6: Operating characteristic curve for testing the hypothesis (H) that the air temperature trend at the Chukchi coastal site is the same as that at the Beaufort coastal site. The level of significance is set at 75% ($1 - \alpha = 0.25$). Vertical line shows the detection limit, 0.54 K decade^{-1} in this case. The hypothesis is accepted if the trends are in fact the same, or if they differ by no more than 0.54 K decade^{-1}. Otherwise the hypothesis is rejected.

Table 9.2: Test of the hypothesis that the air-temperature trends at the Chukchi coast (Chu-C), Beaufort coast (Bea-C), northeastern NPR-A (NE), and Arctic Foothills sites are equal.

	H: air temperature trends are equal				Detection Limit (K decade^{-1})			
Area	Chu-C	Bea-C	NE	Foothills	Chu-C	Bea-C	NE	Foothills
Chu-C	—	accept	accept	accept	—	0.54	0.55	0.57
Bea-C	accept	—	accept	accept	0.54	—	0.55	0.57
NE	accept	accept	—	accept	0.55	0.55	—	0.58
Foothills	accept	accept	accept	—	0.57	0.57	0.58	—

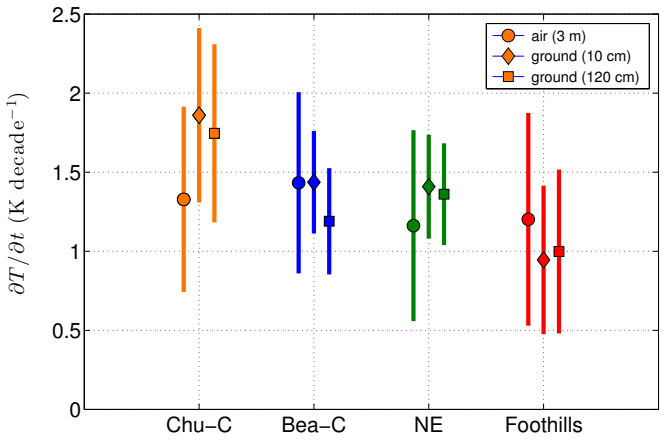

Figure 9.7: Air- and ground-temperature trends in the NPR-A over the period 1999–2015. Vertical lines show the 90% confidence limits.

focus areas shows that they are the same except for the Chukchi site (**Table 9.3**). As already discussed, the Chukchi ground-temperature values (and its trend) must be viewed with caution. Excluding the Chukchi value, we find that 120-cm ground temperatures have been warming at 1.32 K decade^{-1} in the NPR-A since 1999, a value very similar to the air temperature trend. With the exception of the Chukchi site, the ground-temperature trend has been relatively uniform across the NPR-A to within our current detection limit (0.3–0.5 K decade^{-1}). Hypothesis tests confirm that the air and 120-cm ground-temperature trends are the same at each site, with the possible exception of the Chukchi coastal site. The detection limit for these tests is about 0.5 K decade^{-1}. The similarity of the air- and ground-temperature trends (1.28 and 1.32 K decade^{-1}) suggests that since 1999, air-temperature change has been the primary driver for the observed permafrost warming in the NPR-A. On the decadal time-scale, no other mechanism such as a thickening snowpack or earlier snowmelt is required to explain the warming of permafrost in this region.

9.3 Site calibration

The objective of the site calibration is to find a set of shallow thermal properties that are consistent with the available information. This is accomplished through a 2-step optimization process utilizing the permafrost thermal model developed in Chapter 7. The first step is to find those thermal conductivity profiles that yield our best estimate of the temperature profile at a borehole soon after the well was drilled. The stipulation

Table 9.3: Test of the hypothesis that the 120-cm ground-temperature trends at the Chukchi coast (Chu-C), Beaufort coast (Bea-C), northeastern NPR-A (NE), and Arctic Foothills sites are equal.

	H: ground-temperature trends are equal				Detection Limit (K decade^{-1})			
Area	Chu-C	Bea-C	NE	Foothills	Chu-C	Bea-C	NE	Foothills
Chu-C	—	reject	accept	reject	—	0.45	0.45	0.52
Bea-C	reject	—	accept	accept	0.45	—	0.27	0.42
NE	accept	accept	—	accept	0.45	0.27	—	0.42
Foothills	reject	accept	accept	—	0.52	0.42	0.42	—

that we use the temperature field soon after drilling allows us to temporarily set aside the thermal effects of the reserve pit and drill pad which take several years to influence temperatures at the wellbore (below 20 m). The model domain is taken to be at least 400 m deep so as to include the entire permafrost zone. Below the 10–20 m thick surficial layer (or 10–50 m thick sand sheet in the northeastern NPR-A), the sediment texture and porosity are set to appropriate values for the rock units at each well site established in Chapter 8. Except for the northeastern NPR-A, the surficial layers are assumed to consist of silty clay; in the northeastern NPR-A, the surficial layer is taken to be a quartz-rich sand. At the lower boundary, the geothermal flux for a well is set equal to the value reported by *Deming et al.* [1996]. Although the uncertainties of their geothermal fluxes are large ($2\sigma = 40$–60%), the resulting shallow thermal properties are insensitive to the exact values. Since the temperature field above 120–140 m has been responding to surface temperature changes over the past century, a time-dependent upper boundary condition must be specified to match the temperature profile above these depths. As shown in Section 9.2, the mean-annual air-temperature series determined for the coastal areas, coastal plain, and foothills are well-correlated with each other, and with the Bieniek air-temperature series [*Bieniek et al.*, 2014]. Thus, the Bieniek record should provide a good representation of the air-temperature history at any site in the NPR-A back to 1920 as long as we take into account the offset between local air temperatures and the North Slope average provided by *Bieniek et al.* [2014]. We also found in Section 9.2 that 120-cm ground-temperature trends on the Arctic Slope have been essentially the same as the air-temperature trends over the past 15 years. For the site calibration, we assume that this equivalence also held further back in

time. We can then use the local air-temperature record estimated from the Bieniek series, offset by an amount ΔT_{ag} to account for the local long-term air-to-ground temperature difference, to provide the upper boundary condition for the permafrost model back to 1920. Temperatures deeper than 120–140 m are a response to mean surface temperatures during the 1800s. To initialize the model, we assume average surface temperatures during the 1800s were equal to a value T_{s0}. Although the initial surface temperature T_{s0}, the air-to-ground offset ΔT_{ag}, and shallow grain conductivity K_g profile are unknown, only unique combinations of these factors can result in simulated temperature profiles that match our best estimate of the temperature field soon after a well was drilled.

Step 1 of the calibration procedure is illustrated in **Figures 9.8–9.9** for the East Simpson #1 well which was completed in 1979. In this case, we use the drilling-corrected 1983 temperature log to establish the relationship between T_{s0}, ΔT_{ag}, and the K_g profile. If the mean surface temperature was $-11°C$ during the 1800s, then the local long-term air-to-ground temperature offset is required to be 3.07 K (**Figure 9.8a**) and the grain conductivity below the surficial layer (20–60 m) must be ~ 1.7 W m^{-1} K^{-1} (**Figure 9.8b**) in order for the simulated temperatures to match the 1983 drilling-corrected temperature log (**Figure 9.9**).

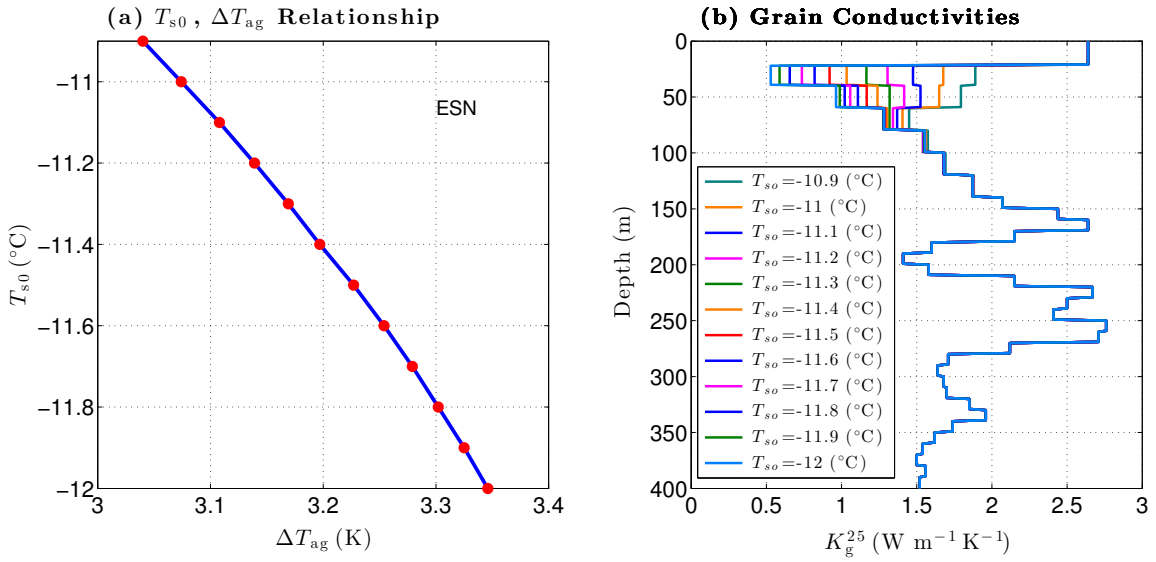

Figure 9.8: Relationship between the 1800s surface temperature T_{s0} and the mean long-term air-to-ground temperature difference ΔT_{ag} required for simulated temperatures at the East Simpson well to match the 1983 drilling-corrected temperature log (a). Panel (b) shows the associated grain-conductivity profiles. In this case, the surficial layer is 22 m thick and geothermal flux $q_b = 50$ mW m^{-2}.

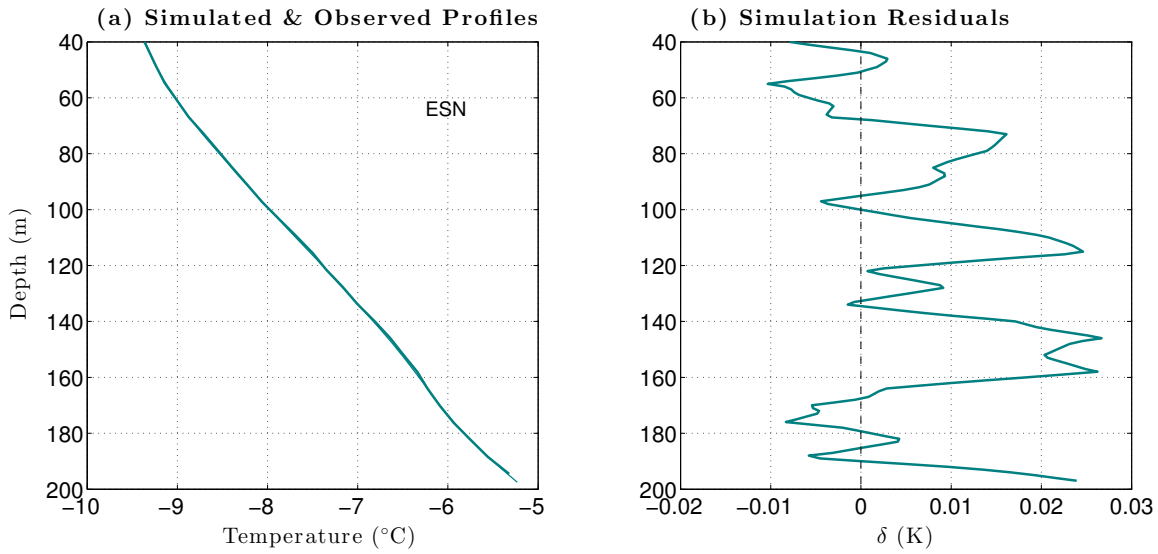

Figure 9.9: Simulated (black line) and drilling-corrected (green) 1983 temperatures at the East Simpson No. 1 well (a). Panel (b) shows the difference δ between the simulated temperatures and the 1983 drilling-corrected temperature log.

However, if T_{s0} was $-11.5°C$, then ΔT_{ag} is required to be 3.23 K and the 20–60 m grain conductivities must be $\sim$ 1.0 W m^{-1} K^{-1} in order to match the 1983 log. Thus, there is a unique ΔT_{ag} value and K_g profile linked to every possible T_{s0}. Although not a perfect match, the simulated temperature profiles are able to match the drilling-corrected 1983 temperature log to within $\sim$ 9 mK (1σ) at East Simpson using the parameter values determined using this calibration procedure. The reliability of the procedure hinges on the quality of the early temperature logs and on the drilling-disturbance corrections.

At this point in the site calibration process, the temperature difference ΔT_{pad} between the drill pad and the surrounding tundra is unknown. Step 2 of the site calibration attempts to place bounds on this very important quantity. To do this, temperatures are simulated at the wellbore from the time the well was spudded until the present using the 2-D cartesian permafrost model (Chapter 7), or the 3-D version if the well is located near a corner of the drill pad. These simulations introduce the effects of the reserve pit and drill pad into the site calibration. Utilizing the air-to-ground temperature offsets and grain-conductivity profiles found in Step 1, the 2-norm of the difference between the 2007–2008 simulated and drilling-corrected borehole temperatures is computed for a likely range of T_{s0} and ΔT_{pad} values. To increase our sensitivity to the reserve pit and

drill pad effects, the norms are calculated over a restricted depth range, nominally 25–50 m. Residuals above 25 m are ignored at this stage since they are sensitive to real short-term (1–4 year) differences between local mean-annual air-temperature and near-surface ground-temperature time series (Section 9.2, **Figure 9.2**). **Figure 9.10** shows the 2-norms calculated for the East Simpson #1 well. The true values for T_{s0} and ΔT_{pad} are taken to be those where the simulated temperatures best match (smallest norm) the drilling-corrected temperature logs. In the case of East Simpson, the optimal fit occurs when the drill pad is 1.3 K colder than the surrounding tundra and the mean 1800s surface temperature is $-11.8°C$. The corresponding grain-conductivity profile is given by the $T_{s0} = -11.8°C$ curve in **Figure 9.8b**. This completes the site calibration for the East Simpson well.

9.4 East Simpson well site, Beaufort Sea coast

The East Simpson No. 1 well is located on a low-lying (elev. 4 m) section of the Beaufort Sea coast, 90 km east of Point Barrow. Although the thickness of the Gubik Formation is unknown at this site, sensitivity tests during site calibration provide the best fit to the temperature logs with a 22-m thick surficial layer. Transitional Nanushuk rocks derived from the buildout of both the Corwin and Umiat deltas occur at this site below the Gubik Formation. According to the drill-cuttings description, silty clay occurs in the 26–62 m depth range at this well while 'very poorly indurated' shale with abundant fish remains oc-

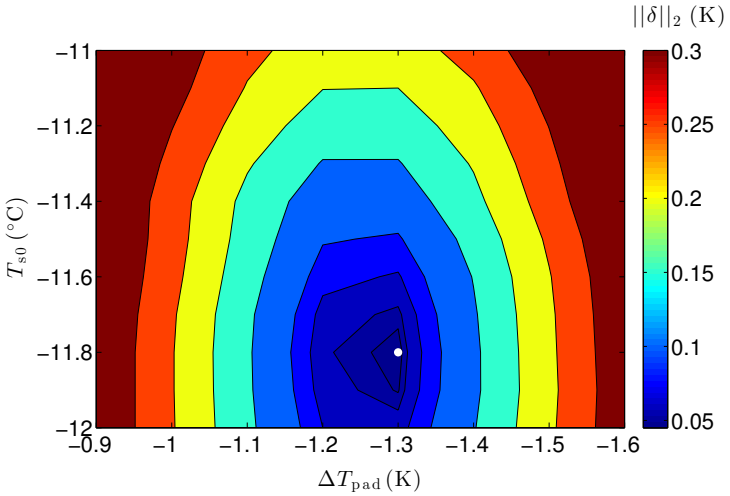

Figure 9.10: Norm of the 25–50 m temperature simulation residuals δ for the East Simpson No. 1 well found during Step 2 of the site calibration process. White point shows the location of the best (smallest norm) solution.

curs at 62–80 m [*Husky Oil NPR Operations*, 1983c]; no cuttings were recovered above 26 m. From the site calibration (Section 9.3), the bulk conductivity in the 22-62 m depth range is $\sim$ 1.0 W m^{-1} K^{-1}. Although low, it is close to the measured value (1.07 W m^{-1} K^{-1}) for a Nanushuk claystone at the nearby Ikpikpuk No. 1 well [*Deming et al.*, 1996]. The presence of abundant fish remains at shallow depths may further reduce the thermal conductivity as the conductivity of animal tissues and bones typically range 0.2–0.5 W m^{-1} K^{-1} at -5°C to -7°C [*Choi and Bischof*, 2010]. A full set of thermophysical properties determined for the East Simpson permafrost zone is shown in **Figure 9.11**. With these values, the base of ice-rich permafrost (B-IRP) is correctly predicted to be at 339 m and the 0°C isotherm defining the base of permafrost is at 366 m. Bulk conductivities of these Nanushuk rocks vary from about 1–1.5 W m^{-1} K^{-1} in the clays and shales to about 2 W m^{-1} K^{-1} in some of the sandstones (e.g., 254–272 m). Thermal diffusivities are low throughout the

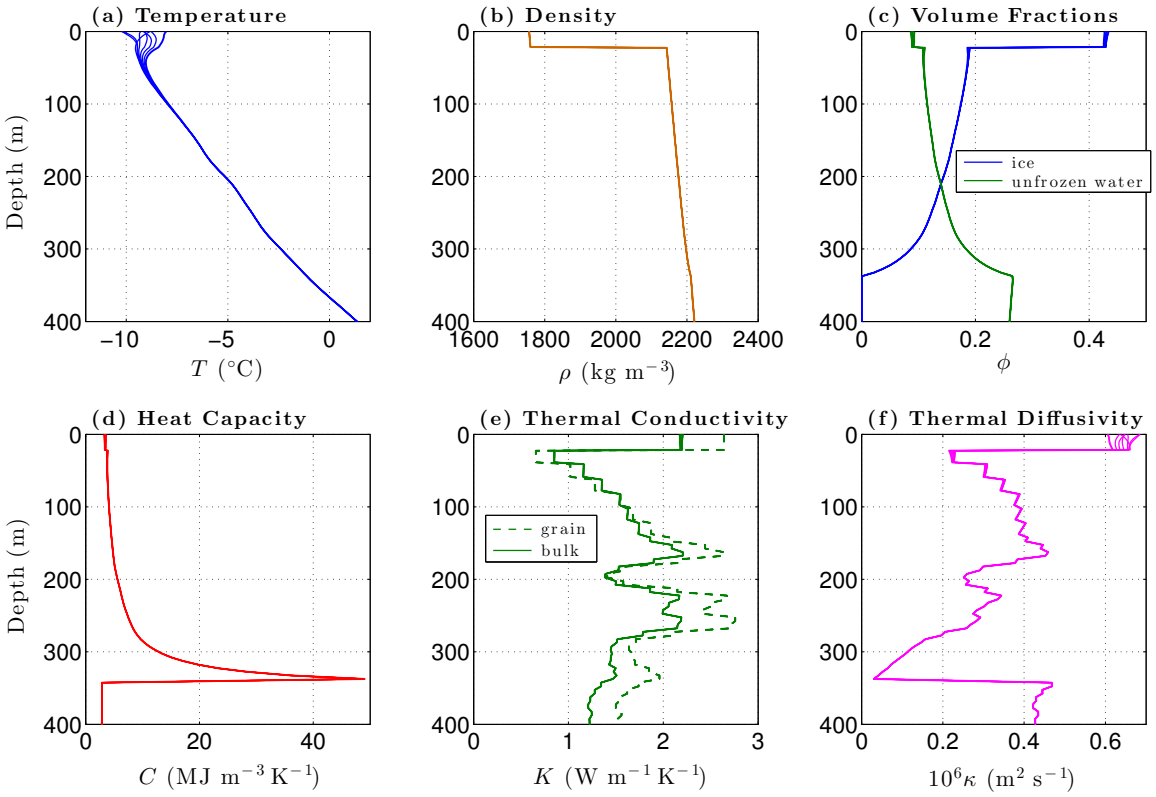

Figure 9.11: Thermophysical properties at the East Simpson No. 1 well site, including: bulk densities (b), volume fractions of ice and unfrozen water (c), volumetric heat capacity (d), grain and bulk thermal conductivities (e), and bulk thermal diffusivity (f). For reference, the (simulated) temperature profile every two years since the well was spudded is shown in panel (a).

climatologically interesting zone, about 0.65×10^{-6} m^2 s^{-1} in the surficial (Gubik) layer and $0.22–0.40 \times 10^{-6}$ m^2 s^{-1} at 22–150 m. Near the surface where temperatures are the coldest ($\sim -9°$C), at least 1/3 of the pore water within the Nanushuk rocks is predicted to be in the unfrozen state. Large amounts of unfrozen water contribute to the low thermal diffusivity at this site.

During site calibration, we found that the drill pad at East Simpson tends to be about 1.3 K cooler than the surrounding tundra. This is a consequence of poor vegetation recovery on the pad due to salt spray carried by the prevalent northeast winds off the Arctic Ocean (**Figure 9.12**). Counteracting the subsurface cooling by the pad is the relative warmth of the adjacent reserve pit. In this case, the drill-pad disturbance is the larger of the two, so the combined landscape-change effect is one of cooling at the well. Since 1984, the net cooling at the standard permafrost reporting depth (20 m) has varied between 0.1 K and 0.25 K (**Figure 9.13**). Applying the reserve pit and drill-pad disturbances as a correction to the drilling-corrected temperature logs yields the projected temperature profiles beneath the nearby undisturbed tundra (**Figure 9.14**).

Based on the fully-corrected logs, temperatures beneath the undisturbed tundra have progressively warmed 0.58 K decade^{-1} at the 20-m permafrost reporting depth since 1989 at East Simpson (**Figure 9.15**). This rate of warming is somewhat less than that experienced at the West Dock permafrost observatory 230-km east along the Beaufort Sea coast at

Figure 9.12: Logging the East Simpson No. 1 well on the Beaufort Sea coast. Vegetation is extremely sparse on the drill pad (foreground) compared to the undisturbed tundra seen beyond the reserve pit.

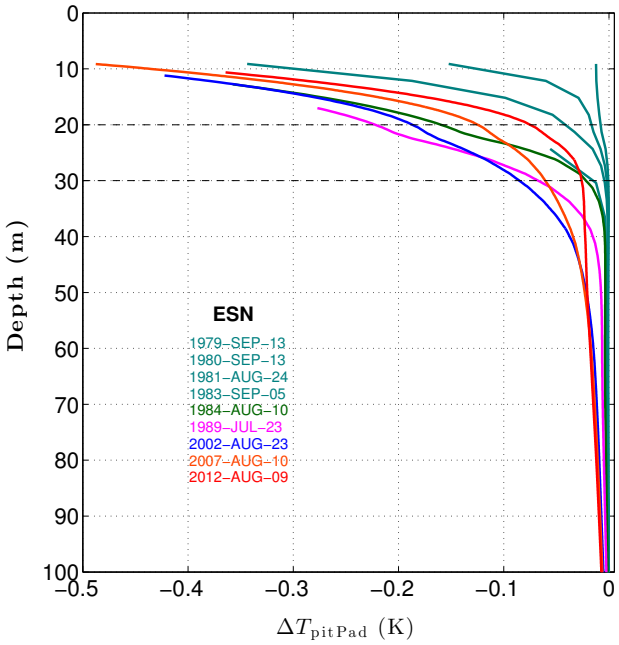

Figure 9.13: Thermal disturbance at the East Simpson No. 1 well due to the combined effects of the reserve pit and drill pad. Dashed horizontal lines show the reference depths, 20 and 30 m.

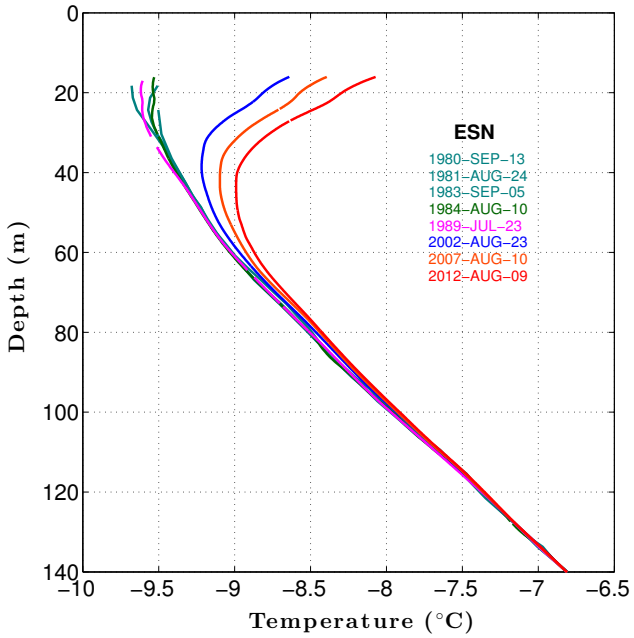

Figure 9.14: East Simpson No. 1 temperature logs corrected for the combined effects of the drilling disturbance, the reserve-pit disturbance, and the drill-pad disturbance. The fully corrected logs are equivalent to the expected temperature profiles beneath the nearby undisturbed tundra.

Prudhoe Bay [*Romanovsky et al.*, 2011]. The different warming rate at the two sites during the 1990s and 2000s may: (a) represent a real regional climate difference, (b) be due to the way the different vegetation types at the two sites respond to climate change, and/or (c) be the result of the lower thermal diffusivity beneath the Gubik Formation at East Simpson. The East Simpson well is located within a drained lake basin where the dominant vegetation types are classified as moist-meadow and wet-meadow tundra based on analysis of data from Landsat's Multispectral Scanner [*Morrissey and Ennis*, 1981]. In contrast, the West Dock permafrost observatory is located in drier terrain classified as a moist-or-dry herbaceous tundra [*Walker and Acevedo*, 1987]. It is likely that permafrost temperatures beneath the two vegetation types respond differently to a climate warming. In addition, alluvial gravels are common at West Dock. The relatively high thermal diffusivity of such gravels will allow the post-1989 surface warming to diffuse much more readily into the permafrost than is the case at East Simpson.

A temperature time series at the 20-m depth is a damped version of what occurs in permafrost at or very near the surface. To find the surface trends and to better connect with other climate records, we need to estimate the surface-temperature history $T_s(t)$ from the borehole information. To do this, we assume the shape of $T_s(t)$ is similar to the air-temperature history $T_{\text{air}}(t)$ when passed through an averaging filter on the order of a decade or more. This assumption is supported by the analysis of air- and ground-temperature data from the DOI/GTN-P Climate Network (Section 9.2). For East Simpson,

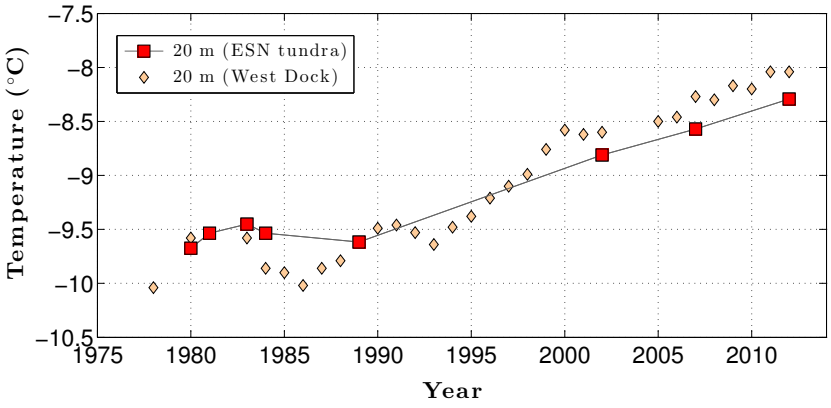

Figure 9.15: 20-m temperatures beneath undisturbed tundra adjacent to the East Simpson No. 1 well site. Also shown are the 20-m temperatures recorded at the West Dock permafrost observatory 230-km to the east in Prudhoe Bay for comparison.

the surface-temperature history just below (1.2 m) the active layer in the undisturbed tundra was found by perturbing the shape of a 9-year running-average air-temperature history by the smallest amount possible that would fit the fully-corrected 20-m borehole temperatures to within 0.01 K. The resulting $T_s(t)$ history for undisturbed tundra shows that surface temperatures at this site warmed 3.1 K between the early 1970s and 2012, or at a rate of 0.73 K decade^{-1} (**Figure 9.16**). Over the same time period, air temperatures warmed 2.9 K or 0.67 K decade^{-1}. The close correspondence of the air- and ground-temperature warming extends to a longer time period (1970–2012) our earlier conclusion that air-temperature changes have been the primary driver of ground-temperature changes on the Arctic Slope.

As noted by *Bieniek et al.* [2014], low-frequency multidecadal variations in Alaskan air temperatures are shared across all 13 Alaska climate divisions, from the Aleutians to the North Slope. These Alaskan air-temperature variations are strongly linked with the dominant mode of sea-surface temperature (SST) variability in the North Pacific Ocean as expressed by the Pacific decadal oscillation (PDO). Thus, air temperatures across Alaska tended to be warm during the 1920s and 1930s when SSTs in the eastern North Pacific Ocean were warm (positive PDO phase) and cool during the 1950s to mid-1970s when the reverse was true. The later cool period ended abruptly in 1976–1977 when the PDO flipped back to its positive phase. Unlike most climate events in Alaska which are associated with the PDO, temperatures in northern Alaskan experienced a pronounced cooling in the early 1980s that appears to be linked to the positive phase of the Arctic Oscillation [*Bieniek et al.*, 2014]. Both the 1976–1981 PDO warming event and the 1982–1988 AO cooling event are apparent in the near-surface (1.2 m) temperature record at East Simpson (**Figure 9.16**b). However, permafrost temperatures during these two events were much cooler than that predicted by the local air-temperature record offset by $\Delta T_{\mathrm{ag}} = 3.30$ K (blue dashed line, **Figure 9.16**b). Thus 1976–1988 is one time period where changes in snowpack or some other factor in addition to air temperature played a significant role in changing permafrost temperatures. By the mid-1990s conditions had changed to the point that near-surface permafrost temperatures were now about 0.2 K warmer than predicted by the local offset air-temperature record. The 1990s air-to-ground temperature transition is coincident with the time that air-temperature anomalies on the Arctic Slope became asynchronous with

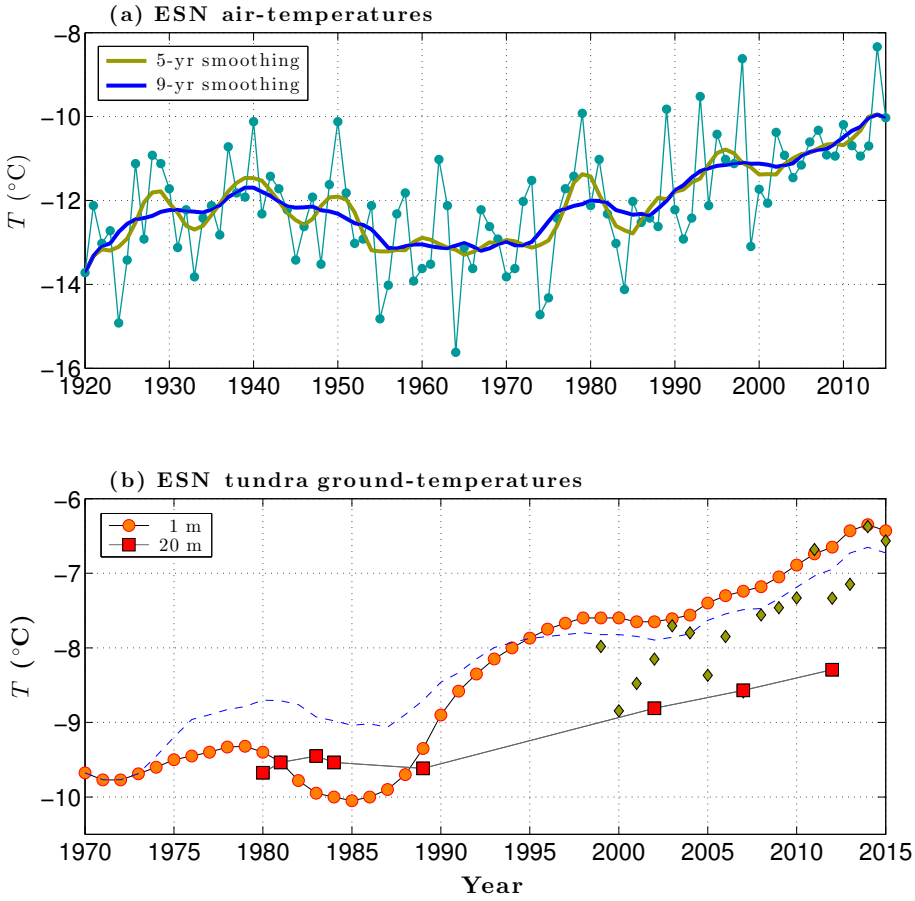

Figure 9.16: Air and ground temperatures at the East Simpson well site. Air temperatures estimated at East Simpson from the Bieniek record before 1999 and from DOI/GTN-P air-temperature measurements after 1999 are shown in (a). Panel (b) shows the 1.2-m and 20-m permafrost temperatures below undisturbed tundra adjacent to the East Simpson well site. Blue dashed line shows the 9-year smoothed air-temperature record offset by $\Delta T_{ag} = 3.30$ K. Green diamonds are the 1.2 m permafrost temperatures at the nearest DOI/GTN-P climate station (Drew Point), 26 km to the east on the Beaufort Sea coast.

the rest of the state, and with the PDO. This decoupling is associated with the massive loss of sea ice along the northern coast of Alaska. Just offshore from East Simpson, the number of open-water days on the Arctic Ocean more than doubled from $\sim$ 45 in 1979 to 95 in 2009, allowing the relatively dark ocean a longer period to warm up in response to solar radiation [*Overeem et al.*, 2011]. The subsequent delay in sea-ice freeze-up has led to exceptionally warm autumns on the western Arctic Slope [*Bieniek et al.*, 2014].

During site calibration, it was found that the long-term (1920–2012) air-to-ground temperature offset ΔT_{ag} is about 3.30 K at East Simpson. This long-term value falls in the middle of the modern ΔT_{ag} range (3.1–3.5 K) for the Arctic Coastal Plain determined from

analysis of DOI/GTN-P Climate Network data (Section 9.2). Thus, ΔT_{ag} does not appear to have substantively changed at East Simpson over the last century as would have been the case if factors other than air temperature had been a significant contributor to ground-temperature changes during this time. Thus, the local offset air-temperature record can be used to estimate near-surface permafrost temperatures over the period 1920–1970. Actual permafrost temperatures during this time are expected to have deviated from the air-based estimate over short periods, as witnessed during 1976–1988. We also found during site calibration that the mean surface temperature at East Simpson during the 1800s was about −11.8°C. Assembling the mean 1800s surface temperature, the air-based estimate of the 1920–1970 surface temperatures, and the borehole-based 1970–2012 surface temperatures, provides a view of permafrost warming at East Simpson since the end of the Little Ice Age (**Figure 9.17**). Permafrost temperatures at this site warmed 2.0 K between the 1800s and 1970, and an additional 3.1 K between 1970 and 2012. The total warming since the end of the LIA is then 5.1 K at this site.

There are few records with which to compare these values. In the original analysis of North Slope borehole temperature logs, *Lachenbruch and Marshall* [1986] found that near-surface temperatures had warmed 2–4 K over the several decades to century prior to 1984 based on wells with minor thermal conductivity variations. Our East Simpson warming over the same time period is near the bottom end of their range. The large variance in their warming estimate probably stems from the thermal conductivity vari-

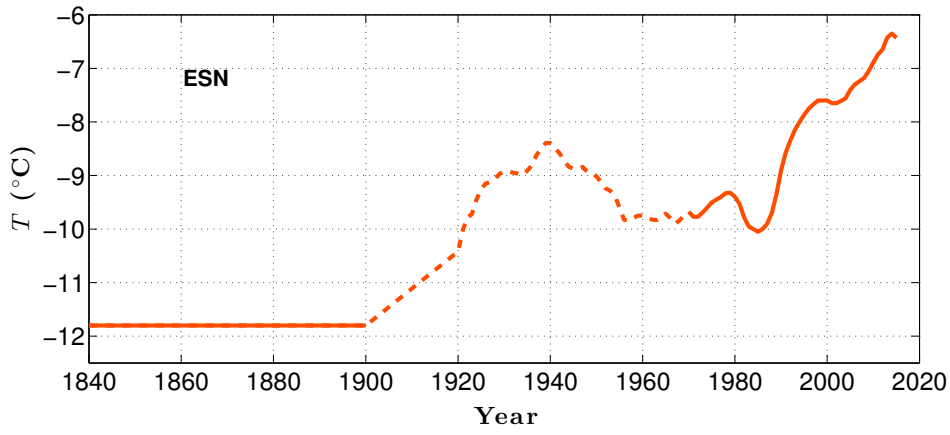

Figure 9.17: Permafrost temperatures (1.2-m) beneath undisturbed tundra adjacent to the East Simpson well site since the 1800s.

ations that we now recognize occur in even the best of wells in the NPR-A. The only other estimate of temperature during the 1800s in arctic Alaska comes from analysis of tree-ring data obtained near the boreal forest treeline. Unfortunately, these data were lumped with similar data obtained across Canada. It is now recognized that temperature changes in the northern boreal forests have been quite different in arctic Alaska, northwestern Canada, and northeastern Canada. Nonetheless, *Jacoby and D'Arrigo* [1989] report arctic temperatures in North America warmed about 1 K between the mid-1800s and 1970. Our value on the Beaufort Sea coast is twice that value.

Permafrost on the Arctic Slope has been thick and continuous for thousands of years. However, this situation may soon change. Surface temperatures in undisturbed permafrost at East Simpson are now about $-6.5°$C. Direct measurement of 1.2 m temperatures at the Drew Point climate station 26 km to the east have been giving similar values for the last couple of years. As a rule of thumb, the boundary between continuous and discontinuous permafrost occurs at locations where the mean-annual ground temperature is $-5°$C. At the current warming rate (0.73 K decade^{-1}), East Simpson will reach this transition point in about 20 years. However, it would take some time for the surface warming to reach the base of permafrost. Should that happen, the landscape of the area will change dramatically as the hydrologic system completely reorganizes. In Alaska, the boundary between continuous and discontinuous permafrost is currently located south of the Brooks Range.

9.5 Summary and conclusions

Through the site calibration process, we are able to establish the shallow (< 50 m) thermal properties needed to assess the thermal disturbance caused by the reserve pit and drill pad at a well site. Once these local landscape-change effects have been determined, the portion of the observed borehole temperature warming caused by climate change can be found. Applying this methodology to borehole temperature data acquired in the East Simpson No. 1 well on the Beaufort Sea coast, we find the following: (a) Air-temperature changes have been the primary driver of permafrost warming in this area over the last century. Although factors other than air-temperature change (e.g., changes in the seasonal snowpack) have played a significant role in changing permafrost temperatures over short periods, there is no indication that this has been the case on the century timescale. (b)

A transition occurred in the derived air-to-ground temperature offset during the 1990s that coincides with the time air-temperature anomalies on the Arctic Slope became asynchronous with the rest of the state, and with the PDO. This decoupling of the Arctic Slope is associated with the massive loss of sea ice in the neighboring Beaufort and Chukchi seas that has occurred since the mid-1980s. (c) Near-surface permafrost has warmed 5.1 K in this area since the 1800s. Of this, 3.1 K of warming has occurred since 1970. The current rate of warming in this area is 0.73 K decade^{-1}. (d) Should the warming continue at the current rate, near-surface permafrost temperatures will reach -5°C within 20 years. As East Simpson is located on the Beaufort coast near the coldest part of the Arctic Slope, this would mark the beginning of the transition of the entire Arctic Slope from continuous to discontinuous permafrost. Such a transition would cause significant landscape and environmental changes.

9.6 References

Barnhart, K.R., Anderson, R.S., Overeem, I., Wobus, C., Clow, G.D., and Urban, F.E. (2014), Modeling erosion of ice-rich permafrost bluffs along the alaskan Beaufort Sea coast, *J. Geophys. Res. Earth Surf.*, 119, doi:10.1002/2013JF002845.

Bieniek, P.A., Walsh, J.E., Thoman, R.L., and Bhatt, U.S. (2014), Using climate divisions to analyze variations and trends in Alaska temperature and precipitation, *J. Climate*, 27, 2800–2818, doi:10.1175/JCLI-D-13-00342.1.

Bowker, A.H., and Lieberman, G.J. (1972), *Engineering Statistics* (2d ed.), Englewood Cliffs, N.J., Prentice-Hall, 641 p.

Brown, J. (1967), An estimation of the volume of ground ice, coastal plain, northern Alaska, U.S. Army Material Command Cold Regions Research and Engineering Laboratory Research Tech. Note, 22 pp.

Choi, J., and Bischof, J.C. (2010), Review of biomaterial thermal property measurements in the cryogenic regime and their use for prediction of equilibrium and non-equilibrium freezing applications in cryobiology, *Cryobiology*, 60, 52–70, doi:10.1016/j.cryobiol.2009.11.004.

Davis, N. (2001), *Permafrost - A Guide to Frozen Ground in Transition*, Univ. of Alaska Press, Fairbanks, 351 pp.

Deming, D., Sass, J.H., and Lachenbruch, A.H. (1996), Heat flow and subsurface temperature, North Slope of Alaska, in *Thermal Evolution of Sedimentary Basins in Alaska*, USGS Bulletin 2142, 21–44.

Husky Oil NPR Operations (1983a), Design and construction of the Awuna wellsite, prepared by T.E. Brooks, Anchorage, Alaska.

Husky Oil NPR Operations (1983b), Geological report Tunalik Test Well No. 1, prepared by H. Haywood, Anchorage, Alaska.

Husky Oil NPR Operations (1983c), Geological report East Simpson Test Well No. 1, prepared by H. Haywood, Anchorage, Alaska.

Jacoby, G.C., and D'Arrigo, R. (1989), Reconstructed northern hemisphere annual temperature since 1671 based on high-latitude tree-ring data from North America, *Climatic Change*, 14, 39–59.

Lachenbruch, A.H., and Marshall, B.V. (1986), Changing climate: geothermal evidence from permafrost in the alaskan Arctic, *Science*, 234, 689–696.

Morrissey, L.A., and Ennis, R.A. (1981), Vegetation mapping of the National Petroleum Reserve in Alaska using Landsat digital data, *USGS Open-File Report 81-315*, U.S. Geological Survey, 27 pp.

Overeem, I., Anderson, R.S., Wobus, C.W., Clow, G.D., Urban, F.E., and Matell, N. (2011), Sea ice loss enhances wave action on the arctic coast, *Geophys. Res. Lett.*, 38, L17503, doi:10.1029/2011GL048681.

Romanovsky, V., Oberman, N., Drozdov, D., Malkova , G., Kholodov, A., and Marchenko, S. (2011), Permafrost, in *State of the Climate in 2010*, *Bull. Amer. Meteor. Soc.*, 92, S152–S153.

Urban, F.E., and Clow, G.D. (2016), DOI/GTN-P climate and active-layer data acquired in the National Petroleum Reserve–Alaska and the Arctic National Wildlife Refuge, 1998–2014, *USGS Data Series 977*, U.S. Geological Survey, http://dx.doi.org/10.3133/ds977.

Walker, D.A., and Acevedo, W. (1987), Vegetation and a Landsat-derived land cover map of the Beechey Point Quadrangle, Arctic Coastal Plain, Alaska, *CRREL Report 87-5*, USA Cold Regions Research and Engineering Laboratory, Hanover, NH, 52 pp.

CHAPTER 10

SUMMARY AND CONCLUSIONS

The Arctic is highly sensitive to increases in global mean air temperature as exemplified by the large and persistent physical and biological changes currently being observed there. In turn, the Arctic can have a significant impact on the global climate system through ice-albedo feedbacks and the potential loss of vast amounts of methane (a potent greenhouse gas) stored in permafrost to the atmosphere. Despite this, the Arctic remains a data-sparse region, limiting our understanding of critical processes and our ability to project future environmental conditions in the Arctic and at mid-latitudes. To address this issue, several initiatives have been undertaken to develop comprehensive observing systems for the atmosphere, ocean, and terrestrial components of the Arctic climate system (e.g., the Sustaining Arctic Observing Networks initiative). These observing systems are generally built from an aggregation of many national and regional observing networks. The success of these comprehensive observing systems critically depends on the contributions from the individual networks.

One such network is the DOI/GTN-P Deep Borehole Array whose purpose is to monitor the thermal state of permafrost on the Arctic Slope of Alaska, a region of thick continuous permafrost. The origin of the network began 40 years ago with the drilling of deep exploration wells in the National Petroleum Reserve–Alaska (NPR-A). Periodic temperature measurements in these monitoring wells have shown a strong near-surface warming, particularly since $\sim$ 1990. Ordinarily, thick continuous permafrost would be an ideal medium in which to monitor the response of the solid earth to a changing climate. However, several challenges unique to deep arctic boreholes have hampered our ability to interpret the warming observed in these wells. These challenges include: (a) Large amounts of heat were pumped into the permafrost surrounding the wells when they were drilled. Because of the magnitude of the heat involved and the duration of drilling, all the temper-

ature measurements acquired in these wells are disturbed to some extent by the drilling. For the purposes of studying the effects of climate change on permafrost, or using permafrost as a recorder of climate change, the drilling disturbance must be accounted for and removed from the borehole temperature data. This requires a drilling disturbance model that properly accounts for the intermittent drilling of the boreholes, latent-heat effects associated with the melting and subsequent refreezing of permafrost surrounding a wellbore, and boundary effects near the earth's surface. Prior to this study, no models with these capabilities existed. (b) Drilling operations in the NPR-A during the 1970s and 1980s required the construction of a reserve pit to handle the circulating drilling muds and an elevated drill pad to support the drill rig and camp. Upon completion of drilling, attempts were made to revegetate the drill pads while the reserve pits were mostly left to fill with water. In most cases, revegetation was only partially successful. As a result, temperatures beneath both the drill pad and the reserve pit can be substantially different from those under the surrounding 'undisturbed' tundra. Since the well-heads of the NPR-A boreholes are all located near the edge of the drill pad and close to the reserve pit, a multidimensional permafrost thermal model is required to account for the thermal disturbance caused by these local landscape-change features. Again, prior to this study no models with these capabilities existed. (c) All models used to help interpret the observed temperature changes in the wells require information about the thermophysical properties of the materials into which the wells were drilled. Very little has been known about these properties in the NPR-A. What we have known is that permafrost in this area consists primarily of fine-grained sedimentary sequences of claystones, siltstones, and shales. The properties of frozen fine-grained sediments are complicated by the existence of substantial amounts of unfrozen water at temperatures well below 0°C, producing strong nonlinear heat-transfer effects at the temperatures experienced on the western Arctic Slope. (d) The temperature data collected over the last 40 years in the DOI/GTN-P Deep Borehole Array were obtained using a variety of logging systems and techniques. A thorough understanding of the instrumentation and data collection methods is required to process the data in a way that produces a homogeneous dataset from all the temperature logs acquired in these wells.

Substantial progress has been made to resolve the issues preventing a clear identification of the climate signal present in the arctic Alaska borehole temperature logs. Based on these efforts, we find:

1. In the absence of sedimentary-core measurements, both the early and more-recently-obtained temperature logs are critical for determining the thermal properties of the subsurface materials present at the well sites. As the thermal disturbance caused by drilling is on the order of 1–4 K in the early USGS temperature logs, careful attention must be given to correcting the logs for this nonclimatic disturbance. An analysis using a new 2-D analytical model shows that the drilling disturbance within 32 well-diameters of a borehole can be up to a factor of two different for intermittently-drilled and uniformly-drilled wells, at least for recovery periods $\delta\tau$ less than or equal to the drilling duration τ_s. Many of the early NPR-A temperature logs fall into this category. In addition, latent-heat effects that occur when drilling through ice-rich permafrost can amplify the drilling disturbance by a factor of 4 at recovery times $\delta\tau \approx 2\tau_s$ and by 1.5 at $\delta\tau \approx 10\tau_s$. The actual amplification depends on the sediment texture and porosity at the well site. Vertical heat-transfer effects are found to be important near the earth's surface, significantly reducing the drilling disturbance from that predicted by expressions based solely on radial heat transfer. The 2-D analytical model indicates the drilling disturbance for the NPR-A boreholes was significantly affected by vertical heat-transfer from the surface to the 70-m depth within 10 years of well completion and to the 140-m depth within 40 years of well completion. This encompasses the depth range of primary interest for climate-change studies. As the nonlinear heat-transfer effects endemic to fine-grained permafrost are best studied with a numerical model, the drilling-disturbance correction for each well site was determined using the 2-D cylindrical version of the numerical heat-transfer model (CVPM) developed for this study.

2. By analyzing the recovery of temperatures from the drilling disturbance, the base of ice-rich permafrost (B-IRP) has been identified in 80% of the wells. The depth of the B-IRP provides the freezing point T_f for interstitial ice in permafrost. Although the depth of the B-IRP is found to be quite variable in the NPR-A, even over distances as short as 20 km, the freezing point is found to be much more uniform. For example, the freezing point of Nanushuk-*Corwin* rocks in the western NPR-A is found range -0.7°C to -0.8°C. Colville-B rocks in the eastern NPR-A have the lowest freezing point, about -5°C. Most of

the other NPR-A permafrost units have freezing points ranging $-1°C$ to $-2°C$.

3. The freezing point T_f and a transient heat-flow analysis provide constraints on the average sediment texture, porosity, and grain thermal conductivity of the rock units present in the permafrost zone of the NPR-A. As expected from geologic reports, permafrost porosities are found to be low ($< 17\%$) in the western NPR-A. Porosities are both higher and more variable in the eastern NPR-A. Mean grain conductivities are generally low (0.6–1.5 W m^{-1} K^{-1}) for NPR-A mudrocks. The Colville-B unit in the eastern NPR-A has a significantly higher grain conductivity (2.5–3.5 W m^{-1} K^{-1}) than the other permafrost units, most likely due to a higher sand content. Sediment textures range from kaolinite/Suffield-silty-clay mixtures (Colville-B) to Fairbanks-silt/very-fine-sand mixtures (Nanushuk-*Corwin*). These textures in conjunction with the porosities produce the observed freezing point depressions, T_f. Below the surficial layer, the volume fraction of ice tends to be low ($< 10\%$) for most of the permafrost in the NPR-A, explaining the difficulty of detecting interstitial ice using non-thermal geophysical logs. Lithologic variations are great enough in the NPR-A to mask the expected change in the temperature gradient at the B-IRP due to the thermal conductivity contrast between ice and water. Colville-B rocks have the highest heat capacities, primarily due to the proximity of near-surface temperatures to the freezing point of these rocks. Paralleling the grain conductivities, bulk thermal conductivities are generally low ($<$ 1.5 W m^{-1} K^{-1}) in the NPR-A. An exception are the occasional sandstone layers which have higher conductivities. Thermal diffusivities are generally very low (0.1–0.5 $\times 10^{-6}$ m^2 s^{-1}) below the surficial layer in the NPR-A. This partly stems from the behavior of unfrozen water in fine-grained permafrost. Given the sensitivity of the unfrozen water content to temperature, the bulk thermal conductivities and diffusivities are expected to change significantly in the upper 50 m over time in response to changing climate conditions.

4. Water-filled reserve pits adjacent to the drill pads produce a substantial subsurface warming at the wells that are increasing with time. The strength of this effect has been enhanced by a reduction of the maximum seasonal ice thickness on the reserve pits since $\sim$ 1980, another ramification of arctic climate change. At present, the reserve-pit warming at the standard permafrost reporting depth (20 m) in these wells ranges from almost zero to $+1$ K, depending on the distance of the well head from the edge of the reserve pit.

The reserve-pit warming at the Awuna well is exceptionally large due to the erosion of the pit towards the well. In this case, the thermal disturbance due to the reserve pit is the dominant contributor to the presently observed warming in the well. There is a continuum of vegetation states on the NPR-A drill pads, ranging from extremely sparse at several coastal locations to being much taller than the surrounding undisturbed tundra in the southern NPR-A. The ability of the pad vegetation to catch and retain snow in the ever-present arctic winds is the dominant factor controlling the temperature difference between the drill pads and the surrounding undisturbed tundra. This leads to a cooling effect beneath some some drill pads and a warming beneath others. The magnitudes of the drill-pad disturbance likely ranges between -0.9 K and $+0.5$ K at the 20-m depth at the location of the wells. The magnitude of reserve pit and drill-pad disturbances are large enough that they must be carefully considered when inferring climatic changes from the NPR-A borehole temperature logs. Given the strong lateral heat-flow effects near the wells and near-surface lithological variations, an assessment of these disturbances requires a multidimensional numerical heat-transfer model of permafrost. The proximity of the ocean to some of the coastal wells has had a negligible effect on the temperatures measured in these wells.

5. By assimilating local meteorological information into a multidimensional heat-flow analysis guided by the average thermophysical properties of rock units in the NPR-A, we are able to resolve the shallow thermal conductivity structure needed to assess the reserve pit and drill-pad disturbances. This 'site calibration' process also yields the mean temperature difference between the drill pad and the surrounding undisturbed tundra ΔT_{pad}, the long-term air-to-ground temperature difference ΔT_{ag}, and the mean surface temperature during the 1800s (T_{s0}). Applying the reserve pit and drill-pad disturbances as a correction to the drilling-corrected temperature logs yields temperature profiles free of the dominant non-climatic effects. These profiles represent the changing thermal conditions beneath undisturbed tundra adjacent to the well site. Implementing this methodology with the borehole temperature data acquired in the East Simpson No. 1 well on the Beaufort Sea coast, we find that: (a) Near-surface permafrost in this area has warmed 5.1 K since the 1800s. Of this, 3.1 K (60%) of the warming has occurred since 1970. Based on the 1970–2012 record, the current rate of near-surface permafrost warming in this area is 0.73 K decade^{-1}.

(b) Air-temperature changes have been the primary driver of permafrost warming over the last century. On multidecadal timescales, no other mechanism such as a thickening snowpack or earlier snowmelt is required to explain the warming of permafrost in this region. (c) A transition that occurred in the air-to-ground temperature offset ΔT_{ag} during the 1990s coincides with the time air-temperature anomalies on the Arctic Slope became asynchronous with the rest of the state and with the primary pattern of climate variability that controls temperatures in Alaska, the Pacific Decadal Oscillation (PDO). This climatic decoupling of the Arctic Slope is associated with the massive loss of sea ice in the neighboring Beaufort and Chukchi seas since the mid-1980s. Environmental conditions in the Arctic Basin have changed so dramatically over the last 30 years that conditions in the North Pacific Ocean have a much reduced role in controlling the climate of the Arctic Slope.

Despite its importance in the global climate system, the Arctic remains a data-sparse region. The methodology developed during this study potentially will allow climatic information to be extracted from a large source of information, temperature measurements made in deep boreholes drilled through permafrost in Alaska, Canada, and Siberia. Climate information obtained in this way can provide a historical context for the current Arctic warming, advance our understanding of processes controlling the response of permafrost to climate change, be used to test and improve climate models, and improve our ability to project future environmental conditions in the Arctic. Prior to this study the only estimate of temperatures on the Arctic Slope of Alaska during the 1800s came from the original work of *Lachenbruch and Marshall* [1986], although it wasn't clear at the time that the estimate pertained to the 1800s due to the uncertainty about the thermal properties of permafrost at the well sites. Studies presenting temperature estimates during the 1800s based on proxy climate data have been reported. However, these studies lumped several climate regions together (e.g., all of northern Alaska and Canada) so it's difficult to assess how their results pertain specifically to arctic Alaska. In addition, it is unclear to what extent the proxy results represent true mean-annual temperatures. The current study substantially revises the only thermometrically determined estimate of temperature change on the Arctic Slope since the 1800s. Although based on results from a single well, the availability of 20 wells in the array provides ample opportunity to verify these results

and to search for spatial patterns within the NPR-A study area. Finally, the availability of permafrost thermophysical properties resulting from this study vastly improves our ability to project how this region will respond to future climate change. Should the current warming rate continue, near-surface temperatures near the Beaufort coast (the coldest part of the Arctic Slope) will reach -5°C within 20 years. This would mark the beginning of the transition of the entire Arctic Slope from continuous to discontinuous permafrost. Such a transition would cause significant landscape and environmental changes. The northeastern NPR-A is likely to be one of the first areas to transition due to the exceptionally low freezing point (-5°C) of Colville-B rocks in the permafrost zone there.

10.1 References

Lachenbruch, A.H., and Marshall, B.V. (1986), Changing climate: geothermal evidence from permafrost in the alaskan Arctic, *Science*, 234, 689–696.